Theoretical Characterisation of Spheroidal PbSe/PbS Core/Shell Colloidal Quantum Dot Heterostructures

Thomas M. Walsh

Ph.D. Thesis

University of Salford

School of Computing, Science, and Engineering

2016

CONTENTS

LIST OF FIGURES

LIST OF TABLES

ACKNOWLEDGEMENTS

I would like to extend my unreserved thanks to the many people who have made this work possible. Without their support and encouragement, the current work could not exist.

First and foremost, to my supervisor Professor Stanko Tomić. His expertise and guidance have made this work possible. His patience and diligence as a mentor have been invaluable, and helped to develop my skills as a researcher.

To Dr. Jacek Milosewski, for many invaluable discussions on colloidal quantum dots, theoretical modelling techniques, general programming advice, collaborative efforts, and constant encouragement. Also for occasional lifts in his car.

To Mark Lundie, for invaluable discussions on quantum mechanics and theoretical condensed matter physics, as well as for his diligent work in maintaining the local cluster on which all calculations presented in this work were performed.

To all of the staff and students in the Physics department at the University of Salford for their continued support over the last three years, especially Professor Ian Morrison, Dr. Graham McDonald and Bruce Lewis for keeping the department in good working order. To all of the other residents of the postgraduate office, especially Slobodan Čičić, Alex Marshall, Dean Smith and Simon Steel, for many interesting, if not strictly relevant, discussions.

To the many members of staff in the postgraduate research and finance offices at the University of Salford, in particular Catriona Nardone and Vanda Thomlinson, for their help and extreme patience with matters of paperwork, especially when things did not go according to plan.

To the organisers and committees of the various conferences and meetings at which I have been permitted to present my work, as well as the various scientists and scholars with whom I have had the opportunity to spoke with at these events, of which there are too many to name.

Finally, I would like to thank the EPSRC for doctoral training account (DTA) funding over the last three-and-a-half years, as well as the Royal Society for the equipment provided by their grant (No. RG120558): "High Performance Computing in Modelling of Innovative Photo-Voltaic Devices."

To my friends and family. *This* is what I do.

Abstract

Nanocrystal quantum dots (NQDs) show great promise in the advancement of the field of photovoltaics. While the maximum efficiency of conventional solar cell (SC) devices is limited to $\sim 31\%$ (Shockley-Queisser limit), devices based on NQDs may attain a maximal thermodynamic efficiency of 42% through the exploitation of multiple exciton generation (MEG). In this process, several electron-hole pairs are created by the absorption of a single high energy photon, as opposed to the single excitons created in conventional solar cell devices. IV-VI semiconductor nanocrystals (PbS, PbSe) are of particular interest as candidates for the exploitation of MEG due to the narrow band gap, high confinement energies, and long radiative carrier lifetimes observed in these systems. In order to realise the full potential of MEG devices, full characterisation of the optoelectronic properties of the underlying nanoparticles is desirable.

While the size-dependent properties of NQDs are well understood, the effects of NQD shape are less so. This thesis investigates the effect of ellipticity on the optoelectronic properties associated with spheroidal NQDs. To this end, a four-band, anisotropic, and radially variant $\mathbf{k} \cdot \mathbf{p}$ system Hamiltonian is expanded in a planewave basis in order to calculate single-particle eigenenergies and eigenfunctions of colloidal PbSe/PbS core/shell heterogeneous NQDs of varying ellipticity. Many-body effects are accounted for via a full configuration interaction (CI) Hamiltonian, the basis of which is comprised of the single-particle states. Excitonic and bi-excitonic corrections are then found by mixing of the basis states. In this manner, such diverse electronic and optical properties as quasi-particle binding energies, momentum matrix elements, and charge carrier lifetimes, both radiative and non-radiative, may be predicted.

All results presented in this work have been obtained using the highly parallel `kppw` code, which has been augmented with new functionality pertaining to the description of spheroidal NQDs.

1

INTRODUCTION

The dominant means of energy production in the modern age are derived from the burning of fossil fuels. Current projections indicate that by the year 2040 the global demand for energy will increase by 37% (a growth rate of between 1% to 2% year-on-year), while carbon emissions correspondingly increase by 16% [1]. It is thought, given current trends, that 84% of energy production will still be derived from fossil fuel sources in 2030, while economically recoverable oil, coal, and gas reserves are expected to be depleted by the years 2040, 2042, and 2112 respectively [2]. Moreover, the environmental damage caused by the burning of fossil fuels is devastating. Recent climate data shows that global temperatures have increased by almost 1 °C above the 20^{th} century average (see figure 1.1) [3]. It is generally agreed upon that should global temperatures 2 °C above pre-industrial revolution levels, the effects of climate change will be catastrophic and irreversible. To this end, the agreement reached by the COP 21 meeting in Paris pledged to limit global warming to a maximum of 1 °C, with an ideal limit of 0.5 °C [4]. If these targets are to be met, a paradigm shift toward more environmentally friendly methods of power production must begin.

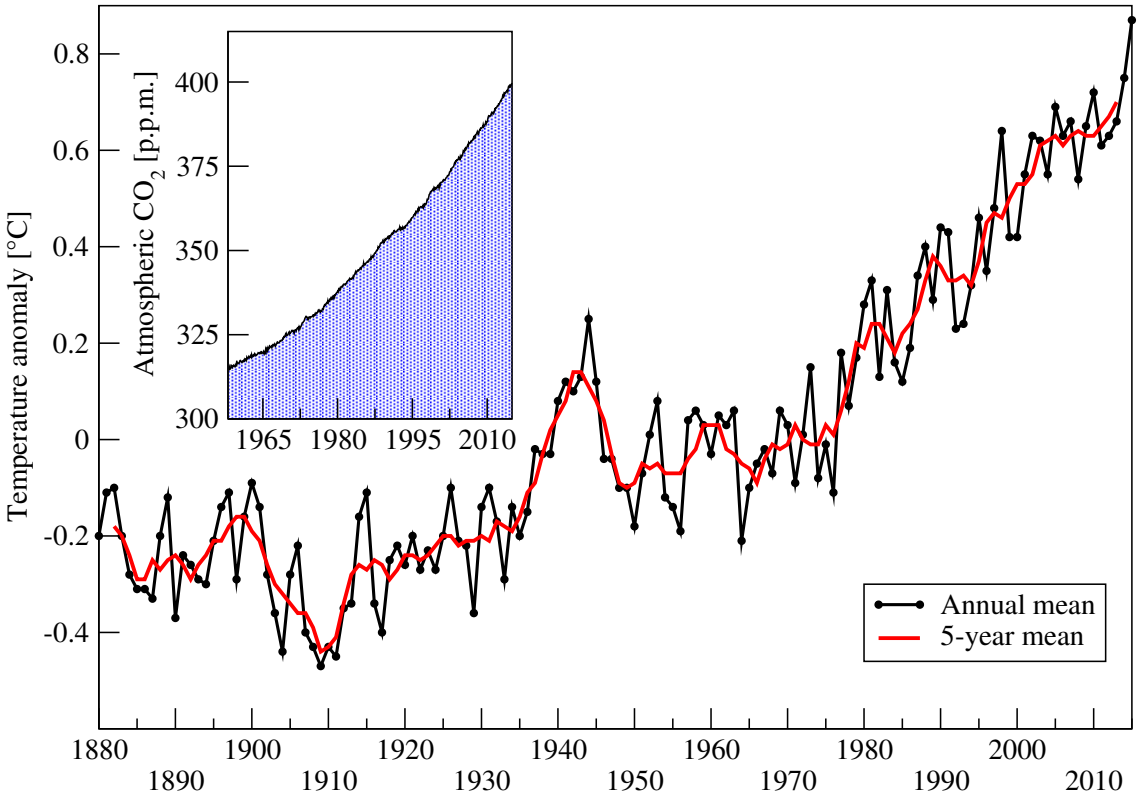

Figure 1.1.: Annual (black) and five-year (red) mean global temperature anomaly relative to the period 1951-1980. Inset: Atmospheric CO_2 levels over the period 1958-2015. Data obtained from NASA's public access records, which may be found in reference [3].

1.1 PHOTOVOLTAICS AS A POWER SOURCE

Photovoltaic solar cell devices are cheap to manufacture, require very little maintenance, and are easily installed, even in remote locations. The current (second) generation is limited in its attainable efficiency, however, by the intrinsic physical processes by which the solar cell devices operate. The maximum theoretical efficiency, known as the Shockley-Queisser limit, has been obtained from detailed balance calculations performed for an ideal solar cell. For a silicon based device with the standard p-n junction arrangement under unconcentrated solar illumination, and assuming both the Sun and the solar cell to be perfect blackbodies, the Shockley-Queisser limit is 30% [5]. The fundamental principles behind the operation of the second generation photovoltaic solar cell device will be outlined below.

Several schemes have been suggested by which the Shockley-Queisser limit may be surpassed. These schemes, collectively referred to as third generation solar cell devices, briefly comprise solar concentrators, multijunction solar cell devices, intermediate band devices, and devices which promote and exploit the process of multiple exciton generation (impact ionisation) [6–12]. Each of these will be discussed in turn below.

1.2 THESIS PREMISE

The third generation of photovoltaic solar cell devices is widely expected to be based upon semiconductor nanocrystal technology [13]. Such semiconductor nanocrystals exhibit the effects of *quantum confinement*. When the size of the nanocrystal is lesser than the de Broglie wavelength of its associated charge carriers, the carrier wavefunctions are localised strongly within the volume of the nanostructure, dramatically altering the electronic properties of the crystal. Semiconductor nanocrystals may exhibit quantum confinement in one, two,

or three spatial dimensions; the corresponding structures are termed quantum wells (or quantum films), quantum wires, and quantum dots (QDs), respectively. Confinement of the charge carriers has several effects on the electronic structure of the nanocrystal, the most dramatic of which is the discretization of the energy bands, along with an opening up of the interband energy gap (band gap) and intraband energy gaps. The discrete nature of the electronic states in nanocrystal quantum dots is high reminiscent of atomic energy spectra. Consequently, quantum dots are occasionally given the moniker of "artificial atoms." It has been predicted that, due to the *phonon bottleneck* effect observed in confined systems, the process of impact ionisation (where several electron-hole pairs are produced by absorption of a single photon) may be highly efficient in quantum dot based solar cells [14].

To date, the vast majority of research has been directed towards spherical quantum dots. From an experimental standpoint, this is largely due to the ease with which spherical colloidal QDs may be synthesised, while, computationally speaking, spherical symmetry greatly simplifies the calculations undertaken. In the current work, the effects of ellipticity (i.e. the eccentricity of the ellipsoidal cross-section of an ellipsoid of rotation) are analysed for spheroidal quantum dots from a theoretical standpoint. Due the their narrow bulk bulk bandgaps, the QDs studied are of those consisting of lead-chalcogenide nanostructures. Core/shell heterostructures of varying degrees of ellipticity are modelled. Single-particle properties are found by solving the Four-band $\mathbf{k} \cdot \mathbf{p}$ Hamiltonian in the inverse space, with excitonic corrections being included via a complementary configuration interaction (CI) calculation. This approach allows for the calculation of such diverse properties as: single-particle and many-particle eigenstates and eigenfunctions; exciton and biexciton binding energies; dipole, momentum, and optical matrix elements; transition strength and oscillator strengths; absorption cross-sections; and radiative and nonradiative carrier lifetimes. All calculations mentioned thus far have been implemented in-house

within the `kppw` code (originally developed by Stanko Tomić and colleges at Daresbury Laboratory) [15].

1.3 THESIS OUTLINE

The structure of the current work is as follows. Chapter 2 aims to familiarise the reader with the current generation of solar cell technology. A brief outline of the major developments in the field is given, followed by revision of the fundamental processes of solar energy conversion. The mechanisms by which energy is lost in the conversion process are detailed, including relaxation dynamics and recombination processes. The principles by which the maximum theoretical efficiency of a conventional solar cell device may be calculated are summarised.

The following chapters detail the proposed methods by which the Shockley-Queisser limit may be circumvented. Chapter 3 presents the various architectural schemes by which solar cell efficiency may be enhanced, including multijunction solar cell devices, intermediate band solar cells, and, perhaps most importantly, direct carrier multiplication via the impact ionisation process. Chapter 4 explores the effects of quantum confinement, and describes the mechanisms by which confined systems may exhibit improved carrier multiplication efficiencies (known as multiple exciton generation in colloidal quantum dots). Chapter 5 introduces in detail the unusual properties of bulk lead-chalcogenides, the properties of lead chalcogenide based quantum dots, and discusses core/shell PbSe/PbS heterostructures and spheroidal QD geometries.

The various modelling techniques used throughout the current work are detailed in Chapter 6. The limits of ab initio methods are presented, and the $\mathbf{k} \cdot \mathbf{p}$ perturbation theory introduced and extended to the four-band model used to calculate single-particle properties of the lead-based quantum dots. An overview of the plane wave basis in which the $\mathbf{k} \cdot \mathbf{p}$ Hamiltonian is represented is also presented. The configuration interaction (CI) method of obtaining many-particle

corrections to the eigenvalues of the $\mathbf{k} \cdot \mathbf{p}$ Hamiltonian is introduced. Finally, calculation of carrier lifetimes for radiative recombination and for direct carrier multiplication is discussed, with the explicit derivation of the required matrix elements given in appendix B.

Chapter 7 presents the findings of the current work. Single-particle energy states and the momentum matrix elements associated with interband transitions are presented for PbSe QDs and PbSe/PbS QD heterostructures for both spherical and spheroidal nanocrystals. It will be seen that in all cases anisotropy exists between those transitions polarised along the $\langle \bar{1}\bar{1}2 \rangle / \langle 1\bar{1}0 \rangle$ and the $\langle 111 \rangle$ crystallographic directions, and that for QDs elongated along either transverse direction, additional anisotropy is introduced between the $\langle \bar{1}\bar{1}2 \rangle$ and $\langle 1\bar{1}0 \rangle$ directions. Excitonic corrections are then added to the single-particle states via a CI calculation. It will be seen that strong size-dependent excitonic binding energy exists in the PbX QDs.

A summary of the conclusions from chapter 7 is given in chapter 8, and areas of further work are suggested.

2

PHOTOVOLTAIC SOLAR CELL DEVICES

Semiconductor crystals form a class of materials somewhere between insulators and conductors. They are characterised, as a consequence of the discrete nature of the atomic orbitals of their constituent atoms, and of the Pauli exclusion principle, by the formation of "energy bands"—quasi-continua of allowed energy states—separated by "energy gaps" consisting of forbidden states. The vast majority of modern technology is based on semiconductor physics, from the simple diodes and transistors which make up all computer technology to, perhaps as importantly, photovoltaic solar cell devices.

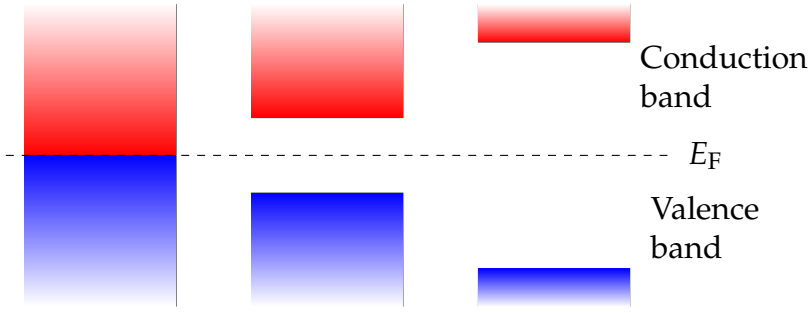

Figure 2.1.: Metallic (left), semiconductor (centre), and insulator (right) band structures about the Fermi level (dashed line).

The current chapter details the underlying physical processes by which photovoltaic cells based on bulk semiconductor technology with a p-n junction architecture operate. The major developments in the field since its beginnings in the 19th century to the present day are outlined. The photovoltaic effect and p-n junction are discussed, followed by the various loss mechanisms present in

realistic solar cell devices. Finally, the maximum theoretical efficiency (detailed balance limit of efficiency) for an ideal bulk solar cell device is discussed.

2.1 AN ABRIDGED HISTORY OF PHOTOVOLTAIC SOLAR CELL TECHNOLOGY

The photovoltaic effect was first observed by Alexandre-Edmond Bequerel in 1839 while experimenting with the effects of light when applied to an electrolytic cell [16, 17]. He noted that when two platinum electrodes, one of which was coated in silver chloride, were immersed in aqueous solution, a potential difference was established between the electrodes when illuminated with solar radiation. Little else was reported concerning the photovoltaic effect until the 1880s, when photoconductivity was separately reported in selenium and in metal sulphides by Smith and Braun, respectively [18–20].

While discussed qualitatively over the proceeding years, the photoelectric effect was not explained theoretically until the discovery of the photoelectric effect by Einstein in 1905, in turn based on the work of Plank and Hertz. The electronic band theory subsequently developed by Wigner and Seitz in 1933, coupled with the Czochralski process for growing high quality single crystal semiconductors at large size,[1] lead to the development of the first p-n junction by Ohl and colleges at Bell Laboratories in 1939 [22–26]. Upon attempting to produce purified silicon for use in microwave detectors, Ohl discovered that a photocurrent was produced in the silicon ingots upon exposure to light. It was found that small impurities remained in the ingots, and further that the different impurities separated during the smelting process. The two regions formed a boundary, the first p-n junction, where the photocurrent was produced. In 1946, Ohl was granted a US patent for a "light-sensitive electronic device" [27]. While the first functional solar cell device is attributed to Charles Fritts (a selenium based device with an

1 The Czochralski (CZ) method involves melting the semiconductor material in a crucible, and placing a seed at the surface. The seed is then slowly pulled out of the melt while being rotated. The resulting cylindrical ingots include relatively few crystal defects.[21]

operational efficiency of less than 1%), the first solar cell device to operate with reasonable efficiency was that developed by Ohl [28].

The underlying theory behind semiconductor physics and photovoltaic devices advanced greatly over the following years. The first theory of the p-n junctions was developed by William Shockley in 1949, and was subsequently refined in collaboration with Sah and Noyce [29, 30]. Meanwhile, Shockley, in collaboration with Read, published their theory on trap-assisted nonradiative carrier recombination in semiconductor crystals [31]. At the same time, Hall published his paper describing a similar phenomenon in germanium [32]; the resulting theory is known as the *Shockley-Read-Hall recombination*. This is a process whereby trap states assist carrier recombination, and is a source of inefficiency in photovoltaics. Understanding of the Shockley-Read-hall effect has lead to more efficient solar cell devices.

In 1961, Shockley and Queisser published their landmark paper on the "Detailed balance Limit of Efficiency of p-n Junction Solar cells" [5]. In this groundbreaking work, the principle of detailed balance is applied to a silicon-based solar cell device under solar illumination. By considering only radiative recombination, and the Sun and the solar cell device to be blackbodies in equilibrium with their surroundings, the maximum theoretical limit of efficiency for a perfect silicon SC device was calculated to be 30% under standard solar illumination.

To date, photovoltaic solar cell devices have been manufactured from many different materials and architectures, including the crystalline and monocrystalline (Czochralski method) silicon as discussed above, and thin film solar cells based on cadmium compounds (II-VI semiconductors) and III-V arsenides and nitrides (Ga/Al/In) [33]. Due to its low cost, crystalline silicon cells are by far the most common SC devices in use today. As of March 2016, the efficient record for a crystalline silicon solar cell device stands at 25.6% under standard AM1.5 illumination[2], while the overall efficiency record, set by a multijunction

2 *Air mass coefficient* 1.5 is the standard illumination by which solar cell devices are characterised. The optical path length of solar irradiation is 1.5 times longer than irradiance from the zenith.

GaIn/GaAs/GaInAs/GaIn device under a concentration of 508 suns, stands at 46% [33–36]. The most efficient commercial SC devices currently available exhibit an efficiency of 22.9% [37].

All existing solar cell devices (outside of the lab) are based on the p-n junction and operate on the photovoltaic effect. Accordingly, the next two sections will deal with these two important principles in turn.

2.2 THE SEMICONDUCTOR P-N JUNCTION

The simple semiconductor diode, or p-n junction, is arguably the most important invention of the 20^{th} century. It is the basis of almost all modern electronics, including the photovoltaic solar cell. The p-n junction consists of a semiconductor heterojunction, ideally grown from a single crystal, with different crystal impurities included at either side of the junction (a process known as "doping") [38, 39]. The dopants on the n-side of the junction introduce an excess of negative charge carriers (electrons), while the donors on the p-side provide an excess of positive charge carriers (holes). The positive and negative donors are respectively referred to as donor and acceptor impurities. In the case of a silicon (group IV) based device the donor atoms are the pentavalent group V elements (P, As, Sb, Bi), while the acceptor impurities are the trivalent group III elements (B, Al, Ga, In).

When the two regions are in electrostatic contact, a p-n heterojunction is formed. Once in contact, electrons from the n-region diffuse across the junction to the p-region, while holes from the p-region diffuse likewise to the n-side. While the p and n-regions themselves remain charge-neutral (the additional charge carriers are balanced by the nuclear charges of the dopant atoms), the carrier diffusion results in in a negatively (positively) charged region on the p-side (n-side) of the heterojunction. As charge accumulates in the interface region, the rate of charge transfer is reduced until the carrier diffusion is ex-

actly balanced by the intrinsic electric field (pointing from the n-region to the p-region). This field is known as the *intrinsic bias* of the device. The resulting charged region, where no free carriers exist, is known as the *space-charge region*, or *depletion region* (see figure 2.2). Further charge (i.e. electric current) can only flow across the junction under an applied electric field. Even so, current may only flow easily from the n-side to the p-side (forward bias); in order for current to flow in the opposite direction, a large voltage must exist across the junction in order to overcome the intrinsic field (reverse bias). It is this property of the p-n junction which makes it so useful for electronic applications.

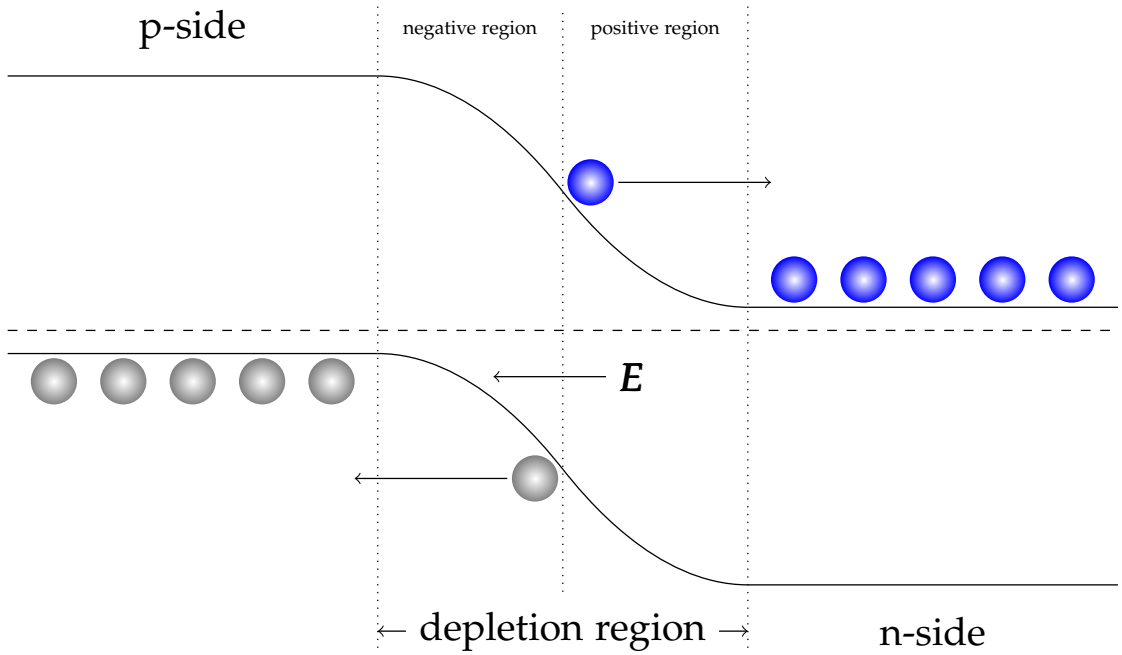

Figure 2.2.: Schematic of a semiconductor p-n junction. Electrons (holes) diffuse into the p-region (n-region) and form a depletion region at the interface containing no free carriers and establishing device bias. Photogenerated charge carriers inside the junction are quickly separated by the intrinsic field $\boldsymbol{E}$.

Should an incident photon be absorbed in the space-charge region, the resulting photoelectron and photohole will quickly be separated by the intrinsic field, with the electron drifting into the n-type region, and to hole to the p-side. If the two sides of the junction are attached to an external circuit, a photocurrent is produced. This process, resulting from the combination of the photovoltaic

effect and p-n junction architecture, is the operation basis of all 2nd generation solar cell devices [38].

2.3 THE PHOTOVOLTAIC EFFECT

Upon illumination of a semiconductor material, there is a chance for light to be absorbed. Should this be the case, the incident photon is annihilated, with its energy being transferred to an electron in the valence band (VB). The electron is then excited across the band gap to into the conduction band (CB), leaving behind a "hole" in the valence band. The electron hole is a quasiparticle representing an empty electron state in the valence band. the hole possesses equal but opposite electronic charge, and has positive effect mass independent to that of the electron. In the language of second quantisation, this event is synonymous to the creation (annihilation) of an electron in the conduction band (valence band) and the simultaneous creation (annihilation) of an electron hole in the valence band (conduction band). The electron and hole are in contact via the Coulomb interaction, and are said to form a bound electron-hole pair (ehp). The resulting quasiparticle is known as an *exciton*. The exciton has a net-zero charge, and positive binding energy. The binding energy of the exciton is, however, in general too weak to be considered a true quasiparticle in the majority of bulk materials; in the rest of this thesis, the term "exciton" will be reserved to describe the strongly bound electron-hole states found in quantum nanocrystals.

From the band theory of solids and considerations of energy conservation, it is clear that incident photons of sub-bandgap energy $h\nu < E_g$ cannot be absorbed (since the photoelectron would be forced to occupy a state in the forbidden region between the energy bands, see figure 2.3). Further, except in the exceptional case that the photon energy is exactly equal to the band gap, there will be an energy excess: the photoelectron and photohole will not be created at the conduction band minimum (CBM) and valence band maximum (VBM). In this case,

the excess energy of the photon $h\nu - E_g$ is resolved in the kinetic energy of the charge carriers (photons with energy $h\nu > E_g$ will henceforth be referred to as "high-energy" photons). Conservation of momentum dictates that the charge carrier with the lighter effective mass be imparted with the greater share of the photon energy [40, 41]. For the majority of inorganic semiconductor materials it is the electron which has the smaller effective mass, however some notable exceptions include the lead-chalcogenides (see chapter 5). The excess energy is divided between the photoelectron and photohole carriers as

$$\Delta E_e = \left(h\nu - E_g\right)\left[1 + \frac{m_e^*}{m_h^*}\right]^{-1} \tag{2.1}$$

and

$$\Delta E_h = \left(h\nu - E_g\right) - \Delta E_e, \tag{2.2}$$

where m_e^* and m_h^* are the charge carrier effective masses, ΔE_e is the energy of the electron relative to the CBM, and ΔE_h is the hole energy relative to the VBM. In confined systems, the partition of the excess photon energy is restricted by the discrete nature of the energy structure and the selection rules between these quantised states.

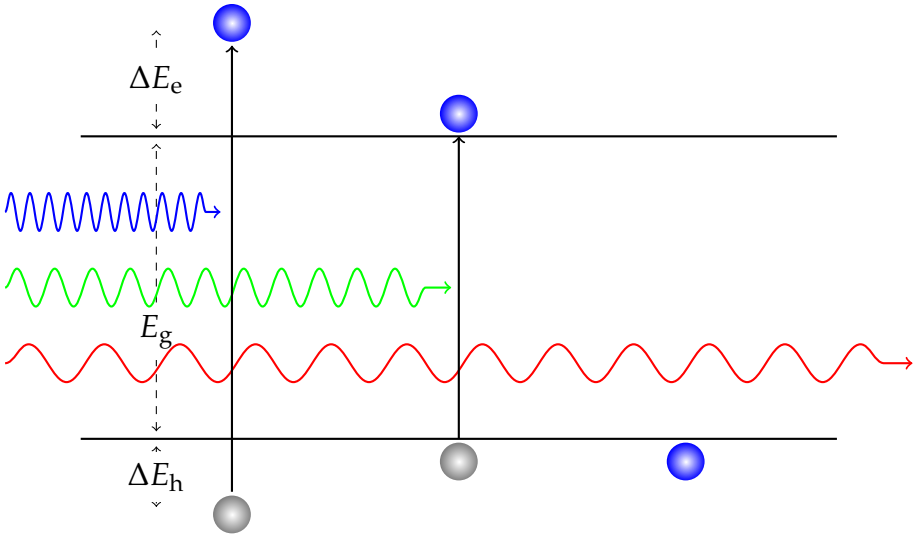

Figure 2.3.: Photoabsorption in a photovoltaic cell. High energy photons (blue) excite electrons (holes) far above (below) the CBM (VBM) by energy ΔE_e (ΔE_h). The cell is transparent to photons of sub-bandgap energy.

The kinetic energy of the charge carriers produces an effective temperature in excess of the (ambient) temperature of the crystal lattice. Accordingly, such high-energy charge carriers are often referred to as "hot carriers." The charge carrier effective temperature may be as much as an order of magnitude higher than the lattice temperature [42]. Due to their large effective masses in most inorganic semiconductors, hot holes tend to equilibrate with the lattice at a faster rate than hot electrons.

Before they are extracted in order to contribute to the photocurrent, hot carriers must first cool to the band edges (one notable exception being hot-carrier extraction cells, where carriers are extracted before cooling). Thermalisation typically occurs via several relaxation processes. Such process represent severe loss mechanisms in conventional photovoltaic cells, and will be dealt with in the following sections.

2.4 CARRIER RELAXATION DYNAMICS

Photoexcited charge carriers are often found far from their respective band edges immediately following photoabsorption. For an ensemble of hot photocarriers, not only are the electrons and hole far from equilibrium with the lattice, but they may further be found far from equilibrium from one another. On cooling toward the band edges, hot carriers typically undergo several themalising interactions, the fastest of which is like-carrier scattering.

Through scattering with like charges, the excess energy of initially hot carriers is distributed more evenly amongst electrons high above the VBM and holes far below the CBM, with the carriers forming two independent Boltzmann distribution within their respective bands [13]. The two distributions will then equilibrate with one another via electron-hole scattering between the bands. These processes take place in time periods on the order of 10 ps [13].

Hot carriers further equilibrate with the lattice via phonon emission [43, 44]. This process may be either direct or indirect. In the latter process, one carrier relaxes to the band edge while the excess energy is transferred to a second carrier (Auger process). The rate of Auger cooling is much less than the rate of direct relaxation in most systems. The system is considered to be in equilibrium once all carriers are found within $\sim k_B T$ of the band edges. Complete thermalisation of the charge carriers usually takes place over hundreds of picoseconds [13]. The phonons involved in these processes are longitudinal, optical phonons.

Once in equilibrium with the lattice, charge carriers may be extracted (for example, from within a p-n junction), and are free to add to the photocurrent of the device. Isolation of the carriers must take place in sufficient time as to avoid carrier recombination across the band gap. Carrier recombination may be either radiative, in which case the downward electron transition is accompanied by emission of a photon of energy $h\nu \approx E_g$, or non-radiative, for example in Auger recombination where a secondary charge carrier (usually an electron) is imparted with energy E_g.

For each of the processes mentioned above the scattering rates, and therefore carrier lifetimes, may be found using *Fermi's golden rule*. As such, the next subsection will be devoted to familiarising the reader with Fermi's golden rule for the transition probability before each of the scattering processes are addressed in the following subsections in turn.

2.4.1 *Fermi's Golden Rule*

Fermi's golden rule gives a measure of the probability per unit time for an optical transition from initial energy eigenstate $|i\rangle$ to final energy state $|f\rangle$. The golden rule was first derived by Paul Dirac in the 1920s [45]. In a paper presented to the Royal Society, Dirac derived equations to describe photoabsorption and photoemission in an atom; this paper was the first step toward a full

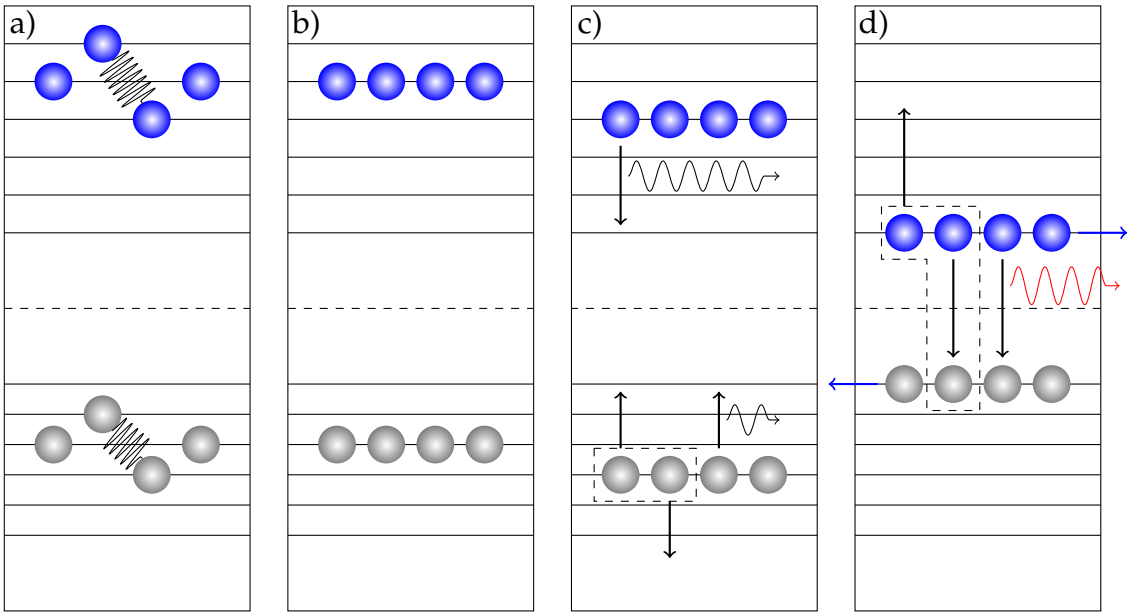

Figure 2.4.: Schematic of thermalisation processes of hot carriers: a) like-carrier scattering produces independent Boltzmann distributions in the bands; b) electron-hole scattering equilibrates the distributions; c) carriers cool via phonon emission (small Auger component); d) carriers are extracted or recombine either radiatively or nonradiatively.

description of light-matter interactions in the language of quantum mechanics (quantum electrodynamics, QED). He found that the rate of photoemission was not time-dependent, and proportional only to the matrix element $\langle \mathrm{f}|H'|\mathrm{i}\rangle$ of the time-dependent perturbation between initial and final states, and to the energy density of final states. From this result, it follows that the transition rate in any quantum system is (approximately) a constant (in the limit that $t \to \infty$). Despite first being derived by Dirac, the golden rule is named for Enrico Fermi, who referred to it as "Golden Rule No. 2" the 1950's [46, 47].

Consider the time-dependent Schrödinger equation:

$$\mathcal{H}\left|\psi\left(t\right)\right\rangle = i\hbar\frac{d}{dt}\left|\psi\left(t\right)\right\rangle, \tag{2.3}$$

where the Hamiltonian $\mathcal{H}$ is equal to steady-state Hamiltonian H_0 plus a time-dependent perturbation Hamiltonian H', where H' is in some sense much smaller

than H_0. The wavefunction $|\psi(t)\rangle$ may be expanded in terms of known solutions to the eigenvalue equation $H_0 |\phi_n\rangle = E_0 |\phi_n\rangle$ as

$$|\psi(t)\rangle = \sum_n c_n(t) \exp\left[-\frac{iE_n^{(0)}t}{\hbar}\right] \left|\phi_n^{(0)}\right\rangle, \tag{2.4}$$

where $\{c_n(t)\}$ are unknown coefficients of the expansion, which may be determined using standard time-dependent perturbation theory. Since they are time-dependent, $c_n(t)$ are related to the time-dependent perturbation H'. Once $\{c_n(t)\}$ has been found, the probability for a transition between initial and final states $|\mathrm{i}\rangle$ and $|\mathrm{f}\rangle$ is then equal to the square modulus;

$$\begin{aligned} P_{\mathrm{i}\to\mathrm{f}} &= \left|\langle f \mid H' \mid i\rangle\right|^2 \\ &\times \left| \frac{\cos\left[\left(E_f^{(0)} - E_i^{(0)}\right) t/\hbar\right] - 1}{E_f^{(0)} - E_i^{(0)}} + i\frac{\sin\left[\left(E_f^{(0)} - E_i^{(0)}\right) t/\hbar\right]}{E_f^{(0)} - E_i^{(0)}} \right|^2 \end{aligned} \tag{2.5}$$

where the superscript "(0)"s have been added to emphasise that the energy states E_i and E_f are those of H_0. The transition probability per unit time is then found in the time derivative of equation 2.5, and by integrating over the final density of states:

$$W_{\mathrm{i}\to\mathrm{f}} = \frac{2}{\hbar^2}\left|\langle \mathrm{f} \mid H' \mid \mathrm{i}\rangle\right|^2 \int dE \rho(E) \left[\frac{\sin\left\{\left(E_f^{(0)} - E_i^{(0)}\right) t/\hbar\right\}}{E_f^{(0)} - E_i^{(0)}}\right]^2, \tag{2.6}$$

with the integral being replaced by a summation in the limit that the final density of states, $\rho(E)$ is discrete (as is the case for quantum dots). Since the unperturbed eigenstates are assumed to be known, then, in accordance with Heisenburg's uncertainty principle

$$\left(E_\mathrm{f}^{(0)} - E_\mathrm{i}^{(0)}\right) \Delta t \geq \frac{\hbar}{2}, \tag{2.7}$$

the transition time is long. In the limit $t \to \infty$, the integral in equation 2.6 may be approximated by a Dirac delta function, leading to

$$W_{\mathrm{i}\to\mathrm{f}} = \frac{1}{\tau} = \frac{2\pi}{\hbar} \left|\left\langle \mathrm{f} \,\middle|\, H' \,\middle|\, \mathrm{i} \right\rangle\right|^2 \delta\left(E_{\mathrm{f}}^{(0)} - E_{\mathrm{i}}^{(0)}\right), \tag{2.8}$$

where τ is the carrier lifetime. The δ-function may be thought of as an energy conservation term. Equation 2.8 is the expression for Fermi's golden rule. The transition rate from in initial state $|\mathrm{i}\rangle$ to final state $|\mathrm{f}\rangle$ is (approximately) constant, and depends solely on the matrix element $\langle \mathrm{i}|H'|\mathrm{f}\rangle$, subject to energy conservation. This important result is applicable to any quantum systems, provided that the time interval is sufficiently long. The various processes in photovoltaic solar cells to which equation 2.8 may be applied are detailed in the following sections. The treatment herein closely follows in the approach of Singh [43, 44].

2.4.2 *Carrier-Carrier Scattering*

Hot carriers forming an ensemble equilibrate amongst themselves by undergoing two-particle Coulomb scattering events. Like-carrier and electron-hole scattering events are similar processes, however, while the outcome of the latter is always a distinguishable result, the former, depending on the spin states of the particles, may be an indistinguishable process. For any elastic scattering process the sums over the initial and final wavevectors must be conserved (conservation of momentum), i.e., for a process involving two particles,

$$\boldsymbol{k}_1 + \boldsymbol{k}_2 = \boldsymbol{k}_1' + \boldsymbol{k}_2'. \tag{2.9}$$

In the case that the two particles are indistinguishable fermions, for every scattering process $(\boldsymbol{k}_1, \boldsymbol{k}_2) \to (\boldsymbol{k}_1', \boldsymbol{k}_2')$ with scattering angle θ, there exists an equivalent process $(\boldsymbol{k}_1, \boldsymbol{k}_2) \to (\boldsymbol{k}_2', \boldsymbol{k}_1')$ with scattering angle $\pi - \theta$ (see figure 2.5).

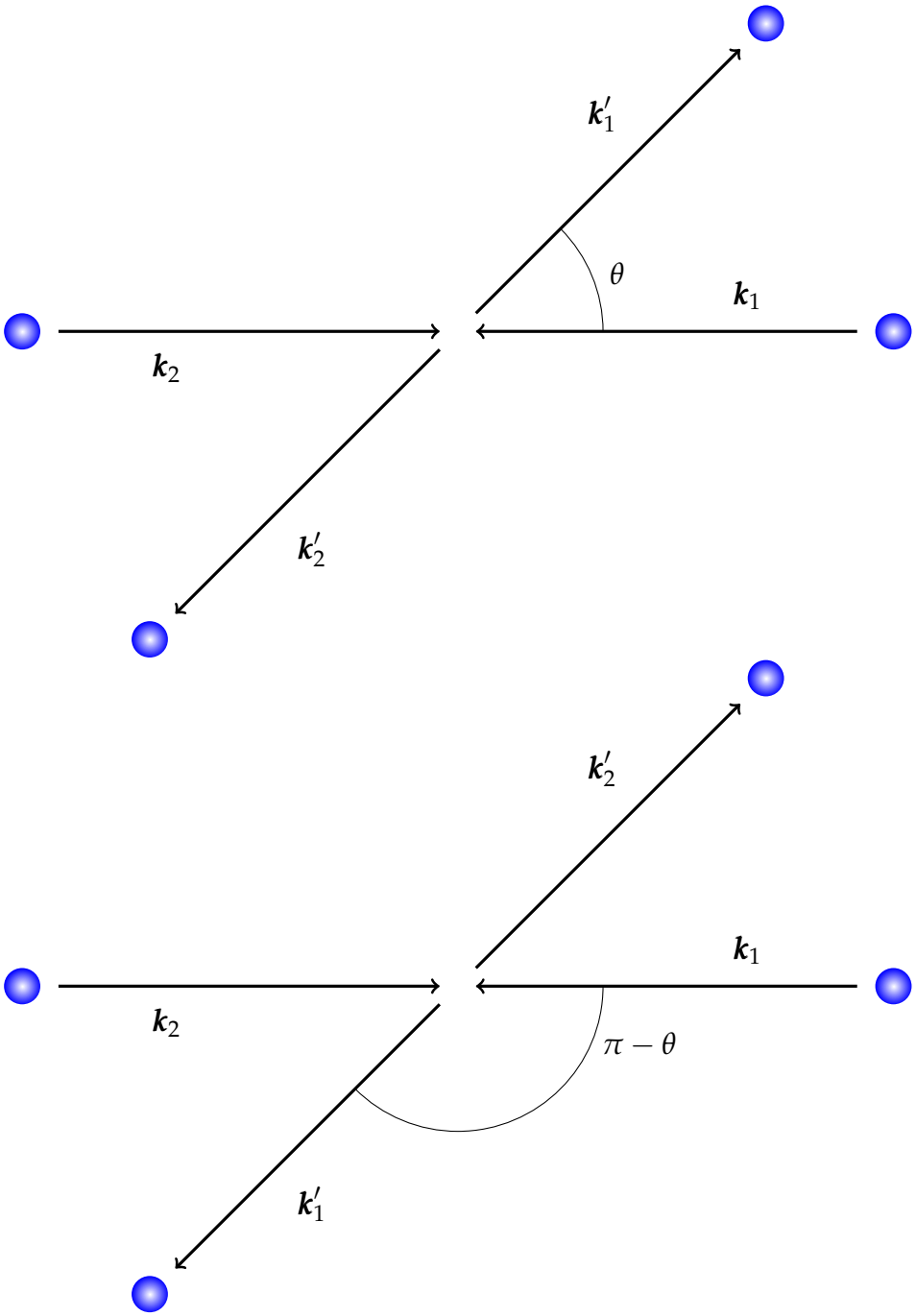

Figure 2.5.: For every scattering process $(k_1, k_2) \to (k_1', k_2')$ between indistinguishable fermions, there exists an equivalent process $(k_1, k_2) \to (k_2', k_1')$.

Where the particles are distinguishable, the probability of either particle being scattered by angle θ is

$$|f(\theta)|^2 + |f(\pi - \theta)|^2, \tag{2.10}$$

while for indistinguishable particles, the probability is

$$|f(\theta) \pm f(\pi - \theta)|^2, \tag{2.11}$$

taking the upper sign for identical bosons and the lower sign for fermions.

Like-carriers in opposing spin states may be identified as such; they are therefore not distinguishable, and the probability amplitude is given by equation 2.10.

In either case, the matrix element which describe the carrier-carrier scattering interaction is

$$\begin{aligned}\left\langle \boldsymbol{k}_1', \boldsymbol{k}_2' \,\middle|\, V \,\middle|\, \boldsymbol{k}_1, \boldsymbol{k_2} \right\rangle = \mathcal{I}\left(\boldsymbol{k}_1, \boldsymbol{k}_1'\right) \mathcal{I}\left(\boldsymbol{k}_2, \boldsymbol{k}_2'\right) \\ \times \frac{1}{\Omega^2} \int\int d^3\boldsymbol{r}_1 d^3\boldsymbol{r}_2 e^{-i\left(\boldsymbol{k}_1' \cdot \boldsymbol{r}_1 + \boldsymbol{k}_1 \cdot \boldsymbol{r}_1\right)} \frac{q^2}{4\pi\epsilon} \frac{e^{-\lambda|\boldsymbol{r}_1 - \boldsymbol{r}_2|}}{|\boldsymbol{r}_1 - \boldsymbol{r}_2|} e^{-i\left(\boldsymbol{k}_2' \cdot \boldsymbol{r}_2 + \boldsymbol{k}_2 \cdot \boldsymbol{r}_2\right)},\end{aligned} \tag{2.12}$$

where $|\boldsymbol{k}\rangle = u_{n\boldsymbol{k}}(\boldsymbol{r}) \exp(i\boldsymbol{k} \cdot \boldsymbol{r})$ is the Bloch state with wavevector $\boldsymbol{k}$, band index n, and cell-periodic function $u_{n\boldsymbol{k}}(\boldsymbol{r})$. Ω is a macroscopic distance which normalises the (planewave) basis set. The Coulomb interaction

$$V = \frac{q^2}{4\pi\epsilon} \frac{e^{-\lambda|\boldsymbol{r}_1 - \boldsymbol{r}_2|}}{|\boldsymbol{r}_1 - \boldsymbol{r}_2|}, \tag{2.13}$$

with dielectric permittivity $\epsilon = \epsilon_r \epsilon_0$ includes screening factor $\exp(\lambda|\boldsymbol{r}_1 - \boldsymbol{r}_2|)$ and dielectric permittivity $\epsilon = \epsilon_r \epsilon_0$. Finally, $\mathcal{I}(\boldsymbol{k}_1, \boldsymbol{k}_1')$ and $\mathcal{I}(\boldsymbol{k}_1, \boldsymbol{k}_1')$ are the overlap integrals of the cell-periodic part of the Bloch functions, where

$$\mathcal{I}\left(\boldsymbol{k}_1, \boldsymbol{k}_1'\right) \mathcal{I}\left(\boldsymbol{k}_2, \boldsymbol{k}_2'\right) = \int_{\text{cell}} d^3\boldsymbol{r}_1 {u_{\boldsymbol{k}_1}}'^{*}(\boldsymbol{r}_1) u_{\boldsymbol{k}_1}^{*}(\boldsymbol{r}_1) \times \int_{\text{cell}} d^3\boldsymbol{r}_2 {u_{\boldsymbol{k}_2}}'^{*}(\boldsymbol{r}_2) u_{\boldsymbol{k}_2}^{*}(\boldsymbol{r}_2). \tag{2.14}$$

the overlap integrals are assumed to be equal to unity near the zone centre. In the centre of mass frame, equation 2.12 becomes

$$M_{\boldsymbol{K}_{12}\boldsymbol{K}'_{12}} = \left\langle \boldsymbol{K}'_{12} \,\middle|\, V \,\middle|\, \boldsymbol{K}_{12} \right\rangle = \mathcal{I}\left(\boldsymbol{k}_1, \boldsymbol{k}'_1\right) \mathcal{I}\left(\boldsymbol{k}_2, \boldsymbol{k}'_2\right) \times \frac{1}{\Omega} \int d^3\boldsymbol{r}_{12} e^{-i\boldsymbol{K}'_{12}\cdot\boldsymbol{r}_{12}} \frac{q^2}{4\pi\epsilon} \frac{e^{-\lambda \boldsymbol{r}_{12}}}{\boldsymbol{r}_{12}} e^{i\boldsymbol{K}_{12}\cdot\boldsymbol{r}_{12}}, \tag{2.15}$$

where $\boldsymbol{K}_{12} = (\boldsymbol{k}_1 - \boldsymbol{k}_2)/2$, and $\boldsymbol{r}_{12} = \boldsymbol{r}_1 - \boldsymbol{r}_2$. Upon evaluation of the integral, this becomes

$$M_{\boldsymbol{K}_{12}\boldsymbol{K}'_{12}} = \frac{q^2}{\epsilon\Omega} \frac{1}{\left|\boldsymbol{K}'_{12} - \boldsymbol{K}_{12}\right|^2 + \lambda^2}. \tag{2.16}$$

Combining this result with Fermi's golden rule (equation 2.8) gives the scattering rate for *distinguishable* particles as

$$W^{\text{e-h}}_{\boldsymbol{K}'_{12}\boldsymbol{K}_{12}} = \frac{2\pi}{\hbar^2} \frac{q^2}{\epsilon\Omega} \frac{1}{\left|\boldsymbol{K}'_{12} - \boldsymbol{K}_{12}\right|^2 + \lambda^2}. \tag{2.17}$$

For *indistinguishable* particles, the amplitude $|M|^2$ is found by adding the amplitudes of the individual processes

$$|M|^2 = \left|M_{\boldsymbol{K}_{12}\boldsymbol{K}'_{12}}\right|^2 + \left|M_{\boldsymbol{K}_{12}\boldsymbol{K}'_{21}}\right|^2 - \frac{1}{2}\left[M_{\boldsymbol{K}_{12}\boldsymbol{K}'_{12}} M^*_{\boldsymbol{K}_{12}\boldsymbol{K}'_{12}} + M_{\boldsymbol{K}_{12}\boldsymbol{K}'_{21}} M^*_{\boldsymbol{K}_{12}\boldsymbol{K}'_{21}}\right], \tag{2.18}$$

and the scattering rate is

$$W^{\text{e-e}}_{\text{i}\to\text{f}} = \frac{2\pi}{\hbar^2} |M|^2 \delta\left(E'_{\boldsymbol{K}_{12}} - E_{\boldsymbol{K}_{12}}\right). \tag{2.19}$$

2.4.3 *Carrier-Phonon Scattering*

Hot carriers equilibrate with the crystal lattice through the emission of phonons. The phonons involved in such processes are the longitudinal modes in the op-

tic branch of the dispersion curves (LO phonons). Being bosons, Bose-Einstein statistics give the LO phonon population as

$$n_{\boldsymbol{k}} = \frac{1}{\exp\left(\frac{\hbar\omega}{k_{\mathrm{B}}T}\right) - 1}, \tag{2.20}$$

where $n_{\boldsymbol{k}}$ is the number of photons with particular wavevector $\boldsymbol{k}$. In the language of second-quantisation, the phonon energy is described by the normal modes of the quantum harmonic oscillator,

$$E_{\boldsymbol{k}} = \left(n_{\boldsymbol{k}} + \frac{1}{2}\right)\hbar\omega_{\boldsymbol{k}}; \tag{2.21}$$

thus the phonon energy is quantised in units of $\hbar\omega_{\boldsymbol{k}}$, and $n_{\boldsymbol{k}}$ is the number of quanta in the system. The number operator $|n_{\boldsymbol{k}}\rangle$ may be written in terms of creation and annihilation operators

$$n_{\boldsymbol{k}} = \hat{c}^{\dagger}_{\boldsymbol{k}}\hat{c}_{\boldsymbol{k}}. \tag{2.22}$$

The phonon creation and annihilation operators ($c^{\dagger}_{\boldsymbol{k}}$ and $c_{\boldsymbol{k}}$ respectively) have the properties of adding to or removing from the system a quanta of energy (phonon):

$$\langle n_{\boldsymbol{k}}|\hat{c}^{\dagger}_{\boldsymbol{k}}|n_{\boldsymbol{k}} - 1\rangle = \langle n_{\boldsymbol{k}} - 1 \,|\, \hat{c}_{\boldsymbol{k}} \,|\, n_{\boldsymbol{k}}\rangle = \sqrt{n_{\boldsymbol{k}}}. \tag{2.23}$$

Further, the operators $c^{\dagger}_{\boldsymbol{k}}$ and $c_{\boldsymbol{k}}$ obey the anticommutation relation

$$\left\{\hat{c}_{\boldsymbol{k}}, \hat{c}^{\dagger}_{\boldsymbol{k}'}\right\} = \hat{c}_{\boldsymbol{k}}\hat{c}^{\dagger}_{\boldsymbol{k}'} + \hat{c}^{\dagger}_{\boldsymbol{k}'}, \hat{c}_{\boldsymbol{k}} = \delta\left(\boldsymbol{k}, \boldsymbol{k}'\right) = \begin{cases} 1 & \boldsymbol{k} = \boldsymbol{k}' \\ 0 & \boldsymbol{k} \neq \boldsymbol{k}' \end{cases}. \tag{2.24}$$

With this notation, phonon states may be expressed in terms of the product of individual phonon states $|n_{\boldsymbol{\kappa}p}\rangle$, where $\boldsymbol{\kappa}$ and p denote the phonon wavevector

and phonon polarisation, respectively. The initial and final scattering states are then

$$|\mathrm{i}\rangle = \psi_{\boldsymbol{k}'}(\boldsymbol{r}) \prod_{\boldsymbol{\kappa p}} \left| n'_{\boldsymbol{\kappa p}} \right\rangle \tag{2.25}$$

and

$$|\mathrm{f}\rangle = \psi_{\boldsymbol{k}}(\boldsymbol{r}) \prod_{\boldsymbol{\kappa p}} \left| n_{\boldsymbol{\kappa p}} \right\rangle . \tag{2.26}$$

For the sake of brevity, only the final matrix element will be stated here (for an explicit derivation, see the works of Singh) [43, 44]. The carrier-phonon scattering element is

$$\left| \left\langle \mathrm{f} \right| H_{\text{e-p}} \left| \mathrm{i} \right\rangle \right|^2 = \frac{\hbar}{2NM} \frac{H_{\boldsymbol{qb}} \sum_{\mu,\mu'} I_{\mu,\nu'}\left(\boldsymbol{k},\boldsymbol{k}'\right)}{2\omega_{\boldsymbol{qb}}} \left[n\left(\omega_{\boldsymbol{qb}}\right) + \frac{1}{2} \mp \frac{1}{2} \right] \delta_{\boldsymbol{k}\pm\boldsymbol{q}-\boldsymbol{k}',0}, \tag{2.27}$$

where N is the number of unit cells over which the scattering takes place, M is the mass of the crystal nuclei, $I_{\mu\mu'}(\boldsymbol{k}\boldsymbol{k}')$ is the overlap integral between initial and final wavevectors for carriers in spin states μ and μ', $H_{\boldsymbol{qb}}$ is the energy of the phonon with wavevector $\boldsymbol{q}$ and polarisation $\boldsymbol{b}$, $\omega_{\boldsymbol{qb}}$ is the frequency of said phonon, $n(\omega_{\boldsymbol{qb}})$ is the phonon occupation number of a particular mode, and $\delta_{\boldsymbol{k}\pm\boldsymbol{q}-\boldsymbol{k}',0}$ is an energy conservation term. The upper and lower signs in 2.27 correspond to phonon absorption and phonon emission respectively.

The rate of carrier-phonon scattering is found by inserting the matrix element 2.27 with the expression for Fermi's golden rule (2.8):

$$\begin{aligned} W_{\mathrm{i}\to\mathrm{f}}^{\text{phon}} = \frac{1}{8\pi^2 NM} \int d^3\boldsymbol{k}' \frac{H_{\boldsymbol{qb}}^2 G\left(\boldsymbol{k},\boldsymbol{k}'\right)}{\omega_{\boldsymbol{qb}}} \left[n\left(\omega_{\boldsymbol{q}acevb}\right) + \frac{1}{2} \mp \frac{1}{2} \right] \\ \times \delta_{\boldsymbol{k}\pm\boldsymbol{q}-\boldsymbol{k}',0} \delta\left(E_{\boldsymbol{k}'} - E_{\boldsymbol{k}} \mp \hbar\omega_{\boldsymbol{qb}} \right). \end{aligned} \tag{2.28}$$

Once the charge carriers have reached equilibrium with the lattice they may be extracted by some applied external potential such as the intrinsic field within the depletion region of a p-n heterojunction. Carrier extraction must occur on a timescale faster than the carrier recombination rate. Carrier recombination may be either radiative, in which case the downward electron transition is accompa-

nied by the emission of a photon, or nonradiative, such as in an Auger process. Both cases, outlined below, play an important role in the overall efficiency of the photovoltaic device.

2.5 RADIATIVE CARRIER RECOMBINATION

Spontaneous radiative recombination of charge carriers is an unavoidable loss mechanism in photovoltaics [48]. The upper limit to the efficiency of a solar cell device is ultimately determined by the rate at which spontaneous radiative carrier recombination occurs. It is therefore extremely desirable to be able to characterise the radiative recombination rate. The probability for a spontaneous downward electron transition may be found using standard time-dependent perturbation theory in a similar manner as used to derive the Fermi golden rule (section 2.4.1).

The interaction Hamiltonian between an electronic charge e and electromagnetic field with vector potential $\boldsymbol{A}$ and scalar potential ϕ is

$$H = \frac{p^2}{2m_0} - \frac{e}{m_0}\boldsymbol{A}\cdot\boldsymbol{p} + \frac{ie\hbar}{2m_0}\nabla\cdot\boldsymbol{A} + \frac{e^2}{2m_0}A^2 + e\phi + V(\boldsymbol{r}), \tag{2.29}$$

which satisfies the time-dependent Schrödinger equation (2.3).Writing equation 2.29 in the radiation gauge, terms in $\nabla\cdot\boldsymbol{A}$ and ϕ vanish. The remaining terms in $\boldsymbol{A}$ and A^2 may then be treated as a perturbation to the steady-states Hamiltonian. The transition rate for electron-phonon scattering from initial state $|\mathrm{i}\rangle$ to final state $|\mathrm{f}\rangle \in \{|\mathrm{f}\rangle\}$ is then given by Fermi's golden rule 2.8 as

$$W^{\mathrm{rad}}_{\mathrm{i}\to\mathrm{f}} = \frac{2\pi}{\hbar}\sum_f \left|\left\langle \mathrm{f}\right| H' \left|\mathrm{i}\right\rangle\right|^2 \delta\left(E_\mathrm{f} - E_\mathrm{i} \mp \hbar\omega\right), \tag{2.30}$$

with the upper sign corresponding to photoabsorption and the lower sign to photoemission. Since photoabsorption and photoemission correspond to removing from or adding to the system a photon, the initial and final states may be

written in terms of the wavevector of the charge carrier and photon population number n_γ:

$$|\mathrm{i}\rangle = |k_\mathrm{i}, n_\gamma\rangle\,; \qquad |\mathrm{f}\rangle = \begin{cases} |k_\mathrm{f}, n_\gamma - 1\rangle & \text{photoabsorption} \\ |k_\mathrm{f}, n_\gamma + 1\rangle & \text{photoemission.} \end{cases} \tag{2.31}$$

Writing the vector potential as

$$A_0 = \sqrt{\frac{\hbar}{2\epsilon\mathcal{V}}}\left(\hat{c}^\dagger + \hat{c}\right), \tag{2.32}$$

the photoabsorption and photoemission rates (summed over final states $|\mathrm{f}\rangle$) become

$$W_{\mathrm{i}\to\mathrm{f}}^{(\mathrm{abs.})} = \frac{2\pi}{\hbar}\frac{e^2}{m_0}\frac{\hbar}{2\omega\epsilon} n_\gamma \sum_\mathrm{f} |\langle k_\mathrm{f}\,|\,\boldsymbol{a}\cdot\boldsymbol{p}\,|\,k_\mathrm{i}\rangle|^2\,\delta\left(E_\mathrm{i} - E_\mathrm{f} + \hbar\omega\right) \tag{2.33}$$

and

$$W_{\mathrm{i}\to\mathrm{f}}^{(\mathrm{em.})} = \frac{2\pi}{\hbar}\frac{e^2}{m_0}\frac{\hbar}{2\omega\epsilon}\left(n_\gamma + 1\right) \sum_\mathrm{f} |\langle k_\mathrm{f}\,|\,\boldsymbol{a}\cdot\boldsymbol{p}\,|\,k_\mathrm{i}\rangle|^2\,\delta\left(E_\mathrm{i} - E_\mathrm{f} - \hbar\omega\right) \tag{2.34}$$

respectively. The two terms which emerge in equation 2.34 account for both stimulated and spontaneous photoemission, respectively. Separating equation 2.34, the stimulated and spontaneous emission rates are

$$W_{\mathrm{i}\to\mathrm{f}}^{(\mathrm{stim.})} = \frac{2\pi}{\hbar}\frac{e^2}{m_0}\frac{\hbar}{2\omega\epsilon} n_\gamma \sum_\mathrm{f} |\langle k_\mathrm{f}\,|\,\boldsymbol{a}\cdot\boldsymbol{p}\,|\,k_\mathrm{i}\rangle|^2\,\delta\left(E_\mathrm{i} - E_\mathrm{f} - \hbar\omega\right), \tag{2.35}$$

and

$$W_{\mathrm{i}\to\mathrm{f}}^{(\mathrm{spon.})} = \frac{2\pi}{\hbar}\frac{e^2}{m_0}\frac{\hbar}{2\omega\epsilon} \sum_\mathrm{f} |\langle k_\mathrm{f}\,|\,\boldsymbol{a}\cdot\boldsymbol{p}\,|\,k_\mathrm{i}\rangle|^2\,\delta\left(E_\mathrm{i} - E_\mathrm{f} - \hbar\omega\right), \tag{2.36}$$

respectively. When the system is in equilibrium, the absorptive rate and rate of stimulated emission must, by definition, exactly oppose one another. It is these three processes (2.33, 2.35, and 2.36) which must be balanced when calculating the upper limit to solar cell efficiency within the detailed balance limit (section 2.7).

The rate of spontaneous radiative recombination described by equation 2.36 ultimately determines the maximum efficiency of a solar cell device. There are various schemes by which solar cell efficiency may be improved, however, each must compete with the carrier lifetime for radiative recombination

$$\tau_{\text{rad.}}^{\text{spon.}} = \frac{1}{W_{\text{i}\to\text{f}}^{(\text{spon.})}} \tag{2.37}$$

The mechanisms behind efficiency enhancement schemes must therefore occur on faster timescales than those predicted by equation 2.37.

While radiative recombination cannot be avoided, it is not the only recombination factor which limits the efficiency of photovoltaic technology; nonradiative process may also contribute egregious losses in solar cell devices.

2.6 NONRADIATIVE RECOMBINATION MECHANISMS

In addition to recombining radiatively, bandedge charge carriers may also recombine without the accompanying emission of a photon. The two most significant nonradiative processes are Auger recombination and the Shockley-Read-Hall (SRH) effect. In the former, the excess energy of an electron as it crosses the bandgap is transferred to a secondary charge carrier (usually an electron), while in SRH recombination, the electron falls into a so-called "trap state;" the trapped carrier cannot then be extracted. Each of these processes will be described in the following sections.

2.6.1 *Auger Recombination*

Rather than recombining radiatively, an electron-hole pair may recombine by instead imparting the energy excess of at least E_{g} to a secondary charge carrier. The secondary carrier may be either a conduction band electron or valence band

hole. The Auger process may be direct, stimulated by phonons in the system, or involve occupation of a trap site located within the fundamental bandgap (figure 2.6). Trap sites arise from crystal impurities (such as dopants), which may be included intentionally, or by crystal defects, such as atomic vacancies and dislocations. The direct Auger process is the most important in the vast majority of systems and is the focus of the current section [43, 44].

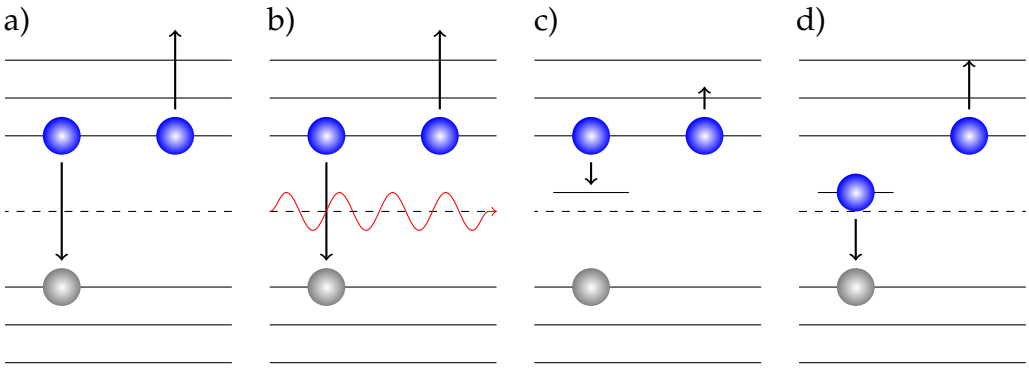

Figure 2.6.: Schematic of various Auger processes: a) an electron recombines with a hole–the excess energy is transferred to a secondary electron in the CB; b) an Auger process similar to in a) is stimulated by phonon; c) an electron drops into a trap state; d) the electron continues from the trap state to the VB.

Since the direct Auger process involves the scattering of two indistinguishable electrons (as do all Auger processes), both direct and exchange contributions must be accounted for (see section 2.4.2). The direct contribution is

$$\left\langle \boldsymbol{K}_{12} \middle| M \middle| \boldsymbol{K}'_{12} \right\rangle = \frac{q^2}{\epsilon\Omega} \frac{\mathcal{I}\left(\boldsymbol{k}_1, \boldsymbol{k}'_1\right) \mathcal{I}\left(\boldsymbol{k}_2, \boldsymbol{k}'_2\right)}{\left|\boldsymbol{k}'_1 - \boldsymbol{k}_1\right|^2 + \lambda^2}, \tag{2.38}$$

while the matrix element for the exchange part is

$$\left\langle \boldsymbol{K}_{12} \middle| M \middle| \boldsymbol{K}'_{12} \right\rangle = \frac{q^2}{\epsilon\Omega} \frac{\mathcal{I}\left(\boldsymbol{k}_1, \boldsymbol{k}'_2\right) \mathcal{I}\left(\boldsymbol{k}_2, \boldsymbol{k}'_1\right)}{\left|\boldsymbol{k}'_1 - \boldsymbol{k}_2\right|^2 + \lambda^2}, \tag{2.39}$$

where the overlap integrals have been retained. The total scattering amplitude is then given by equation 2.18. In order for Auger recombination to occur, there must simultaneously be an electron in initial state $|k_1\rangle$ in the conduction band, a hole (electron vacancy) in initial state $|k'_1\rangle$ in the valence band, and a second

electron in state $|k_2\rangle$ in the conduction band. The final state of the Auger electron, $|k_2'\rangle$ is an electron state far above the conduction band minimum, and is therefore considered to always be empty. In general, Auger rates should be calculated numerically from Fermi-Dirac statistics; for a system of nondegenerate states, however, the Auger rate may be calculated analytically.

For a system comprising of nondegenerate energy states, the probability for an Auger transition to occur is

$$P\left(\boldsymbol{k}_1, \boldsymbol{k}_2, \boldsymbol{k}_1'\right) = f\left(\boldsymbol{k}_1\right) f\left(\boldsymbol{k}_2\right) \left[1 - f\left(\boldsymbol{k}_1'\right)\right], \tag{2.40}$$

where

$$f\left(\boldsymbol{k}_{1,2}\right) = \frac{n}{N_{\mathrm{C}}} \exp\left(-\frac{E_{\boldsymbol{k}_{1,2}\in\mathrm{CB}}}{k_{\mathrm{B}}T}\right) \tag{2.41}$$

and

$$1 - f\left(\boldsymbol{k}_1'\right) = \frac{p}{N_{\mathrm{V}}} \exp\left(-\frac{E_{\boldsymbol{k}_1'\in\mathrm{VB}}}{k_{\mathrm{B}T}}\right), \tag{2.42}$$

where n and p are the electron and hole densities, and N_{C} and N_{V} are the local densities of states in the conduction band and valence band, respectively. The probability 2.40 is maximised when the total energy after the interaction is minimised, i.e. when

$$\boldsymbol{k}_1 + \boldsymbol{k}_1' + \boldsymbol{k}_2 = \boldsymbol{k}_2. \tag{2.43}$$

The resultant probability is

$$P\left(\boldsymbol{k}_1, \boldsymbol{k}_2, \boldsymbol{k}_1'\right) = \frac{n}{N_{\mathrm{C}}} \exp\left(-\frac{1+2\mu}{1+\mu}\frac{E_{\mathrm{g}}}{k_{\mathrm{B}}T}\right), \tag{2.44}$$

where $\mu = m_{\mathrm{C}}^*/m_{\mathrm{V}}^*$ is the effective mass ratio for electrons in the CB and VB. Combining this result with equation 2.43, the final energy of the Auger electron is then

$$E_{\boldsymbol{k}_2'\in\mathrm{VB}} = \frac{1+2\mu}{1+\mu} E_{\mathrm{g}}. \tag{2.45}$$

Taking the limit that $\mu << 1$ (i.e. the $m_V^* >> m_C^*$) gives the result

$$E_{\boldsymbol{k}_2' \in \mathrm{VB}} \approx (1+\mu)\, E_g; \tag{2.46}$$

This condition implies a minimum threshold for Auger recombination. From considerations of energy conservation, this threshold must be *at least* equal to the bandgap energy of the material, however, it is often found to be higher; the threshold energies for Auger recombination for several illustrative materials are shown in table 2.1. Using Fermi's golden rule, the rate of Auger recombination

Material	Bandgap (eV)	Threshold energy (eV)	Auger coefficient ($m^6 s^{-1}$)
GaAs[49–51]	1.42	1.144	$\sim 10^{-30}$
GaSb[49, 50]	0.70	1.162	$\sim 10^{-29}$
InP[50, 52]	1.34	1.203	$\sim 10^{-30}$
InAs[50, 53]	0.35	1.328	$\sim 10^{-26}$
InSb[54–57]	0.18	0.183	$\sim 10^{-26}$
CdSe[58, 59]	1.84		$\sim 10^{-29}$
CdTe[58, 60]	1.75		$\sim 10^{-29}$
PbS[61, 62]	0.41		$\sim 10^{-29}$
PbSe[63, 64]	0.28		$\sim 10^{-28}$

Table 2.1.: Energy threshold and coefficients for Auger recombination for sample bulk semiconductors.

is given by

$$\begin{aligned} W_{\mathrm{Auger}} = 2\left(\frac{2\pi}{\hbar}\right)\left(\frac{e^2}{\epsilon}\right)^2 \frac{1}{(2\pi)^9} \int\int\int d^3k_2 d^3k_1' d^3k_2' \, |M|^2 \\ \times P\left(\boldsymbol{k}_1, \boldsymbol{k}_2, \boldsymbol{k}_1'\right) \delta\left(E_{\boldsymbol{k}_1 \in \mathrm{CB}} + E_{\boldsymbol{k}_2 \in \mathrm{CB}} - E_{\boldsymbol{k}_1' \in \mathrm{VB}} - E_{\boldsymbol{k}_2' \in \mathrm{CB}}\right), \end{aligned} \tag{2.47}$$

where $P(\boldsymbol{k}_1, \boldsymbol{k}_2, \boldsymbol{k}_1')$ is given by equation 2.44. Hence, the Auger recombination rate varies exponentially with the temperature of the lattice, and is greater in materials of smaller bandgap energy. For high carrier concentrations, the Auger

recombination rates are often given in terms of "Auger coefficients." In this representation, the Auger rates are

$$W_{\mathrm{n}}^{\mathrm{Auger}} = \gamma_{\mathrm{n}} n^2 p \tag{2.48}$$

where the secondary carrier is an CB electron, and

$$W_{\mathrm{p}}^{\mathrm{Auger}} = \gamma_{\mathrm{p}} n p^2 \tag{2.49}$$

where the secondary carrier is a VB hole [65]. In equations 2.48 and 2.49, γ_{n} and γ_{p} are the Auger coefficients for processes involving secondary electrons and secondary holes, respectively (see table 2.1 for typical values). Under the assumption that electron and hole carrier concentrations are the same (not an unreasonable assumption for photogenerated carriers), the total rate for Auger recombination is

$$W_{\mathrm{tot}}^{\mathrm{Auger}} = \left(\gamma_{\mathrm{n}} + \gamma_{\mathrm{p}}\right) n_i^3, \tag{2.50}$$

where $n = p = n_i$ is the carrier density.

Auger recombination is not the only nonradiative process by which charge carrier may recombine. In the presence of material defects, and for high carrier concentrations and at low temperature, the Shockley-Read-Hall process becomes of consequence.

2.6.2 *Shockley-Read-Hall Recombination*

In any realistic semiconductor sample, crystal impurities will inevitably be included at the point of manufacture. These impurities may be included deliberately, as in doping for p-n heterojunctions, or accidentally. These impurities often introduce energy levels within the forbidden region between the energy

bands: such energy levels are known as "trap states." The trap states may also be added by crystal defects.

The process of trap-assisted carrier recombination was first described from a theoretical perspective by William Shockley and William Read, and independently by Robert Hall in the same year [31, 32]. There are four basic process which are collectively referred to as Shockley-Read-Hall (SRH) processes, namely electron capture, electron emission, hole capture, and hole emission; the former pair are each others inverse process, and like-wise for the latter pair (see figure 2.7). The trap state is assumed to be either full, in which case an electron occupies the trap state, or empty, in which case the trap state is occupied by a hole.

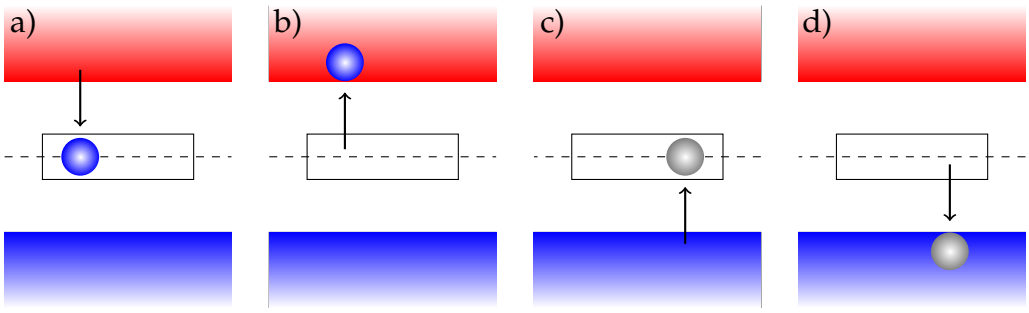

Figure 2.7.: Four SRH processes: a) electron capture, b) electron emission, c) hole capture, d) hole emission. Here, the trap level lies in the middle of the band gap. The trap energy level is not in general coincident with the Fermi level (dashed line).

The rate at which electrons from the conduction band are captured by trap states is

$$R_{n\in CB}^{capture} = C_n N_{trap} \left[1 - f\left(E_{trap}\right)\right] n, \tag{2.51}$$

where C_n is a constant proportional to the cross-section for electron capture and N_{trap} is the concentration of trap states. $f(E_{trap})$ is the Fermi-Dirac distribution function for a trap at energy E_{trap}: the probability that the trap state is occupied.

The probability that the trap state is empty is then $[1 - f(E_{\text{trap}})]$ [31, 32, 38]. The rate of electron emission is

$$R_{\text{n}\in\text{trap}}^{\text{emission}} = E_{\text{n}} N_{\text{trap}} f\left(E_{\text{trap}}\right). \tag{2.52}$$

Similar expressions may be derived for the processes involving holes.

When in thermal equilibrium, the capture rate is exactly opposed by the emission rate (as is required by the principle of detailed balance). For a crystal where the impurity density is sufficiently rarefied, and the carrier densities are the same (such as where carriers have been produced by photogeneration), the electron-hole recombination rate due to trap-assisted processes is

$$R_{\text{SRH}} = \frac{\left(np - n_i^2\right)}{t_{\text{p}}\left(n + n'\right) + t_{\text{n}}\left(p + p'\right)}, \tag{2.53}$$

where n' and p' are the carrier concentrations when the trap level coincides with the Fermi level, and t_n and t_p are the lifetimes for holes and electrons respectively. The equilibrium lifetime is

$$\tau = \lim_{\delta n \to 0} \frac{t_{\text{p}}\left(n + n'\right) + t_{\text{n}}\left(p + p'\right)}{n + p} \tag{2.54}$$

Each of the processes discussed above constitute energy loss mechanisms in photovoltaic solar cell devices. The only process which it is impossible to suppress (to at least some degree) is that of radiative recombination. The maximum theoretical efficiency of a solar cell is therefore attained when spontaneous radiative recombination is the only loss mechanism present. This maximum efficiency is dealt with in the next section.

2.7 THE SHOCKLEY-QUEISSER LIMIT OF EFFICIENCY

The maximum efficiency of an ideal solar cell device is obtained when the only loss mechanism present is (unavoidable) radiative recombination. When calculating the maximum efficiency of a solar cell device, it is therefore assumed that carrier relaxation occurs instantaneously, and also that nonradiative recombination processes (such as Auger and SRH processes) are entirely absent. Under these assumptions the maximum theoretical solar cell efficiency may be calculated by consideration of the *principle of detailed balance*.

In essence, for a system comprising of several separable processes, detailed balance is satisfied when each process is exactly opposed by its counter-process. The principle of detailed balance was first applied to solar cell devices by William Shockley and Hans Queisser in their groundbreaking paper "Detailed Balance Limit of Efficiency of p-n Junction solar Cells" [5]. Due to the importance of their work, the detailed balance limit of efficiency is more commonly known as the "Shockley-Queisser limit."

For the detailed balance calculation to become tractable, several assumptions are made when considering solar cell devices. Firstly, the Sun is considered to be a perfect blackbody radiator at $T_s = 6,000$ K, the spectral radiance of which is given by Plank's law for radiation [39]:

$$B_\omega = \frac{8\pi^2\hbar\omega^3}{c^2}\frac{1}{\exp\left(\frac{\hbar\omega}{k_B T_s}\right) - 1}, \tag{2.55}$$

Further, the cell itself is considered to be a blackbody at 300 K in thermal equilibrium with its surroundings. The cell is not a perfect blackbody, however, as absorption of a photon with $\hbar\omega < E_g$ is forbidden by energy conservation. In order to negate the effects of carrier cooling, it is assumed that all photons with $\hbar\omega \geq E_g$ are absorbed, producing a single bandedge electron-hole pair.

Under these assumptions, the ultimate maximum efficiency for a room temperature solar cell device is given by

$$\eta\left(x_g, x_c, t_s, f\right) = t_s u\left(x_g\right) v\left(f, x_c, x_g\right) m\left(v x_g / x_g\right) \tag{2.56}$$

where: $x_g \equiv E_g / k_B T$; $x_c \equiv T_c / T_g$; t_s is the probability that a solar photon will be absorbed and generate an ehp; f accounts for various geometrical and transmission factors; v is the fraction of the energy gap open circuit voltage obtained from the cell; and m is the impedance factor. $u(x_x)$ is the maximum efficiency for a spherical blackbody solar cell maintained at 0 K while in thermal contact with a bath of blackbody radiation at 6,000 K, given by

$$u\left(x_g\right) = \left[x_g \int_{x_g}^{\infty} \frac{x^2}{e^x - 1} dx\right] \times \left[\int_0^{\infty} \frac{x^3}{e^x - 1} dx\right]^{-1}, \tag{2.57}$$

where $x = \hbar\omega / k_B T_s$. Using this result, Shockley and Queisser calculated the maximum theoretical efficiency of a 1.1 eV bandgap (silicon) flat-panel solar cell to be 30%. Similar results may be obtained for other systems.

2.8 CHAPTER SUMMARY

The various loss mechanisms in conventional solar cell devices have been outlined, including carrier cooling through carrier-carrier scattering, intraband cooling through phonon emission, radiative carrier recombination, and nonradiative carrier recombination. The maximum efficiency for a second generation solar cell device has been outlined; the aforementioned processes limit the efficiency of a (silicon) solar cell device to 30%.

In order to better exploit solar energy as a power source, more efficient devices must be designed, which may increase or bypass the Shockley-Queisser limit. These devices, collectively known as "third generation solar cells," are the focus of the next chapter.

3

THIRD GENERATION PHOTOVOLTAICS

The predictions made by detailed balance calculations impose an upper bound to the efficiency of a conventional solar cell device. In order to make solar conversion a more practical method of power generation, it is desirable to bypass this limit. Several designs have been proposed by which the maximum solar cell efficiency may be augmented, including multijunction device architecture, solar cell devices containing an intermediate energy state within the forbidden region, and, perhaps most notably, devices which exploit inverse the Auger process to produce several electron-hole pairs from absorption of a single photon: a process known as *impact ionisation* (II). Each of these device designs will be reviewed in the following sections.

3.1 MULTIJUNCTION SOLAR CELLS

Multijunction solar cell devices consist of a battery of different semiconductor materials connected in series and separated from one another by tunnel diodes [66, 67]. The concept of the multijunction solar cell was first proposed by Trivich and Flinn at a symposium in 1953, with the first patented device registered by Edmund Jackson of Texas Instruments in 1955 [6, 7, 68].

The major loss mechanisms in conventional photovoltaic cells arise from the inability to absorb photons with sub-bandgap energy, as well as from thermal

losses after absorption of high-energy photons. The multijunction solar cell architecture aims to mitigate these losses by connecting in series a battery of solar converters of differing bandgap energies, arranged such that the material of highest bandgap energy lies on the front face of the cell, while subsequent absorbers have sequentially smaller bandgaps (see figure 3.1). In this way, higher energy photons are absorbed near the front of the device, while longer wavelengths penetrate into deeper layers. Thus, electron-hole pairs are formed near to the band edge in each subcell.

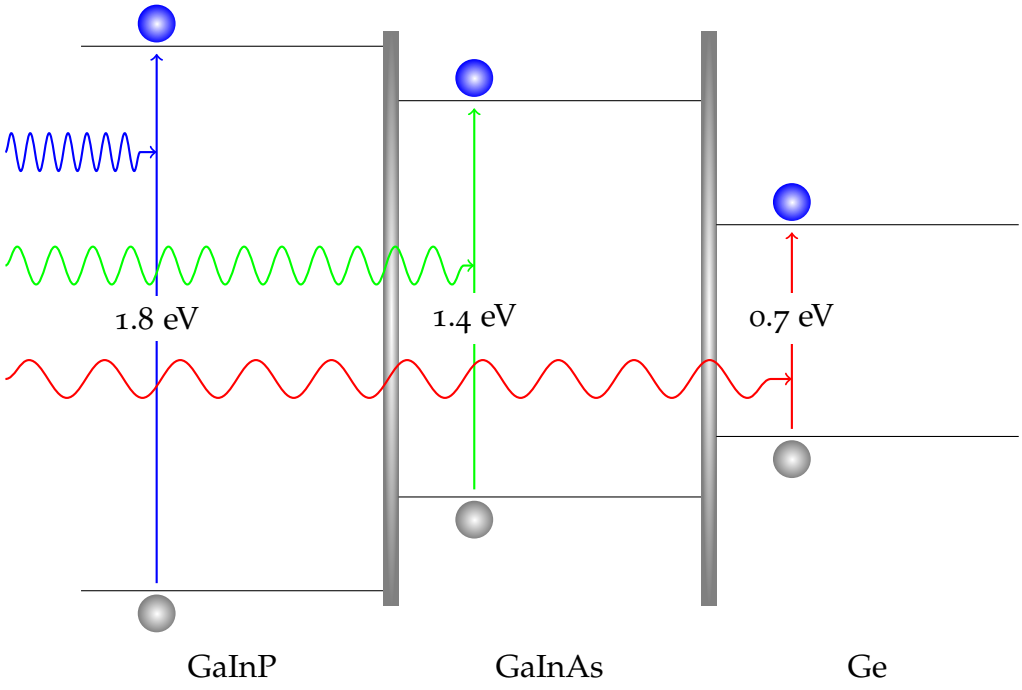

Figure 3.1.: Schematic of a multijunction solar cell. A typical multijunction may consist of (top to bottom) GaInP/GaInAs/Ge separated by tunnel diodes. The bandgap energies of the subcells are 1.8 eV/1.4 eV/0.7 eV.

Each absorber in the cell is separated from its neighbours by a tunnel diode (also known as an Esaki diode after its inventor, Leo Esaki, who was awarded the Nobel prize for his invention in 1973) [69]. The tunnelling diode consists of a heavily doped p-n heterojunction with a depletion region on the scale of 100 Å. Due to the narrow space-charge region and high intrinsic field, there is a chance for an electron in the n-side of the junction to tunnel into the p-side under small

forward bias. When incorporated into a multijunction solar cell, this allows for carrier extraction in much the same way as outlined for the basic p-n junction in section 2.2.

Finally, electrical contacts at the front and back edges of the cell connect to an external circuit allowing for charge extraction. The back contact is often reflective so as to increase photoabsorption by giving those photons not absorbed on the way in a second pass through the cell.

Multijunction solar cells my be grown "monolithically" as a single crystal, or each subcell may be grown separately on different substrates and later stacked mechanically [70]. The former is the more common method due to its simplicity and low cost, however, materials with ideal band gap ratios often have large lattice mismatches leading to misfit dislocations and trap states being created in the band gap (see section 2.6.2). Mechanically assembled multijunction cells are less prone to crystal defects, however the production cost usually outweighs the increase in efficiency; this method is generally only used where the efficiency is of utmost importance (for example in extraterrestrial photovoltaics, where the power-to-weight ratio is the prohibitive factor).

A common triple-junction solar cell in use today consists of a top layer of GaInP, middle layer of GaInAs, and bottom layer of Ge, the bandgaps of which are 1.8 eV, 1.4 eV, and 0.7 eV, respectively, as illustrated in figure 3.1 [70]. While a greater proportion of the spectrum is absorbed to produce bandedge charge carriers, a significant proportion of the photocarriers are hot; for example, an incident photon of energy 1.3 eV will be absorbed in the germanium layer, producing an electron hole pair with an energy excess of 600 meV—46% of the incident photon energy is lost as heat. For this reason, the overall efficiency of the device increases as more subcells are incorporated, however, it is also the case that each additional subcell increases the device efficiency with diminishing returns. As such, most practical multijunctions are limited to three to five subcells [70]. The

maximum theoretical efficiency for several multijunction solar cell devices have been calculated by several authors, a selection of which are shown in table 3.1.

Number of Junctions	Under 1 Solar illumination	Maximum efficiency
1	30%[1]	37%[2]
2	42%[1]	50%[2]
3	49%[1]	56%[2]
36		72%[2]
∞	68[1]	86%[1]

Table 3.1.: Maximum efficiency of an N-junction solar cell. Values taken from [1]reference [71] and [2]reference [72].

It is worth noting that the detailed balance limit of efficiency given in table 3.1 for the ∞-junction solar cell device, which covers the entire solar spectrum with no heat loss due to carrier cooling, is lower than the thermodynamic limit of efficiency of 93% [72, 73]. The discrepancy between these two values is a consequence of the unavoidable loss associated with radiative carrier recombination.

The triple-junction device provides good compromise between efficiency and cost/device complexity. The current efficiency record for a triple-junction device is held by a metamorphic GaInP/GaInAs/Ge cell at 40.1% under AM1.5 illumination at a concentration factor of 240 Suns [74]. The overall record for solar cell efficiency, held by the a quadruple-junction GaIn/GaAs/GaInAs/GaIn device under a concentration of 508 suns, stands at 46% [33, 35, 36].

Solar cell devices incorporating a large number of subcells are technically difficult to build and prohibitively expensive. The addition of intermediate bands within the N-junction cell is one method by which the cell efficiency may be further enhanced. These intermediate bands form new bandgaps within the structure, thereby reducing the amount of energy lost to carrier cooling. The underlying material of the intermediate bands may consist of an ensemble of *nanocrystal quantum dots* (NQDs, see chapter 4). The tunable nature of the NQD band structure allows NQDs to be used in any material. The inclusion of a single intermediate band has the potential to increase the efficiency of a single-junction from 30% to 63.1%, rising to 71.7% with the inclusion of two bands [8, 75]. Fur-

ther, for a series of NQDs whose energy gaps approach a continuum, the device efficiency would approach that of the ∞-junction SC. The potential of the intermediate band approach cannot be overstated, and will be discussed in the next section.

3.2 INTERMEDIATE BAND SOLAR CELL DEVICES

The spectral range over which a fixed-gap photovoltaic solar cell operates may be extended by the inclusion of an intermediate band (IB) within the forbidden region of the bulk host material in the intrinsic part of a p-i-n heterojunction (a p-n junction with an intrinsic layer between the p and n-sides, see figure 3.2). With the additional energy band, the gap is split into two sub-bands; low energy photons may then stimulate an electronic transition from the valence band to the intermediate band, or from the intermediate band to the conduction band of the host (the VB and CB energies are unchanged). A VB-IB transition accompanied by an IB-CB transition is equivalent to the VB-CB transition in the conventional cell with the same bandgap [8–10]. In order to simultaneously facilitate both VB-IB transitions and IB-CB transitions, the intermediate band should ideally be half populated at all times so that is can both accept electrons from the valence band and donate electrons to the conduction band. The IB must then coincide with the Fermi level.

The intermediate band may be added in a number of ways, such as by crystal impurities or inclusion of a *nanocrystal superlattice* [76–78]. The superlattice consists of an ensemble of quantum dots (QDs) in contact via the Coulomb force. For identical QDs, the energy levels form a series of minibands rather than a single intermediate band. By appropriately populating the QDs with charge carriers, the intermediate band may be aligned with the Fermi level of the structure [79]. Such devices have already been demonstrated in the lab with observed efficiencies of up to 18.3% [80, 81]

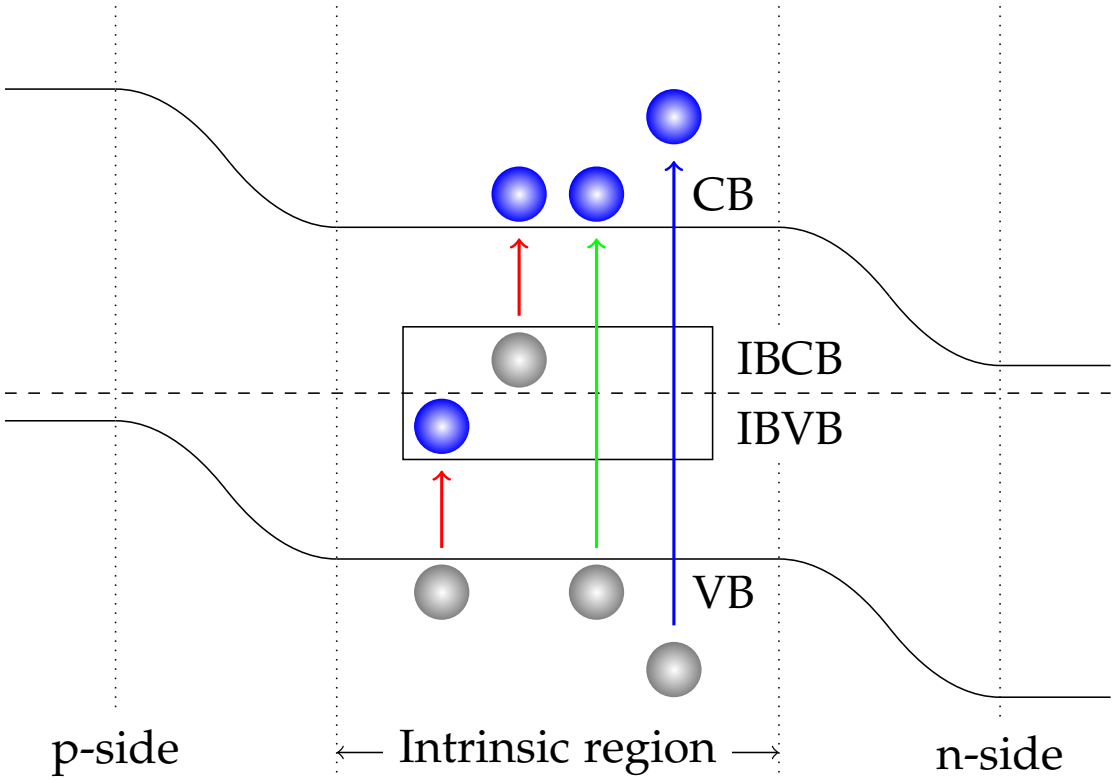

Figure 3.2.: A solar cell containing an intermediate band within the band gap of the intrinsic region of a p-i-n heterojunction. The intermediate band should ideally be half-populated in order to both accept electrons from the valence band and supply electrons to the conduction band. The intermediate band should also be aligned with the Fermi energy.

The maximum theoretical efficiency of an IBSC device incorporating a single intermediate band is the same as that of the triple-junction solar cell with corresponding bandgaps (see table 3.1). The number of added bands may be extended to an arbitrary number [76]. The limiting efficiency of the IBSC incorporating a single intermediate band has been calculated by Luque and Martí to be 63.2% [8].

Despite the successes of the intermediate band approach to efficiency enhancement, much of the energy from high frequency incident photons is lost as heat. The efficiency of the solar cell device can be further enhanced if instead this excess energy is used to create further electron-hole pairs. This is achieved via impact ionisation.

3.3 IMPACT IONISATION

Carrier cooling processes constitute one of the greatest sources of inefficiency in photovoltaic cell devices [82]. Intermediate band solar cells do nothing to reduce carrier cooling losses, while multijunction cells comprised of more than about five subcells are prohibitively expensive and technologically difficult to manufacture. One way in which such loss mechanisms may be mitigated is by the exploitation of *impact ionisation*.

In the impact ionisation (II) process, a hot carrier far above the band edge cools while simultaneously exciting a secondary charge carrier (electron) from the valance band into the conduction band, thus cooling the initially hot carrier by at least E_g. In this sense, impact ionisation is the inverse of the direct Auger process (see figure 3.3) [43, 44].

Recalling that in the detailed balance treatment of the conventional solar cell device it was assumed that any absorbed photon of energy $\hbar\omega > E_g$ had exactly the same effect as photoabsorption at the bandgap energy (no hot carriers), and further that all carrier recombination was radiative (no Auger processes). The ef-

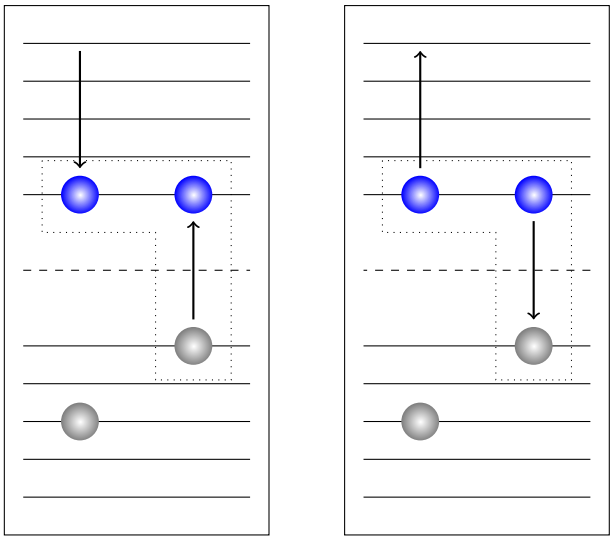

Figure 3.3.: Impact ionisation (left) is the inverse of the direct Auger process (right). Both processes involve three charge carriers.

fects of carrier multiplication were not accounted for in the treatment of Shockley and Queisser. Accordingly, the Shockley-Queisser limit of efficiency may be surpassed if the quantum yield (QY)—the number of electron-hole pairs generated per photon absorbed—is increased through impact ionisation [13, 83, 84]. Due to the assumptions of the Shockley-Queisser model, the QY in their calculations was implicitly assumed to be 100% (i.e. one ehp per photon absorbed).

From considerations of energy conservation, there is an energy threshold below which impact ionisation cannot occur. Since impact ionisation, like the Auger process, involves the interaction of three charge carriers (either a hot electron or hot hole creating a second ehp), the electron-hole pair creation energy must originate from a single charge carrier. Thus, the initial hot electron or hot hole, and not the initial ehp, must posses energy of at least $2E_g$. Since the excess energy from absorption of a high energy photon is split between the charge carriers constituting the photogenerated electron-hole pair, and according to equations 2.1 and 2.2, the photon threshold energy for impact ionisation

may be estimated as function of the charge carrier effective masses in the solar cell material [43, 44, 83] as

$$h\nu_{\text{thresh.}} = \left(2 + \frac{m_{\text{e}}^*}{m_{\text{h}}^*}\right) E_{\text{g}}. \tag{3.1}$$

Despite being an approximate expression, equation 3.1 agrees well with observation: for example, the predicted threshold for PbSe is $\sim 3E_{\text{g}}$ as compared to measurements of onset between values of $2E_{\text{g}}$ and $3E_{\text{g}}$ [85–87], while for InAs it is $\sim 2.05E_{\text{g}}$ as compared to measured values of $2E_{\text{g}}$ [88].[1]

The timescales associated with the impact ionisation process may be related to the direct Auger process discussed in section 2.6.1. Taking Auger coefficients introduced in equations 2.48 and 2.49 and considering the steady state of detailed balance [65], the equation of balance in which the Auger and inverse Auger processes are exactly opposed is given by

$$\frac{\partial n}{\partial t} = G + \left(\beta_{\text{n}} n - \gamma_{\text{n}} n^2 p\right) + \left(\beta_{\text{p}} p - \gamma_{\text{p}} n p^2\right), \tag{3.2}$$

where β_{n} and β_{p} are the coefficients for impact ionisation, and G is the rate of carrier generation. In the absence of an energy pump $G \to 0$ and the equilibrium rates of Auger recombination and impact ionisation are exactly opposed, as is required by the principle of detailed balance. The terms in each of the brackets are then equal to zero, and the coefficients for impact ionisation are therefore

$$\beta_{\text{n}} = \gamma_{\text{n}} n p \qquad \text{and} \qquad \beta_{\text{p}} = \gamma_{\text{p}} n p. \tag{3.3}$$

In calculating the maximum efficiency of a photovoltaic cell in the presence of impact ionisation, the II must be balanced by the rate of Auger recombination [66, 67]. When the pump field is sufficiently low such that photoexcitation

1 it should be noted that the measurement of impact ionisation is a somewhat complicated process due to the difficulty in identifying which processes correspond to the measurements taken. An in-depth discussion on the subject is presented in reference [84] and references therein.

of charge carriers may be neglected, the maximum efficiency for a single gap solar cell under one solar illumination (bandgap energy of $\sim$ 1 eV) is found to be 42%[89–91]. Under maximum concentration and vanishing bandgap ($E_g \rightarrow 0$), the maximum efficiency is 85% [92].

In order for carrier multiplication to occur with useful prevalence, impact ionisation events must out-compete the carrier cooling rate. Impact ionisation does not, however, occur with great presence in bulk materials. As with the Auger process mentioned in section 2.6.1, impact ionisation becomes important only for narrow-gap materials or in the presence of high intensity electric fields [43, 48, 83]. It has been suggested, however, that the impact ionisation process may become significantly enhanced in solar cell devices based on nanocrystal quantum dot technology, where the discrete nature of the energy states in NQDs restricts the final density of states for phonon mediated carrier relaxation events [13]. When the intraband energy separation becomes larger that the phonon energy, $\hbar\omega_{\text{phon}}$, simultaneous emission of multiple phonons are required in order to facilitate a downward electronic transition (upward hole transition). As a result, the rate of carrier cooling is much longer in QDs than in the bulk—an effect known as the *phonon bottleneck*. The phonon bottleneck and impact ionisation, known as *multiple exciton generation* in strongly confined structures, are discussed at length in sections 4.3 and 4.4.

3.4 CHAPTER SUMMARY

In this section several energy enhancement schemes have been discussed: multijunction cells, where several absorbing materials of appropriate band gap energies make better use of the solar spectrum; intermediate band solar cells, where an additional energy level is introduced into the interstice between the HOMO and LUMO of the bulk absorbed, thereby allowing for photoabsorption at subbandgap energy; and impact ionisation solar cells, where high energy carriers

may create further electron-hole pairs (carrier multiplication) instead of losing their excess energy as heat. Each of schemes may be realised by with the use of quantum nanocrystal technology, as discussed in the next chapter.

4

QUANTUM NANOCRYSTALS

Conventional solar cell technology is based on the properties of bulk semiconductor materials. Such systems are subject to the Shockley-Queisser limit of efficiency. It is widely agreed upon that in order to bypass this limit the next (third) generation of photovoltaic solar cells will be based on nanotechnology. Nanomaterials offer several advantages over bulk semiconductors. First, within the regime of quantum confinement, the optoelectronic properties of the structures are strongly dependent on the size of the crystal [93]. This allows for the selection of the electronic energy states at the point of synthesis, known as "dot tuning" in zero-dimensional systems (quantum dots) [84]. Second, the discrete nature of the atomic levels in the dimensions of confinement has strong consequences on carrier mobilities and densities of states [94]. The nanostructures therefore show great promise for use in the enhancement schemes discussed in the previous chapter. Finally, nanocrystals are cheap and relatively straightforward to manufacture, often grown colloidally with "one-pot" synthesis methods where, by adding the relevant chemicals after the correct reaction time, high quality monodisperse samples may be produced with a high degree of consistency [95].

The current chapter details the properties of quantum confined nanocrystals and explains how quantum confinement may be used to enhance the impact ionisation process in nanocrystal quantum dots. To this end, the various de-

grees of confinement will be discussed (3D, 2D, 1D, and 0D systems), as well as comparison of various semiconductor materials which may be used.

4.1 QUANTUM CONFINEMENT

When a semiconductor crystal is sufficiently small (typically on the order of 10^{-9} metres), it exhibits *quantum confinement*. In a bulk semiconductor, charge carriers are free to move about the crystal as free particles with effective mass m^*. If, however, the crystal is smaller than the exciton Bohr radius, h/p, of the carrier, then the carrier wavefunction is localised within the crystal. The carrier is then said to be confined. When considering an electron-hole pair as a quasiparticle, i.e. as an *exciton*, the confining crystal must be smaller than the average separation of the constituent electron and hole—the *exciton Bohr radius*, so-called due to the ehps resemblance to the hydrogen atom. The exciton Bohr radius may be calculated as

$$a_X = \frac{4\pi\epsilon_0\epsilon_r\hbar^2 m_0}{m_e^* e^2}\left(\frac{m_e^* + m_h^*}{m_e^* m_h^*}\right) = \frac{\hbar\epsilon_r}{m_e^* c\alpha}\frac{m_0}{\mu}, \tag{4.1}$$

where α is the fine structure constant and $\mu = m_e^* m_h^*/(m_e^* + m_h^*)$ is the reduced mass of the ehp (i.e. the mass of the exciton) [21, 39]. Due to its dependence on the effective masses of the particles comprising the electron-hole pair, the exciton Bohr radius is highly material-specific. Some illustrative values of a_X are given in table 4.1.

Quantum nanocrystals may exhibit confinement in one, two, or all three spatial dimensions [13]. The resulting structures are known respectively as quantum wells (or quantum films), quantum wires, and quantum dots. The densities of states of these structures are two dimensional, one-dimensional, and zero-dimensional, respectively (see table 4.2). Each of these structures will be detailed below.

Material	Exciton Bohr radius (Å)
GaAs[1]	11.2
InAs[2]	340
InP[1]	113
CdSe[2]	60
CdTe[1]	12.2
PbSe[2]	460
PbS[2]	200

Table 4.1.: Exciton Bohr radii for various materials. Values taken from [1]reference [21] and [2]reference [94].

Structure	Dimensions of confinement	Density of states
Bulk crystal	0D	3D
Quantum well	1D	2D
Quantum wire	2D	1D
Quantum dot	3D	0D

Table 4.2.: The dimensionallity of confinement for different structures.

4.1.1 *Unconfined Systems—The Bulk*

In studying a bulk semiconductor, the crystal is typically regarded as being infinite in extent; edge effects are neglected, and the infinite crystal is modelled by a small unit cell under periodic boundary conditions. Within the free-electron model, electrons in the crystal are treated as a free electron gas (Fermi gas). Electron-electron scattering is ignored, and effect of the nuclear potential is included via the charge carrier effective masses. The one-electron time independent Schrödinger equation reduces to just the kinetic energy of the particle with effective mass m_e^* [96], suggesting the parabolic band dispersion relation

$$E = \frac{\hbar^2 k^2}{2m_e^*}. \tag{4.2}$$

In an unconfined system, the allowed values of wavevector $\boldsymbol{k}$ form a quasi-continuum: a band structure comprised of continua of allowed energy states

(bands) separated by forbidden regions (bandgaps). The values of $\boldsymbol{k}$ which an electron may take are discrete and given by

$$k_x = 2\pi\frac{n_x}{L_x} \qquad k_y = 2\pi\frac{n_y}{L_y} \qquad \text{and} \qquad k_z = 2\pi\frac{n_z}{L_z}, \tag{4.3}$$

where n_x, n_y, and n_z are integers, L_x, L_y, and L_z are the spatial dimensions of the crystal with volume $V = L_x L_y L_z$ [38, 97]. The range of allowed $\boldsymbol{k}$ values for a particular energy lie on the surface of a sphere of constant energy in the $\boldsymbol{k}$-space, and the density of $\boldsymbol{k}$-points may be found by taking the volume element between two concentric spheres with thickness $d\boldsymbol{k}$ [98]. The density of states per unit energy interval (see figure 4.3, page 53) is then

$$\rho_{3D}(E) = \frac{1}{2\pi^2}\left(\frac{2m_e^*}{\hbar^2}\right)^{\frac{3}{2}} E^{\frac{1}{2}} \tag{4.4}$$

4.1.2 *Confinement in One Dimension—Quantum Wells*

The two-dimensional quantum well was the first system to be studied in the quantum confined regime [99]. A typical structure consists of a nanometres thick sheet of semiconducting material sandwiched between two (often identical) bulk semiconductors. The bulk materials posses a wider bandgap than that of the nanosheet, forming a type I "straddling gap" heterojunction on each side of the sheet. The resulting potential barriers are large and confine the carriers to the well in the direction of growth (usually referred to as the z-axis). The charge carriers are free to move in any lateral direction and, depending on the alignment between the bands of the sheet and bulk materials, it is possible that only electrons or only holes are confined along the z-axis [13].

The quantum well need not necessarily exist in isolation. A series of quantum wells may be formed by growing alternate layers of bulk and sheet material (figure 4.1). If the bulk layers are sufficiently thick as to eliminate electronic

coupling between the wells then each well in the array exists in isolation: the resultant devices is known as a "multiple quantum well." If, however, the bulk layers are thin, then the carrier wavefunctions overlap and a series of minibands are formed. This is termed a "superlattice. [13]"

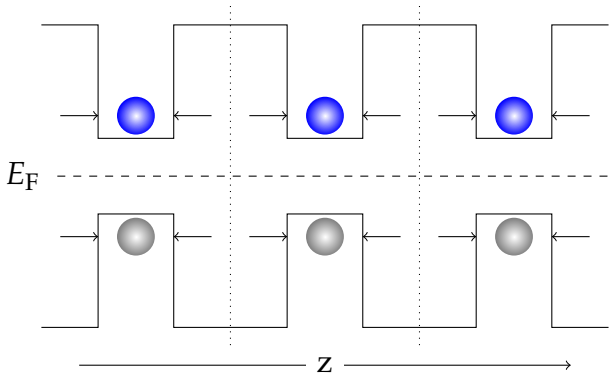

Figure 4.1.: Schematic of a multiple quantum well structure. Charge carriers are confined to the wells by the potential at the interfaces. The region between the dotted lines forms a type I heterojunction.

The eigenvalues and eigenvectors of the single quantum well are those of the well-known "particle in a box" problem. The density of states for such a system may be found by considering the number of $\boldsymbol{k}$-points within the area of thickness d$\boldsymbol{k}$ bounded by two concentric circles of constant energy in the two-dimensional $\boldsymbol{k}$-space, and is given by (see figure 4.3 below)

$$\rho_{2D}(E) = \frac{m_e^*}{\pi\hbar^2} \sum_{n_z} \Theta(E - E_{n_z}), \tag{4.5}$$

where $\Theta(E - E_{n_z})$ is the Heaviside unit step function, equal to 0 when $E < E_{n_z}$, and equal to 1 otherwise [21, 100].

4.1.3 *Confinement in Two Dimensions—Quantum Wires*

A system which exhibits quantum confinement in two dimensions is known as a *quantum nanowire* [13]. While the nanowire must have lateral dimensions smaller than the exciton Bohr radius of the constituent material, there is no specific limit

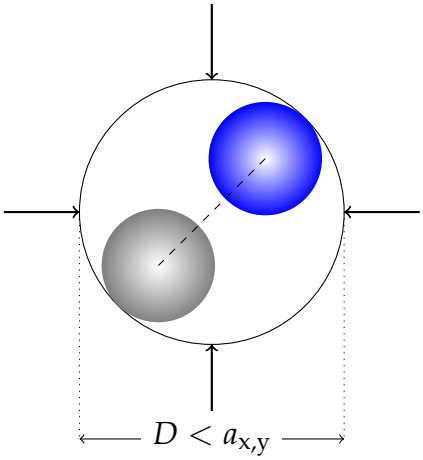

Figure 4.2.: Cross-section of a quantum nanowire Carrier are confined along the lateral dimensions of the nanowire.

for the third (longitudinal) dimension, with aspect ratios on the order of 20:1 being commonplace [101], while aspect ratios as high as 200:1 have been reported in the literature [102]. Charge carriers confined within the quantum nanowire posses only one degree of freedom, and the $\boldsymbol{k}$-space is therefore one-dimensional. The density of states for the nanowire may be found by taking length element $d\boldsymbol{r}$ in the $\boldsymbol{k}$-space [103]. The one-dimensional electronic density of states is then (see figure 4.3 below)

$$\rho_{1D}(E) = \sqrt{\frac{2m_e^*}{\pi^2\hbar^*}} \sum_{n_x,n_y} \left(E - E_{n_x,n_y}\right)^{-\frac{1}{2}} \Theta\left(E - E_{n_x,n_y}\right). \tag{4.6}$$

4.1.4 *Confinement in Three Dimensions—Quantum Dots*

When a semiconductor exhibits quantum confinement in all three spatial dimensions, the nanocrystal is termed a *quantum dot* [104]. The electronic structure of the quantum dot is regarded as being zero-dimensional; the QD itself posses internal structure, being made of atoms. Since the charge carriers are completely

confined within the dot, possessing no internal degree of freedom, the density of states for an ideal quantum dot consists of a series of delta functions:

$$\rho_{0D}(E) = 2 \sum_{n_x,n_y,n_z} \delta\left(E - E_{n_x,n_y,n_z}\right), \tag{4.7}$$

where the factor of 2 accounts for spin degeneracy [103].The carrier may only be found in particular discrete energy states, related to the $\boldsymbol{k}$-values given in equation 4.3 (see figure 4.3). Due to the resemblance of the quantum dot electronic structure to that of an isolated atom, QDs are sometimes referred to as "artificial atoms."

Since the allowed values of wavevector $\boldsymbol{k}$ are inversely proportional to the length of the confinement region, so too are the gaps between energy states inversely dependent upon the physical size of the QD [93]. Accordingly, a large blue shift is observed in the energy spectrum of the dot as compared to the spectrum of the material in bulk. The degree of the blue shift is larger for smaller QDs. Although no such energy bands exist in zero-dimensional nanocrystals, the size-dependent optical gap between the highest occupied molecular orbital (HOMO) and lowest unoccupied molecular orbital (LUMO) is often referred to as the quantum dot bandgap.

The discrete nature of the zero-dimensional density of states has the potential to greatly enhance the rates of Auger and inverse Auger (impact ionisation) processes in nanocrystal quantum dots due to the existence of the phonon bottleneck [14]. This important effect of quantum confinement will be discussed in the section 4.3.

4.2 NANOCRYSTAL QUANTUM DOTS—ARTIFICIAL ATOMS

Quantum dots were first observed in silicate glass by H. P. Rocksby in the 1930s [105]. It was noted that the red and yellow colouration of the glass was

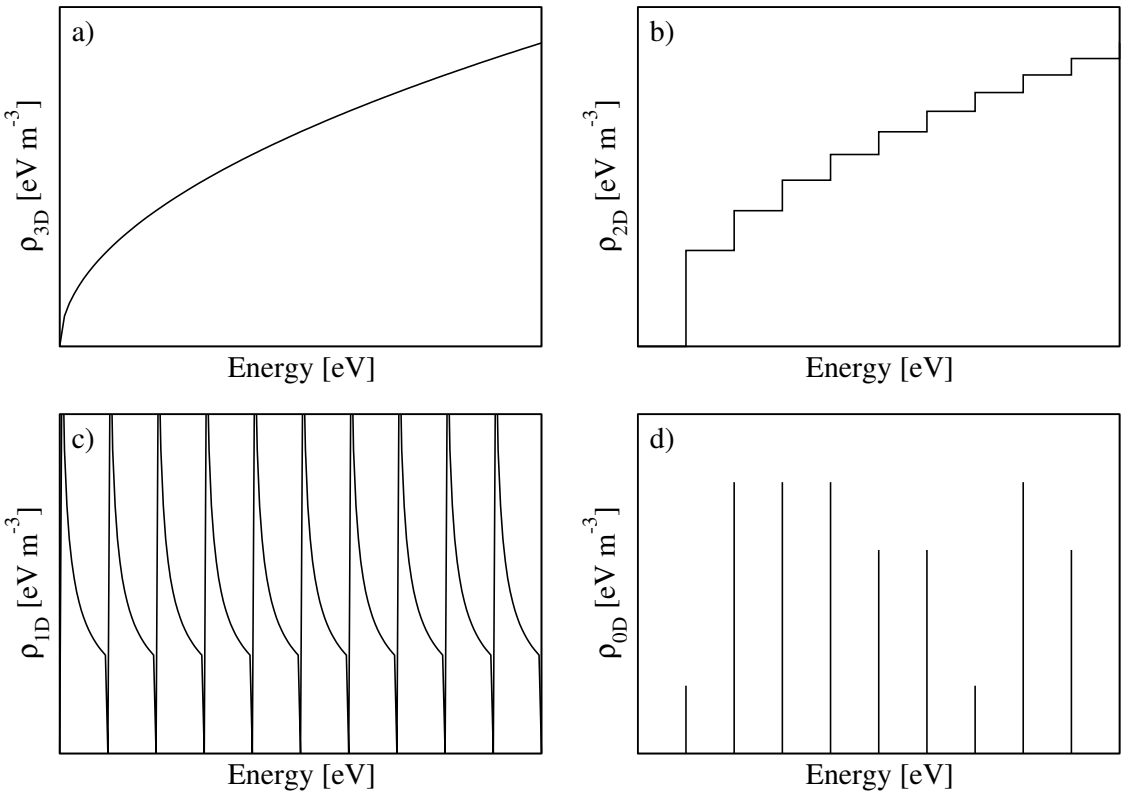

Figure 4.3.: Density of states for a) bulk (3D), b) quantum well (2D), c) quantum wire (1D), and d) quantum dot (0D).

caused by microscopic impurities of cadmium included in the glass. At the time, Rocksby referred to these impurities as *microcrystals*. The microcrystals were later given the moniker "quantum dot" to better emphasis the fact that the microcrystals have zero-dimensional electronic properties [106]. It was not until some fifty years later that the mechanism by which cadmium microcrystals altered the colour of the glass was explained, when Alexy Ekimov described the *quantum size effect* (quantum confinement effect) in copper chloride microcrystals embedded in a glass matrix [93]. The different pigmentations of Rocksby's glass samples could be attributed to the size-dependent optical gaps of the cadmium microcrystals.

An expression to estimate the size-dependent bandgap energy (HOMO-LUMO gap) of the microcrystals was developed by Louis Brus in 1984:

$$E \approx \frac{\hbar^2 \pi^2}{2R^2}\left[\frac{1}{m_e}+\frac{1}{m_h}\right] - \frac{1.8e^2}{\epsilon_{QD}\boldsymbol{R}} + \frac{e^2}{\boldsymbol{R}}\overline{\sum_{n=1}^{\infty} a_n \left(\frac{\boldsymbol{r}}{\boldsymbol{R}}\right)^{2n}}, \tag{4.8}$$

where the overbar denotes an average over a particular ψ, ϵ_{QD} is the dielectric constant of the dot, and R is the radius [107]. Brus went on to discover the existence of colloidal quantum dots in 1986 [108].

Artificial quantum dots were first synthesised by Ekimov and colleagues in 1985, with more sophisticated techniques being developed by Murray et. al. in the early 1990s, leading to the high-quality, monodisperse samples produced by colloidal chemistry today [109, 110].

Presently, colloidal nanocrystal quantum dots are routinely produced from a variety of semiconductors, including: II-VI materials such as CdS, CdSe, and CdTe [110]; various III-V structures such as InGaAs on GaAs substrate and in AlGaAs matrix [111, 112], and InAlAs in AlGaAs matrix [113, 114]; and IV-VI lead chalcogenide compounds, PbS, PbSe, and PbTe in colloid [115–117]. Quantum dots made of silicon, carbon, and graphene have also been reported [118, 119].

4.3 EFFICIENT CARRIER MULTIPLICATION IN NANOCRYSTAL QUANTUM DOTS

As has been discussed previously, impact ionisation, the reverse Auger processes, has the potential to significantly improve upon the efficiency of the conventional solar cell. Upon absorption of a high-energy photon (of energy *at least* equal to the bandgap), the excess energy is used to generate secondary electron-hole pairs—a process known as *carrier multiplication*. Since carrier multiplication usually involves the scattering of only one of the hot photocarriers comprising the initial ehp (with the division of energy being given by equations 2.1 and 2.2) , the incident photon must therefore have sufficient energy to excite at least one of the carriers to twice the bandgap energy. As a result, impact ionisation provides only an extremely small proportion of the overall photocurrent in bulk semiconductor devices, becoming important typically only at ultraviolet frequencies,

far above the peak in the solar spectrum. It has been predicted, however, that carrier multiplication may be a much more efficient process in zero-dimensional systems (quantum dots) due to greatly slowed carrier cooling rates, even at arbitrarily low illumination, due to the phonon bottleneck effect [14, 120–122]. Efficient carrier multiplication in nanocrystal quantum dots was first demonstrated by Schaller and Klimov in 2003 [123].

4.3.1 *Phonon Bottleneck*

Slowed hot carrier cooling in nanocrystal quantum dots was first predicted by Boudreaux et. al. in 1980 [120]. They were to first group to note that phonon mediated carrier cooling should be suppressed when the (intraband) energy gaps in the discrete QD energy spectrum are greater than the phonon energy, $\hbar\omega_{\text{phon}}$. Simultaneous scattering of multiple phonons is therefore necessary in order to facilitate a downward electronic transition. In their paper, Boudreaux and colleges suggested an approximate expression for the multiphonon relaxation time of

$$\tau_{\text{C}} \sim \omega_{\text{phon}}^{-1} \exp\left(\frac{\Delta E}{k_{\text{B}} T}\right), \tag{4.9}$$

where ω_{phon} is the phonon angular frequency and ΔE is the transition energy (energy level separation). The theory put forward by Boudreaux has since been refined by other authors such as Bockelmann [121, 124] and Bensity [14, 122].

The phonon bottleneck has been demonstrated by the phenomenon of photoluminescence (PL) blinking present in (CdSe) quantum dot structures [125, 126]. When two ehps have been generated via two separate photoexcitation events, one the pairs may recombine in an auger process, transferring energy to one of the carriers comprising the second ehp (which carrier would depend on the band offsets and confinement energies of the carriers). The excited carrier is then ionised to the surface of the nanostructure (or, in the case of core/shell structures, into the shell). The QD then possesses a net charge, and an electric

dipole is established in the dot. The ionisation of the crystal leads to a reduced screening factor and a resultant increase in the (Coulomb mediated) Auger interaction. Further photocarriers generated in the dot then overwhelmingly recombine through nonradiative means until the ionised carrier returns to the dot. The timescale during which the PL is "on" is inversely proportional to the intensity of the illumination. Since Auger processes become so prominent in the presence of the phonon bottleneck, so too may the inverse process become significant.

There have been many reports which either support [127] or reject [128] the presence of a phonon bottleneck effect in nanocrystal quantum dot systems.[1] While long lifetimes for radiative recombination are known to occur in NQDs, those articles which argue against the existence of a phonon bottleneck point out that the lifetimes should in principle by infinite, and that no photoluminescence should be observed. The measured lifetimes are however of an order of magnitude longer than in the corresponding bulk material, which suggests that the phonon bottleneck is present, at least to some extent. When the radiative carrier lifetime is on the order of 10 ps, Auger processes may compete to be the dominant mechanism for carrier relaxation [129].

There are several ways in which the phonon bottleneck may be broken. Firstly, Auger processes where the excess electron energy is transferred to a hole in the valence band may lead to fast carrier cooling in systems where $m_h^* >> m_e^*$. The hole may rapidly cool due to its high effective mass and the narrow energy spacing in the VB (compared to the conduction band energy spacing) [130]. Other mechanisms by which the phonon bottleneck may be circumvented include electron-hole scattering [131], deep level trap-assisted thermalisation [132], and processes involving both longitudinal optical and longitudinal acoustic phonons [133, 134].

Detailed balanced calculations undertaken by Klimov show that the maximum theoretical efficiency of a quantum nanocrystal in the presence of multi-

1 For a comprehensive list of such articles see the review article by Arthur Nozik [13].

ple exciton generation and Auger recombination is 42% for the ideal case where $h\nu_{\text{thresh.}} = 2E_g$, reducing to 36% when $h\nu_{\text{thresh.}} = 3E_g$, however, as will be seen in the next section, these limits of efficiency may be enhanced with proper design of the nanocrystal structures [91].

4.4 MEG ENHANCEMENT IN CORE/SHELL QUANTUM DOT HETEROSTRUCTURES

Detailed balance calculations to find the upper bound to the efficiency of a photovoltaic cell with various device architectures in the presence of direct carrier multiplication have been undertaken by several authors [48, 86]. Notably, calculations on single-junction bulk structures undertaken by Hanna and Nozik predict a maximum efficiency of 44% [48], while Klimov's calculations for monodisperse quantum dot structures predicts a limiting efficiency of 42% in the case that the MEG threshold is $2E_g$.

In both of the treatments mentioned above, the systems under consideration consist of a single semiconductor species. However, it has recently been predicted [120, 135], and, in some cases, experimentally verified [136], that carrier cooling in quantum dot heterostructures may differ greatly from their monocrystalline analogues. The most easily realised, and therefore most studied systems are *core/shell quantum dot heterostructures*. First grown synthetically by Hines and Guyet-Sionnest [137], the core/shell QD is comprised of a single-crystal "core" region enveloped by a second "shell" region of a different semiconductor species (see figure 4.4). The shell region usually possesses a larger bandgap than the core region. In either configuration, appropriate materials have type-II band alignment. The convention for such heterostructures is to denote the core and shell materials as <core material>/<shell material>.

The addition of the shell has two main effects. Firstly, the shell serves to passivate dangling bonds at the surface of the dot (surface ligands) which arise

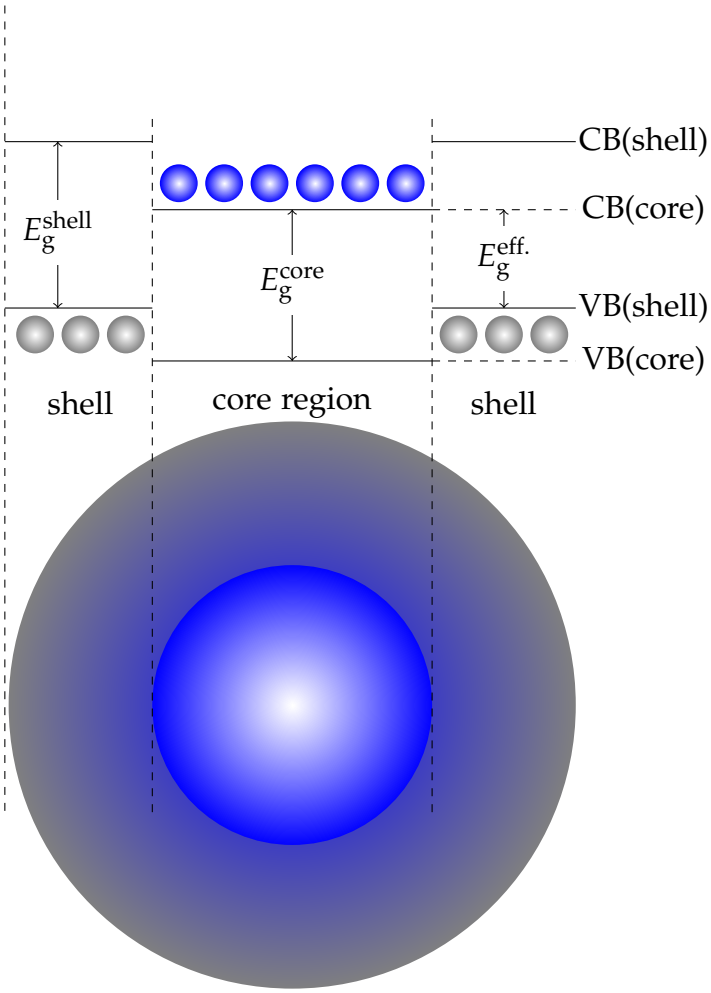

Figure 4.4.: Type-II band alignment for core/shell QD cross-section. The core region is enveloped by a semiconductor with band alignment such that a "staggered gap" interface is formed. This results in an effective band gap being established in the dot and carrier confinement to the core and shell region (here, CB electrons are confined to the core, while VB holes are confined to the shell.

from the lack of coordination in atoms at the dot surface, vastly reducing the number of trap states near the surface [138]. This reduces the strength of the phonon bottleneck, and PL blinking is less prominent. Secondly, the energy offsets forming the type-II heterostructure result in confinement of the charge carriers into separate regions of the dot: electrons are confined to the core while holes are confined to the shell region, or vice-versa, depending on the relative band alignment between the two regions [139]. The confinement is a result of the effective bandgap established between the VB of one material and the CB of the other (see figure 4.4). The strength of the confinement is in part determined by the physical size of the core and shell regions.

It has recently been shown that the addition of the shell, while modifying the electronic structure and energy gaps of the dot, does not necessarily lead to removal of the phonon bottleneck effect [138]. By using an 8-band $\mathbf{k} \cdot \mathbf{p}$ and configuration interaction approach, it has been predicted that the addition of a CdTe shell on a spherical CdSe core results in reduction of the intraband energy level separation, however, phonon bottle necks remain for the shell thickness studied. The rate of phonon cooling was not found to increase significantly for shell thicknesses up to 3 Å, even at energies above the threshold for multiple exciton generation. Reduction in the electron and hole carrier wavefunctions by spatial separation to the core and shell regions reduces the rate of Auger cooling without an accompanied increase in the rate of phonon mediated cooling, with increased carrier lifetimes observed as a consequence. These predictions were confirmed experimentally for a bare CdSe QD of radius 1.80 ± 0.20 nm (averaged over 100 samples) and CdSe/CdTe QD with the same core radius and CdTe shell thickness $\sim$ 2 nm (estimated, based on the shift in the absorption peak as compared to the bare core). Detailed balance calculations indicate a maximum efficiency of 36.5% for CdSe/CdTe QDs with thick shells; the efficiency is expected to be higher for materials with lower bandgap energy.

4.4.1 *Observation of MEG in real systems*

Multiple exciton generation in quantum nanocrystals was first reported in PbSe QDs by Schaller and Klimov in 2004 [123]. In the time since, MEG has been observed in many nanocrystalline semiconductors, including PbS [85], PbTe [140], CdSe [86], CdTe [141], CdTe/CdSe [142], InAs [143], and Si [144], and even in other, higher-dimensional structures, such as carbon nanotubes [145].

The experimental probing of multiple exciton generation is a complicated task, with ongoing discussion regarding how measurements should be interpreted [84]. This has lead to some controversy in the past, with MEG being reported in several systems, but with subsequent investigations being unable to be replicated the results of those experiments [143, 146–148]; perhaps the most notable of these disagreements being the report [87] and refutation [149] of up to 7 excitons generated from absorption of a single photon in PbSe QDs.

One possible reason for the discrepancies in experimental results arose from the short biexciton[2] lifetimes in the nanocrystals. The lifetime for biexcitons is typically in the 10-100 ps range, and thus must be measured (and under photovoltaic operation, extracted) before recombination can occur [84]. Ultra fast femtosecond pulse laser probes may be used to take such measurements. The problem then lies in making the distinction between biexcitons produced by MEG processes and those arising from two separate photoabsorption events. The rate of photoexcitation may be higher than the rate of carrier recombination for a single exciton. The pump fluence must therefore be sufficiently low that the chance for biexcitons to be produced by absorption of two photons becomes negligible.

Other factors which were suggested sources of discrepancy, and were later ruled out, include: uncertainty in the absorption cross-section, σ for the QD at the pump wavelength [144, 148], arising from the difficulty of determining σ; in-

2 excitons may form bound states in an analogous manner as to how electrons and holes form the excitons themselves. Two excitons may bind to form a biexciton, for example.

homogeneities in the pump beam [83], where the beam fluence is larger at some points on the dot than at others, leading to biexcitons being produced from multiple photoabsorption events; inhomogenous chemistry at the dot surface [83], resulting from differing solutions used to fabricate/wash the dots [150] or the formation of oxide layers at the dot surface [151].

The likely candidate for the irreproducibility of early reports, however, is thought to be photocharging of the QD by the pump beam [152]. In this process, three carriers are excited (two electrons and one hole, or vice-versa), while the fourth is isolated, say, in a surface trap state. The three free carriers may then from a *trion*, a quasiparticle of charge ± 1 (see figure 4.5). Since they are three-body quasiparticles, trions may decay by Auger processes on similar timescales as do biexcitons. The presence of trions may therefore be easily confused with the presence of biexcitons, leading to mistaken reports either for or against the presence of MEG. Reports have shown that laminar flow [153] or sample stirring [154] can remove the photocharging effect from the sample, leading to accurate determination of the quantum yield. Surface passivation achieved through the addition of a thin shell also removes the artefacts of photocharging by removing surface trapping states [138].

Since multiple exciton generation relies on photoabsorption at energies in excess of the bandgap, the greatest potential for exploitation of the solar spectrum is found for materials of narrow bandgap energy. The lead-based IV-VI semiconductor compounds (lead-chalcogenides) represent an exemplary material class in which to explore the physics behind the MEG process. On overview of the material properties for these compounds is given in the next chapter.

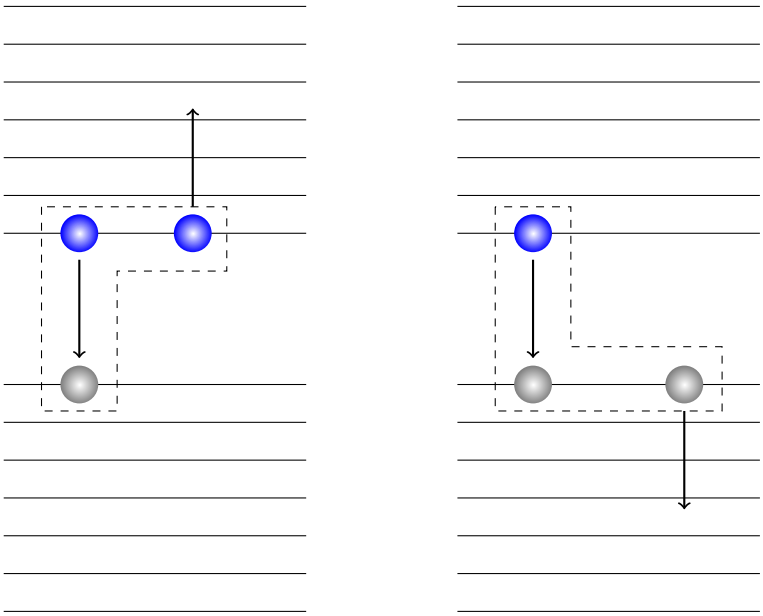

Figure 4.5.: Positive and negative trions cause charge imbalance in the dot. Each may recombine nonradiatively leading to misidentification as biexcitons in early MEG investigations

5

LEAD-CHALCOGENIDE QUANTUM DOTS

Lead sulphide (PbS), lead selenide (PbSe), and lead telluride (PbTe) form a group of materials collectively known as the lead chalcogenides, often denoted by "PbX", where X = S, Se, or Te. Lead is a group IV post-transition metal, while the chalcogenides are from group VI of the periodic table. The lead chalcogenides are, due to their large exciton Bohr radii, excellent candidates with which to explore structures under strong confinement] [94]. Further, due to their electronic properties, lead-chalcogenides have the potential for use in highly efficient solar photovoltaic cell devices which operate under direct carrier multiplication (MEG) processes [85].

Lead chalcogenide compounds form a rock-salt face-centred cubic (FCC) crystal structure; the FCC lattice consists of a two-atom basis, with the lead cation located at the $(0, 0, 0)$ position and the chalcogenide anion at the $(1/2, 1/2, 1/2)$ position (see figure 5.1) [39]. Due to the somewhat unusual electronic structure of the PbX compounds (see section 5.1), the the valency of the lead cation is effectively four [155]. The lead cation therefore binds monotomically with chalcogenide anions. Due to the group II-like valency of the Pb cation, the PbX compounds are sometimes referred to as "Pseudo II-VI" compounds [155]. More commonly, due to the rock-salt crystal structure, the lead chalcogenides are often referred to as *lead-salts*. The lead-salts exhibit several useful properties which facilitate multiple exciton generation processes, which are the focus of the current chapter.

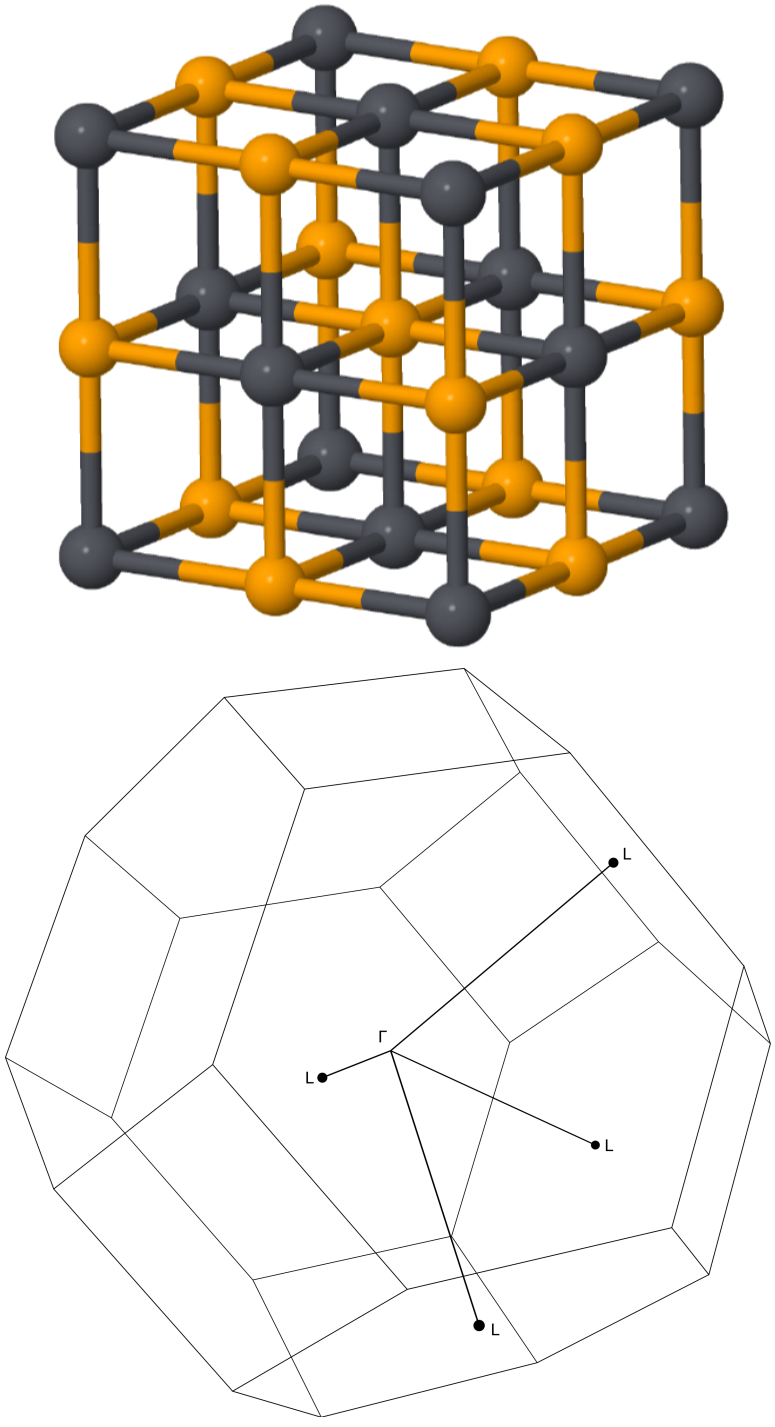

Figure 5.1.: Top: rock-salt crystal structure of lead (black) selenide (yellow). Bottom: Brillouin zone for the FCC lattice. The HOMO and LUMO of the lead-salts are found at the high-symmetry *L*-point of the Brillouin zone.

5.1 THE UNUSUAL ELECTRONIC PROPERTIES OF PBX COMPOUNDS

The lead chalcogenides are known to posses very narrow bandgap energies as compared to many other important semiconductor compounds in the bulk, as outlined in table 2.1. The bandgap energies for PbS, PbSe, and PbTe are 0.41 eV, 0.28 eV, and 0.32 eV, respectively [61, 63, 156]. It is noteworthy that, unlike most other semiconductor compounds, the bandgap energy of the lead-salts does not increase monotomically with the species of anion: $E_g(\text{PbSe}) < E_g(\text{PbTe}) < E_g(\text{PbS})$. These narrow bulk band bandgap energies are ideal for use in solar cell devices which exploit multiple exciton generation. While a larger bandgap, such as that of silicon (1.1 eV), is well suited in traditional photovoltaic applications, the narrow bandgaps of the lead-salts are ideal for MEG applications, with lower photon energies being required to activate the carrier multiplication (lower threshold energy $h\nu_{\text{thresh.}}$).

The lead-salts are direct gap materials (the valence band maximum and conduction band minimum are coincident in the $\boldsymbol{k}$-space), however, the bandgap, in contrast to the majority of direct-gap semiconductor materials, is located at the L-point of the first Brillouin zone, as opposed to at the zone centre (Γ-point, see figures 5.1-5.3) [157]. The band-edge symmetries are therefore distinct from those of the more familiar zone-centre direct-gap (e.g. III-V) materials. For the III-Vs, where the basis states are taken along the cubic unit cell axes, states at the bottom of the conduction band have s-like ($n = 1,\ l = 0,\ m = 0$) spatial symmetry, while states at the top of the valence band have atomic p-like ($n = 2,\ l = 0, 1,\ m = 0, \pm 1$) symmetry, resulting in the degenerate "light-hole" and "heavy-hole" bands, while the spin split-off band emerges when the relativistic spin-orbit interaction is accounted for (see figure 5.2) [43]. Conversely, in the IV-VI PbX systems the z-axis is taken towards one of the four equivalent L-points of the first Brillouin zone (e.g. along the $\langle 111 \rangle$ direction). In these systems, it is the states at the top of the valence band which have atomic s-like

spatial symmetry, while states at the bottom of the conduction band exhibit p_z-like symmetry, where z is oriented toward the L-point. States at the band edges are spin-degenerate, with additional four-fold degeneracy arising from the existance of the other three L-valleys, resulting in eight-fold degeneracy when all four L-points are accounted for (the degeneracy at a particular L-point, however, remains two-fold) [157]. There is no distiction made between heavy holes and light holes (the effective masses are the same for all hole states), and the spin split-off band is not observed (see the band structures in figures 5.2 and 5.3).

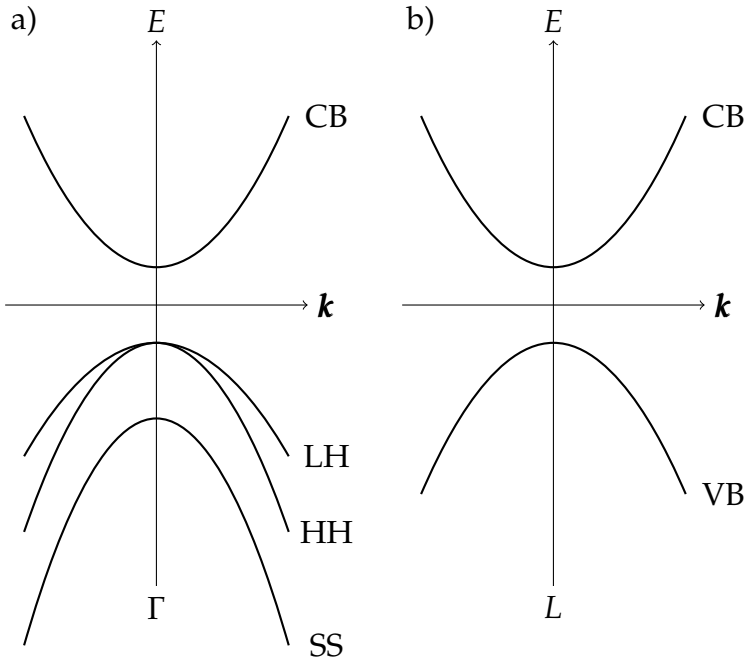

Figure 5.2.: Band structure near the extrema for: a) many zone-centre direct bandgap materials, where the VB is split into light hole (LH), heavy hole(HH), and spin split-off (SS) bands, while the CB is spin-degenerate; and b) PbX with a direct gap at the L-point, where both the CB and VB consist of a single, four-fold degenerate band (exclusive of spin degeneracy)

At first glance, the p_z-like symmetry of the conduction band minimum of the lead-salts shuold preclude electronic transitions between the CBM and the s-like VBM when the excitoation photon is polarised in the x or y directions. For a particular choice of z-axis (i.e. particular L-point), such transitions are permitted

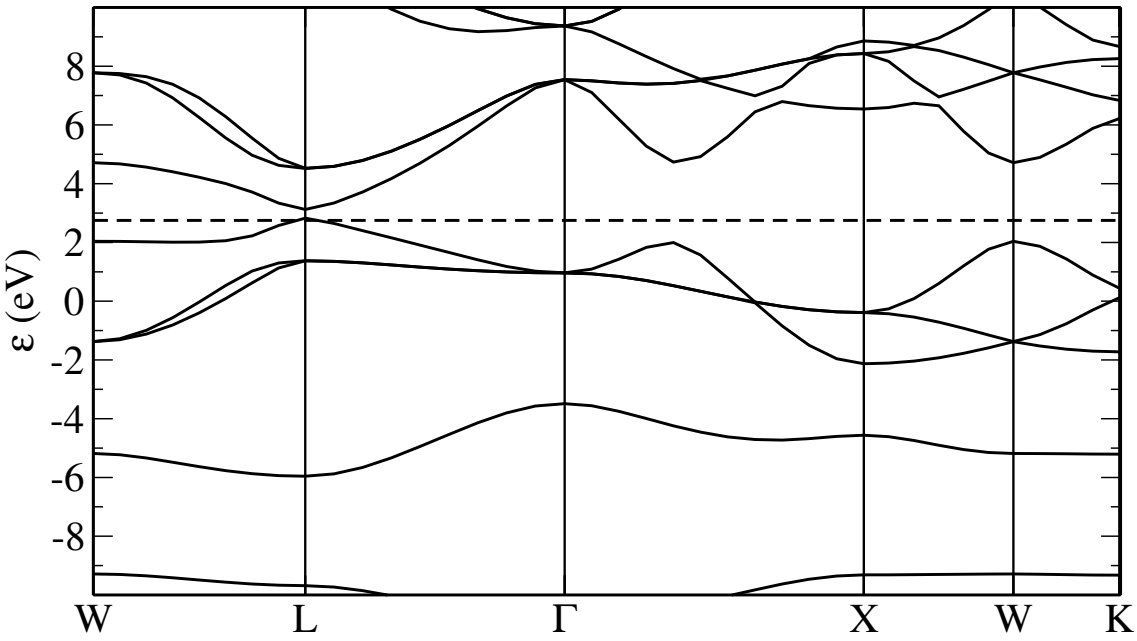

Figure 5.3.: Bandstructure for PbSe. The bandgap is narrow and lies at the *L*-point of the first Brillouin zone. This bandstructure was calculated via time-independent DFT (CASTEP) using a PBE exchange-correlation functional.

where the transition occurs at one of the other three *L*-valleys of the Brillouin zone, where the p_z orbital is differently oriented.

5.2 CARRIER EFFECTIVE MASSES

In the majority of semiconductor species the effective masses of the holes are significantly larger than the electron effective mass: often $m_h^* \sim 10 m_e^*$ [130]. This leads to closer spacing of the energy levels of the valence band in confined systems, and consequently much faster cooling times for hot holes [13]. Further, hot electrons may cool by undergoing an Auger process , transferring their excess energy, ΔE_e, to a hole in the VB, which then cools rapidly towards the band edge through phonon emission. The phonon bottleneck is thus broken.

Conversely, in the lead-salts, the electron and hole effective masses are approximately equal [83, 157]. As a result, carrier cooling via phonon emission is suppressed (where the intraband energy separation is large), and Auger pro-

cesses do not break the bottleneck. Unfortunately, as predicted by equation 3.1, the threshold photon energy required for carrier multiplication is dependent on the ratio of the effective masses of the charge carriers. With $m_e^* \approx m_h^*$, the threshold photon energy is $h\nu_{\text{thresh.}} \approx 3E_g$: far greater than the ideal, thermodynamic threshold of $2E_g$. The experimental results of several authors predict similar values for the threshold photon energy. Initial observations of MEG in PbSe QDs were reported by Schaller and Klimov for photon energies greater than $3E_g$ [87, 123]. They later revised the energy threshold down to $2.85E_g$ [158]. Quantum yields of of 3.0 and 2.8 were respectively reported in PbSe and PbS at photon energies of $h\nu \sim 4E$g and $h\nu \sim 4.5E_g$ by Ellingson et al. [85], suggesting a threshold photon energy between $2E_g$ and $3E_g$. The same group also measured a MEG threshold energy of $\sim 3E_g$ in PbTe nanocrystals [140] with quantum yields comparable to those in reference [85].

Despite the relatively high MEG threshold energies, the lead-salts are still excellent candidates for PV devices incorporating multiple exciton generation into their design. While the threshold of $3E_g$ is large, the bandgap energies themselves are small (E_g^{bulk}(PbSe) = 0.28 eV). While quantum confinement blueshifts the energy spectra of the QD, the bandgap energy tends to remain in the the near-infrared part of the spectrum; incident photon energies are still large enough to stimulate carrier multiplication, even at three times the bandgap. The large exciton Bohr radii of the lead chalcogenides allow for easy access to the strong confinement regime in PbX nanocrystals of much larger size than in comparable systems such as CdX QDs (see table 4.1). Further, the confinement energy is much larger in PbX QDs than in many other systems for QDs of equal size of similar size. As a result, the variation of the energy structure of PbX NQDs is highly exaggerated.

5.3 SPHEROIDAL QUANTUM DOTS

While the size-dependence properties of quantum confined nanostructures are well understood, less so are the effects of the shape of the nanocrystal on QD electronic properties. It is in general mathematically and computationally complex to model nanostructures without spherical symmetry. The simplest deviation from spherical symmetry lies in the the *spheroids of revolution* (see figure 5.4). A

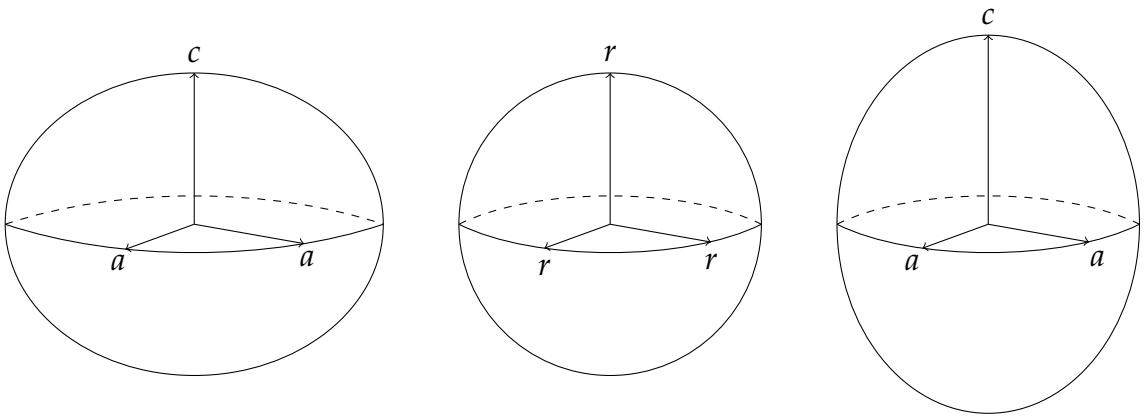

Figure 5.4.: Spheroids of revolution are generated by rotating an ellipse about the c axis. For $c < a$, the spheroid is oblate (left), while for $c > a$ the ellipsoid is prolate (right).

general ellipsoid is described by

$$\frac{a^2}{x^2} + \frac{b^2}{y^2} + \frac{c^2}{z^2} = 1, \tag{5.1}$$

where a, b, and c are the axes of the ellipsoid aligned with the x, y, and z directions. In the limiting case that $a = b = c = r$, the familiar equation for a sphere, $x^2 + y^2 + z^2 = r^2$ is returned. The case that $a = b \neq c$ describes the spheroids of revolution:

$$a^2 \left(\frac{1}{x^2} + \frac{1}{y^2} \right) + \frac{c^2}{z^2} = 1. \tag{5.2}$$

In the case that $c < a = b$, the spheroid is termed *oblate*, while for $c > a = b$, the spheroid is *prolate* (see figure 5.4). It should be emphasised that while the prolate spheroid posses one dimension which is longer than the others, a prolate

spheroidal quantum dot is not synonymous with a quantum wire (section 4.1.3). While the shape is somewhat similar, being smaller laterally than longitudinally, the longitudinal dimension of the quantum dot is smaller than the Bohr radius of the underlying lattice material; thus quantum dots with the prolate spheroidal geometry maintain a zero-dimensional electronic structure. As will be seen in chapter 7, the shape of the QD exerts a subtle influence on the electronic structure of the dot.

6

THEORY

The calculations presented in the current work are based on the $\mathbf{k} \cdot \mathbf{p}$ perturbation method expanded in a planewave basis. The $\mathbf{k} \cdot \mathbf{p}$ equation is a single-particle equation, commonly used to determine the electronic states of a system within the single-particle approximation. Excitonic corrections were obtained via state mixing in a subsequent *configuration interaction* (CI) calculation. Once single-particle (sp) and many-particle (mp) states were obtained, further properties derived from knowledge of these states were found using a suit of stand alone `FORTRAN` scripts which complement the main in-house code—`kppw`—with which the sp states were found. The current section describes in detail the mathematical and computational techniques used to this end.

6.1 LIMITS OF AB INITIO METHODS

When modelling complex quantum mechanical systems, exact solutions to the many-body Schrödinger equation are almost universally intractable. Under appropriate approximations, ab initio methods may make highly accurate predictions. The most popular atomistic modelling technique is *density functional theory* (DFT), wherein the complex, many-body system is associated with a non-interacting analogue which has the same set of eigenvalues and eigenvectors, and the same ground state electronic density, n_0, as the original system. Within

the DFT framework, all properties of the system are represented as functionals of n_0. A set of coupled equations (the Kohn-Sham equations) is then solved. In principle, solutions to the Kohn-Sham equations are exact, however, in order to deal with the many-body effects of *exchange* and *correlation*, some approximation must be made to the exchange-correlation potential. Approximations such as the *local density approximation* (LDA) or the *generalised gradient approximations* (GGA) provide excellent predictions of the ground state properties of the many-body system.

Unfortunately however, DFT is a computationally expensive method. Since it is an atomistic approach, DFT is most effective when dealing with systems comprised of a small number of atoms: either small molecules or highly periodic structures (i.e. small number of electrons). Since nanocrystal quantum dots do not exhibit translational symmetry, a simulation cell for a NQD typically contains several thousands of atoms. For a PbSe QD, the coordination number of the FCC lattice is four, and the valencies of lead and selenium are 4 and 2 respectively. Thus, the simulation cell for a PbSe QD of radius 30 Å contains $\sim$5,000 atoms and $\sim$20,000 electrons—a monumental undertaking for ab initio approaches.

6.2 $\boldsymbol{k} \cdot \boldsymbol{p}$ PERTURBATION THEORY

It is clear that atomistic approaches are unfeasible when considering the electronic properties of nanocrystal quantum dots. It is therefore necessary to turn to phenomenological modelling techniques. One such method, first developed by Kane in the 1950s, is the $\mathbf{k} \cdot \mathbf{p}$ perturbation method [159–161]. The $\mathbf{k} \cdot \mathbf{p}$ method is a perturbative approach to determine the band structure from empirically (or in practice, calculated) input parameters. Despite originally being applied to bulk structures, the $\mathbf{k} \cdot \mathbf{p}$ method has successfully been extended for use with non-periodic structures, such as crystal defects, molecules, and quan-

tum nanocrystals. It is therefore possible to calculate optoelectronic properties of quantum dots from the parameters of the corresponding bulk material.

6.2.1 *The Parabolic Effective Mass Approximation*

The $\mathbf{k} \cdot \mathbf{p}$ method is an effective mass approximation, whereby electrons in the crystal are treated as free, non-interacting particles (electron/Fermi gas). This is realised by treating the real particles as particles with effective mass m^*, which differs from the electron rest mass m_0 by an amount determined by the local environment. In the presence of parabolic band dispersion, the particle effective mass emerges from Newton's second law of motion when taken with the group velocity as

$$\frac{1}{m^*} = \frac{1}{\hbar^2} \frac{\partial^2}{\partial k^2} E\left(\boldsymbol{k}\right). \tag{6.1}$$

Energy states around the band edge are then given by given by

$$E\left(\boldsymbol{k}\right) = E_0 + \frac{\hbar^2}{2m^*} \left|\boldsymbol{k} - \boldsymbol{k_0}\right|^2, \tag{6.2}$$

where E_0 and k_0 are the bandedge eigenenergies and wavevectors, respectively. If the bandedge is coincident with the zone centre, then $k_0 \to 0$.

The parabolic band approximation is, however, insufficient for the description of most physical systems. For example, the parabolic approximation does not account for band anisotropy. The effective mass in equation 6.1 should in general be replace by *effective mass tensor*

$$\frac{1}{m^*_{\mu,\nu}} = \delta_{\mu,\nu} - \frac{2\hbar^2}{m_0} \sum_{i \neq j} \frac{\left\langle i0 \,\middle|\, \nabla_\mu \,\middle|\, j0 \right\rangle \left\langle j0 \,\middle|\, \nabla_\nu \,\middle|\, i0 \right\rangle}{E_0^i - E_0^j}, \tag{6.3}$$

where $\mu, \nu = x, y, z$.

6.2.2 *The Single-Particle $\boldsymbol{k} \cdot \boldsymbol{p}$ Perturbation Method*

One of the main strengths of the $\mathbf{k} \cdot \mathbf{p}$ method lies in its relative simplicity from a conceptual perspective. In its simplest implementation, as applied to a single band, the one-band $\mathbf{k} \cdot \mathbf{p}$ equation for the bandstructure of solids modifies the single-particle Schrödinger equation,

$$\left[\frac{p^2}{2m_0} + V(\boldsymbol{r})\right] |\psi_{n\boldsymbol{k}}\rangle = E_{n\boldsymbol{k}} \psi_{n\boldsymbol{k}}, \tag{6.4}$$

where n is the band index and $\hat{p} = -i\hbar\nabla$ is the quantum mechanical momentum operator, by representing the electron wavefunction, $|\psi_{n\boldsymbol{k}}\rangle$, in terms of *Bloch functions*,

$$\psi_{n\boldsymbol{k}} = u_{n,\boldsymbol{k}}(\boldsymbol{r}) \exp(i\boldsymbol{k} \cdot \boldsymbol{r}), \tag{6.5}$$

where $u(\boldsymbol{r}) = u(\boldsymbol{r} + R)$ is a function with the periodicity of the crystal lattice (R being a reciprocal lattice vector), in accordance with Bloch's theorem [162]. The set of Bloch functions are complete and orthogonal, and this have the respective properties:

$$\sum_{n\boldsymbol{k}} |\psi_{n\boldsymbol{k}}\rangle \langle\psi_{n\boldsymbol{k}}| = 1 \tag{6.6}$$

and

$$\langle\psi_{n'\boldsymbol{k}'} \mid \psi_{n\boldsymbol{k}}\rangle = \delta_{n',n}\delta_{\boldsymbol{k}',\boldsymbol{k}}. \tag{6.7}$$

Combining equations 6.4 and 6.5 yields the new Schrödinger equation

$$H_{\boldsymbol{k}\cdot\boldsymbol{p}} u_{n,\boldsymbol{k}}(\boldsymbol{r}) = E_{n,\boldsymbol{k}} u_{n,\boldsymbol{k}}(\boldsymbol{r}), \tag{6.8}$$

where the $\mathbf{k} \cdot \mathbf{p}$ Hamiltonian

$$H_{\boldsymbol{k}\cdot\boldsymbol{p}} = \frac{p^2}{2m_0} + \frac{\hbar^2 k^2}{2m_0} + \frac{\hbar}{m_0}\boldsymbol{k} \cdot \boldsymbol{p} + V(\boldsymbol{r}), \tag{6.9}$$

Equation 6.8 is the one-band $\mathbf{k} \cdot \mathbf{p}$ equation, so-called due to the term proportional to the product $\mathbf{k} \cdot \mathbf{p}$. The additional terms in the $\mathbf{k} \cdot \mathbf{p}$ Hamiltonian may be treated as perturbations to the known groundstate of the system, such that

$$H_{\boldsymbol{k}\cdot\boldsymbol{p}} = H_0 + H', \tag{6.10}$$

where H_0 is the unperturbed Hamiltonian of the single-particle Schrödinger equation (6.4), and the perturbation Hamiltonian

$$H' = \frac{\hbar^2 k^2}{2m_0} + \frac{\hbar}{m_0}\boldsymbol{k} \cdot \boldsymbol{p}, \tag{6.11}$$

where it has been assumed that $\boldsymbol{k}_0 = 0$. Since the terms included in the perturbation Hamiltonian are linearly and quadratically dependent on $\boldsymbol{k}$, the $\mathbf{k} \cdot \mathbf{p}$ approximation is most accurate near to the band edges. By including enough terms of higher order in the perturbative expansion, it is however possible to represent the bandstructure throughout the first Brillouin zone to a reasonable degree of accuracy. For non-degenerate bands, corrections to the unperturbed eigenstates up to second order are

$$u_{n,\boldsymbol{k}} = u_{n,\boldsymbol{k}_0} + \frac{\hbar}{m_0} \sum_{n \neq n'} \frac{\left\langle u_{n\boldsymbol{k}_0} \,\middle|\, \boldsymbol{k} \cdot \boldsymbol{p} \,\middle|\, u_{n',\boldsymbol{k}_0} \right\rangle}{E_{n,\boldsymbol{k}_0} - E_{n',\boldsymbol{k}_0}} u_{n',\boldsymbol{k}+0} \tag{6.12}$$

while corrections to the energy eigenvalues are given by

$$E_i = E_i^{(0)} + E_i^{(1)} + E_i^{(2)} = E_i^{(0)} + \left\langle i0 \,\middle|\, H' \,\middle|\, j0 \right\rangle + \sum_{i \neq j} \frac{\langle i0 \mid H' \mid j0 \rangle \langle j0 \mid H' \mid i0 \rangle}{E_i^{(0)} - E_j^{(0)}}, \tag{6.13}$$

where superscripts denote the order of the perturbation. Since the first term in the perturbation (first term in equation 6.11) contains no operator, the properties of orthonormality lead to

$$\left\langle i0 \,\middle|\, \frac{\hbar^2 k^2}{2m_0} \,\middle|\, j0 \right\rangle = \frac{\hbar^2 k^2}{2m_0} \langle i0 \mid j0 \rangle = \frac{\hbar^2 k^2}{2m_0} \delta_{i,j}. \tag{6.14}$$

Thus, first order corrections appear only on the main diagonal of the Hamiltonian matrix. Since the summation in equation 6.13 is over $i \neq j$, second order corrections are nonzero only away from the main diagonal, a consequence of the Hermitian properties of the momentum operator. A further consequence is that second order corrections are symmetric about the main diagonal; the $\mathbf{k} \cdot \mathbf{p}$ Hamiltonian is self-adjoint (Hermitian).

An explicit expression for non-degenerate corrections up to second order is found by inserting H_0 and H' into equation 6.13, resulting in

$$E_i = -\frac{\hbar^2}{2m_0}\nabla^2 + V(\boldsymbol{r}) + \frac{\hbar^2 k^2}{2m_0} + \left(\frac{\hbar}{m_0}\right)^2 \sum_{i \neq j} \frac{\langle i0 \,|\, \boldsymbol{k}\cdot\boldsymbol{p} \,|\, j0\rangle \,\langle j0 \,|\, \boldsymbol{k}\cdot\boldsymbol{p} \,|\, i0\rangle}{E_i^{(0)} - E_j^{(0)}} \tag{6.15}$$

$$= -\frac{\hbar^2}{2m_0}\nabla^2 + V(\boldsymbol{r}) + \frac{\hbar^2 k^2}{2m_0} + \left(\frac{\hbar}{m_0}\right)^2 \sum_{i \neq j} \sum_{\mu,\nu} \boldsymbol{k}_\mu \boldsymbol{k}_\nu \frac{\langle i0 \,|\, \boldsymbol{p} \,|\, j0\rangle \,\langle j0 \,|\, \boldsymbol{p} \,|\, i0\rangle}{E_i^{(0)} - E_j^{(0)}} \tag{6.16}$$

$$= E_i^{(0)} + \frac{\hbar^2}{2m_0} \sum_{\mu,\nu} \frac{\boldsymbol{k}_\mu \boldsymbol{k}_\nu}{m^*_{\mu,\nu}}, \tag{6.17}$$

where

$$\frac{1}{m^*_{\mu,\nu}} = \delta_{\mu,\nu} + \frac{2\hbar^2}{m_0} \sum_{i \neq j} \frac{\langle i0 \,|\, \boldsymbol{p} \,|\, j0\rangle \,\langle j0 \,|\, \boldsymbol{p} \,|\, i0\rangle}{E_i^{(0)} - E_j^{(0)}} \tag{6.18}$$

is the effective mass tensor.

The treatment so far has been focused only on non-degenerate eigenstates. More generally, second order corrections should include summation over degeneracies. Corrections to the unperturbed eigenvalues up to second order are then

$$E_i = E_i^{(0)}\delta_{a,b} + \left\langle ai0 \,\middle|\, H' \,\middle|\, bj0\right\rangle + \sum_{i \neq j} \sum_{a=1}^{g_n} \sum_{b=1}^{g_n} \frac{\langle ai0 \,|\, H' \,|\, bj0\rangle \,\langle bj0 \,|\, H' \,|\, ai0\rangle}{E_i^{(0)} - E_j^{(0)}}, \tag{6.19}$$

where a and b denote the degeneracy level within the state $|i\rangle$. When considering many-particle states within the configuration interaction calculation, it is important to sum over all degeneracies within a particular state (see below).

6.2.3 *The Spin-Orbit Interaction*

Another strength of the $\mathbf{k} \cdot \mathbf{p}$ method is the straightforward inclusion of relativistic effects within the $\mathbf{k} \cdot \mathbf{p}$ Hamiltonian. A well-known physical effect in atoms with high atomic number is the *spin-orbit interaction*, whereby the orbital angular momenta of the electrons are coupled to the electron spin state, with the effect becoming larger as more electrons are added to the system (i.e. for heavier elements/higher degrees of degeneracy). The spin-orbit interaction is responsible for the spin split-off band in semiconductors with the valence band maximum at the zone centre. The spin-orbit effect is introduced to the Hamiltonian as [163, 164]

$$H = H_0 + H_{\mathrm{SO}}, \tag{6.20}$$

where the spin-orbit Hamiltonian is given by

$$H_{\mathrm{SO}} = \frac{\hbar^2}{4c^2m^2} \left(\boldsymbol{\nabla} V \times \boldsymbol{p}\right) \cdot \boldsymbol{\sigma}, \tag{6.21}$$

and $\boldsymbol{\sigma}$ is the famous *Pauli spin matrix*, the components of which are

$$\sigma_x = \begin{pmatrix} 0 & 1 \\ 1 & 0 \end{pmatrix}, \qquad \sigma_y = \begin{pmatrix} 0 & -\mathrm{i} \\ \mathrm{i} & 0 \end{pmatrix}, \qquad \text{and} \qquad \sigma_z = \begin{pmatrix} 1 & 0 \\ 0 & -1 \end{pmatrix}. \tag{6.22}$$

The $\mathbf{k} \cdot \mathbf{p}$ Hamiltonian including the spin-orbit interaction is then

$$H_{\boldsymbol{k}\cdot\boldsymbol{p}} = \frac{p^2}{2m_0} + V\left(\boldsymbol{r}\right) + \frac{\hbar^2k^2}{2m_0} + \frac{\hbar}{m_0}\boldsymbol{k} \cdot \boldsymbol{p} + \frac{\hbar^2}{4c^2m^2} \left(\boldsymbol{\nabla} V \times \boldsymbol{p}\right) \cdot \boldsymbol{\sigma}. \tag{6.23}$$

This is a cumbersome equation, and is often rewritten as

$$\frac{p^2}{2m_0} + V\left(\boldsymbol{r}\right) + \frac{\hbar^2k^2}{2m_0} + \frac{\hbar}{m_0}\boldsymbol{k} \cdot \boldsymbol{\pi}, \tag{6.24}$$

where

$$\boldsymbol{\pi} = \boldsymbol{k} \cdot \boldsymbol{p} + \frac{1}{4\hbar m_0 c^2} (\boldsymbol{\sigma} \times \boldsymbol{\nabla} V) \cdot (\boldsymbol{k} + \boldsymbol{p}) \,. \tag{6.25}$$

6.2.4 *The Four-Band $\boldsymbol{k} \cdot \boldsymbol{p}$ Equation for Lead-Salt Quantum Dots*

While $\mathbf{k} \cdot \mathbf{p}$ theory is most commonly expanded about the zone centre ($\boldsymbol{k} = 0$), it is an equally valid approach for wavevectors $\boldsymbol{k}$ in the vicinity of any arbitrary point in the $\boldsymbol{k}$-space. Since the lead-chalcogenides posses a direct bandgap at the L-point of the first Brillouin zone, the $\mathbf{k} \cdot \mathbf{p}$ equation should be expanded about the point $\boldsymbol{k} = L$. Expanded about the L-point, the appropriate basis functions, in the double-group notation, are $|L_6^-, \alpha\rangle$, $|L_6^-, \beta\rangle$, $|L_6^+, \alpha\rangle$, and $|L_6^+, \beta\rangle$, where the superscript "-" and "+" denote electrons in the conduction band and holes in the valence band, respectively, while α and β respectively represent particles of spin $+1/2$ and $-1/2$. respectively [157].

Due to the nature of the underlying rock-salt crystal structure (face-centred cubic), the energy bands of the leadsalts are anisotropic, with the degree of anisotropy increasing monotomically with the species of anion. One choice of coordinate system, which is used throughout the current work, defines the z-direction as lying along the $\langle 111 \rangle$ crystallographic direction (across the diagonal of the cubic cell), termed the *longitudinal axis*, l, while the x and y directions are chosen to lie along the mutually isotropic $\langle \bar{1}\bar{1}2 \rangle$ and $\langle 1\bar{1}0 \rangle$ directions, termed the *transverse axes*, t [165].

The $\mathbf{k} \cdot \mathbf{p}$ Hamiltonian used to represent lead-salt QD systems, which uses this choice of coordinates, was first derived Inuk Kang and Frank Wise [157],

based on the works of Mitchell and Wallis [166] and later Dimmock [167]. The four-band $\mathbf{k} \cdot \mathbf{p}$ equation expanded at the L-point is given by

$$H = \begin{bmatrix} \frac{E_g}{2} + \frac{\hbar^2 k_t^2}{2m_t^-} + \frac{\hbar^2 k_z^2}{2m_l^-} & 0 & \frac{\hbar}{m_0} P_l k_z & \frac{\hbar}{m_0} P_l \left(k_x - ik_y\right) \\ 0 & \frac{E_g}{2} + \frac{\hbar^2 k_t^2}{2m_t^-} + \frac{\hbar^2 k_z^2}{2m_l^-} & \frac{\hbar}{m_0} P_l \left(k_x + ik_y\right) & -\frac{\hbar}{m_0} P_l k_z \\ \frac{\hbar}{m_0} P_l k_z & \frac{\hbar}{m_0} P_l \left(k_x - ik_y\right) & -\frac{E_g}{2} - \frac{\hbar^2 k_t^2}{2m_t^+} - \frac{\hbar^2 k_z^2}{2m_l^+} & 0 \\ \frac{\hbar}{m_0} P_l \left(k_x + ik_y\right) & -\frac{\hbar}{m_0} P_l k_z & 0 & -\frac{E_g}{2} - \frac{\hbar^2 k_t^2}{2m_t^+} - \frac{\hbar^2 k_z^2}{2m_l^+} \end{bmatrix}. \tag{6.26}$$

In equation 6.26, E_g is the bandgap energy of the corresponding bulk material, and P_t and P_l are the respective transverse and longitudinal momentum matrix elements between the band extrema (the *Kane parameters*). The notation $m_t^{\pm}$ and $m_l^{\pm}$ for the transverse and longitudinal carrier effective masses in the valence (+) and conduction (-) band arising from far-band contributions, respectively. The first two columns of the Hamiltonian matrix correspond to spin-up and spin-down electrons in the conduction band, while the last two columns describe spin-up and spin-down hole states in the valence band. The spin-orbit interaction is automatically included in the off-diagonal matrix elements. The relevant input parameters required by equation 6.26 are given in table 6.1. Equation 6.26 may

Parameter	PbS	PbSe
E_g [eV]	0.41	0.28
m_0/m_t^-	1.9	4.3
m_0/m_t^+	2.7	8.7
m_0/m_l^-	3.7	3.1
m_0/m_t^+	3.7	3.3
m_0/m^-	2.5	3.9
m_0/m^+	3.0	6.9
$2P_t^2/m_0$ [eV]	3.0	3.0
$2P_l^2/m_0$ [eV]	1.6	1.7
$2P^2/m_0$ [eV]	2.5	2.6

Table 6.1.: Input parameters for the $\mathbf{k} \cdot \mathbf{p}$ Hamiltonian [157]

be written in a more compact notation as

$$H = \begin{bmatrix} \left(\frac{E_g}{2} + \frac{\hbar^2 k_t^2}{2m_t^-} + \frac{\hbar^2 k_z^2}{2m_l^-}\right) I & \frac{\hbar}{m_0}\left[P_t\left(k_x + k_y\right) + P_l k_z\right] \cdot \boldsymbol{\sigma} \\ \frac{\hbar}{m_0}\left[P_t\left(k_x + k_y\right) + P_l k_z\right] \cdot \boldsymbol{\sigma} & -\left(\frac{E_g}{2} + \frac{\hbar^2 k_t^2}{2m_t^-} + \frac{\hbar^2 k_z^2}{2m_l^-}\right) I \end{bmatrix}, \tag{6.27}$$

where I is the 2×2 identity matrix, and $\boldsymbol{\sigma}$ is the Pauli spin matrix as described in equation 6.22.

The Hamiltonian 6.26 verifies the secular equation

$$\left[H - E\left(\boldsymbol{k}\right)\right] \psi\left(\boldsymbol{k}\right) = 0, \tag{6.28}$$

for which nontrivial solutions exist when the determinant of the matrix $H - E(\boldsymbol{k})$ is equal to zero. By taking this determinant, the dispersion relation for the system may be obtained:

$$\begin{aligned} \left[\frac{E_g}{2} + \frac{\hbar^2 k_t^2}{2m_t^-} + \frac{\hbar^2 k_z^2}{2m_l^-} - E\left(\boldsymbol{k}\right)\right] \times \left[-\frac{E_g}{2} - \frac{\hbar^2 k_t^2}{2m_t^-} - \frac{\hbar^2 k_z^2}{2m_l^-} - E\left(\boldsymbol{k}\right)\right] \\ = \frac{\hbar^2}{m_0}\left[P_t^2 k_t^2 + P_l^2 k_l^2\right]. \end{aligned} \tag{6.29}$$

The dispersion relation for the lead chalcogenides is therefore highly non-parabolic. While the non-parabolicity of PbS and PbSe is sufficiently small to be treated as a perturbation to a spherically homogenised version of equation 6.26, the degree of directional anisotropy is too large for PbTe to be included as such. It is thus preferable to turn away from analytic solutions to 6.26 in favour of numerical approaches.

6.2.5 *Selection Rules*

The interband dipole transition strengths and selection rules for those transitions are derived from the transition matrix elements between the bands, given by

$$M = \left| \left\langle \Psi_{\mathrm{CB}}\left(\boldsymbol{r}\right) \left| \, \hat{\boldsymbol{e}} \cdot \boldsymbol{p} \, \right| \Psi_{\mathrm{VB}}\left(\boldsymbol{r}\right) \right\rangle \right|^2, \tag{6.30}$$

where $\hat{e}$ is the light polarisation vector. In the notation used by Kang and Wise [157], the total wavefunction may be written as a function of the four bands as

$$\left|\Psi\left(\boldsymbol{r}\right)\right\rangle = F_1 \left| L_6^-, \alpha \right\rangle + F_2 \left| L_6^-, \beta \right\rangle + F_3 \left| L_6^+, \alpha \right\rangle + F_4 \left| L_6^+, \beta \right\rangle \tag{6.31}$$

where F_{i} is the envelope function of the appropriate band. The matrix element for direct transitions (i.e. within a particular L-valley) are given by

$$\begin{aligned} M = \Bigg| \int d\boldsymbol{r} \Psi^{\dagger}_{\pi,j,m\in CB}\left(\boldsymbol{r}\right) \left(\hat{\boldsymbol{e}} \cdot \boldsymbol{p}\right) \Psi_{\pi,j,m\in VB}\left(\boldsymbol{r}\right) + \left(\hat{e} \cdot \hat{z}\right) P_{\mathrm{l}} \\ \times \int d\boldsymbol{r} \Psi^{\dagger}_{\pi,j,m\in CB}\left(\boldsymbol{r}\right) \left(\sigma_x \otimes \sigma_z\right) \Psi_{\pi,j,m\in VB}\left(\boldsymbol{r}\right) \Bigg|^2 \end{aligned} \tag{6.32}$$

After summation over the four L-valleys, the matrix element becomes isotropic. Selection rules may then be written:

$$\Delta j = 0, \pm 1, \qquad \Delta m = 0, \pm 1, \qquad \text{and} \qquad \pi_{\mathrm{CB}} \pi_{\mathrm{VB}} = -1, \tag{6.33}$$

where j is the total angular momentum quantum number, m is the magnetic quantum number, and π is the parity quantum number, which denotes the parity of the states. It can be seen that transitions involving a change in spin (spin-flip) are forbidden, and further that only transitions which involve a change in parity are permitted. As will be seen later, deviation from spherical symmetry, at least in the spheroidal geometry, does not alter the allowed quantum states for carriers in the nanocrystal.

6.3 EXPANSION IN THE PLANE WAVE BASIS

In order to solve the $\mathbf{k}\cdot\mathbf{p}$ Hamiltonian, an appropriate set of basis functions must be chosen. Due to the overwhelming number of electrons which one must include in the calculation, an envelope function method is preferred when dealing with all but the smallest of QDs. In an envelope function calculation, the true wavefunctions are expanded in terms of some known set of orthonormal and complete eigenfunctions. One such basis set, and the choice which is used to obtain single-particle states in the current work, based on the work of Vukmirovć and Tomić [97], is the planewave basis set. The basis of planewaves provides several advantages over other basis sets: within the planewave basis, quantum mechanical operators based on the position and momentum operators are analytic in nature, avoiding the need for further approximation; strain tensors may be calculated analytically (in inverse space); all the relevant physical properties may be expressed in terms of expansion coefficients, avoiding the need for arduous real-space integration; and finally, the system may be represented to a high degree of accuracy using only a (relatively) small number of planewaves in the expansion of the wavefunction [97].

In wavefunction expansion methods, a general wavefunction $|\psi\rangle$ may be expanded in terms of known solutions to the eigenvalue problem $H\phi_i = E_i\phi_i$, provided that the set $\{\phi_i\}$ is both orthonormal and complete. The expansion takes the form

$$|\psi\rangle = \sum_i c_i |\phi_i\rangle , \tag{6.34}$$

where c_i are indeterminate coefficients of the expansion. This expansion of $|\psi\rangle$ is exact only if $\{\phi_i\}$ is both complete and orthonormal, however, with enough terms included in the expansion, the equality in equation 6.34 may be replaced

by an approximation to great effect. In the case that the basis consists of the eigenfunctions of free particles, the planewave basis, equation 6.34 becomes

$$|\psi_{n\boldsymbol{k}}\rangle = \sum_{n,\boldsymbol{k}} c_{n\boldsymbol{k}}\phi_{\boldsymbol{k}} = \sum_{n,\boldsymbol{k}} c_{n\boldsymbol{k}} \exp\left(i\boldsymbol{k}\cdot\boldsymbol{r}\right), \tag{6.35}$$

where the summation is over the $\boldsymbol{k}$-values for each band $n \in \{1,\ldots,N\}$ and $\phi_{\boldsymbol{k}} = \exp(i\boldsymbol{k}\cdot\boldsymbol{r})$ [97, 168, 169].

The planewave expansion inherently imposes periodic boundary conditions on the QD system. This consequence is not necessarilyy adverse, depending on the system of study: for example, in considering a quantum superlattice, where a series of interacting quantum dots are arranged in a regular pattern, periodic conditions are ideal, however, in the study of single QD heterostructures, periodicity of the system introduces several artefacts which must be eliminated. These interactions between the dots are the electronic coupling of states in neighbouring dots, the propagation of the strain field between adjacent simulation cells, and, most influentially, the Coulomb interaction between the QD of interest and its nearest neighbours. Each of these effects become important at different length scales which may be labelled as $L^{(\mathrm{e})}$, $L^{(\mathrm{s})}$, and $L^{(\mathrm{C})}$, respectively. The electronic coupling occurs on the shortest length scale, with the electronic wavefunctions decaying exponentially outside the QD boundary. Next is the strain field, which follows a polynomial decay. Finally, the Coulomb interaction takes place on the largest length scale, being in principle infinite in extent. Thus, the inequality $L^{(\mathrm{e})} < L^{(\mathrm{s})} < L^{(\mathrm{C})}$ may be written.

In order to eliminate interactions between quantum dots in the superlattice, the simulation cell must be large enough such that Coulombic interaction with neighbouring dots is vanishing. It is, however, also true that as the simulation cell is made larger, a greater number of planewaves must be included in the expansion of the electronic wavefunction. This is a consequence of the discretization of the $\boldsymbol{k}$-space which results when embedding the QD in a finite

cell. For a cell of real-space dimensions L_x, L_y, and L_z, and real-space volume $V = L_x \times L_y \times L_z$, the components of the $\boldsymbol{k}$-space are discretized as

$$k_x = \frac{2\pi}{L_x} n_x, \qquad k_y = \frac{2\pi}{L_y} n_y, \qquad \text{and} \qquad k_z = \frac{2\pi}{L_z} n_z, \tag{6.36}$$

where n_x, n_y, and n_z are integers. When solving the $\mathbf{k} \cdot \mathbf{p}$ equations in inverse space, the computation time scales like $k_x \times k_y \times k_z$, with the maximal values of n_x, n_y, and n_z being equal to the number of planewaves in the planewave expansion. The time-scaling for $n_x = n_y = n_z$ is therefore cubic with the number of planewaves. In order for the calculations to be tractable, the number of $\boldsymbol{k}$-points must be finite. To this end, a wavevector cutoff is imposed on the system, such that $|n_x| \leq m_x$, $|n_y| \leq m_y$, and $|n_z| \leq m_z$, where m is the maximum allowed value of n, and is specific to the system of study. In principle, it is not necessarily the case that $m_x = m_y = m_z$. Further, different wavevector cutoffs may be employed for different bands, based on the band effective masses, however, since the effective masses of the leadsalts are approximately equal, the same cutoff values are used in each of the four bands of the $\mathbf{k} \cdot \mathbf{p}$ Hamiltonian. In the current work, single-particle states are calculated using planewave cut-off values $m_x = m_y = m_z = 8$, with the rank of the resulting Hamiltonian matrix being $(2m_x + 1) \times (2m_y + 1) \times (2m_z + 1) = 4913$. This choice for the cut-off value provides good comprimise between computation speed and accuracy.

Combining the planewave expansion 6.35 with the single-particle Schrödinger equation, the expression for the eigenvalue problem becomes

$$\sum_{n,\boldsymbol{k}} \mathcal{H}_{in}\left(\boldsymbol{k}, \boldsymbol{k}'\right) c_{n\boldsymbol{k}} = E_{n\boldsymbol{k}} c_{n\boldsymbol{k}}, \tag{6.37}$$

where

$$\mathcal{H}_{in}\left(\boldsymbol{k}, \boldsymbol{k}'\right) = \left\langle \phi_{\boldsymbol{k}'} \,\middle|\, H \,\middle|\, \phi_{\boldsymbol{k}} \right\rangle = \frac{1}{V^{(\mathrm{C})}} \int_{V^{(\mathrm{C})}} d^3\boldsymbol{r} \exp\left(-i\boldsymbol{k}' \cdot \boldsymbol{r}\right) H_{in} \exp\left(i\boldsymbol{k} \cdot \boldsymbol{r}\right), \tag{6.38}$$

where the cell volume $V^{(C)}$ has been used to normalise the basis.

By solving the four-band $\mathbf{k}\cdot\mathbf{p}$ eigenvalue problem described above in the planewave basis, single-particle states of the lead-salt QD structures may be found for spherical, spheroidal, and core/shell NQDs. The single-particle description, however, excludes several important physical effects which must be accounted for in order to obtain accurate description of QD energy states. This may be achieved by executing a subsequent configuration interaction calculation based on the single-particle states. This approach is detailed in the next section.

6.4 THE CONFIGURATION INTERACTION METHOD

Single-particle states near to the L-point bandedges of the leadsalts as calculated in sections 6.2.4-6.3 may be mixed in order to provide excitonic corrections to the non-interacting system. This is a necessary correction, since charge carriers within the quantum dot structure interact strongly via the Coulomb force. Excitonic corrections due to the interaction between two carriers is found through evaluation of *Coulomb integrals* between the two states of the form

$$V_{ijkl} = \left\langle ij \left| V\left(\left|\boldsymbol{r}-\boldsymbol{r}'\right|\right) \right| kl \right\rangle = \int d^3\boldsymbol{r} \int d^3\boldsymbol{r}' \psi_i^*\left(\boldsymbol{r}\right) \psi_j^*\left(\boldsymbol{r}'\right) V\left(\left|\boldsymbol{r}-\boldsymbol{r}'\right|\right) \psi_k\left(\boldsymbol{r}'\right) \psi_l\left(\boldsymbol{r}\right), \tag{6.39}$$

where

$$V\left(\left|\boldsymbol{r}-\boldsymbol{r}'\right|\right) = \frac{e^2}{4\pi\epsilon}\frac{1}{\left|\boldsymbol{r}-\boldsymbol{r}'\right|} \tag{6.40}$$

is the classical Coulomb interaction between two particles located at $\boldsymbol{r}$ and $\boldsymbol{r}'$.

The general many-body (many-particle, mp) Hamiltonian for an interacting system may be split into single-particle contributions (i.e. the single-particle energies from the $\mathbf{k}\cdot\mathbf{p}$ calculation) and contributions due to Coulomb integrals

$$H = \mathcal{H}^{(1)} + \mathcal{H}^{(2)} = \sum_{ij} T_{ij} c_i^\dagger c_j + \frac{1}{2}\sum_{ijkl} V_{ijkl} c_i^\dagger c_j^\dagger c_k c_l, \tag{6.41}$$

where $\mathcal{H}^{(1)}$ are the single-particle contributions (i.e. known single-particle energies $\{T_{ij}\}$), $\mathcal{H}^{(2)}$ are the two-particle contributions (the Coulomb integrals), and $c_i^\dagger$ and c_i are the creation and annihilation operators for electrons which obey the anticommutation rules for fermions[46]:[1]

$$\left\{c_i, c_j\right\} = \left\{c_i^\dagger, c_j^\dagger\right\} = 0, \qquad \left\{c_i, c_j^\dagger\right\} = \delta_{ij}. \tag{6.42}$$

In order to calculate many-particle corrections to the single-particle states, it is desirable to construct the interaction Hamiltonian in terms of the quasi-electrons and quasi-holes of the Fock space. The resulting Hamiltonian may then be solved for all possible configurations of four single-particle states (of *i*,*j*,*k*, and *l*). Since it is based on the interaction of all sp configurations, this method is known as the *configuration interaction*, or *CI* approach. The CI method is in principle an exact method of determining electronic structure (provided the complete set of single-particle states used as a basis is accurate), and is inclusive of the effects of both *exchange* and *correlation*.

6.4.1 *Quasiparticle Description of the Many-Body Hamiltonian*

Before the configuration interaction Hamiltonian can be constructed in the quasiparticle representation, a reference state must first be defined. Following in the approach of Korkusinski et al. [170, 171], the reference is chosen to be the true groundstate of the Fock space, that is where the valence band is fully populated by electrons while the conduction band is completely empty. This reference state is written as

$$|0\rangle = \prod_{i \in \mathrm{VB}} c_i^\dagger \, |\mathrm{vac}\rangle \,, \tag{6.43}$$

where $c_i^\dagger$ attempts to create an electron in the valence band, and $|\mathrm{vac}\rangle$ is the vacuum state in which the CB is depopulated and the VB is full. The quasi-

1 see section 2.4.3

electron and quasi-hole operators, which create/destroy an electron in the conduction band and create/destroy a hole in the valence band of the Fock space, respectively, may now be defined. The quasi-electron creation and annihilation operators are the same as the real-electron operators:

$$e_i^\dagger = c_i^\dagger \qquad \text{and} \qquad e_i = c_i, \tag{6.44}$$

while the quasi-hole operators are defined as

$$h_i^\dagger = c_i \qquad \text{and} \qquad h_i = c_i^\dagger \tag{6.45}$$

Since the valence band is full and the conduction band empty, the following relations hold:

$$h_{i\in\mathrm{VB}} \left|\mathrm{vac}\right\rangle = 0, \tag{6.46}$$

since a hole cannot be created in the full valence band, and

$$e_{i\in\mathrm{CB}} \left|\mathrm{vac}\right\rangle = 0, \tag{6.47}$$

since an electron cannot be destroyed in the empty conduction band.

With these definitions, the interaction Hamiltonian 6.41 may be written explicitly in terms of creation and annihilation operators. The initial step in doing so is to divide the many-body Hamiltonian 6.41 into conduction and valence band

states and applying the quasi-particle definitions described in equations 6.44 and 6.45:

$$\begin{aligned} H_{\mathrm{CI}} = &\sum_{ij} T_{ij} e_i^\dagger e_j + \sum_{ij} T_{ij} h_i h_j^\dagger + \frac{1}{2}\sum_{ijkl} V_{ijkl} e_i^\dagger e_j^\dagger e_k e_l + \frac{1}{2}\sum_{ijkl} V_{ijkl} e_i^\dagger e_j^\dagger e_k h_l^\dagger \\ &+ \frac{1}{2}\sum_{ijkl} V_{ijkl} e_i^\dagger e_j^\dagger h_k^\dagger e_l + \frac{1}{2}\sum_{ijkl} V_{ijkl} e_i^\dagger h_j e_k e_l + \frac{1}{2}\sum_{ijkl} V_{ijkl} h_i e_j^\dagger e_k e_l + \frac{1}{2}\sum_{ijkl} V_{ijkl} e_i^\dagger e_j^\dagger h_k^\dagger h_l^\dagger \\ &+ \frac{1}{2}\sum_{ijkl} V_{ijkl} e_i^\dagger h_j e_k h_l^\dagger + \frac{1}{2}\sum_{ijkl} V_{ijkl} h_i e_j^\dagger e_k h_l^\dagger + \frac{1}{2}\sum_{ijkl} V_{ijkl} h_i e_j^\dagger h_k^\dagger e_l + \frac{1}{2}\sum_{ijkl} V_{ijkl} h_i h_j e_k e_l \\ &+ \frac{1}{2}\sum_{ijkl} V_{ijkl} e_i^\dagger h_j h_k^\dagger e_l + \frac{1}{2}\sum_{ijkl} V_{ijkl} e_i^\dagger h_j h_k^\dagger h_l^\dagger + \frac{1}{2}\sum_{ijkl} V_{ijkl} h_i e_j^\dagger h_k^\dagger h_l^\dagger \\ &+ \frac{1}{2}\sum_{ijkl} V_{ijkl} h_i h_j e_k h_l^\dagger + \frac{1}{2}\sum_{ijkl} V_{ijkl} h_i h_j h_k^\dagger e_l + \frac{1}{2}\sum_{ijkl} V_{ijkl} h_i h_j h_k^\dagger h_l^\dagger, \end{aligned} \tag{6.48}$$

The resulting expression is in 18 terms: two which describe the single-particle energies in terms of the quasi-particles, and 16 which concern the interaction between quasi-electron and quasi-hole states. The factors of $1/2$ account for summations over repeated indices. The terms of equation 6.48 can further be grouped into two classes: those which conserve the number of particles in the Fock space, and those which do not. The former consists of the single-particle contributions and the Coulomb integrals which destroy a quasi-electron/quasi-hole for each quasi-electron/quasi-hole they create (and vice-versa). The latter consists of the Coulomb integrals with an imbalance between the number of creation/annihilation operators for quasi-electrons and quasi-holes, thereby increasing or decreasing the number of particles in the Fock space by one quasi-electron and one quasi-hole, or by two of each. These terms contain either three quasi-electron operators and one quasi-hole operator, three quasi-hole operators and one quasi-electron operator, or four creation or four annihilation operators (two each of electron and hole operators).

Equation 6.48 can be rewritten using the anti-commutation rules for fermions. Using equations 6.42, the single-particle hole terms may be written

$$\sum_{ij} T_{ij} h_i h_j^\dagger = \sum_{ij} T_{ij}\delta_{ij} - \sum_{ij} h_i^\dagger h_j = \sum_i T_{ii} - \sum_{ij} T_{ij}^* h_i^\dagger h_j, \tag{6.49}$$

since T_{ij} is Hermitian.

The Coulomb integrals can also be rewritten using commutation and anti-commutation relations for four fermions (see appendix A):

$$[ab, cd] = a[b, cd] + [a, cd]b = a\{b, c\}d - ac\{b, d\} + \{a, c\}db - c\{a, d\}b \tag{6.50}$$

and

$$\{ab, cd\} = a[b, cd] + \{a, cd\}b = a\{b, c\}d - ac\{b, d\} + [a, c]db + c\{a, d\}b, \tag{6.51}$$

where a,b,c, and d are fermions. Consider the hole creation/annihilation term $\mathcal{H}_{\text{h-h}} = \sum_{ijkl} V_{ijkl} h_i h_j h_k^\dagger h_l^\dagger$ (final term in equation 6.48). One may write

$$\begin{aligned}
V_{ijkl}\left[h_i h_j h_k^\dagger h_l^\dagger\right] &= V_{ijkl} h_i \{h_j, h_k^\dagger\} h_l^\dagger - V_{ijkl} h_i h_k^\dagger \{h_j, h_l^\dagger\} \\
&\quad + V_{ijkl}\{h_i, h_k^\dagger\} h_l^\dagger h_j - V_{ijkl} h_k^\dagger \{h_i, h_l^\dagger\} h_j \\
&= V_{ijkl} h_i h_l^\dagger \delta_{jk} - V_{ijkl} h_i h_k^\dagger \delta_{jl} \\
&\quad + V_{ijkl} h_l^\dagger h_j \delta_{ik} - V_{ijkl} h_k^\dagger h_j \delta_{il} \\
&= V_{ijkl}\delta_{il}\delta_{jk} - V_{ijkl}\delta_{jk} h_l^\dagger h_i \\
&\quad - V_{ijkl}\delta_{ik}\delta_{jl} + V_{ijkl}\delta_{jl} h_k^\dagger h_i \\
&\quad + V_{ijkl} h_l^\dagger h_j \delta_{ik} - V_{ijkl} h_k^\dagger h_j \delta_{il} \\
&= V_{ijji} - V_{ijij} + V_{ijkj} h_k^\dagger h_i - V_{ijjl} h_l^\dagger h_i + V_{ijil} h_l^\dagger h_j - V_{ijki} h_k^\dagger h_j \\
&= \left(V_{ijji} - V_{ijij}\right) + \left(V_{jkik} - V_{jkki} + V_{kjki} - V_{kjik}\right) h_i^\dagger h_j,
\end{aligned} \tag{6.52}$$

where the indices of the last four terms have been rearranged in the last step. Summing over these terms, the final creation/annihilation terms for the quasi-holes can be found:

$$\begin{aligned}
H_{\text{h-h}} &= \frac{1}{2}\sum_{ijkl} V_{ijkl}\left(\left[h_i h_j h_k^\dagger h_l^\dagger\right] + h_k^\dagger h_l^\dagger h_i h_j\right) \\
&= \frac{1}{2}\sum_{ijkl} V_{klij} h_i^\dagger h_j^\dagger h_k h_l + \frac{1}{2}\sum_{ij}\left(V_{ijji} - V_{ijij}\right) \\
&\quad + \frac{1}{2}\sum_{ij}\sum_{k}\left(V_{jkik} - V_{jkki} + V_{kjki} - V_{kjik}\right) h_i^\dagger h_j \\
&= \frac{1}{2}\sum_{ijkl} V_{lkji} h_i^\dagger h_j^\dagger h_k h_l + \frac{1}{2}\sum_{ij}\left(V_{ijji} - V_{ijij}\right) \\
&\quad + \frac{1}{2}\sum_{ij}\sum_{k}\left(V_{jkik} - V_{jkki} + V_{kjki} - V_{kjik}\right) h_i^\dagger h_j \\
&= \frac{1}{2}\sum_{ijkl} V_{lkji} h_i^\dagger h_j^\dagger h_k h_l + \frac{1}{2}\sum_{ij}\left(V_{ijji} - V_{ijij}\right) \\
&\quad + \sum_{ij}\sum_{k}\left(V_{jkik} - V_{jkki}\right) h_i^\dagger h_j .
\end{aligned} \tag{6.53}$$

As the quasi-electron creation and annihilation operators are identical to the real-electron operators, the same arguments need not be applied to the term $\mathcal{H}_{\text{e-e}}$, which will remain unchanged.

The electron-hole interactions must also be rewritten in the quasi-particle representation. The terms conserving particle number (i.e. not involving a transition) are composed of equal numbers of creation and annihilation operators. These terms are

$$\begin{aligned}
\mathcal{H}_{\text{e-h}} &= \frac{1}{2}\sum_{ijkl} V_{ijkl} e_i^\dagger h_j e_k h_l^\dagger + \frac{1}{2}\sum_{ijkl} V_{ijkl} e_i^\dagger h_j h_k^\dagger e_l \\
&\quad + \frac{1}{2}\sum_{ijkl} V_{ijkl} h_i e_j^\dagger e_k h_l^\dagger + \frac{1}{2}\sum_{ijkl} V_{ijkl} h_i e_j^\dagger h_k^\dagger e_l .
\end{aligned} \tag{6.54}$$

These terms may be rearranged as:

$$\begin{aligned} V_{ijkl} e_i^\dagger h_j e_k h_l^\dagger &= -V_{ijkl} e_i^\dagger h_j h_l^\dagger e_k = -V_{ijkl} e_i^\dagger \left(\delta_{jl} - h_l^\dagger h_j\right) e_k \\ &= -V_{ijkl} e_i^\dagger e_k \delta_{jl} + V_{ijkl} e_i^\dagger h_l^\dagger h_j e_k \\ &= V_{iklj} e_i^\dagger h_j^\dagger h_k e_l - V_{ikjl} e_i^\dagger e_j \delta_{kl} \\ &= V_{iklj} e_i^\dagger h_j^\dagger h_k e_l - V_{ikjk} e_i^\dagger e_j, \end{aligned} \tag{6.55}$$

$$\begin{aligned} V_{ijkl} e_i^\dagger h_j h_k^\dagger e_l &= V_{ijkl} e_i^\dagger \left(\delta_{jk} - h_k^\dagger h_j\right) e_l \\ &= V_{ijkl} e_i^\dagger e_l \delta_{jk} - V_{ijkl} e_i^\dagger h_k^\dagger h_j e_l \\ &= V_{ilkj} e_i^\dagger e_j \delta_{kl} - V_{ikjl} e_i^\dagger h_j^\dagger h_h e_l \\ &= V_{ikkj} e_i^\dagger e_j - V_{ikjl} e_i^\dagger h_j^\dagger h_h e_l, \end{aligned} \tag{6.56}$$

$$\begin{aligned} V_{ijkl} h_i e_j^\dagger e_k h_l^\dagger &= V_{ijkl} e_j^\dagger h_i h_l^\dagger e_k = V_{ijkl} e_j^\dagger \left(\delta_{il} - h_l^\dagger h_i^\dagger\right) e_k \\ &= V_{ijkl} e_j^\dagger e_k \delta_{il} - V_{ijkl} e_j^\dagger h_l^\dagger h_i^\dagger e_k \\ &= V_{kijl} e_i^\dagger e_j \delta_{kl} - V_{kilj} e_i^\dagger h_j^\dagger h_k^\dagger e_l \\ &= V_{kijk} h_i h_j^\dagger - V_{kilj} h_i e_j e_k^\dagger h_l^\dagger, \end{aligned} \tag{6.57}$$

and

$$\begin{aligned} V_{ijkl} h_i e_j^\dagger h_k^\dagger e_l &= -V_{ijkl} e_j^\dagger h_i h_k^\dagger e_l = -V_{ijkl} e_j^\dagger \left(\delta_{ik} - h_k^\dagger h_i\right) e_l \\ &= -V_{ijkl} e_j^\dagger e_l \delta_{ik} - V_{ijkl} e_j^\dagger h_k^\dagger h_i e_l \\ &= V_{kijl} e_i^\dagger h_j^\dagger h_k e_l - V_{kilj} e_i^\dagger e_j \delta_{kl} \\ &= V_{kijl} e_i^\dagger h_j^\dagger h_k e_l - V_{kikj} e_i^\dagger e_j. \end{aligned} \tag{6.58}$$

Summing over $\{ijkl\}$, the electron-hole static interaction is

$$\begin{aligned} \mathcal{H}_{\text{e-h}} &= \frac{1}{2} \sum_{ijkl} \left(V_{iklj} - V_{ikjl} + V_{kijl} - V_{kilj}\right) e_i^\dagger h_j^\dagger h_k e_l \\ &\quad + \frac{1}{2} \sum_{ij} \sum_{k} \left(V_{ikkj} - V_{ikjk} + V_{kijk} - V_{kikj}\right) e_i^\dagger e_j \\ &= \sum_{ijkl} \left(V_{iklj} - V_{ikjl}\right) e_i^\dagger h_j^\dagger h_k e_l + \sum_{ij} \sum_{k} \left(V_{ikkj} - V_{ikjk}\right) e_i^\dagger e_j. \end{aligned} \tag{6.59}$$

Finally, the terms of the many-body Hamiltonian 6.48 which annihilate or create one electron and one hole (i.e. carrier recombination/multiplication) are

$$\begin{aligned}\mathcal{H}_{\text{rec}} = &\frac{1}{2}\sum_{ijkl} V_{ijkl} e_i^\dagger h_j h_k^\dagger h_l^\dagger + \frac{1}{2}\sum_{ijkl} V_{ijkl} h_i e_j^\dagger h_k^\dagger h_l^\dagger + \frac{1}{2}\sum_{ijkl} V_{ijkl} h_i h_j e_k h_l^\dagger + \frac{1}{2}\sum_{ijkl} V_{ijkl} h_i h_j h_k^\dagger e_l \\ &+ \frac{1}{2}\sum_{ijkl} V_{ijkl} h_i e_j^\dagger e_k e_l + \frac{1}{2}\sum_{ijkl} V_{ijkl} e_i^\dagger h_j e_k e_l + \frac{1}{2}\sum_{ijkl} V_{ijkl} e_i^\dagger e_j^\dagger h_k^\dagger e_l + \frac{1}{2}\sum_{ijkl} V_{ijkl} e_i^\dagger e_j^\dagger e_k h_l^\dagger \\ &+ \frac{1}{2}\sum_{ijkl} V_{ijkl} e_i^\dagger e_j^\dagger h_k^\dagger h_l^\dagger + \frac{1}{2}\sum_{ijkl} V_{ijkl} h_i h_j e_k e_l.\end{aligned} \tag{6.60}$$

These terms may be rearranged in a fairly straightforward manner by taking in pairs the terms of equation 6.60, and where appropriate changing the order of operators, and relabelling the indices:

$$\begin{aligned}\frac{1}{2}\sum_{ijkl} V_{ijkl} e_i^\dagger h_j h_k^\dagger h_l^\dagger + \frac{1}{2}\sum_{ijkl} V_{ijkl} h_i e_j^\dagger h_k^\dagger h_l^\dagger &= \frac{1}{2}\sum_{ijkl}\left(V_{ijkl} h_i e_j^\dagger h_k^\dagger h_l^\dagger - V_{ijkl} h_j e_i^\dagger h_k^\dagger h_l^\dagger\right) \\ &= \frac{1}{2}\sum_{ijkl}\left(V_{ijkl} - V_{jikl}\right) h_i e_j^\dagger h_k^\dagger h_l^\dagger,\end{aligned} \tag{6.61}$$

$$\begin{aligned}\frac{1}{2}\sum_{ijkl} V_{ijkl} h_i h_j e_k h_l^\dagger + \frac{1}{2}\sum_{ijkl} V_{ijkl} h_i h_j h_k^\dagger e_l &= \frac{1}{2}\sum_{ijkl}\left(V_{ijkl} h_i h_j h_k^\dagger e_l - V_{ijkl} h_i h_j h_l^\dagger e_k\right) \\ &= \frac{1}{2}\sum_{ijkl}\left(V_{ijkl} - V_{ijlk}\right) h_i h_j h_k^\dagger e_l,\end{aligned} \tag{6.62}$$

$$\begin{aligned}\frac{1}{2}\sum_{ijkl} V_{ijkl} h_i e_j^\dagger e_k e_l + \frac{1}{2}\sum_{ijkl} V_{ijkl} e_i^\dagger h_j e_k e_l &= \frac{1}{2}\sum_{ijkl}\left(V_{ijkl} e_i^\dagger h_j e_k e_l - V_{ijkl} e_j^\dagger h_i e_k e_l\right) \\ &= \frac{1}{2}\sum_{ijkl}\left(V_{ijkl} - V_{jikl}\right) e_i^\dagger h_j e_k e_l,\end{aligned} \tag{6.63}$$

$$\begin{aligned}\frac{1}{2}\sum_{ijkl} V_{ijkl} e_i^\dagger e_j^\dagger h_k^\dagger e_l + \frac{1}{2}\sum_{ijkl} V_{ijkl} e_i^\dagger e_j^\dagger e_k h_l^\dagger &= \frac{1}{2}\sum_{ijkl}\left(V_{ijkl} e_i^\dagger e_j^\dagger e_k h_l^\dagger - V_{ijkl} e_i^\dagger e_j^\dagger e_l h_k^\dagger\right) \\ &= \frac{1}{2}\sum_{ijkl}\left(V_{ijkl} - V_{ijlk}\right) e_i^\dagger e_j^\dagger e_k h_l^\dagger,\end{aligned} \tag{6.64}$$

while the final two terms remain unchanged. The non-conserving part of the many-body Hamiltonian may then be written

$$\begin{aligned}\mathcal{H}_{\text{rec}} = &\frac{1}{2}\sum_{ijkl}\left(V_{ijkl} - V_{jikl}\right) h_i e_j^\dagger h_k^\dagger h_l^\dagger + \frac{1}{2}\sum_{ijkl}\left(V_{ijkl} - V_{ijlk}\right) h_i h_j h_k^\dagger e_l \\ &+ \frac{1}{2}\sum_{ijkl}\left(V_{ijkl} - V_{jikl}\right) e_i^\dagger h_j e_k e_l + \frac{1}{2}\sum_{ijkl}\left(V_{ijkl} - V_{ijlk}\right) e_i^\dagger e_j^\dagger e_k h_l^\dagger \\ &+ \frac{1}{2}\sum_{ijkl} V_{ijkl} e_i^\dagger e_j^\dagger h_k^\dagger h_l^\dagger + \frac{1}{2}\sum_{ijkl} V_{ijkl} h_i h_j e_k e_l.\end{aligned} \tag{6.65}$$

Taking equation 6.48 with equations 6.49, 6.53, 6.59, and 6.65, the many-body CI Hamiltonian can now be written in terms of the creation and annihilation operators for quasi-electrons and quasi-holes:

$$\begin{aligned}H_{\text{CI}} = &E_0 + \sum_{ij} H_{ij}^{\text{e}} e_i^\dagger e_j - \sum_{ij} H_{ij}^{\text{h}} h_i^\dagger h_j + \frac{1}{2}\sum_{ijkl} V_{ijkl} e_i^\dagger e_j^\dagger e_k e_l \\ &+ \frac{1}{2}\sum_{ijkl} V_{lkji} h_i^\dagger h_j^\dagger h_k h_l - \sum_{ijkl}\left(V_{ikjl} - V_{iklj}\right) e_i^\dagger h_j^\dagger h_k e_l + \mathcal{H}_{\text{rec}},\end{aligned} \tag{6.66}$$

where $\mathcal{H}_{\text{rec}}$ is given by equation 6.65 and

$$E_0 = \sum_{i\in\text{VB}} T_{ii} + \frac{1}{2}\sum_{ij}\left(V_{ijji} - V_{ijij}\right) \tag{6.67}$$

is the reference state energy in the Fock space consisting of the single-particle energies of the real electrons which fill the valence band in the ground state and the Coulomb interactions between those electrons. Further,

$$H_{ij}^{\text{e}} = T_{ij} + \sum_k\left(V_{ikkj} - V_{ikjk}\right) \tag{6.68}$$

and

$$H_{ij}^{\mathrm{h}} = T_{ij}^{*} + \sum_{ij}\sum_{k}\left(V_{jkki} - V_{jkik}\right) \tag{6.69}$$

are the single-particle Hamiltonians for the quasi-electrons and quasi-holes constructed from the real-particle Hamiltonians and the Coulomb integrals between single-particle states and the full valance band of the ground state.

It is further possible to represent equation 6.66 in terms of the wavefunctions of the quasi-electrons and quasi-holes. As was implied in equation 6.49, the quasi-hole wavefunctions are defined by the complex conjugate of the real electron wavefunctions, while quasi-electron wavefunctions are the same as the real wavefunctions, i.e.

$$\psi_i^{\mathrm{h}}\left(\boldsymbol{r}\right) = \psi_i^{*}\left(\boldsymbol{r}\right) \qquad \text{and} \qquad \psi_i^{\mathrm{e}} = \psi_i\left(\boldsymbol{r}\right) \tag{6.70}$$

In this representation, the single-particle term for the quasi-holes becomes

$$T_{ij} = \langle i \mid T \mid j\rangle = \langle i \mid T \mid j\rangle^{*} = \langle j \mid T \mid i\rangle = T_{ji}^{\mathrm{qp}} \tag{6.71}$$

for the reference state and

$$T_{ij}^{*} = \left(T_{ji}^{\mathrm{qp}}\right)^{*} = \langle j \mid T^{\mathrm{qp}} \mid i\rangle^{*} = \left\langle i \mid (T^{*})^{\mathrm{qp}} \mid j\right\rangle = (T^{*})_{ij}^{\mathrm{qp}} \tag{6.72}$$

for the quasi-hole contribution to the many-body Hamiltonian.

The Coulomb matrix elements may also be written in terms of the quasi-particle wavefunctions. The matrix elements between quasi-holes is

$$\begin{aligned} V_{ijkl\in\mathrm{VB}} &= \int d^3\boldsymbol{r}\int d^3\boldsymbol{r}'\psi_i^{*}\left(\boldsymbol{r}\right)\psi_j^{*}\left(\boldsymbol{r}\right)V\left(\boldsymbol{r},\boldsymbol{r}'\right)\psi_k\left(\boldsymbol{r}'\right)\psi_l\left(\boldsymbol{r}\right) \\ &= \int d^3\boldsymbol{r}\int d^3\boldsymbol{r}'\psi_i^{\mathrm{h}}\left(\boldsymbol{r}\right)\psi_j^{\mathrm{h}}\left(\boldsymbol{r}\right)V\left(\boldsymbol{r},\boldsymbol{r}'\right)\psi_k^{\mathrm{h}*}\left(\boldsymbol{r}'\right)\psi_l^{\mathrm{h}*}\left(\boldsymbol{r}\right) \\ &= \int d^3\boldsymbol{r}\int d^3\boldsymbol{r}'\psi_l^{\mathrm{h}*}\left(\boldsymbol{r}\right)\psi_k^{\mathrm{h}*}\left(\boldsymbol{r}\right)V\left(\boldsymbol{r},\boldsymbol{r}'\right)\psi_j^{\mathrm{h}}\left(\boldsymbol{r}'\right)\psi_i^{\mathrm{h}}\left(\boldsymbol{r}\right) \\ &= V_{lkji}^{\mathrm{qp}}, \end{aligned} \tag{6.73}$$

where V^{qp} denotes that the Coulomb integral takes place between quasi-particle wavefunctions, while, by the same mechanism, the matrix elements between electron and hole states which conserve the particle number are

$$V_{ijkl}|_{j,l\in\mathrm{VB}} = \left\langle ij \,\middle|\, V\left(\boldsymbol{r},\boldsymbol{r}'\right) \,\middle|\, kl \right\rangle = \left\langle il \,\middle|\, V\left(\boldsymbol{r},\boldsymbol{r}'\right) \,\middle|\, kj \right\rangle = V^{\mathrm{qp}}_{ilkj} \tag{6.74}$$

and

$$V_{ijkl}|_{j,k\in\mathrm{VB}} = \left\langle ij \,\middle|\, V\left(\boldsymbol{r},\boldsymbol{r}'\right) \,\middle|\, kl \right\rangle = \left\langle ik \,\middle|\, V\left(\boldsymbol{r},\boldsymbol{r}'\right) \,\middle|\, jl \right\rangle = V^{\mathrm{qp}}_{ikjl} \tag{6.75}$$

Non-conserving terms can also be rearranged in a similar way, becoming:

$$\begin{aligned}
V_{ijkl}|_{j,k,l\in\mathrm{VB}} &= \left\langle ij \,\middle|\, V\left(\boldsymbol{r},\boldsymbol{r}'\right) \,\middle|\, kl \right\rangle = \left\langle lk \,\middle|\, V\left(\boldsymbol{r},\boldsymbol{r}'\right) \,\middle|\, ji^* \right\rangle = V^{\mathrm{qp}}_{ljki^*} \\
V_{ijkl}|_{i,k,l\in\mathrm{VB}} &= \left\langle ij \,\middle|\, V\left(\boldsymbol{r},\boldsymbol{r}'\right) \,\middle|\, kl \right\rangle = \left\langle lk \,\middle|\, V\left(\boldsymbol{r},\boldsymbol{r}'\right) \,\middle|\, j^*i \right\rangle = V^{\mathrm{qp}}_{lkj^*i} \\
V_{ijkl}|_{i,j,l\in\mathrm{VB}} &= \left\langle ij \,\middle|\, V\left(\boldsymbol{r},\boldsymbol{r}'\right) \,\middle|\, kl \right\rangle = \left\langle lk^* \,\middle|\, V\left(\boldsymbol{r},\boldsymbol{r}'\right) \,\middle|\, ji \right\rangle = V^{\mathrm{qp}}_{lk^*ji} \\
V_{ijkl}|_{i,j,k\in\mathrm{VB}} &= \left\langle ij \,\middle|\, V\left(\boldsymbol{r},\boldsymbol{r}'\right) \,\middle|\, kl \right\rangle = \left\langle l^*k \,\middle|\, V\left(\boldsymbol{r},\boldsymbol{r}'\right) \,\middle|\, ji \right\rangle = V^{\mathrm{qp}}_{l^*kji}.
\end{aligned} \tag{6.76}$$

With these definitions, the CI Hamiltonian 6.66 may be rewritten in terms of the quasi-particle wavefunctions:

$$\begin{aligned}
H^{\mathrm{qp}}_{\mathrm{CI}} = E_0 &+ \sum_{ij} H^{\mathrm{e}}_{ij} e^\dagger_i e_j - \sum_{ij} H^{\mathrm{h}}_{ij} h^\dagger_i h_j + \frac{1}{2}\sum_{ijkl} V^{\mathrm{qp}}_{ijkl} e^\dagger_i e^\dagger_j e_k e_l \\
&+ \frac{1}{2}\sum_{ijkl} V^{\mathrm{qp}}_{ijkl} h^\dagger_i h^\dagger_j h_k h_l - \sum_{ijkl}\left(V^{\mathrm{qp}}_{ijkl} - V^{\mathrm{qp}}_{ijkl}\right) e^\dagger_i h^\dagger_j h_k e_l + \mathcal{H}^{\mathrm{qp}}_{\mathrm{rec}},
\end{aligned} \tag{6.77}$$

where

$$E_0 = \sum_{i\in\mathrm{VB}} T^{\mathrm{qp}}_{ii} + \frac{1}{2}\sum_{ij}\left(V^{\mathrm{qp}}_{jiji} - V^{\mathrm{qp}}_{ijji}\right), \tag{6.78}$$

$$H^{\mathrm{e}}_{ij} = T^{\mathrm{qp}}_{ij} + \sum_{k}\left(V^{\mathrm{qp}}_{ikjk} - V^{\mathrm{qp}}_{ikkj}\right), \tag{6.79}$$

$$H^{\mathrm{h}}_{ij} = (T^*)^{\mathrm{qp}}_{ij} + \sum_{ij}\sum_{k}\left(V^{\mathrm{qp}}_{ikjk} - V^{\mathrm{qp}}_{kikj}\right), \tag{6.80}$$

and

$$\begin{aligned}\mathcal{H}^{\mathrm{qp}}_{\mathrm{rec}} = &\frac{1}{2}\sum_{ijkl}\left(V^{\mathrm{qp}}_{lkj^*i} - V^{\mathrm{qp}}_{lkji^*}\right) h_i e_j^\dagger h_k^\dagger h_l^\dagger + \frac{1}{2}\sum_{ijkl}\left(V^{\mathrm{qp}}_{l^*kji} - V^{\mathrm{qp}}_{lk^*ji}\right) h_i h_j h_k^\dagger e_l \\ &+ \frac{1}{2}\sum_{ijkl}\left(V_{ij^*kl} - V_{j^*ikl}\right) e_i^\dagger h_j e_k e_l + \frac{1}{2}\sum_{ijkl}\left(V_{ijkl^*} - V_{ijl^*k}\right) e_i^\dagger e_j^\dagger e_k h_l^\dagger \\ &+ \frac{1}{2}\sum_{ijkl} V^{\mathrm{qp}}_{ijk^*l^*} e_i^\dagger e_j^\dagger h_k^\dagger h_l^\dagger + \frac{1}{2}\sum_{ijkl} V^{\mathrm{qp}}_{i^*j^*kl} h_i h_j e_k e_l.\end{aligned} \tag{6.81}$$

6.4.2 *Configuration Interaction and the Plane Wave Representation*

In order to find single-particle solutions within the $\mathbf{k}\cdot\mathbf{p}$ envelope function calculation (section 6.3), the true single-particle wavefunctions were expanded in terms of Bloch functions

$$\psi(\boldsymbol{r})\sum_b u_b(\boldsymbol{r})\,\phi_b(\boldsymbol{r}), \tag{6.82}$$

where $u(\boldsymbol{r}) = u(\boldsymbol{r}+\boldsymbol{R})$ is the periodic Bloch function with periodicity $\boldsymbol{R}$, and $\phi_b(\boldsymbol{r})$ is the slowly varying envelope function. The envelope functions are chosen to be plane waves, such that

$$\psi(\boldsymbol{r}) = \sum_{b,k} A_{b,\boldsymbol{k}} e^{i\boldsymbol{k}\cdot\boldsymbol{r}}, \tag{6.83}$$

The solutions of the $\mathbf{k}\cdot\mathbf{p}$ Hamiltonian when solved in the planewave basis are the energy eigenvalues and envelope functions in the *quasi-particle* description as defined in the previous section. That is, the single-particle eigenenergies automatically already contain all interactions between electrons and holes with the full valence band, and further, the quasi-hole wavefunctions are the complex conjugates of the real electron wavefunctions. As a result, the single-particle Hamiltonians can be rewritten as

$$H^{\mathrm{e}}_{ij} = E^{\mathrm{e}}_{ii}\delta_{ij} \tag{6.84}$$

and

$$H_{ij}^{\mathrm{h}} = E_{ii}^{\mathrm{h}} \delta_{ij} \tag{6.85}$$

The Coulomb integrals (equation 6.39) written in the planewave basis are of the form

$$\begin{aligned} V_{ijkl} &= \left\langle \psi_i \left| \left\langle \psi_j \left| V\left(\boldsymbol{r}, \boldsymbol{r}'\right) \right| \psi_k \right\rangle \right| \psi_l \right\rangle \\ &= \sum_{b_1, b_j, b_k, b_l} \langle u_{b_i} | \langle u_{b_j} | u_{b_k} \rangle \, | u_{b_l} \rangle \, \langle \phi_{i,b_i} | \langle \phi_{j,b_j} | V\left(\boldsymbol{r}, \boldsymbol{r}'\right) | \phi_{k,b_k} \rangle \, | \phi_{l,b_l} \rangle \\ &= \sum_{a,b} \langle \phi_{i,a} | \langle \phi_{j,b} | V\left(\boldsymbol{r}, \boldsymbol{r}'\right) | \phi_{k,b} \rangle \, | \phi_{l,a} \rangle \, , \end{aligned} \tag{6.86}$$

where is has been assumed that $\langle u_i | V\left(\boldsymbol{r}, \boldsymbol{r}'\right) | u_j \rangle = V\left(\boldsymbol{r}, \boldsymbol{r}'\right) \langle u_i | u_j \rangle$ and that $\{ | u_i \rangle \}$ are orthonormal. The Coulomb integral

$$V_{ijkl} = \sum_{a,b} \int d^3\boldsymbol{r} \int d^3\boldsymbol{r}' \phi_{i,a}^*\left(\boldsymbol{r}\right) \phi_{j,b}^*\left(\boldsymbol{r}'\right) V\left(\boldsymbol{r}, \boldsymbol{r}'\right) \phi_{k,b}\left(\boldsymbol{r}'\right) \phi_{l,a}\left(\boldsymbol{r}\right) \tag{6.87}$$

can be rewritten as [97]

$$\begin{aligned} V_{ijkl} &= \int d^3\boldsymbol{r} \int d^3\boldsymbol{r}' \sum_a [\phi_{i,a}^*\left(\boldsymbol{r}\right) \phi_{l,a}\left(\boldsymbol{r}\right)] V\left(\boldsymbol{r}, \boldsymbol{r}'\right) \sum_b [\phi_{j,b}^*\left(\boldsymbol{r}'\right) \phi_{k,b}\left(\boldsymbol{r}'\right)] \\ &= \int d^3\boldsymbol{r} \int d^3\boldsymbol{r}' B_{i,l}\left(\boldsymbol{r}\right) V\left(\boldsymbol{r}, \boldsymbol{r}'\right) B_{j,k}\left(\boldsymbol{r}'\right) , \end{aligned} \tag{6.88}$$

where

$$B_{ij}\left(\boldsymbol{r}\right) = \sum_a \phi_{i,a}^*\left(\boldsymbol{r}\right) \phi_{j,a}\left(\boldsymbol{r}\right) . \tag{6.89}$$

It is then possible to define

$$\begin{aligned} V_{ijkl}^{\mathrm{env.}} &= \int d^3\boldsymbol{r} \int d^3\boldsymbol{r}' B_{i,j}\left(\boldsymbol{r}\right) V\left(\boldsymbol{r}, \boldsymbol{r}'\right) B_{kl}\left(\boldsymbol{r}'\right) \\ &= \sum_{a,b} \int d^3\boldsymbol{r} \int d^3\boldsymbol{r}' \phi_{i,a}^*\left(\boldsymbol{r}\right) \phi_{k,b}^*\left(\boldsymbol{r}'\right) V\left(\boldsymbol{r}, \boldsymbol{r}'\right) \phi_{l,b}\left(\boldsymbol{r}'\right) \phi_{j,a}\left(\boldsymbol{r}\right) , \end{aligned} \tag{6.90}$$

or, after reassigning the indices,

$$V_{ijkl} = V_{iljk}^{\mathrm{env.}} . \tag{6.91}$$

All terms in the CI Hamiltonian in the quasi-particle representation (equation 6.77 which conserve the number of particles in the Fock space can then be written with

$$V^{\mathrm{qp}}_{ijkl} \rightarrow V^{\mathrm{qp,env.}}_{iljk} \tag{6.92}$$

and

$$V^{\mathrm{qp}}_{ijlk} \rightarrow V^{\mathrm{qp,env.}}_{ikjl}. \tag{6.93}$$

The same straightforward substitutions cannot, however, be made for those terms which do not conserve the particle number, since the Bloch functions of such terms are not in general orthogonal; for example, the term

$$\begin{aligned} V^{\mathrm{qp}}_{i^*jkl} &= \langle \psi^*_i | \langle \psi_j | V\left(\boldsymbol{r}, \boldsymbol{r}'\right) | \psi_k \rangle | \psi_l \rangle \\ &= \sum_{b_i b_j b_k b_l} \langle u^*_{b_i} | \langle u_{b_j} | u_{b_k} \rangle | u_{b_l} \rangle \langle \phi^*_{i,b_i} | \langle \phi_{j,b_j} | V\left(\boldsymbol{r}, \boldsymbol{r}'\right) | \phi_{k,b_k} \rangle | \phi_{l,b_l} \rangle \\ &= \sum_{b_i b_j b_k b_l} \langle u^*_{i,b_i} | u_{l,b_l} \rangle \langle \phi^*_{i,b_i} | \langle \phi_{j,b_j} | V\left(\boldsymbol{r}, \boldsymbol{r}'\right) | \phi_{k,b_k} \rangle | \phi_{l,b_l} \rangle \end{aligned} \tag{6.94}$$

Such states cannot be calculated exactly without explicit knowledge of the Bloch functions $\{u_{i,b}\}$, however, under the assumption that Bloch states are approximately orthogonal, the approximation $\langle u_i | u_j \rangle = \delta_{ij}$ may be introduced, in which case the same substitutions can be made for non-conserving terms as was made for the conserving terms. In this case, the CI Hamiltonian in the quasi-particle representation with a plane wave basis may be written as

$$\begin{aligned} H^{\mathrm{qp}}_{\mathrm{CI}} = E_0 &+ \sum_{ij} H^{\mathrm{e}}_{ij} e^\dagger_i e_j - \sum_{ij} H^{\mathrm{h}}_{ij} h^\dagger_i h_j + \frac{1}{2} \sum_{ijkl} V^{\mathrm{qp,env.}}_{iljk} e^\dagger_i e^\dagger_j e_k e_l \\ &+ \frac{1}{2} \sum_{iljl} V^{\mathrm{qp,env.}}_{ijkl} h^\dagger_i h^\dagger_j h_k h_l - \sum_{ijkl} \left(V^{\mathrm{qp,env.}}_{iljk} - V^{\mathrm{qp,env.}}_{ikjl} \right) e^\dagger_i h^\dagger_j h_k e_l + \mathcal{H}^{\mathrm{qp,env.}}_{\mathrm{rec}}, \end{aligned} \tag{6.95}$$

with

$$\begin{aligned}\mathcal{H}_{\text{rec}}^{\text{qp,env.}} = &\frac{1}{2}\sum_{ijkl}\left(V_{likj^*}^{\text{qp,env.}} - V_{li^*kj}^{\text{qp,env.}}\right) h_i e_j^\dagger h_k^\dagger h_l^\dagger + \frac{1}{2}\sum_{ijkl}\left(V_{l^*ikj}^{\text{qp,env.}} - V_{lik^*j}^{\text{qp,env.}}\right) h_i h_j h_k^\dagger e_l \\ &+ \frac{1}{2}\sum_{ijkl}\left(V_{ilj^*k}^{\text{qp,env.}} - V_{j^*lik}^{\text{qp,env.}}\right) e_i^\dagger h_j e_k e_l + \frac{1}{2}\sum_{ijkl}\left(V_{il^*jk}^{\text{qp,env.}} - V_{ikjl^*}^{\text{qp,env.}}\right) e_i^\dagger e_j^\dagger e_k h_l^\dagger \\ &+ \frac{1}{2}\sum_{ijkl} V_{il^*jk^*}^{\text{qp,env.}} e_i^\dagger e_j^\dagger h_k^\dagger h_l^\dagger + \frac{1}{2}\sum_{ijkl} V_{i^*lj^*k}^{\text{qp,env.}} h_i h_j e_k e_l .\end{aligned} \tag{6.96}$$

By taking into account all terms in equation 6.96 with an infinite basis, exact many-particle states may be found. The CI Hamiltonian matrix, however, is vast for even a moderate number of basis states. The basis must therefore be truncated in order to render Hamiltonian matrix soluble. In so doing, care must be taken to avoid splitting degeneracies. The calculations presented herein retain only the terms of the CI Hamiltonian which conserve the number of particles in the Fock space, with non-conserving properties such as radiative recombination, Auger recombination, and direct carrier multiplication (multiple exciton generation) being found by other means (see section 6.5. To further reduce the number of Coulomb integrals which must be evaluated, the basis is restricted to only the first 12 electron and 12 hole states (note the maximum degeneracy of the single-particle states is four-fold, inclusive of spin). Configurations of these 24 state leads to good compromise between accuracy and computational efficiency when diagonalising the CI Hamiltonian matrix.

6.5 RADIATIVE PROCESSES

The ultimate efficiency of any photovoltaic solar cell device is determined by the lifetime for radiative recombination of excited carriers, since all other processes, such as carrier multiplication or carrier extraction must take place before recombination occurs. It is therefore essential to have knowledge of the recombination rates and carrier lifetimes for radiative recombination. Further, when studying

systems which may exhibit multiple exciton generation, rates and lifetimes for Auger processes (and therefore the inverse impact ionisation process) are also desired. These rates may be calculated in the non-interacting limit with knowledge of the interband dipole matrix elements obtained from $\mathbf{k} \cdot \mathbf{p}$ calculations, as well as from the matrix elements between many-particle states from the CI calculation. These matrix elements may then be combined with Fermi's golden rule to provide carrier lifetimes for the given transitions (see section 2.4.1).

6.5.1 *The Hellmann-Fenyman Theorem*

Interband optical matrix elements required for calculations on radiative carrier lifetimes are calculated from the product of momentum matrix elements taken between initial state $|i\rangle$ and final state $|f\rangle$, i.e. as

$$M^2 = |\langle \mathrm{i} \,|\, \hat{\boldsymbol{e}} \cdot \boldsymbol{p}_{\mathrm{i}\to\mathrm{f}} \,|\, \mathrm{f} \rangle|^2 \,, \tag{6.97}$$

where $\hat{\boldsymbol{e}}$ is the unit light polarisation vector [172]. The momentum matrix elements are in turn found through application of the *Hellmann-Feynman theorem*, which relates the derivative of the Hamiltonian matrix with respect to some parameter to the derivative of the energy eigenvalues with respect to that same parameter. In calculating the momentum matrix elements, the Hellman-Feynman theorem may be stated as [172]

$$\boldsymbol{p}_{\mathrm{i}\to\mathrm{f}} = \frac{m_0}{\hbar} \left\langle \mathrm{f} \left| \frac{\partial H_{\boldsymbol{k}}}{\partial \boldsymbol{k}} \right| \mathrm{i} \right\rangle . \tag{6.98}$$

Further, momentum matrix elements $\boldsymbol{p}_{\mathrm{i}\to\mathrm{f}}$ relate to the dipole transition matrix elements as

$$\boldsymbol{p}_{\mathrm{i}\to\mathrm{f}} = i m_{\mathrm{e}} \left(\omega_{\mathrm{f}} - \omega_{\mathrm{i}}\right) \langle \mathrm{f} \,|\, \boldsymbol{r} \,|\, \mathrm{i} \rangle = \frac{i m_{\mathrm{e}} \omega_{\mathrm{fi}}}{q_0} \boldsymbol{\mu}_{\mathrm{i}\to\mathrm{f}}, \tag{6.99}$$

where $\omega_{\mathrm{i,f}} = E_{\mathrm{i,f}}/\hbar$ are the angular frequencies associated with initial and final states $|\mathrm{i}\rangle$ and $|\mathrm{f}\rangle$ with energies E_i and E_f, respectively, and

$$\mu_{\mathrm{i}\to\mathrm{f}} = \langle \mathrm{f}|\boldsymbol{\mu}|\mathrm{i}\rangle = \langle \mathrm{f}|q_0\boldsymbol{r}|\mathrm{i}\rangle \tag{6.100}$$

is the transition dipole matrix element between $|\mathrm{i}\rangle$ and $|\mathrm{f}\rangle$ [173].

The momentum matrix elements may either be the single-particle matrix elements based on the eigenvalues of the $\mathbf{k}\cdot\mathbf{p}$ calculation, or the matrix elements from the full CI calculation.

6.5.2 *Radiative Carrier Recombination*

Once the momentum matrix elements $\boldsymbol{p}_{\mathrm{i}\to\mathrm{f}}$ (and therefore the optical matrix elements M) are known, the rate of radiative recombination in the nanostructure may be calculated using Fermi's golden rule (see section 2.4.1). In terms of the dipole matrix elements, Fermi's golden rule may be written as

$$W_{\mathrm{i}\to\mathrm{f}} = \frac{2\pi}{\hbar}\frac{\hbar}{2\epsilon_0\epsilon_\mathrm{r}V}\sum_{\boldsymbol{k},n}\omega_{\boldsymbol{k}}\left|\hat{\boldsymbol{e}}_n\cdot\boldsymbol{\mu}_{\mathrm{i}\to\mathrm{f}}\right|^2\delta\left(E_\mathrm{f}-E_\mathrm{i}-\hbar\omega_{\boldsymbol{k}}\right), \tag{6.101}$$

where $n = x, y, z$ and ϵ_r is the relative electrical permittivity (dielectric constant) of the material [173].The polarisation $\hat{\boldsymbol{e}}$ of a particular photon is not generally known, however, assuming that no inherent bias exists in the system it is reasonable to assume that spontaneously emitted light has an equal probability to be polarised in all directions. The directionallity of the transitions may therefore be reasonably eliminated by averaging over the directions of polarisation, such that

$$\sum_n\left|\hat{\boldsymbol{e}}_n\cdot\boldsymbol{\mu}_{\mathrm{i}\to\mathrm{f}}\right|^2 \to \frac{1}{3}\left[\left|\mu_{\mathrm{i}\to\mathrm{f}}\right|_x^2+\left|\mu_{\mathrm{i}\to\mathrm{f}}\right|_y^2+\left|\mu_{\mathrm{i}\to\mathrm{f}}\right|_z^2\right] = \frac{1}{3}\mu_{\mathrm{i}\to\mathrm{f}}^2, \tag{6.102}$$

with Fermi's Golden rule for radiative transitions now reading

$$W_{\mathrm{i}\to\mathrm{f}} = \frac{2\pi}{3\epsilon_0\epsilon_{\mathrm{r}}\hbar V}\sum_{\boldsymbol{k}}\mu^2_{\mathrm{i}\to\mathrm{f}}\omega_{\boldsymbol{k}}\delta\left(\omega_{\mathrm{fi}}-\omega_{\boldsymbol{k}}\right). \tag{6.103}$$

The summation over $\boldsymbol{k}$ in equation 6.103 can be replaced by an integral over $\omega_{\boldsymbol{k}}$ by making the transformation

$$\begin{aligned}\sum_{\boldsymbol{k}}\mu^2_{\mathrm{i}\to\mathrm{f}}\omega_{\boldsymbol{k}}\delta\left(\omega_{\mathrm{fi}}-\omega_{\boldsymbol{k}}\right) \to& \frac{V}{(2\pi)^3}\int d^3\boldsymbol{k}\mu^2_{\mathrm{i}\to\mathrm{f}}\omega_{\boldsymbol{k}}\delta\left(\omega_{\mathrm{fi}}-\omega_{\boldsymbol{k}}\right)\\ =&\frac{V}{(2\pi)^3}4\pi\int \boldsymbol{k}^2 d\boldsymbol{k}\mu^2_{\mathrm{i}\to\mathrm{f}}\omega_{\boldsymbol{k}}\delta\left(\omega_{\mathrm{fi}}-\omega_{\boldsymbol{k}}\right)\\ =&\frac{V}{2\pi^2}\int \boldsymbol{k}^2 d\boldsymbol{k}\mu^2_{\mathrm{i}\to\mathrm{f}}\omega_{\boldsymbol{k}}\delta\left(\omega_{\mathrm{fi}}-\omega_{\boldsymbol{k}}\right),\end{aligned} \tag{6.104}$$

and using the dispersion relation

$$\omega_{\boldsymbol{k}} = \frac{c\boldsymbol{k}}{\sqrt{\epsilon_{\mathrm{r}}}}, \tag{6.105}$$

to transform the integral 6.104 from the $\boldsymbol{k}$ space to the $\omega_{\boldsymbol{k}}$-space. The resulting expression for the rate of spontaneous emission is then

$$W_{\mathrm{i}\to\mathrm{f}} = \frac{\sqrt{\epsilon_{\mathrm{r}}}}{3\pi\epsilon_0\hbar c^3}\int d\omega_{\boldsymbol{k}}\omega^2_{\boldsymbol{k}}\mu^2_{\mathrm{i}\to\mathrm{f}}\delta\left(\omega_{\mathrm{fi}}-\omega_{\boldsymbol{k}}\right). \tag{6.106}$$

By making the substitution detailed in equation 6.99, the dipole transition elements may be replaced by the momentum matrix elements 6.98, resulting in

$$W_{\mathrm{i}\to\mathrm{f}} = \frac{q_0^2\sqrt{\epsilon_{\mathrm{r}}}}{3\pi\epsilon_0 m_{\mathrm{e}}^2\hbar c^3}\left(\omega_{\mathrm{f}}-\omega_{\mathrm{i}}\right)p^2_{\mathrm{i}\to\mathrm{f}} = \frac{q_0^2\sqrt{\epsilon_{\mathrm{r}}}}{3\pi\epsilon_0 m_{\mathrm{e}}^2\hbar^2 c^3}\left(E_{\mathrm{f}}-E_{\mathrm{i}}\right)p^2_{\mathrm{i}\to\mathrm{f}}, \tag{6.107}$$

$$p^2_{\mathrm{i}\to\mathrm{f}} = \left|\boldsymbol{p}_{\mathrm{i}\to\mathrm{f}}\right|^2_{\mathrm{x}} + \left|\boldsymbol{p}_{\mathrm{i}\to\mathrm{f}}\right|^2_{\mathrm{y}} + \left|\boldsymbol{p}_{\mathrm{i}\to\mathrm{f}}\right|^2_{\mathrm{z}} \tag{6.108}$$

Equation 6.107 may be further simplified by recognising that it contains the fine structure constant

$$\alpha = \frac{1}{4\pi\epsilon_0}\frac{q^2}{\hbar c}, \tag{6.109}$$

in which case the expression for the rate of spontaneous emission becomes

$$W_{i\to f} = \frac{1}{\tau^{rad}_{i\to f}} = \frac{n\alpha\left(E_f - E_i\right)}{3m_e^2\hbar c^2} p^2_{i\to f}, \tag{6.110}$$

where $n = \sqrt{\epsilon_r}$ is the refractive index of the bulk material [174].

It is generally agreed upon that the effects of dielectric screening in nanocrystal quantum dots differ from the screening effect in the bulk. Further, the dielectric constant of a nanocrystal quantum dot is expected to be size-dependent. A size-dependent dielectric screening factor should therefore be introduced to equation 6.110. Following in the approach of Califano et al. [175], the screening factor used in the current work takes the form

$$F = \frac{3\epsilon_r^{mx}}{\left(\epsilon_{dot} + 2\epsilon_r^{mx}\right)}, \tag{6.111}$$

where ϵ_r^{mx} is the dielectric constant of the embedding matrix (the colloid). The high-frequency dielectric constant of the dot is obtained from a modified Penn model of the form

$$\epsilon_\infty^{dot}(R) = 1 + \left(\epsilon_\infty^{bulk} - 1\right) \frac{\left[E_{gap}^{bulk} + \Delta E\right]^2}{\left[E_{gap}^{dot}(R) + \Delta E\right]^2}, \tag{6.112}$$

where $E_{gap}^{bulk} + \Delta E$ is the bulk bandgap energy of the underlying material plus the distance to the first optically bright transition peak in the bulk spectrum, and similarly $E_{dot}^{bulk} + \Delta E$ is the size-dependent bandgap energy of a quantum dot of radius R plus the distance to the first peak in the bulk absorption spectrum [176]. As will be seen later in section 7.1, and as was implied by the crystal selection rules and spatial symmetry of the band edges, the first allowed transition in lead-chalcogenide systems is the optically bright $\Delta j = 0$, $\Delta m = 0$, $\pi_{VB}\pi_{CB} = 1$ transition between s-like and p_z-like states at the VBM and CBM. Therefore, for quantum dots based on the lead-salts, $\Delta E = 0$ for all radii studied.

The formalism thus far stated is valid only for bare core quantum dots. In order to account for core/shell heterostructures, further modification to the permittivity of the quantum dot is required. In the current work, a volume-weighted average between the core and shell regions of the QD is taken:

$$\epsilon_{\text{dot}}^{\text{core/shell}} = \frac{\epsilon_{\infty}^{\text{core}} \times V^{\text{core}} + \epsilon_{\infty}^{\text{shell}} \times V^{\text{shell}}}{V^{\text{core}} + V^{\text{shell}}}, \tag{6.113}$$

where $\epsilon_{\infty}^{\text{core}}$ and $\epsilon_{\infty}^{\text{shell}}$ are determined using equation 6.112. This is a reasonable assumption, given that the dielectric constant across the core/shell interface and shell/colloid interface would be expected to vary smoothly between the dielectric constant inside the barrier region and the dielectric constant on the outside [177].

With these considerations in mind, the final expression for the radiative lifetime of carriers in a quantum dot is

$$\frac{1}{\tau_{\text{i}\to\text{f}}^{\text{rad.}}} = \frac{n\alpha F\left(E_{\text{f}} - E_{\text{i}}\right)}{3m_{\text{e}}^2\hbar c^2} p_{\text{i}\to\text{f}}^2. \tag{6.114}$$

6.6 MULTIPLE EXCITON GENERATION

Multiple exciton generation (impact ionisation, direct carrier multiplication) has the potential to improve solar conversion efficiency of photovoltaic solar cell devices based on PbX nanocrystal technology up to 42% at the theoretical limit [91]. As has been previously discussed, carrier multiplication may occur where photoabsorption results is the creation of a hot carrier (usually an electron) with at least twice the bandgap energy. It is important to recall that the excess energy must be possessed by one of the carriers comprising the photo-generated exciton, rather than by the exciton as a whole.

The matrix elements which describe the MEG process are, in principle, derived from the non-conserving terms of the CI Hamiltonian, as discussed above

in chapter 6.4. However, inclusion of all possible matrix elements in the CI calculation results in extremely large and unwieldy matrices which must be solved, and as a result, a different approach is used to find the relevant matrix elements. In the current approach, the Coulomb integrals responsible for carrier multiplication are identified, and only these integrals are retained in the calculation. The rate of direct carrier multiplication is then calculated using Fermi's golden rule. For the MEG process, Fermi's golden rule may be written

$$W_n = \frac{2\pi}{\hbar} \int dE \, |M_n|^2 \, \delta \left(E_n - E \right), \tag{6.115}$$

where the integral has been introduced to account for all final states and n is the level of the initial hot carrier. In principle, the discrete nature of the quantum dot energy spectrum should suppress the these processes, since possible transitions between discrete states would rarely be conserving of energy, however, in reality, processes such as phonon emission may allow these transitions to occur. In order to avoid the energy conservation problem, the δ-function in equation 6.115 may be replaced with a Lorentzian [178, 179]. Fermi's golden rule then takes the form

$$W_n = \frac{\Gamma}{\hbar} \sum_m \frac{|M_n|^2}{\left(E_n - E_m \right)^2 + \left(\Gamma/2 \right)^2}, \tag{6.116}$$

where the summation is over final (degenerate and discrete) states m and Γ gives the width of the distribution. In the current work, Γ is chosen to be 35 meV.

In order to evaluate the rate of direct carrier multiplication the matrix elements $|M_n|^2$ must first be obtained. These matrix elements are found in the non-conserving terms of the CI Hamiltonian 6.65, and are of the form

$$\frac{1}{2} \sum_{\alpha\beta\gamma\delta} \left(\langle \alpha\beta \,|\, V \,|\, \gamma\delta \rangle - \langle \alpha\beta \,|\, V \,|\, \delta\gamma \rangle \right) e_\alpha^\dagger e_\beta^\dagger e_\gamma h_\delta^\dagger, \tag{6.117}$$

with

$$\langle \alpha\beta \mid V \mid \gamma\delta \rangle = \int d^3\boldsymbol{r} \int d^3\boldsymbol{r}' \psi_\alpha^* (\boldsymbol{r}) \, \psi_\beta^* (\boldsymbol{r}') \, \frac{1}{4\pi\epsilon_r} \frac{1}{|\boldsymbol{r} - \boldsymbol{r}'|^2} \psi_\gamma (\boldsymbol{r}') \, \psi_\delta (\boldsymbol{r}) \,, \tag{6.118}$$

where it has been assumed that the initial hot carrier is an electron. In most studies of direct carrier multiplication, it is the electron which is considered to occupy the high energy state, while the hole is found at the edge of the valence band. In this case the initial state is written

$$|\mathrm{i}\rangle = \left| e_{ng} h_{0l} \right\rangle , \tag{6.119}$$

where g is the degeneracy of state n. It is assumed that $g \geq 2$ due to spin degeneracy. In the transition from state $|\mathrm{i}\rangle$ to state $|\mathrm{f}\rangle$, where all four carriers are found at the bandedge, the excess energy of the hot electron is passed to a secondary electron-hole pair, while the initial hot electron relaxes to the LUMO level. In terms of the quasi-particle creation and annihilation operators, this is equivalent to the creation of a secondary hole state, h_{mk} near the VBM, the annihilation of the high-energy electron state e_{ng}, and the creation of two further, degenerate electron states, e_{0i} and e_{0j} at the CBM. Thus, the only non-zero matrix elements are those containing the same creation and annihilation operators as in 6.117. In this representation the final state is written

$$|\mathrm{f}\rangle = \left| e_{0i} e_{0j} h_{mk} h_{0l} \right\rangle , \tag{6.120}$$

where h_{mk} is the secondary hole created near the bandedge. The energy conservation terms for this process are

$$\delta \left(E_n - E \right) = \delta \left(\left[E_{e_n} - E_{h_0} \right] - \left[2E_{e_0} - E_{h_0} - E_{h_m} \right] \right) . \tag{6.121}$$

It is important to note that the state h_{0l} does not take part in the carrier multiplication process. As such, h_{0l} must be identical in both $|\mathrm{i}\rangle$ and $|\mathrm{f}\rangle$. Such a state is known as a *spectator* [178].

The matrix element which couples the exciton and biexciton state $|\mathrm{i}\rangle$ to state $|\mathrm{f}\rangle$ (X-XX coupling) is

$$|M_n|^2 = |\langle \mathrm{f} \,|\, H \,|\, \mathrm{i}\rangle|^2 = \left|\left\langle e_{0i} e_{0j} h_{mk} h_{0l} \,\middle|\, H \,\middle|\, e_{ng} h_{0l} \right\rangle\right|^2 . \tag{6.122}$$

The only surviving terms of H are those similar to 6.117, namely[2]

$$\begin{aligned} |M_n|^2 = \Bigg| & \frac{1}{2} \left(\left\langle e_{0i} e_{0j} \,\middle|\, V \,\middle|\, h_{mk} e_{ng} \right\rangle - \left\langle e_{0i} e_{0j} \,\middle|\, V \,\middle|\, e_{ng} h_{mk} \right\rangle \right) \\ & - \frac{1}{2} \left(\left\langle e_{0j} e_{0i} \,\middle|\, V \,\middle|\, h_{mk} e_{ng} \right\rangle - \left\langle e_{0j} e_{0i} \,\middle|\, V \,\middle|\, e_{ng} h_{mk} \right\rangle \right) \Bigg|^2 , \end{aligned} \tag{6.123}$$

which agrees with the expression obtained in reference [180]. Combining this result with the Fermi's golden rule (from equation 6.116), the rate of carrier multiplication is given by

$$W_n = \frac{\Gamma}{\hbar} \sum_{g,l} \sum_{mk \neq 0l} \sum_{i \neq j} \frac{|M_n|^2}{\left(\left[E_{e_n} - E_{h_0} \right] - \left[2E_{e_0} - E_{h_0} - E_{h_m} \right] \right)^2 + (\Gamma/2)^2}, \tag{6.124}$$

where the spectator state h_{0l} has been excluded from the summation over final hole states h_{mk} of the secondary hole. In order to represent the rate of carrier multiplication in terms of the envelope functions of the CI Hamiltonian based on sp states calculated using planewaves, the elements of $|M_n|^2$ must be rewritten using the definitions in section 6.4.2. This is quite straightforward, the substitutions being

$$\begin{aligned} i &\to i \\ j &\to k \\ k &\to l \\ l &\to j \end{aligned} \tag{6.125}$$

2 For an explicit derivation of this result refer to appendix B.

The matrix elements in this representation are then

$$|M_n|^2 = \left| \frac{1}{2} \left(\langle e_{0i} h_{mk} \mid V \mid e_{ng} e_{0j} \rangle - \langle e_{0i} h_{mk} \mid V \mid e_{0j} e_{ng} \rangle \right) - \frac{1}{2} \left(\langle h_{mk} e_{0i} \mid V \mid e_{ng} e_{0j} \rangle - \langle h_{mk} e_{0i} \mid V \mid e_{0j} e_{ng} \rangle \right) \right|^2 . \tag{6.126}$$

If instead the initial hot carrier is a hole in the valence band, then the initial and final states are respectively written

$$|\mathrm{i}\rangle = \left| e_{0i} h_{ng} \right\rangle \tag{6.127}$$

and

$$|\mathrm{f}\rangle = \left| e_{0i} e_{mj} h_{0k} h_{0l} \right\rangle \tag{6.128}$$

and the matrix element describing these transitions is of the form

$$\frac{1}{2} \sum_{\alpha\beta\gamma\delta} \left(V_{\alpha\beta\gamma\delta} - V_{\beta\alpha\gamma\delta} \right) h_\alpha e_\beta^\dagger h_\gamma^\dagger h_\delta^\dagger . \tag{6.129}$$

The matrix element between these two states is

$$|M_n|^2 = \left| \frac{1}{2} \left(\langle e_{mj} h_{ng} \mid V \mid h_{0k} h_{0l} \rangle - \langle e_{mj} h_{ng} \mid V \mid h_{0l} h_{0k} \rangle \right) - \frac{1}{2} \left(\langle h_{ng} e_{mj} \mid V \mid h_{0k} h_{0l} \rangle - \langle h_{ng} e_{mj} \mid V \mid h_{0l} h_{0k} \rangle \right) \right|^2 . \tag{6.130}$$

In terms of the planewave basis, this becomes

$$|M_n|^2 = \left| \frac{1}{2} \left(\langle h_{0k} h_{ng} \mid V \mid h_{0l} e_{mj} \rangle - \langle h_{0k} h_{ng} \mid V \mid e_{mj} h_{0l} \rangle \right) - \frac{1}{2} \left(\langle h_{ng} h_{0k} \mid V \mid h_{0l} e_{mj} \rangle - \langle h_{ng} h_{0k} \mid V \mid e_{mj} h_{0l} \rangle \right) \right|^2 . \tag{6.131}$$

7

RESULTS

Simulations of single colloidal PbSe/PbS nanocrystal quantum dots have been carried out for QDs of varying sizes, shell thicknesses, and ellipticity. First, single-particle energy spectra as calculated via the $\mathbf{k} \cdot \mathbf{p}$ envelope-function method (sections 6.2.4-6.3) are presented for core-only and core/shell spherical and spheroidal QD structures. It will be shown the degree of ellipticity, herein parameterised in the ratio of the semi-major and semi-minor axes, c/a, or as a percentage increase, causes subtle linear variation in the energy spectrum in accordance with the quantum size effect. The momentum matrix elements associated with electronic transitions between theses states (calculated via the Hellmann-Feynman theorem) are detailed, with particular focus on the anisotropy which emerges both between the longitudinal and transverse polarised transitions ($p_x = p_y \neq p_z$) with arises due to crystal anisotropy, as well as the transverse-transverse, x-y anisotropy ($p_x \neq p_y \neq p_z$) which arises from spheroidal geometry of the quantum dot. To the author's knowledge, anisotropy between the transverse-polarised momentum matrix elements has so far gone unreported in the literature.

Next, excitonic corrections to the single-particle states, as calculated via a configuration interaction calculation (section 6.4), are presented. Strong size-dependent excitonic binding energy on the order of 50 meV-150 meV is found, and the associated momentum matrix elements discussed, for which the same anisotropies are observed as in the single-particle case. Further, non-zero ele-

ments are found to be split across the exciton complex which correlates to the single-particle transitions.

The carrier lifetimes for radiative recombination between the states e_0 and h_0o are then presented for the spherical and spheroidal QDs. It will be seen that the radiative lifetimes are on the order of 0.1 µs (in good agreement with experiment), and for the range of QDs studied vary linearly with the size of the dot. Deviation from spherical symmetry by up to 25% (c/a = 1.25) causes subtle change in the carrier lifetimes.

Finally, preliminary results are presented for the timescales for multiple exciton generation for the smallest QD studied (core-only spherical PbSe QD or radius 18.36 Å). It will be shown that direct carrier multiplication cannot occur for PbX QDs at the thermodynamic limit (photoexcitation at $2E_g$) due to low MEG rates at his energy, a result in keeping with the experimental observations of other groups [91, 123]. An order of magnitude analysis is performed which justifies the methodology, predicting MEG lifetimes on the order of 1 ps-10 ps at photoexcitation of $3E_g$. The impact of the width of the Lorentzian distribution used in the calculation of MEG rates is also discussed.

7.1 SINGLE-PARTICLE STATES

Single-particle energy states have been calculated using the $\mathbf{k} \cdot \mathbf{p}$ method as detailed in chapter 6.2.4. The four-band envelope function calculation was performed using a planewave basis with a wavevector cut-off m = 8 (i.e. $2m + 1 = 17$ planewaves) in each of the $x/y/z$ directions. Initial calculations were performed for a series of spherical PbSe core-only NQDs of several radii, chosen to be integer multiples of the PbSe lattice constant (a_{PbSe} = 6.12 Å) in the range 18.36 Å-42.84 Å. Next, a PbS passivating shell region was added the PbSe cores, allowing for alteration of the sp energy states via the modified carrier effective masses and through limited quantum confinement of the wavefunctions of con-

duction band carriers (electrons) to the core region for thick shells. Finally, the effect of ellipticity was studied in prolate spheroidal QDs. The semi-minor axis was fixed to be equivalent to the radius of the corresponding spherical QD (i.e. $R_{\text{sphere}} = a_{\text{spheroid}}$), while the semi-major, c, axis of the spheroid is given in terms of a, either as a percentage increase, or in the ratio c/a. Knowledge of the single-particle properties of the NQDs is important both as a basis for the following full CI calculation, and for the calculation of the rates and lifetimes for multiple exciton generation.

7.1.1 *Spherical PbSe QDs*

Single-particle energy states have been calculated for a range of spherical PbSe NQDs with radii in the range 18.36 Å-42.84 Å (3-7 lattice constants PbSe). The energy spectra of the PbSe QDs are predominantly influenced by the quantum size effect, as can be seen in spectra of figure 7.1. As is to be expected, the single-particle energy states are lower in energy for larger nanocrystals. An interesting result is that the near-degeneracy of certain states groups together several of the electron states to form band-like structures with wide forbidden regions between clusters, while the hole states do so less consistently. The near-degeneracy of the electron states may result from the p_z-like symmetry of the conduction band-edge states near the L-point of the Brillouin zone, while the same effect is not observed for the s-like symmetry at the valence band maximum. For large QDs, the energy states tend toward a quasi-continuum. The bandedge states asymptotically approach the bulk bandgap of PbSe (0.28 eV). The spacing of the energy levels in the valence band (the hole states) is larger than that of the conduction band states. Each of the energy states shown in figure 7.1 is two-fold degenerate, inclusive of spin. The energy level diagrams for QDs of radii 18.36 Å, 24.48 Å, and 30.60 Å (3,4, and 5 lattice constants PbSe) are shown in figure 7.2.

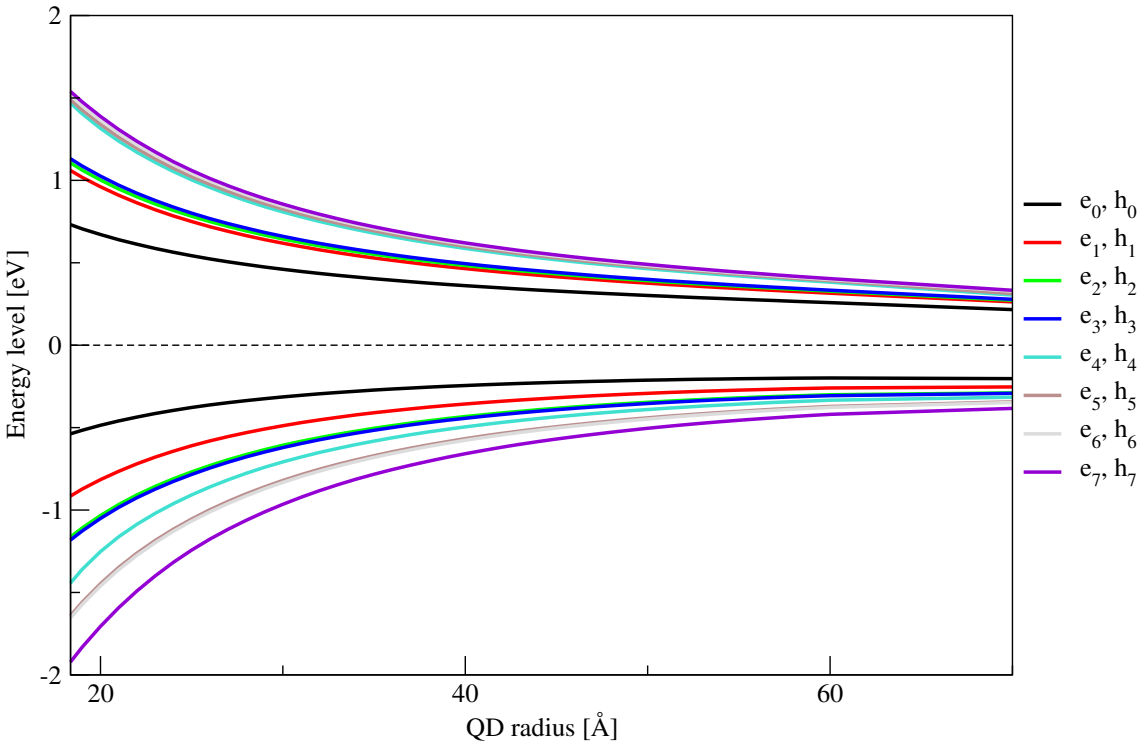

Figure 7.1.: Single-particle states for spherical PbSe QDs of increasing radius. The electron (hole) single-particle energy states decrease (increase) as the radius of the dot is increased.

The energy associated with electronic transition between these states is readily obtained from the single-particle energy spectrum. Perhaps most important are the interband transitions between CB states and ground hole states at the VBM, shown in figure 7.3. As one may expect from the single-particle energy spectrum shown in figure 7.1, the $e_n - h_0$ transitions are highly size-dependent. The dependency of the size-dependent bandgap follows a polynomial decay, proposals for the exact form of which may be found in reference [181]. Further, the transitions form into band-like structures, tending toward a continuum for large structures.

Knowledge of the momentum matrix elements between single-particle energy states is essential for the description of interband transition processes, including for calculations regarding important processes such as carrier lifetimes for radiative recombination and direct carrier multiplication rates, found using Fermi's golden rule. The elements themselves may be calculated via the Hellman-Feynman theorem. The momentum matrix elements for PbSe QDs of

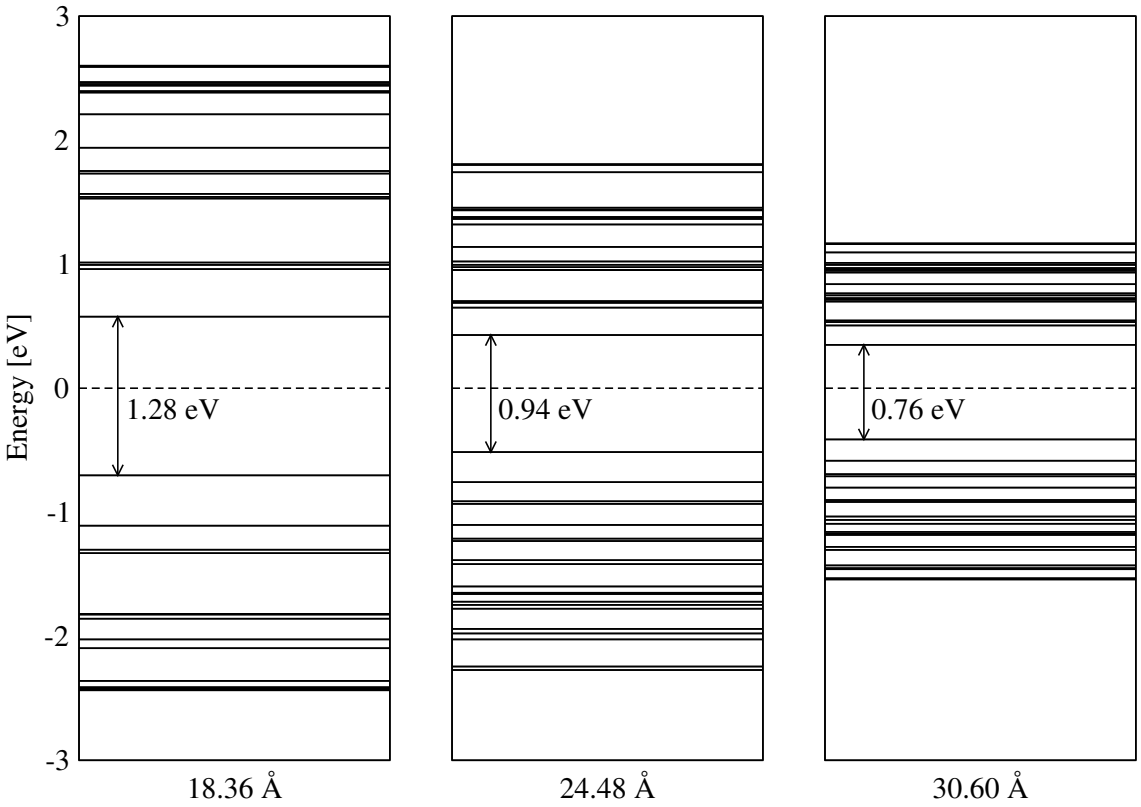

Figure 7.2.: Energy level diagrams for three representative QDs. The energy levels of the smaller dot ($\boldsymbol{R}$ = 18.36 Å, left) are sparse, and the bandgap is large. As the size of the QD increases, the energy levels become bunched, and the bandgap closes. The spectrum becomes more "band-like" as the size of the dot increases. Each of the levels shown are two-fold degenerate.

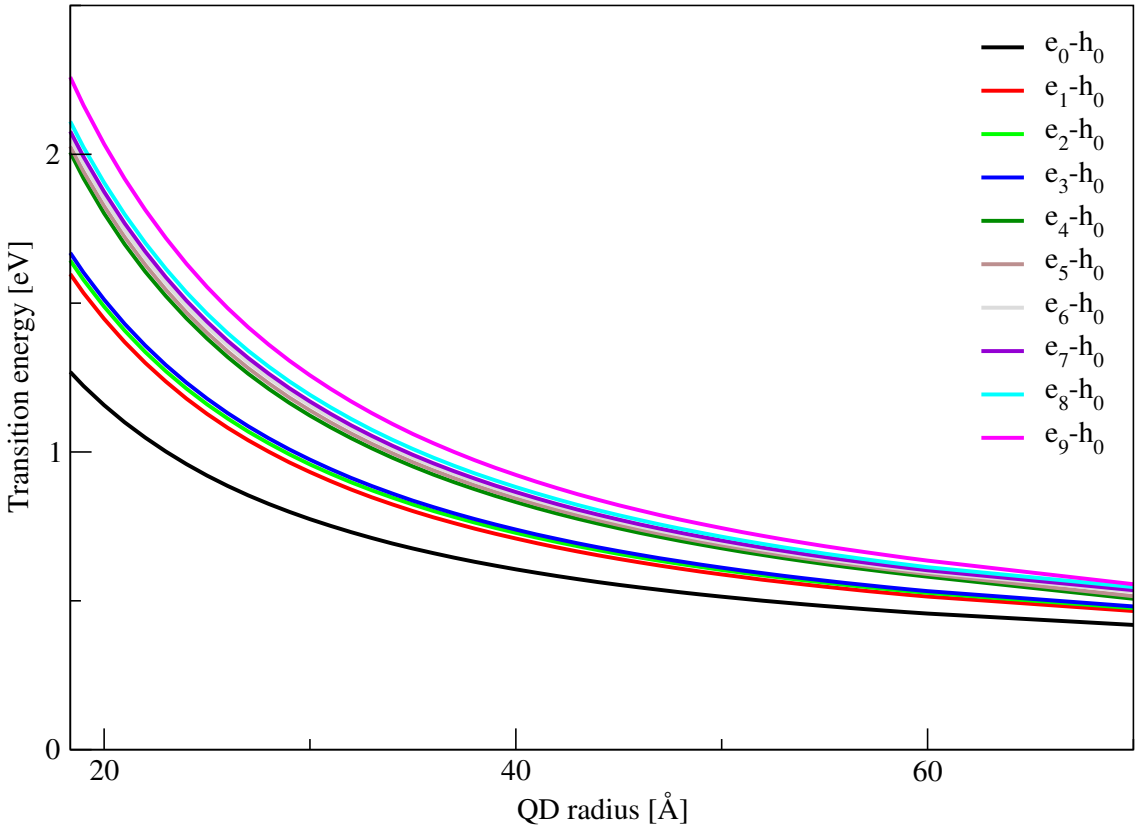

Figure 7.3.: Single-particle $e_n - h_0$ transition energies for QDs of increasing radius. The size-dependence and energy separation follow a similar trend as seen for the CB states in figure 7.1.

radii 18.36 Å, 24.48 Å, and 30.60 Å are shown in figure 7.4. It can be seen that the strength of the matrix elements for transitions polarised in the x or y directions ($\langle\bar{1}\bar{1}2\rangle$ / $\langle 1\bar{1}0\rangle$ crystallographic directions) are significantly larger than those for transitions polarised in the z-direction ($\langle 111\rangle$ crystallographic direction). Furthermore, owing to the transverse symmetry of the underlying PbSe crystal, the matrix elements for transitions polarised in the x and y directions are uniform. The magnitude of the momentum matrix elements is diminished as the size of the nanocrystal is increased; a consequence of the greater separation between the carriers in larger quantum structures. A further noteworthy feature of the momentum matrix elements is that, in many cases, the allowed energy state at which transitions may occur is coincident for all polarisations, however, it is seen consistently that this is not the case in the third transition complex. Here, the energy states at which x/y polarised and z-polarised transitions are allowed are nearly degenerate, yet distinct states.

7.1.2 *PbSe/PbS Core/Shell Quantum Dot Heterostructures*

As has been previously discussed in section 4.4, the addition of a passivating shell region grown around the PbSe core of the QD has the potential to significantly alter the electronic and optical properties of the nanocrystal. In general, the shell region is composed of some material with a higher bulk bandgap energy than that of the core, most often forming a type II semiconductor heterojunction (see figure 4.4 on page 58). Further points of consideration when selecting the shell material are the induced strain due to lattice mismatch at the boundary, as well as the location of the band extrema with in the first Brillouin zone (i.e. whether the core/shell system will form a direct or indirect effective bandgap). With these criteria in mind, two clear choices emerge with which to passivate the PbSe core: PbS and PbTe. Of the two, PbS emerges as the best option for initial investigation for two reasons: firstly, the lattice constants of PbSe

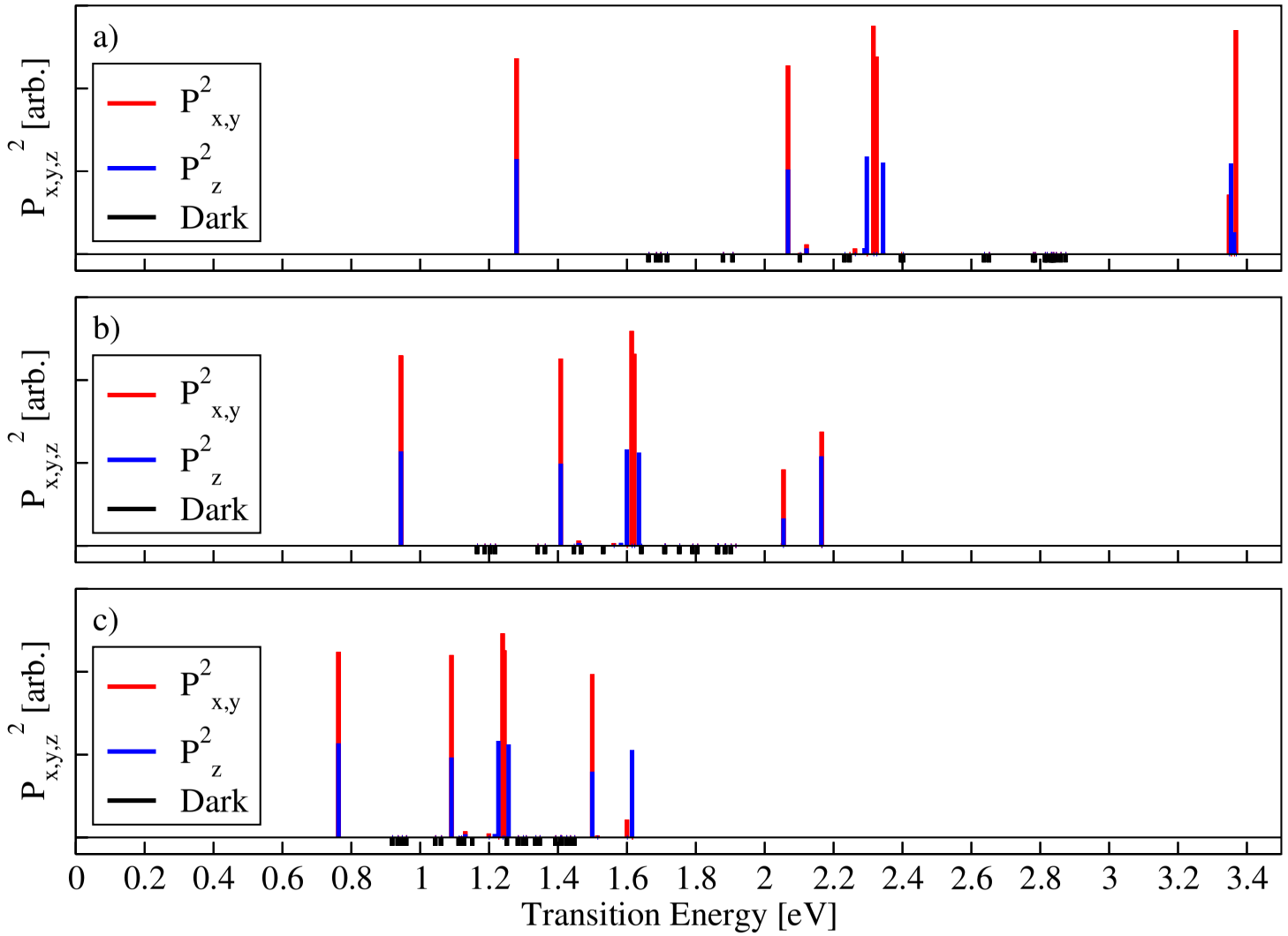

Figure 7.4.: Momentum matrix elements for spherical PbSe core-only QDs of radius a) 18.36 Å, b) 24.48 Å, and c) 30.60 Å. The x/y polarised transitions are of uniform magnitude and greater than those polarised in the z direction. Forbidden transitions are shown in black beneath the x-axis.

and PbS are almost identical, leading to negligible strain effects at the core/shell interface; and secondly, the dielectric mismatch between PbSe and PbS is less extreme than the mismatch between PbSe and PbTe, leading to a reduction in the magnitude of effects such as self-interaction with induced mirror charges at the dielectric boundary, an effect which at present it has not been possible to include for spheroidal nanocrystals. Both PbS and PbTe posses a direct bandgap located at the *L*-point, resulting in a direct effective bandgap between the CBM of the core and the VBM of the shell.

As has been previously reported in the literature, the degree of confinement imposed on the charge carriers in PbSe/PbS quantum dot heterostructures is incomplete. Due to the small offsets between the conduction bands and valence bands of the two materials, both the electron and hole wavefunctions are free to permeate the dot where the shell region is thin, while electron states are more strongly confined to the core region with the addition of the PbS shell (see figure 7.10 on page 123). The PbSe/PbS system should therefore be thought of as a quasi-type II heterostructure. As a result, the modification introduced by the addition of successively larger shell regions is subtle. The bandedge energy states (HOMO/LUMO states) of QDs of fixed core radii $\boldsymbol{R}$ ranging from $3a_{PbSe} - 7a_{PbSe}$ are shown for successively thicker shell regions in figure 7.5. The overall profile of the energy states as the total size of the dot increases is similar to the polynomial variation shown in figure 7.1, with two important distinctions. First, the rate at which the e_0 (h_0) states decrease (increase) in energy is enhanced as the electron and hole wavefunctions become more separated, and second, the energy states (and most notably the effective bandgap energy) tend towards those of bulk PbS rather than PbSe, a consequence of the increased presence of PbS over PbSe. It should be noted that the range of shell thicknesses in figure 7.5 is large, with the thickness of the shell matching or even exceeding the radius of the core region. Knowledge of such large shell regions is useful to visualise the trends in the energy spectra of core/shell quantum dot heterostructures.

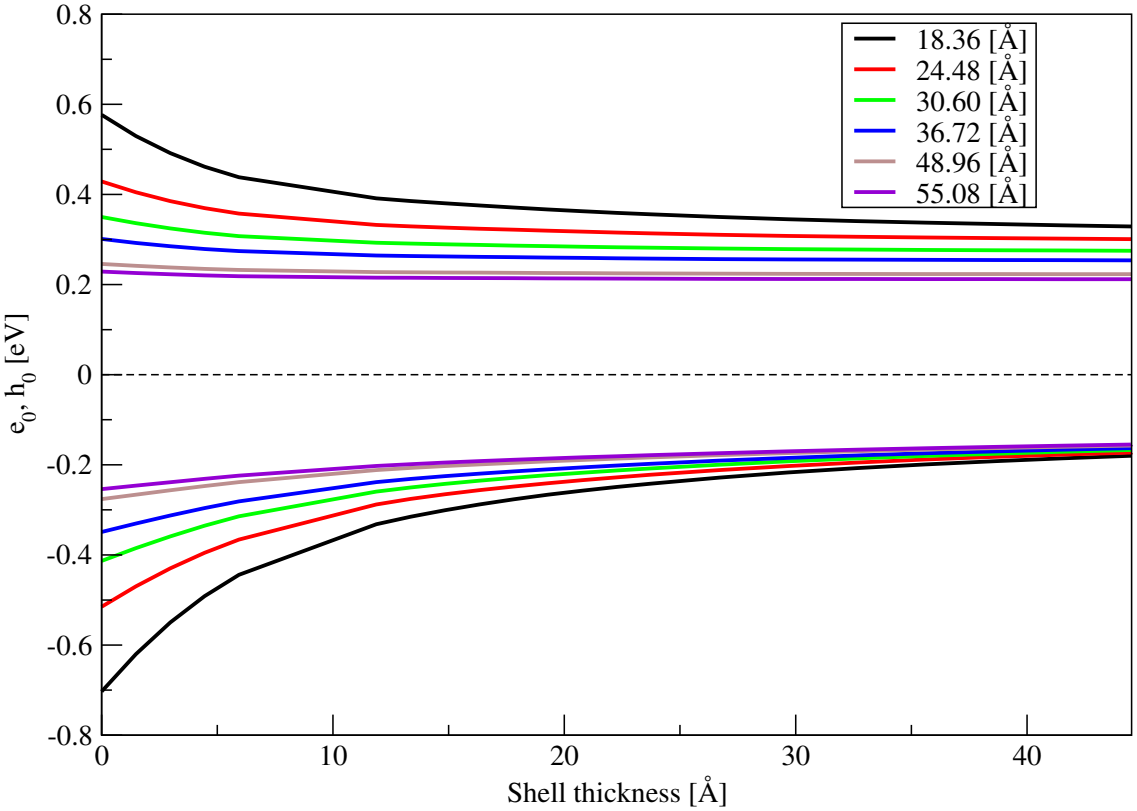

Figure 7.5.: Single-particle bandedge energy states (e_0, h_0) for a selection of spherical PbSe cores as a function of shell thickness.

The effect of shell thickness on the extended electronic spectrum may be studied for a QD with a particular core radius. The spectrum for a core of radius 30.60 Å, chosen for ease of comparison with similar calculations to be found in the literature [1], is shown in figure 7.6. The same overall profile as was seen for the bandedge states persists for higher energy states, while the same grouping of energy states into band-like structures as was seen for the core-only QDs in figure 7.2 may also be seen. Again, the effective bandgap quickly closes as the shell thickness is increased. Energy level diagrams for three values of the shell thickness are shown in figure 7.7.

The energies associated with interband transitions may readily be obtained from the single-particle spectrum shown in figure 7.6. Transition energies between the electron states and the ground hole state are shown in figure 7.8. The transition energies show similar dependence on the size of the dot as for the

1 $\boldsymbol{R} \sim 30$ Å is a common size for PbX NQDs found almost ubiquitously in the literature. For ease of comparison, a core radius of 30.60 Å will be used as a reference size.

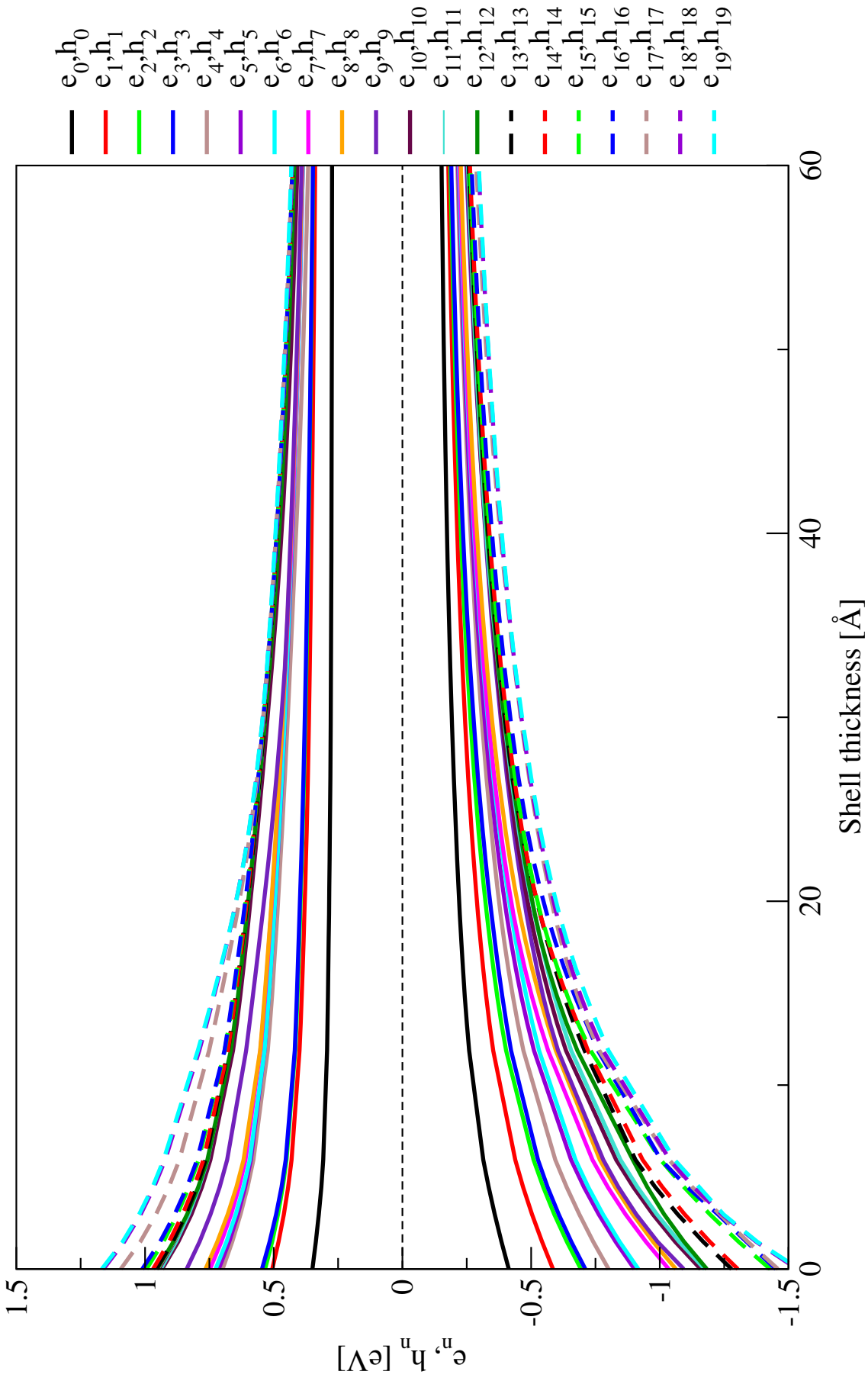

Figure 7.6.: Single-particle energy states for a spherical PbSe QD of radius 30.60 Å with progressively larger PbS shells.

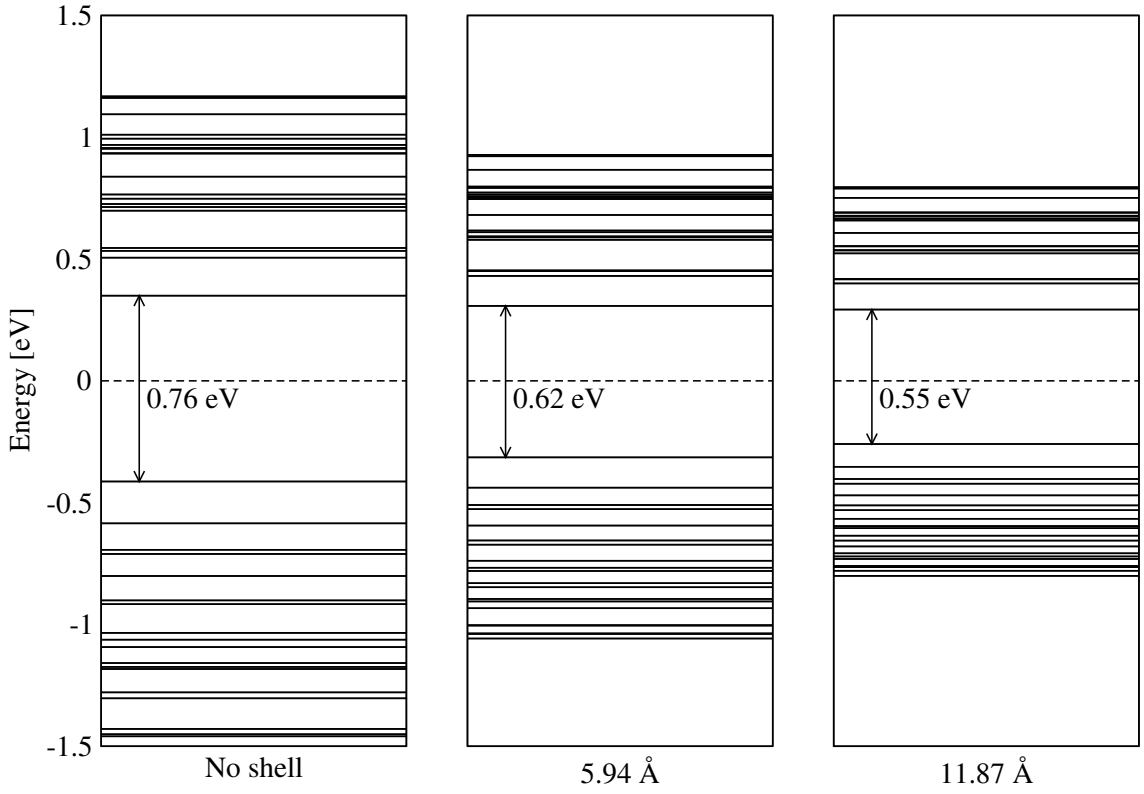

Figure 7.7.: Energy level diagrams for QDS of PbSe core radius 30.60 Å and PbS shell thicknesses of 0 angstrom (no shell), 5.94 Å (a_{PbS}), and 11.87 Å ($2a_{PbS}$). Increased shell thickness reduces the effective bandgap energy and causes bunching of the sp states.

case of increasing core radius (figure 7.3), except with the more rapid reduction in the energy of the e_n states as seen for the sp spectrum of figure 7.6.

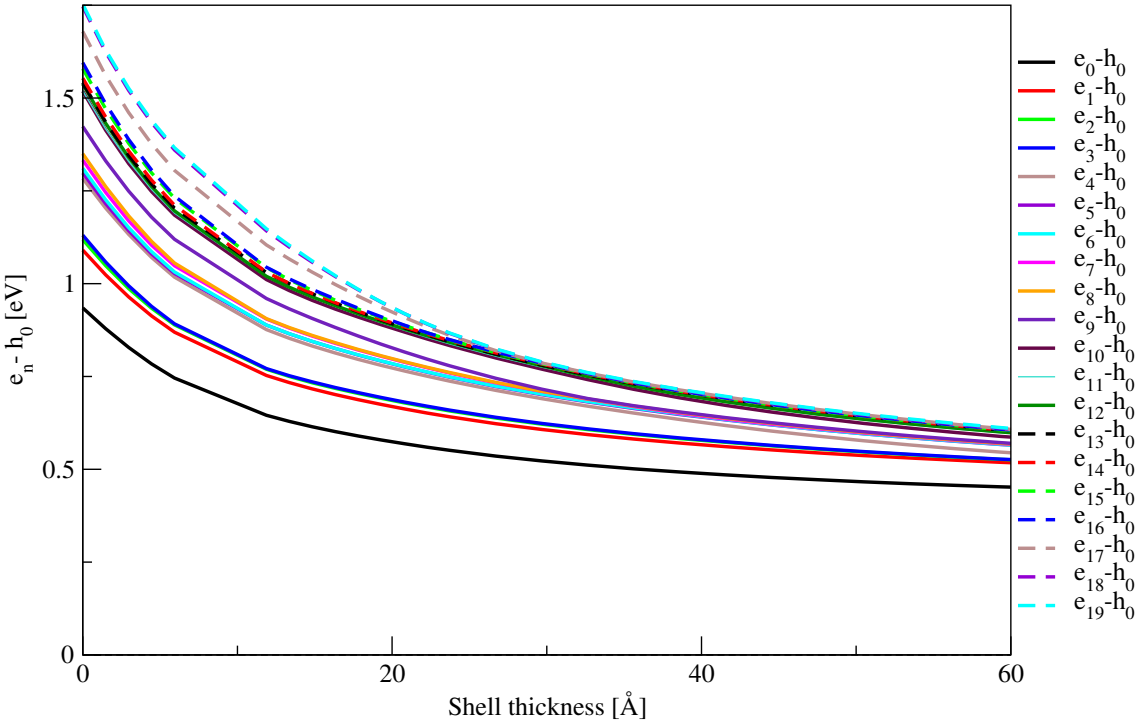

Figure 7.8.: Single-particle $e_n - h_0$ interband transition energies spherical PbSe QD of radius 30.60 Å for progressively thicker PbS shells.

The momentum matrix elements associate with these transitions, shown below in figure 7.9, have been calculated by the same method detailed above. As is to be expected from the selection rules derived by Kang and Wise [157] (shown in section 6.2.5), it can be seen that the addition of the PbS shell does nothing to affect the allowed transitions in the optical spectrum. The addition of the PbS shell does, however, modify the relative magnitudes of the momentum matrix elements, causing a modest reduction for thicker shells. The reduction in the magnitude of the momentum matrix elements arises due to the (limited) confinement of the electron wavefunctions to the core region. As thicker PbS shells are added to the PbSe core the electron and hole wavefunctions become more separated; while hole wavefunctions remain free to permeate the dot, the electrons are confined to the core. The confinement of electron and hole wavefunctions is illustrated in figure 7.10.

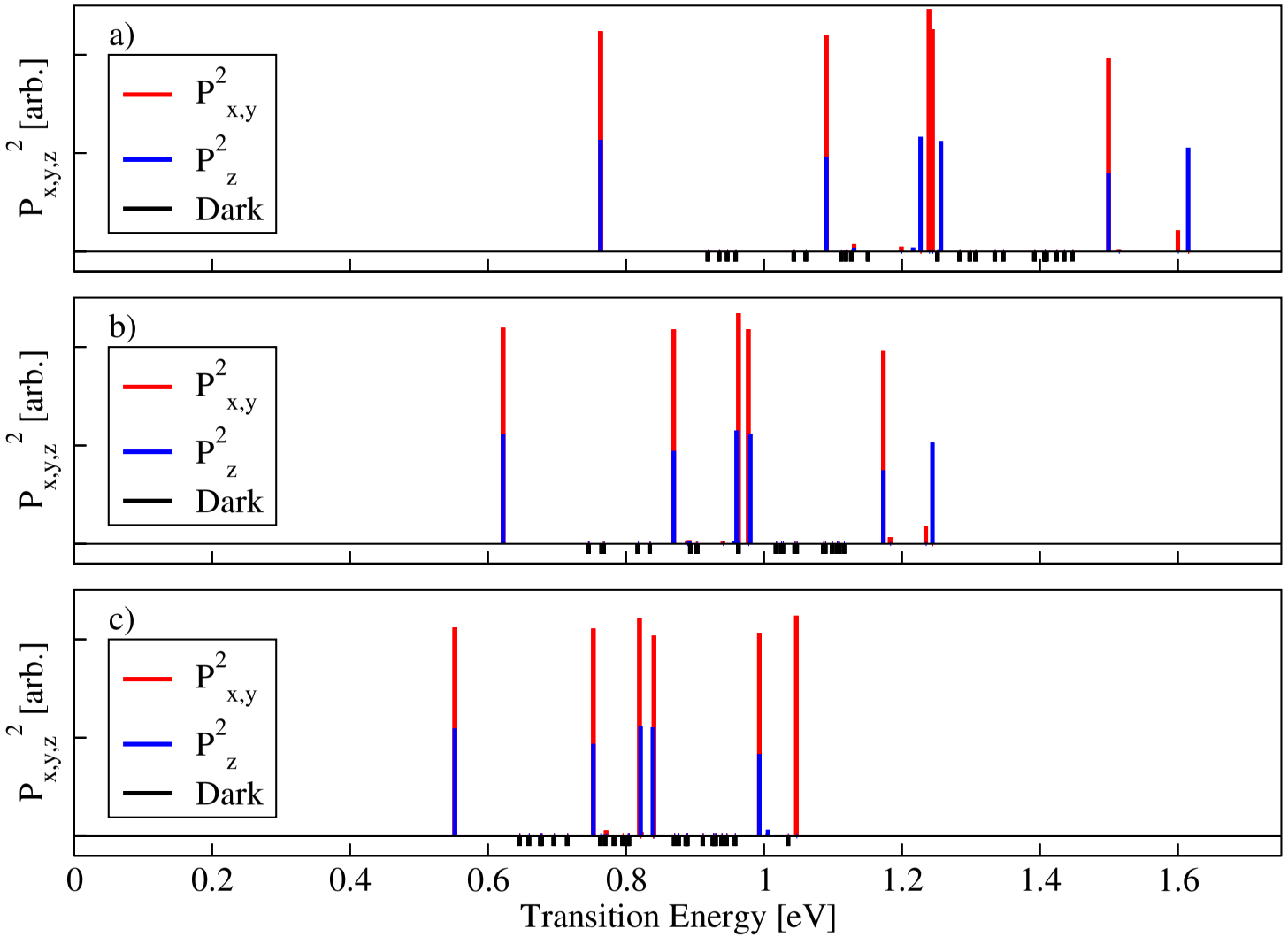

Figure 7.9.: First few transitions for spherical PbSe QD of radius 30.60 Å with a) no shell, b) PbS shell of thickness 5.94 Å, and c) PbS shell of thickness 11.87 Å. Increased shell thickness results in weakening of the interband momentum matrix elements (plotted here on axes of equal increment), while the observed red-shift is a consequence of the quantum size effect.

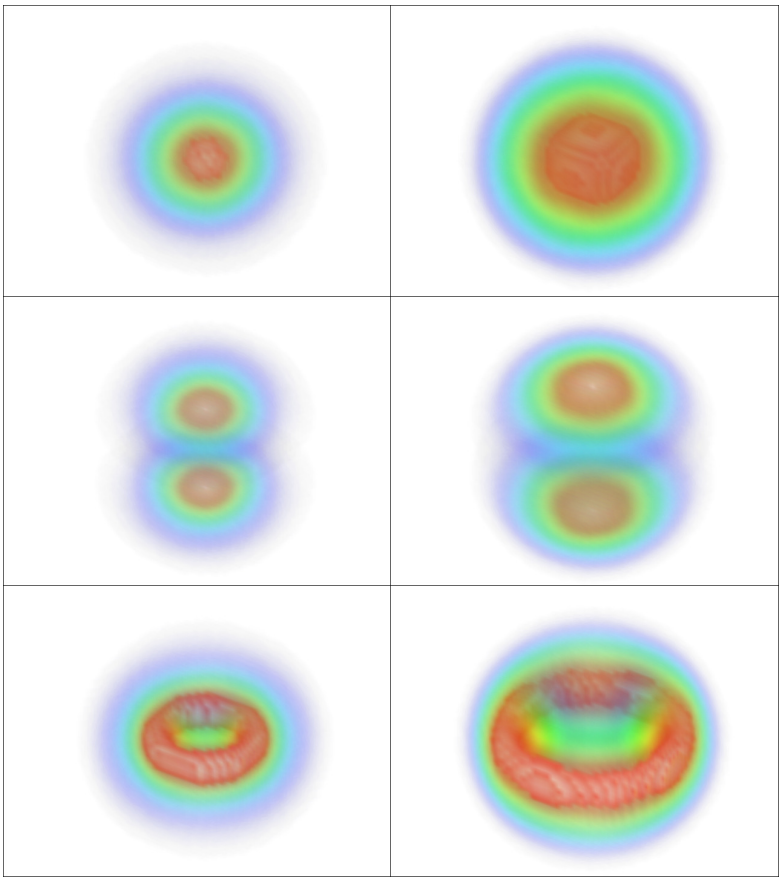

Figure 7.10.: Electron (left) and hole (right) wavefunctions for the three lowest energy states ($n = 1, 2, 3$) in a spherical QD of core radius 30.60 Å and shell thickness 23.744 Å. In this energy range, the electron is confined to the core region, while the hole wavefunction permeates the whole QD structure. The reduced overlap of the carrier wavefunctions diminishes the strength of the interband momentum matrix elements.

There is a strong degree of anisotropy in the magnitudes of the momentum matrix elements polarised in the z-direction and those polarised in the equivalent x/y-directions. This is a direct consequence of the crystal anisotropy resulting from the choice of coordinate system. The longitudinal x and y directions lie along the $\langle \bar{1}\bar{1}2 \rangle$ and $\langle 1\bar{1}0 \rangle$ directions of the crystal, forming the semi-minor axes of a spheroid of constant energy, while the semi-major axis lies along the $\langle 111 \rangle$ (z) direction. The degree of anisotropy may be characterised by:

$$A_p^{\mathrm{t,l}} = \left| \frac{|p_{x,y}|^2 - |p_z|^2}{|p_{x,y}|^2 + |p_z|^2} \right|. \tag{7.1}$$

Using this definition, the anisotropy between longitudinal and transverse polarised momentum matrix elements take on the profile shown in figure 7.11. Here, the momentum matrix elements are those taken between the bandedge states for a series of core radii and as a function of shell thickness. The degree of anisotropy is found to be larger for QDs of smaller radii. This is a consequence of the overall greater magnitude of the matrix elements found in smaller QDs, where the carriers are not well separated. As the shell thickness is increased, the degree of anisotropy is diminished. The rate of reduction is slow for smaller shells, becoming much more rapid as the electron and hole wavefunctions become more strongly separated. Finally, for large shell thicknesses, the momentum matrix elements are small, and the anisotropy between those polarised in the x/y-directions and those polarised in the z-direction is correspondingly lesser.

7.1.3 *Spheroidal PbSe and PbSe/PbS PbS Nanocrystal Quantum Dot Structures*

While highly monodisperse QD ensembles are easily accessible via colloidal chemistry, it is exceedingly difficult to ensure that the sample be comprised of perfectly spherical nanocrystals. It has therefore recently been suggested that,

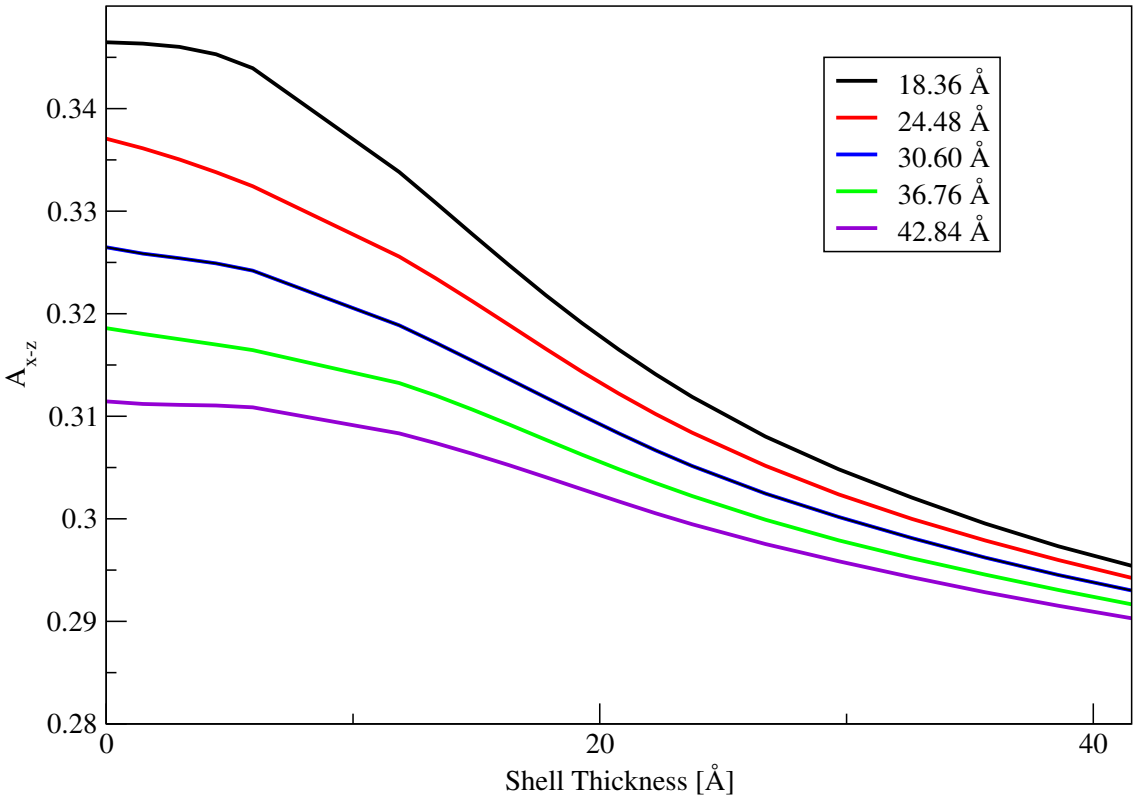

Figure 7.11.: The anisotropy of the between x/y and z-polarised $e_0 - h_0$ transition for representative spherical QDs of various core radius as a function of shell thickness.

rather than working under the usual assumption of perfectly spherical QDs, theoretical calculations would better be concerned with spheroidal QDs [182–184]. Reports of simulation of such structures are few and far between, and reports of calculations regarding aspherical PbX QDs are, to the author's knowledge, nonexistent. In order to address this, the current work details initial investigation into the most basic deviation from the spherical geometry, focusing on the *spheroids of revolution* (see figure 5.4 on page 69). At present, only QDs of the prolate spheroid geometry have been considered. In order to facilitate direct comparison with their spherical counterparts, the semi-minor axes, $\boldsymbol{a}$, of the spheroidal QDs are chosen to match the radii of the corresponding spherical dots (i.e. $\boldsymbol{a}$ is chosen to integer multiples of a_{PbSe}), while the semi-major axis, $\boldsymbol{c}$, is expressed in terms of $\boldsymbol{a}$, either as a percentage increase, or in the ratio $\boldsymbol{c}/\boldsymbol{a}$. In the current work, semi-major axes take values between 100%-125% of $\boldsymbol{a}$, corresponding to an "elongation" of 0%-25%, and to ratios $\boldsymbol{c}/\boldsymbol{a}$ of between 1 and 1.25. Focus

is given to QDs where the axis of elongation lies along the $x/\langle\bar{1}\bar{1}2\rangle$ direction. This is done for two reasons. Firstly, the modifications to the single particle energy spectrum for elongations in the longitudinal and transverse directions are phenomenological similar; discussion of elongation of both directions is in some sense redundant. Secondly, the observed symmetry breaking and resultant energy level splitting is only observed where the axis of elongation lies along one of the longitudinal directions. The axis of elongation is referred to as lying along the x-axis in the text, however, this choice is arbitrary: the same result would be observed where the axis of elongation instead lies along the y-axis.

The single-particle states as calculated for bare core PbSe QDs are shown in figure 7.12 for QDs with an elongated axis of 5%, 10%, and 15%. The elongation of the x-axis results in subtle reduction in the sp energy states of the spheroidal QDs. For the QDs shown here, the reduction in the bandedge states is on the order of 10 meV. As is to be expected, the length of the semi-minor axes $\boldsymbol{a}$ affects the energy states in the same manner as did the radius of the spherical dots shown in figure 7.1. Again, states in the conduction band group together into band-like structures. The differences in the energy states is better illustrated by the energy level diagram for a fixed semi-minor axis (30.60 Å) for each elongation (figure 7.13). As can be seen, for the dots presented, elongation by 5%, 10%, and 15% reduces the size-dependent bandgap by ~ 10 meV, ~ 20 meV, and ~ 30 meV, respectfully, versus the corresponding spherical QD.

Once more, the energy states associated with interband transitions have been obtained (figure 7.14). The transition energies follow the same polynomial dependence as before, since the elongated axis is defined as a function of a. The degree of elongation does, however, lower the transition energy between each state by about 10 meV per 5% elongation.

The momentum matrix elements corresponding to the interband energy transitions have been obtained in the usual way. Sample spectra for QDs with $a = 30.60$ Å are shown in figure 7.15. As a consequence of elongation of the

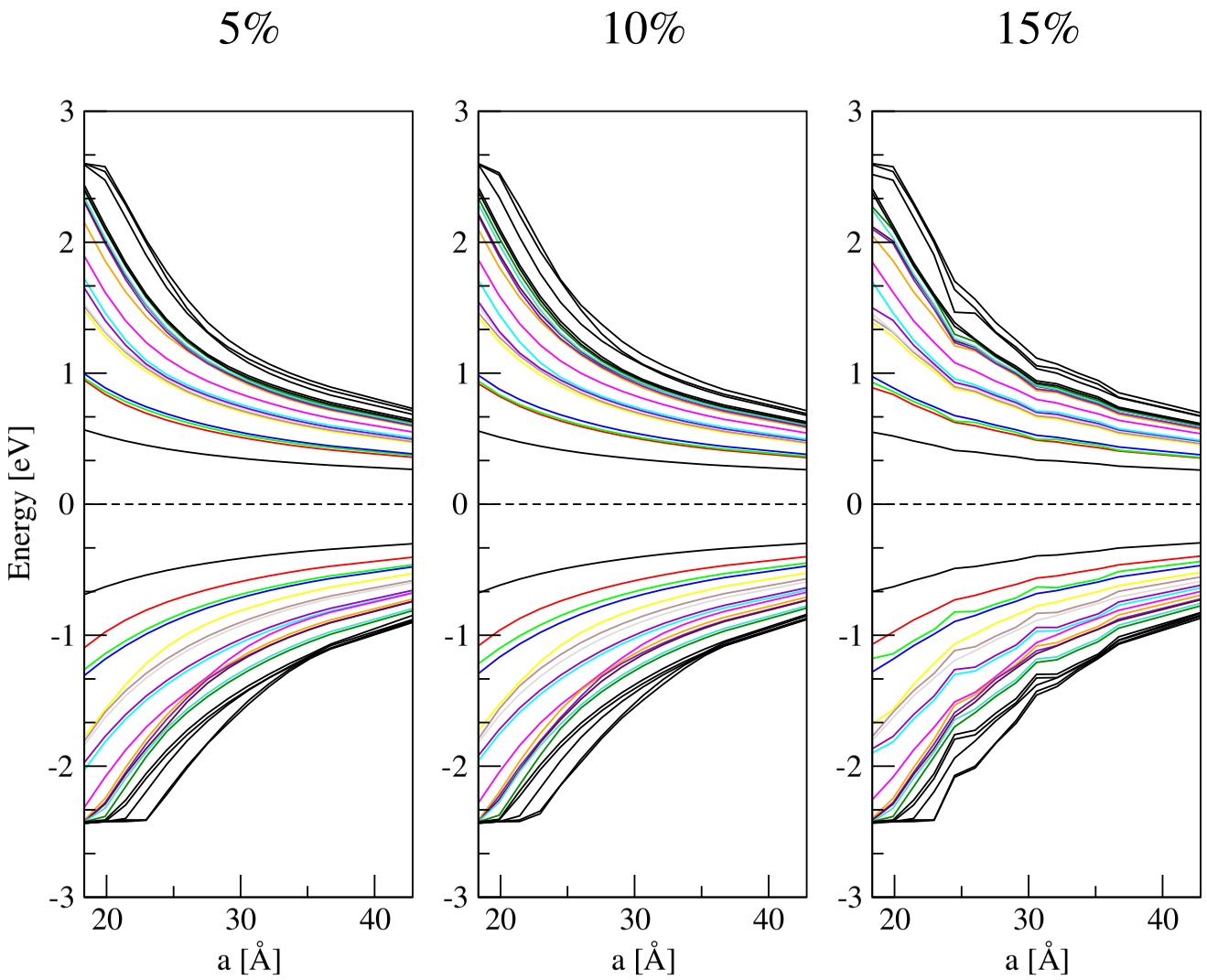

Figure 7.12.: Single-particle states for spheroidal PbSe QDs of varying ellipticity. The *c*-axis is elongated by: a) 5%; b) 10%; and c) 15% of the *a*-axis

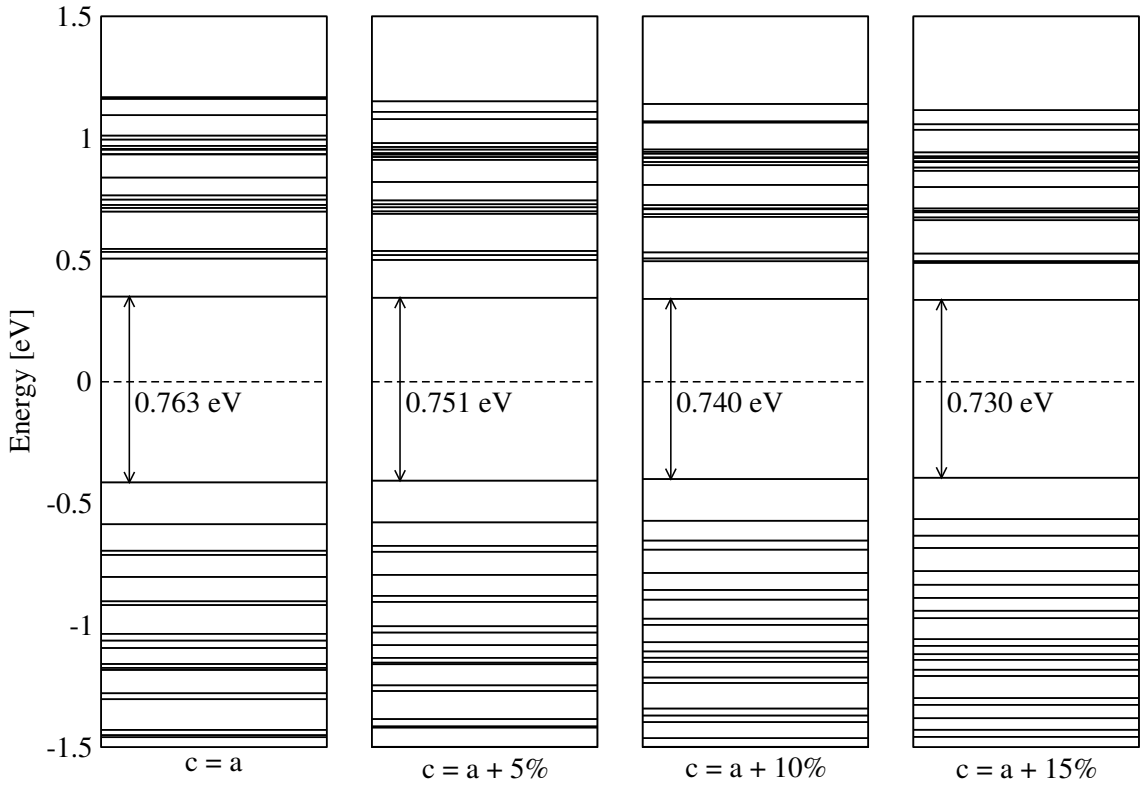

Figure 7.13.: Energy states of spheroidal QDs with semi-minor axis $a = 30.60\,\text{Å}$. For the dots presented, each successive elongation of 5% reduces the effective bandgap on the order of 10 meV.

x-axis, and the resultant symmetry breaking, the x-polarised and y-polarised interband momentum matrix elements are no longer isotropic. The anisotropy, shown in figure 7.16 for QDs of differing semi-minor axes, a, and shell thicknesses, is small, being of the order of about 1%. As such, the anisotropy is greater for smaller nanocrystals (having larger momentum matrix elements). The x/y (transverse-transverse) anisotropy may be characterised in a similar manner as was the x/z (l-t) anisotropy above, that is by

$$A_p^{\text{x-y}} = \left| \frac{|p_x|^2 - |p_y|^2}{|p_x|^2 + |p_y|^2} \right|. \tag{7.2}$$

As one would expect, the degree of anisotropy between the transverse polarisations increases as the dot deviates further from spherical symmetry. The anisotropy in on the order of 1%, with a maximum value of 11% for the most extreme value studied here ($a = 18.34\,\text{Å}$, $c/a = 1.25$, core-only). As a consequence

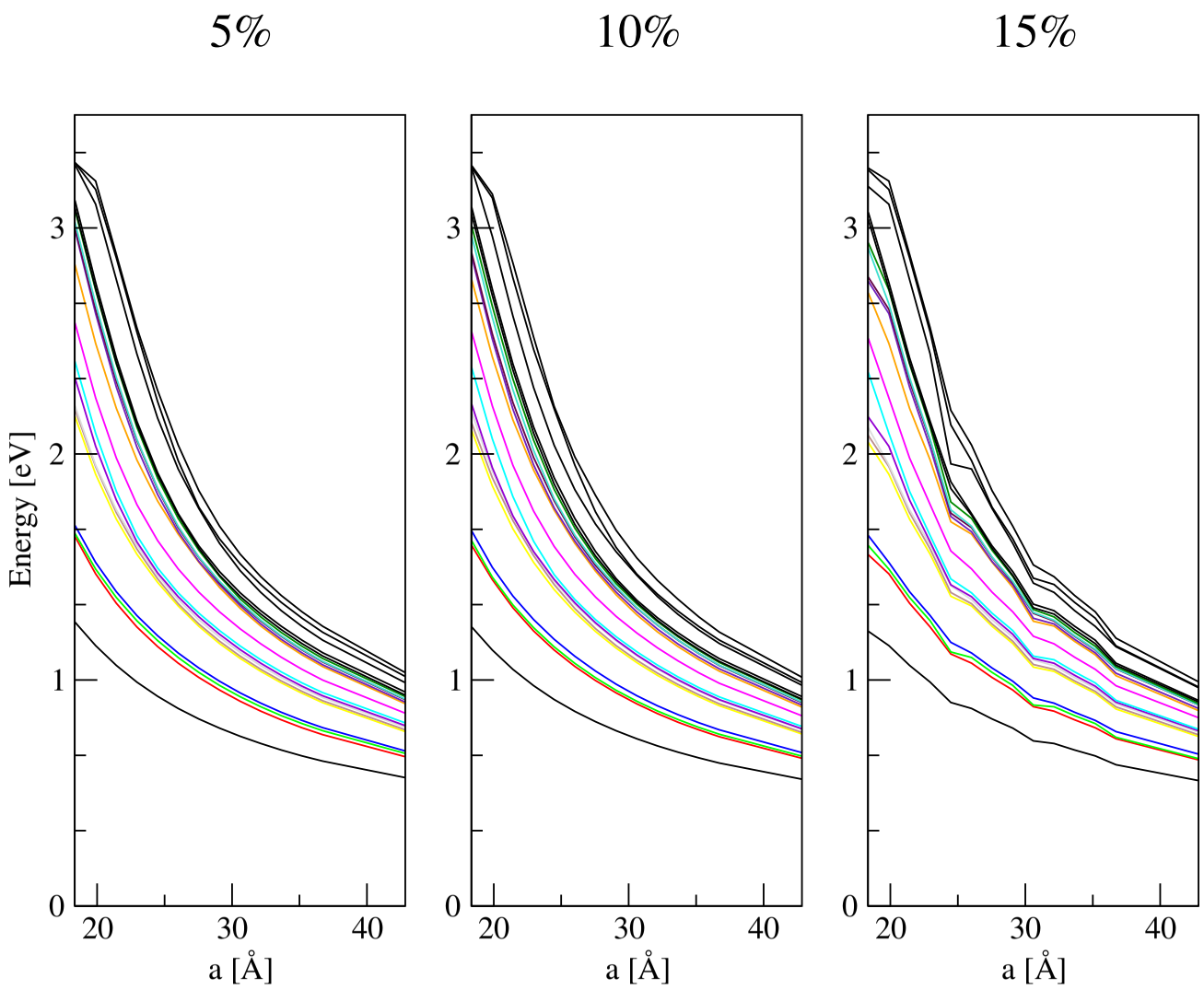

Figure 7.14.: $e_n - h_0$ transition for core QDs of increasing size. The c-axis is elongated by: a) 5%; b) 10%; and c) 15% of the a-axis

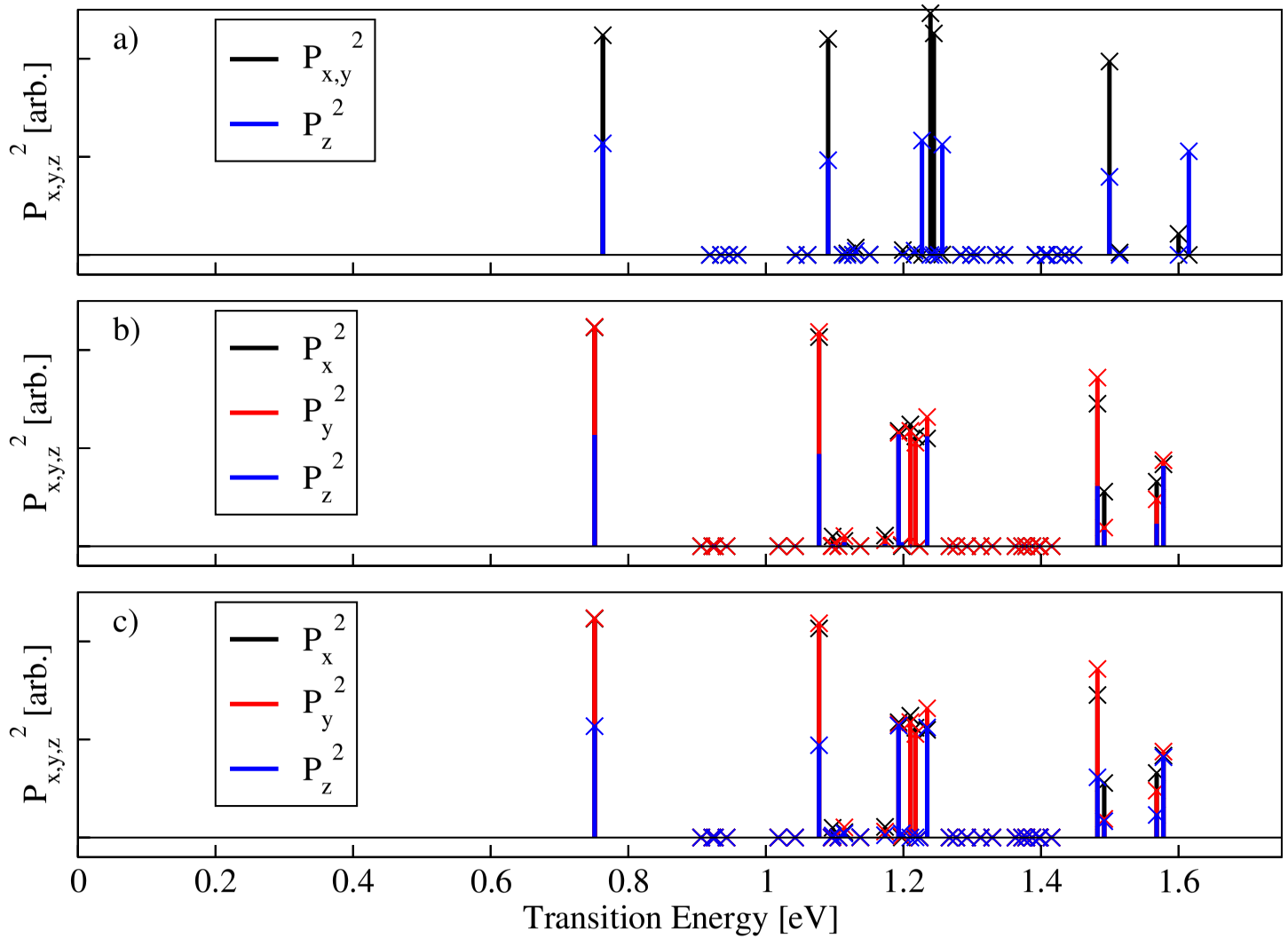

Figure 7.15.: First few optically bright interband momentum matrix elements for PbSe QDs with $a = 30.60\,\text{Å}$ and a) $c = a$, b) $c = a + 5\%$, and c) $c = a + 10\%$. Symmetry breaking results in anisotropy between the x and y-polarised momentum matrix elements in addition to the pre-existing x/z and y/z anisotropy.

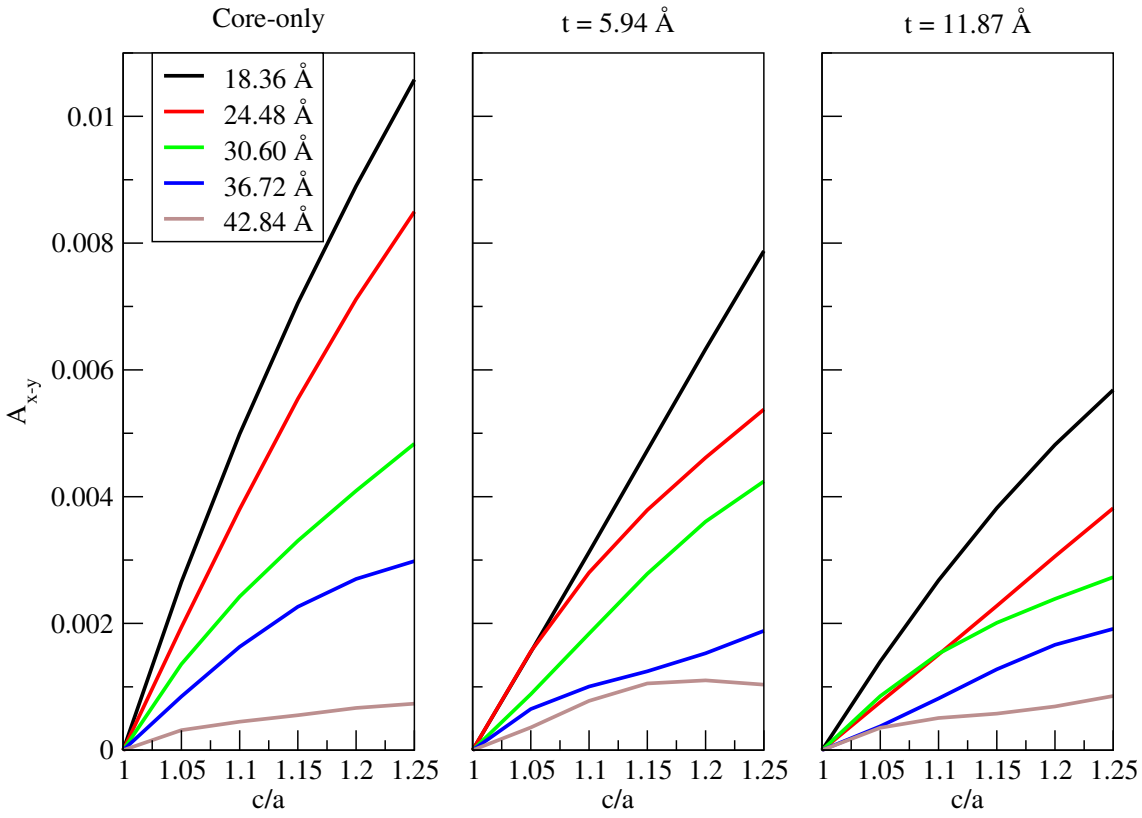

Figure 7.16.: Anisotropy between x-polarised and y-polarised momentum matrix elements for QDs elongated along the x ($\langle \bar{1}\bar{1}2 \rangle$) direction. QDs with no shell (left), shell of one lattice constant (centre), and shell of two lattice constants (right) are shown. The anisotropy is on the order of 1%, being increased for larger ellipticity, and for QDs of smaller volume.

of the diminished magnitude of the momentum matrix elements, addition of the PbS shell results in a reduction to the degree of anisotropy between the elements polarised in the x and y directions.

Further modification may be applied to the spheroidal PbSe QDs through the addition of a PbS shell region. The bandedge states for QDs with c/a = 1.05, 1.10, and 1.15 are shown in figure 7.17 for QDs of varying a as the thickness of the shell is increased. The profile of the energy states matches that of the spherical PbSe/PbS structures, except with slight reduction due to the elongation.

In summary, the overall effect of elongation is two-fold. In the first instance, elongation along either longitudinal or transverse axes results in a modest reduction in the energy levels of the QD as compared to the equivalent spherical dot with $R = a$. The variation, illustrated in figure 7.19 for bandedge states for a series of QDs, is linear with the degree of elongation. This is a direct consequence of the quantum size effect. The variation is linear since the volume of the spheroidal QD is proportional to a^2c—an increase in c leads to a linear increase in volume, and a corresponding linear reduction in the magnitude of the energy states. Similarly, where the length of the c-axis is taken to be a function of a, as in the current work, an increase in a leads to polynomic variation in the energy levels, plus the linear shift due to elongation (c.f. variation of energy states when the radius of a spherical QD is increased). The second effect of elongation is the induced anisotropy between the x and y-polarised interband transition matrix elements. This effect is subtle, being only on the order of 1%. This is, to the authors knowledge, the first time such anisotropy has been reported for PbX NQDs.

7.2 EXCITONIC PROPERTIES

The single-particle properties as calculated via the $\mathbf{k} \cdot \mathbf{p}$ method represent the first step in modelling the electronic structure of the nanocrystal quantum dots.

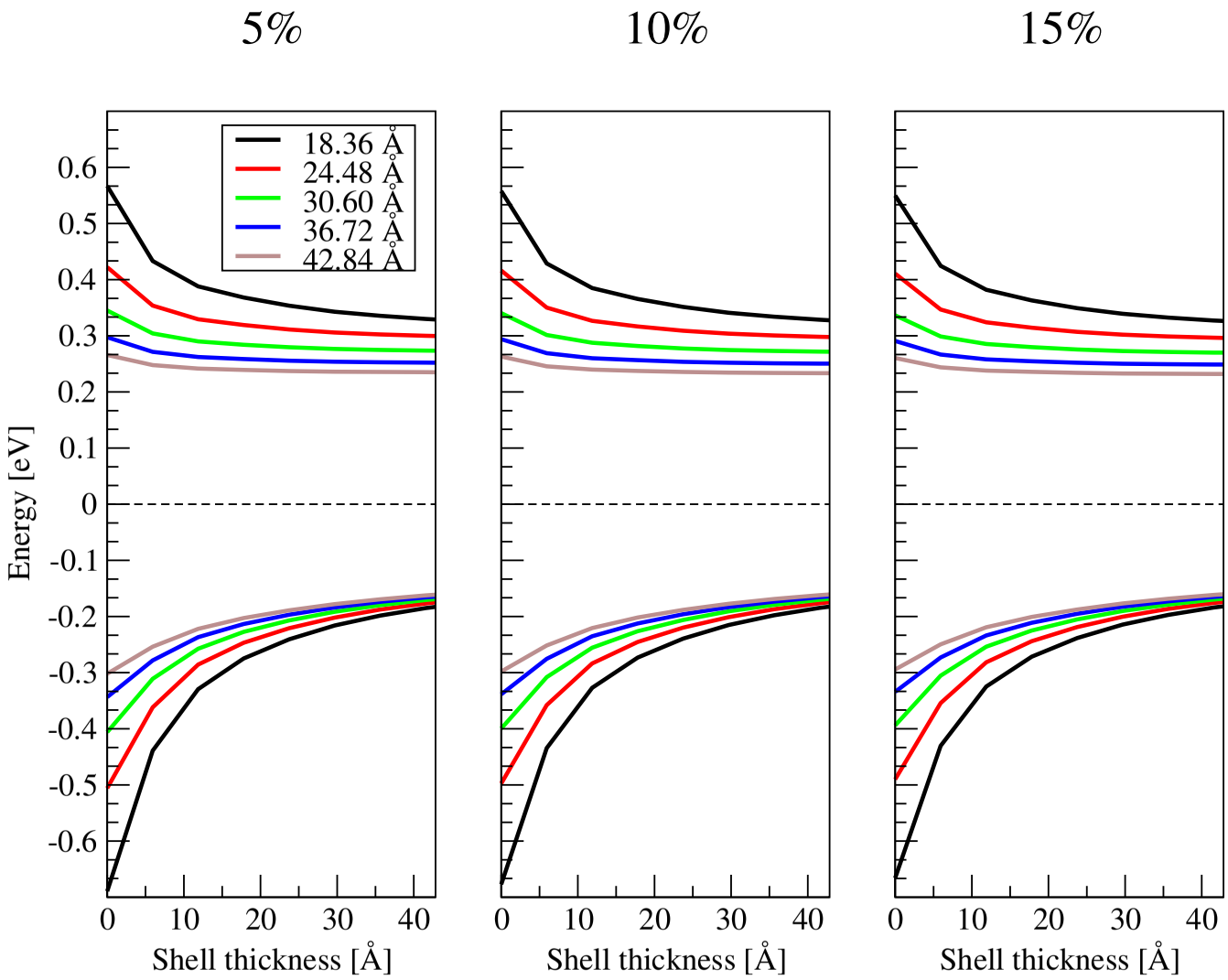

Figure 7.17.: Band-edge energy states for QDs as a function of shell thickness. The *c*-axis is elongated by: a) 5%; b) 10%; and c) 15% of the *a*-axis

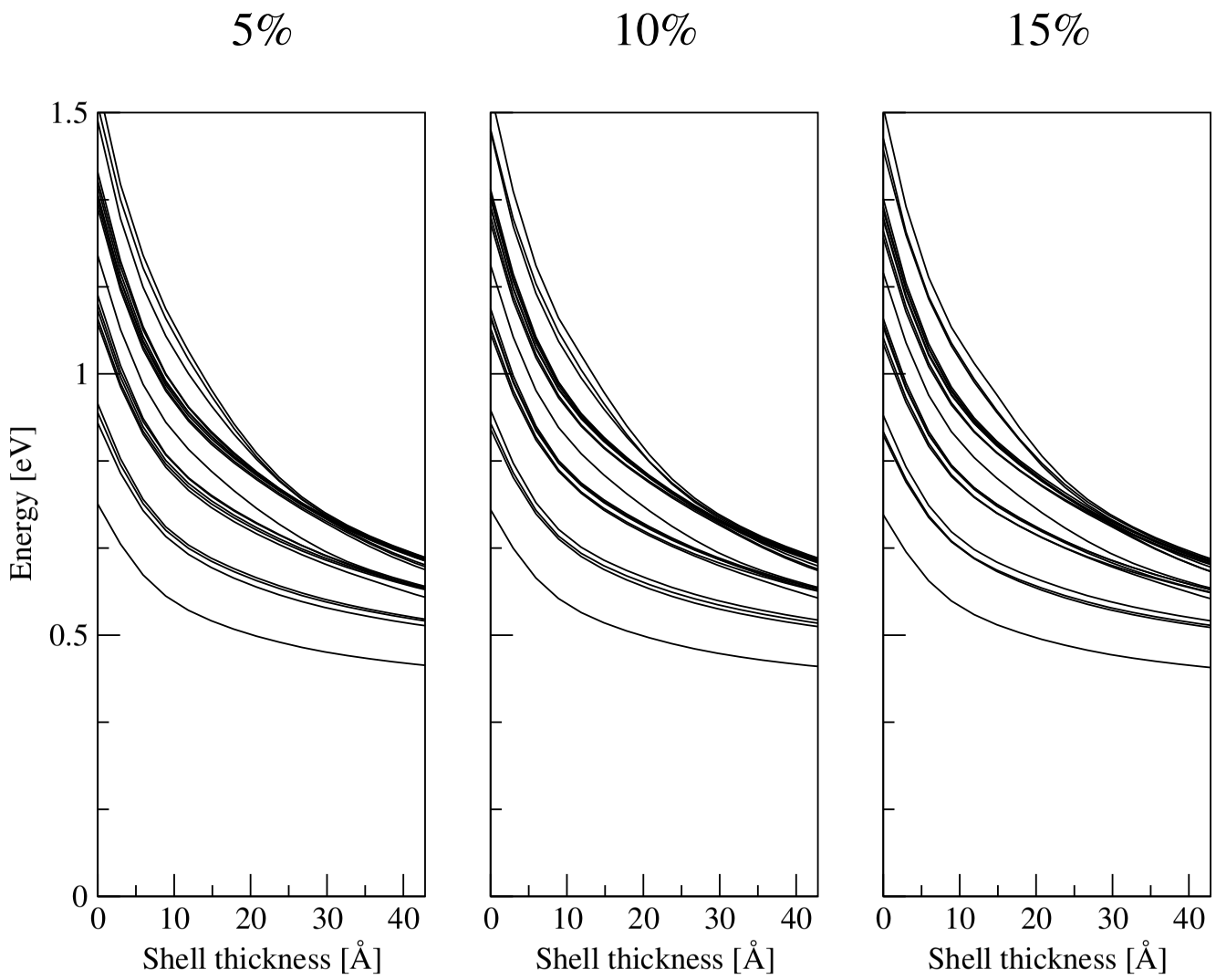

Figure 7.18.: $e_n - h_0$ transitions for spheroidal QDs with a =30.60 Å. The c-axis is elongated by: a) 5%; b) 10%; and c) 15% of the a-axis

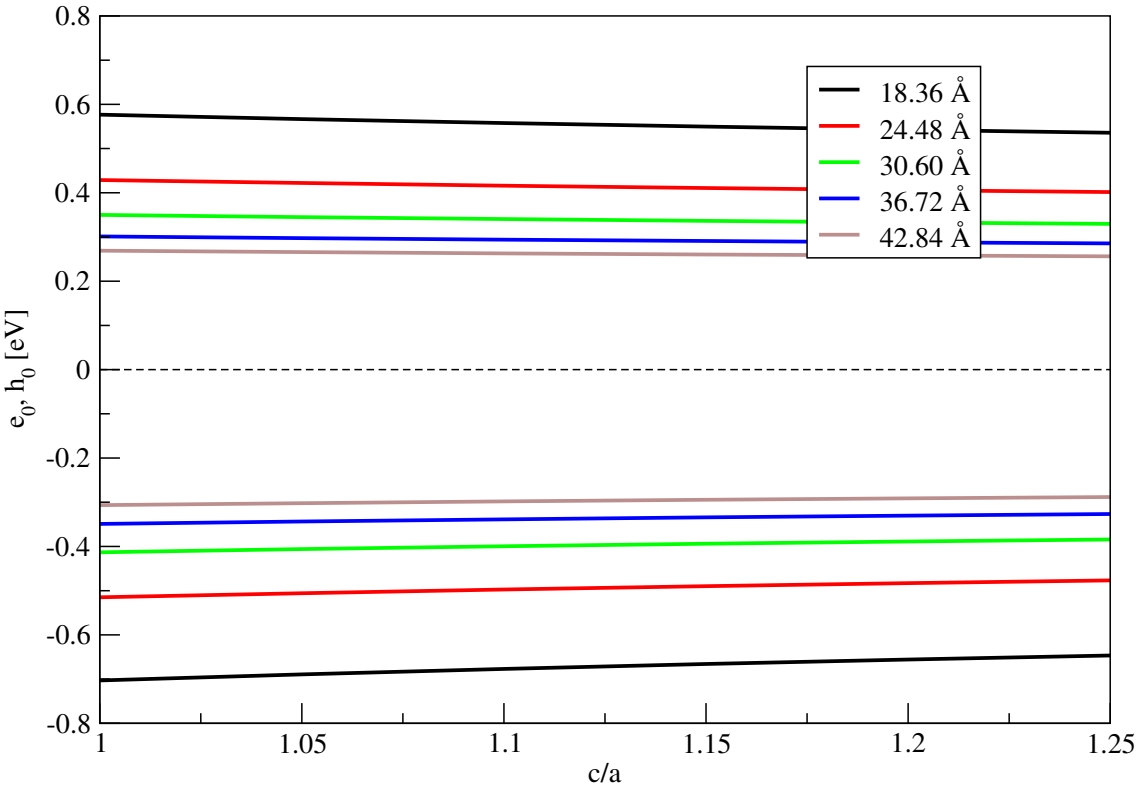

Figure 7.19.: Linear variation of the HOMO and LUMO states as a function of the ratio of the axes of the spheroid. The variation is larger for smaller QDs.

While the single-particle picture provides the major contribution to theoretical description of the QDs, the $\mathbf{k} \cdot \mathbf{p}$ calculation is only a first approximation, where much important physics is neglected. In reality, each of the charge carriers in the nanocrystal is in contact with every other charge carrier via electrostatic interaction. This interaction is accounted for via the Coulomb integrals between states. By taking Coulomb integrals between each configuration of sp states, it is possible to add many-particle corrections to the energy states predicted by $\mathbf{k} \cdot \mathbf{p}$ via state mixing. This is the configuration interaction method discussed in section 6.4. Given a complete and orthonormal set of basis functions, the CI approach is, in principle, an exact method. Such calculations are, of course, intractable, and so a subset of single-particle states must be chosen. The current work uses a truncated basis comprised of 12 electron and 12 hole states. This choice of basis provides good compromise between speed and accuracy. As

discussed above, only those terms which conserve the number of particles in the Fock spaces are included.

7.2.1 *Excitonic states of PbSe core-only NQDs*

The single-particle states calculated via the $\mathbf{k} \cdot \mathbf{p}$ method for spherical PbSe core-only QDs have been mixed using the CI approach to yield excitonic corrections. Since all configurations of 12 electron and 12 hole states have been included in the calculation, the number of exciton states is far greater than the number of single-particle states. Further, since the exciton is a composite quasiparticle comprised of one electron and one hole, the most intuitive comparison between single-particle and excitonic energy spectra is found by considering the transition energy spectra between single-particle states (figure 7.3). The excitonic energy spectrum for the same series of spherical QDs as in chapter 7.1.1 is shown in figure 7.20. The exciton states, being based on the sp states, form into the familiar "band-like" structures seen in the sp-energy levels. Comparing figures 7.20 and 7.3, a strong degree of excitonic binding energy emerges. Since it is difficult to relate an exciton state to a particular sp transition, The only comparison to be made reliably is between the lowest energy exciton state and the HOMO-LUMO sp transition. The binding energy for the X_0 state may be seen along the y-axis in figure 7.26. It is found that the binding energy is greater for smaller dots. For example, the PbSe QD of radius 18.36 Å has an excitonic binding energy (B_X) of 158 meV, while the QD of radius 42.84 Å has a binding energy of $B_X = 67$ meV. This is a consequence of the stronger Coulomb matrix elements between states found in smaller NQDs: as the QD is made larger, the charge carriers separate, and the Coulomb interaction, being inversely proportional to the separation of the carriers $|\boldsymbol{r}_1 - \boldsymbol{r}_2|$, is reduced. For thick shells, the confinement of valence band charge carriers the shell region further reduces the magnitude of the Coulomb matrix elements, and therefore the excitonic binding energy.

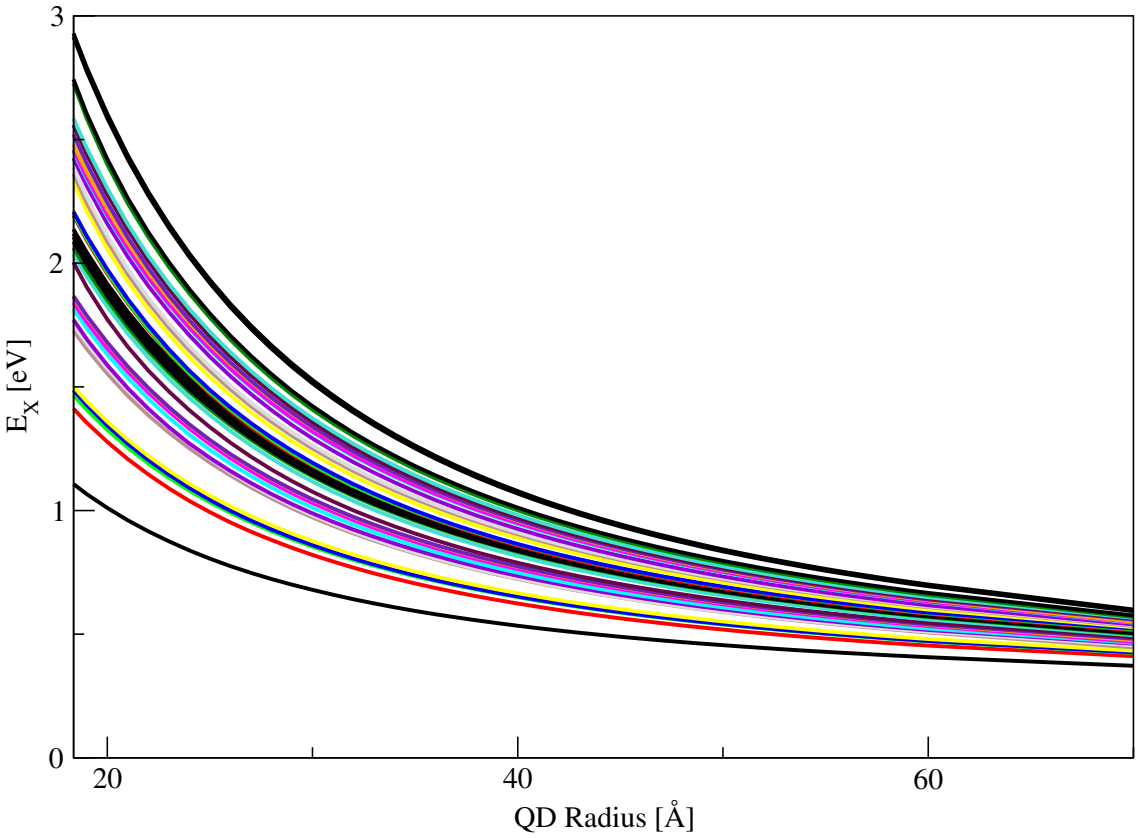

Figure 7.20.: Excitonic energies have been generated via mixing of 12 electron and 12 hole sp states. The energies presented have been averaged over the energy complex in which they are found.

The momentum matrix elements for spherical QDs of radius 18.36 Å, 24.48 Å, and 30.60 Å are shown in figure 7.21. It can be seen that the nonzero x/y-polarised and z-polarised momentum matrix elements no longer occur at coincident energy states. Instead, the different elements occur in energy complexes, being either nonzero for the equivalent x and *polarisation*, or nonzero for the z-polarised transitions, but never simultaneously nonzero for both. Further, as a consequence of the excitonic binding, the magnitude of the matrix elements is approximately doubled versus the single-particle case.

7.2.2 *Excitonic states of PbSe/PbS Quantum Dot Heterostructures*

CI calculations have been performed for core/shell heterostructures for QDs with core radii equal to the radii of the dots above. The lowest exciton energy complex is shown for QDs with core radii between 18.36 Å and 42.84 Å as successively thicker shells are added is shown in figure 7.22. The bandedge states follow the same profile as do the sp states. The full excitonic spectrum as constructed for 12 electron and 12 hole states is shown in figure 7.23 for a spherical QD of core radius 30.60 Å with increasing shell thickness. Comparison with the sp spectrum of figure 7.6 indicates strong excitonic binding for all energy states. Further, the excitonic states for a quasi-continuum for shell thicknesses of only a few lattice constants, except for the lowest exciton state. Similar trends, shown in figure 7.24, are observed for all QDs considered here.

The momentum matrix elements associated with the exciton states have been calculated. A sample spectrum is shown in figure 7.25 for core/shell QDs of core radius 30.60 Å with shell thicknesses of 0 Å, 5.94 Å, and 11.87 Å.

Strong, size-dependent excitonic binding energy has been observed for QDs of all core radii and shell thicknesses considered (see figure 7.26). The binding energy is on the order of 100 meV for the smallest core radii considered (R =

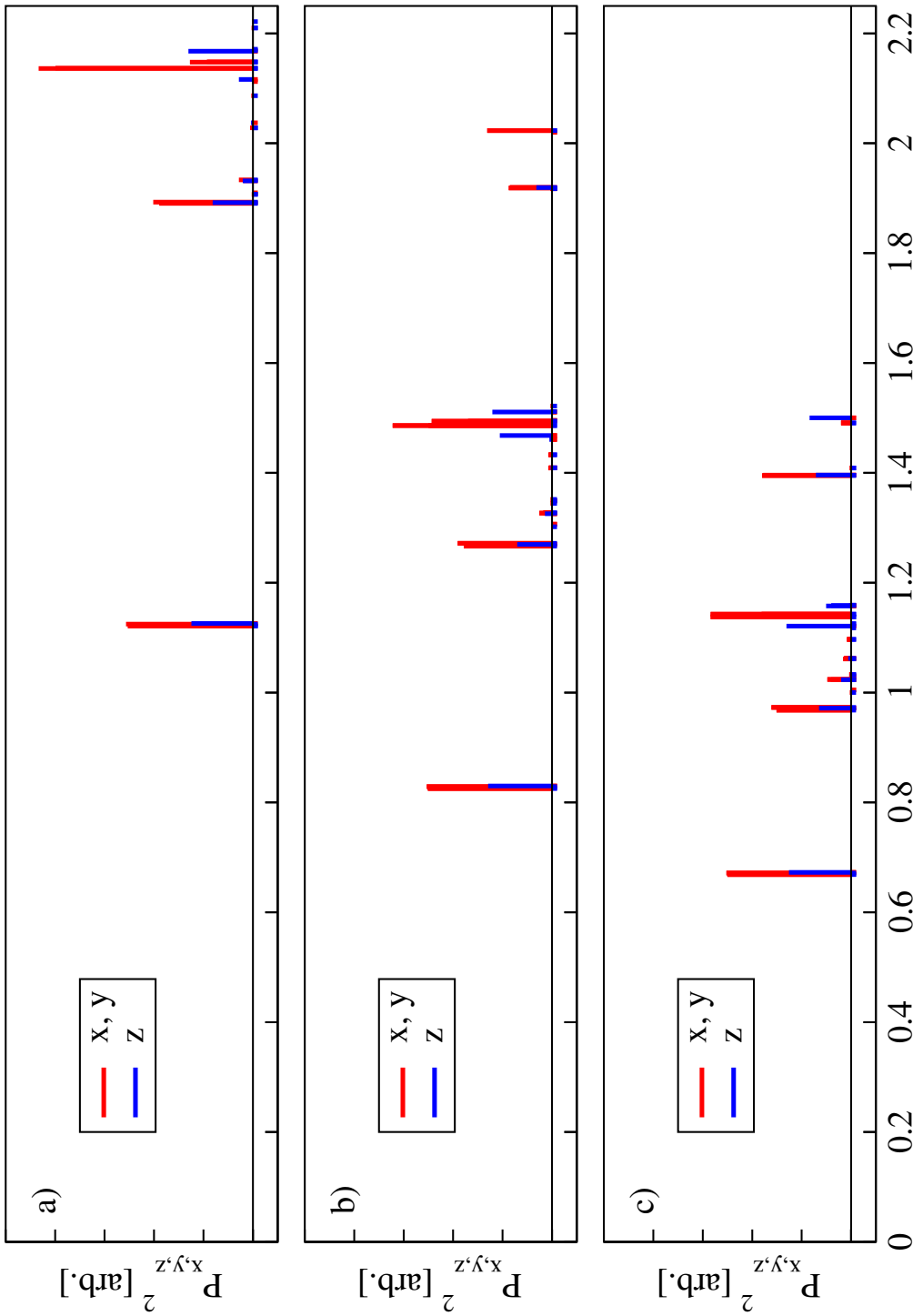

Figure 7.21.: Momentum matrix elements associated with excitonic states for PbSe QDs of radius a) 18.36 Å, b) 24.48 Å, and c) 30.60 Å. Matrix elements are split across energy complexes, while magnitude of the elements is twice as large as in the single-particle case.

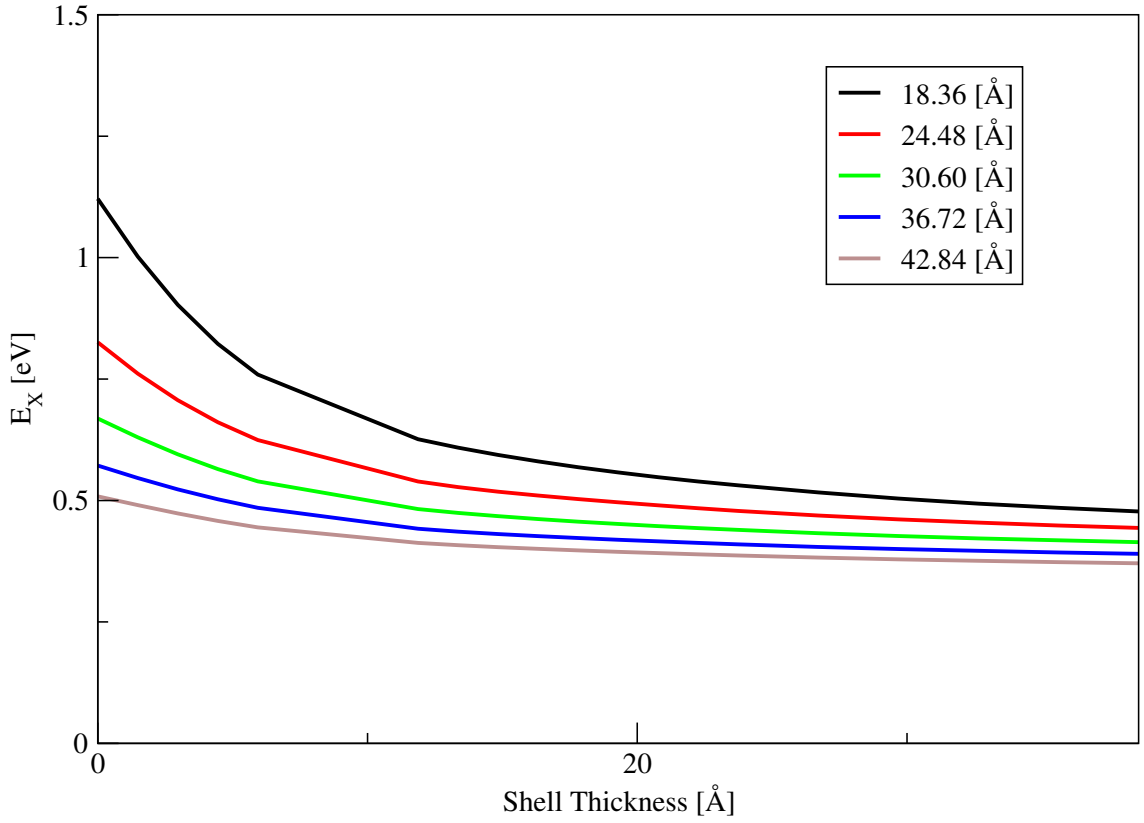

Figure 7.22.: Lowest energy exciton state for QDs of varying core radii as a function of shell thickness.

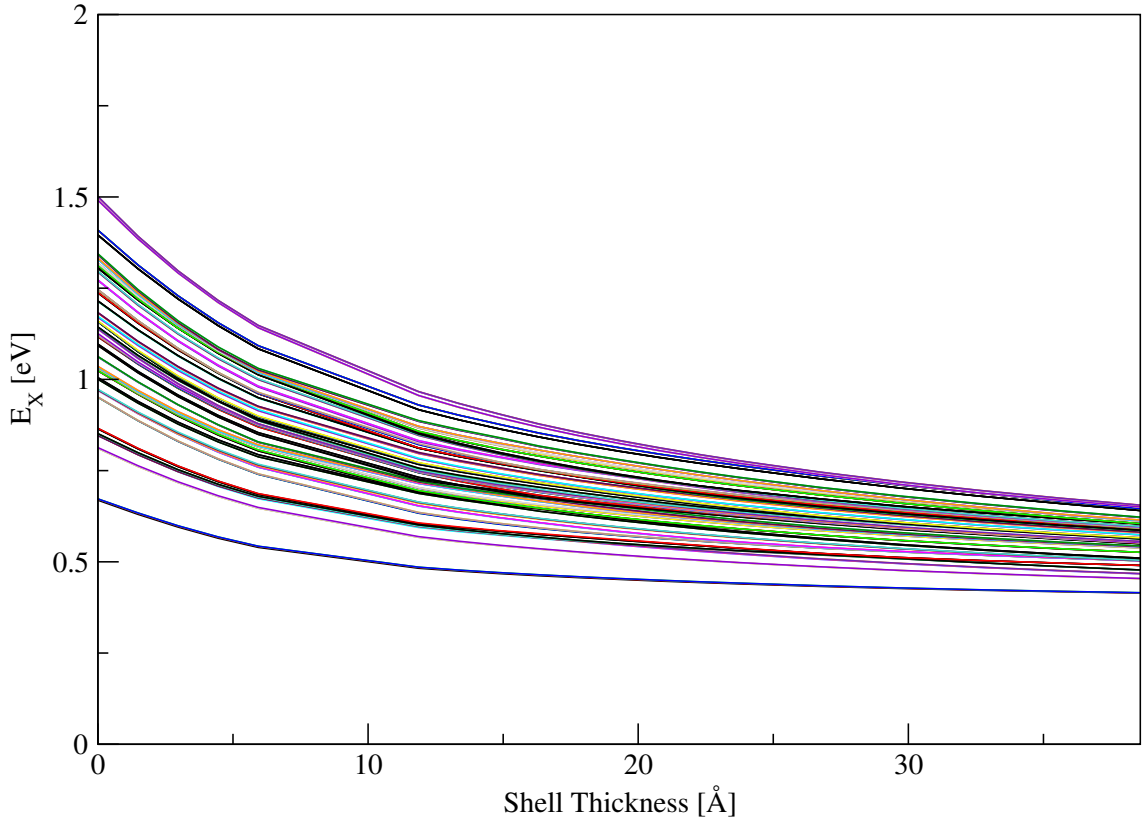

Figure 7.23.: Excitonic energy spectra for core/shell PbSe QD heterostructures with core radius 30.60 Å with increasing shell thickness.

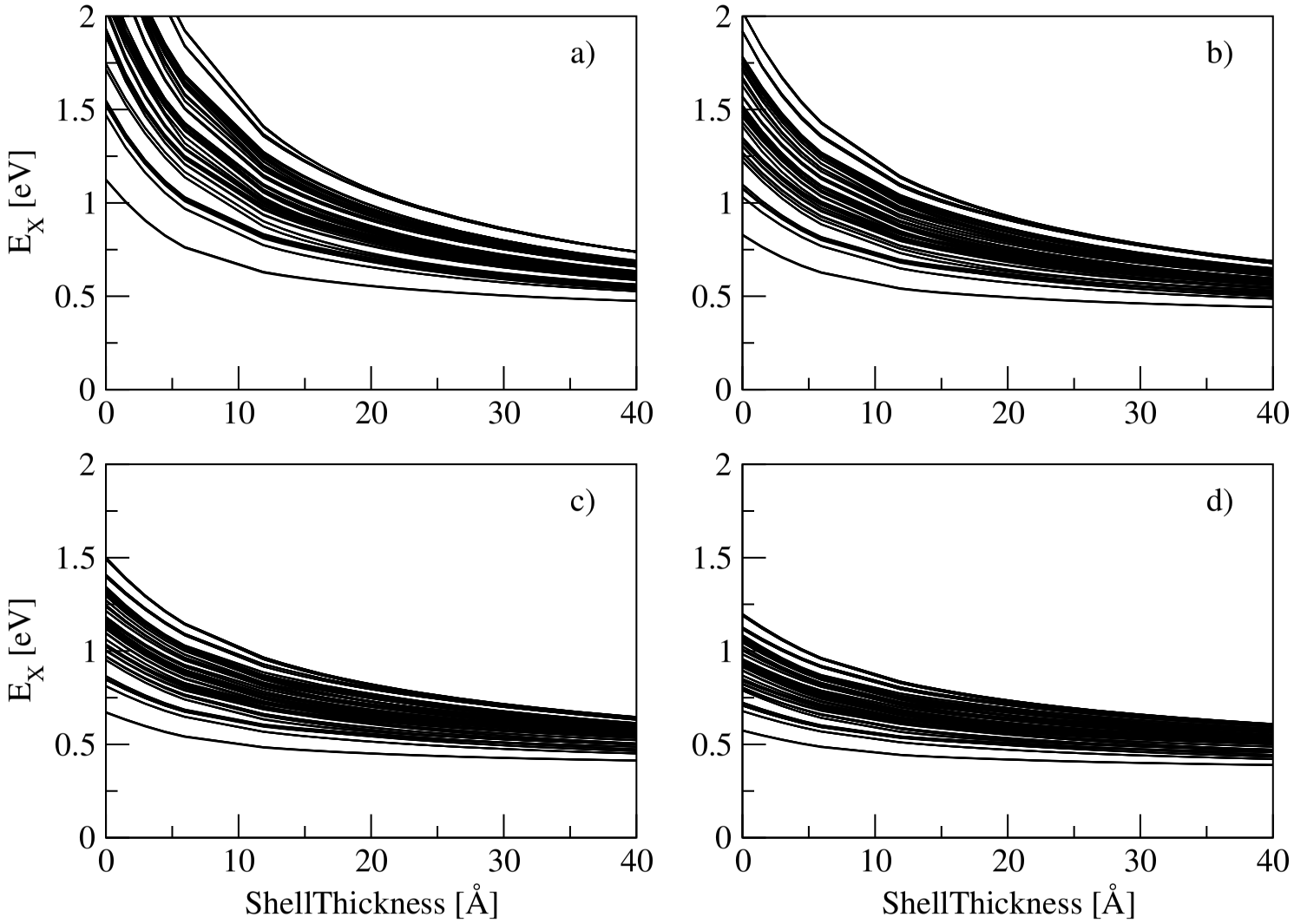

Figure 7.24.: The full spectrum of excitonic states generated by mixing of 12 electron and 12 hole single-particle states as a function of shell thickness for QDs of core radii: a) 18.36 Å; b) 24.48 Å; c) 30.60 Å; and d) 36.72 Å.

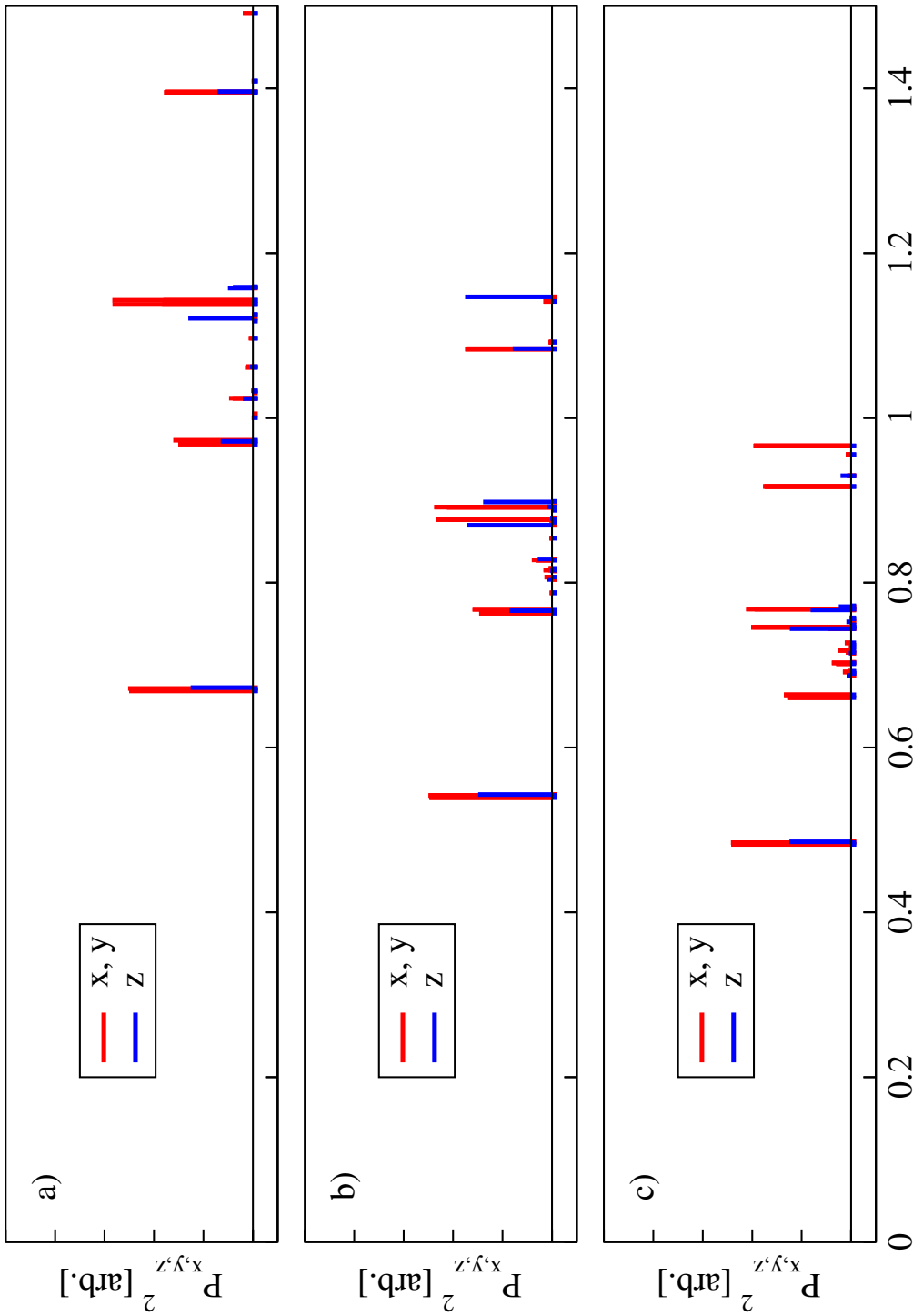

Figure 7.25.: First few momentum matrix elements for QDs of core radius 30.60 and a) no shell, b) 5.94 Å, and c) 11.87 Å. Addition of the PbS shell reduces the energy associated with the momentum matrix elements. The magnitude of the elements is moderately reduced for thicker shells.

18.36 Å), reducing to 67 meV for the largest (42.84 Å). The addition of the PbS shell reduces the binding energy to between 30 meV-40 meV for large shells.

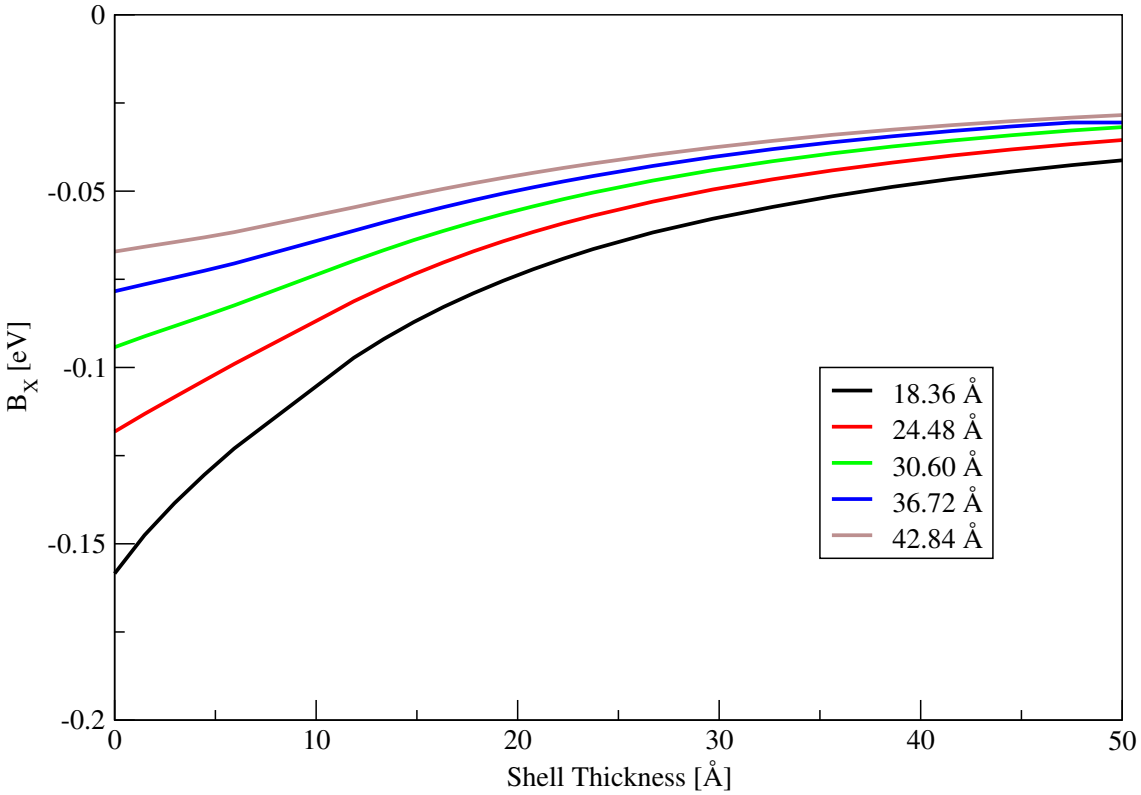

Figure 7.26.: Binding energy B_X for the lowest energy exciton for spherical QDs of varying core radius and shell thickness. The binding energy is greater for smaller dots and thinner shells.

7.2.3 *Excitonic States of Spheroidal PbSe/PbS Quantum Dot Heterostructures*

Excitonic corrections to the single-particle states of spheroidal PbSe/PbS NQDS have been derived by the same mechanism as before. The excitonic energy spectrum for QDs of semi-minor axes 30.60 Å are shown for elongations of 5%, 10%, and 15% in figure 7.27 as a function of shell thickness. Each successive elongation of 5% reduces the exciton energy on the order of a few meV.

The momentum matrix elements associated with the excitonic states of the spheroidal dots are shown in for core-only QDs (a = 30.60 Å) in figure 7.28. As before, elongation of the major-axis of the spheroid results in symmetry breaking between the transverse (x and y) axes, and anisotropy between the x and y-

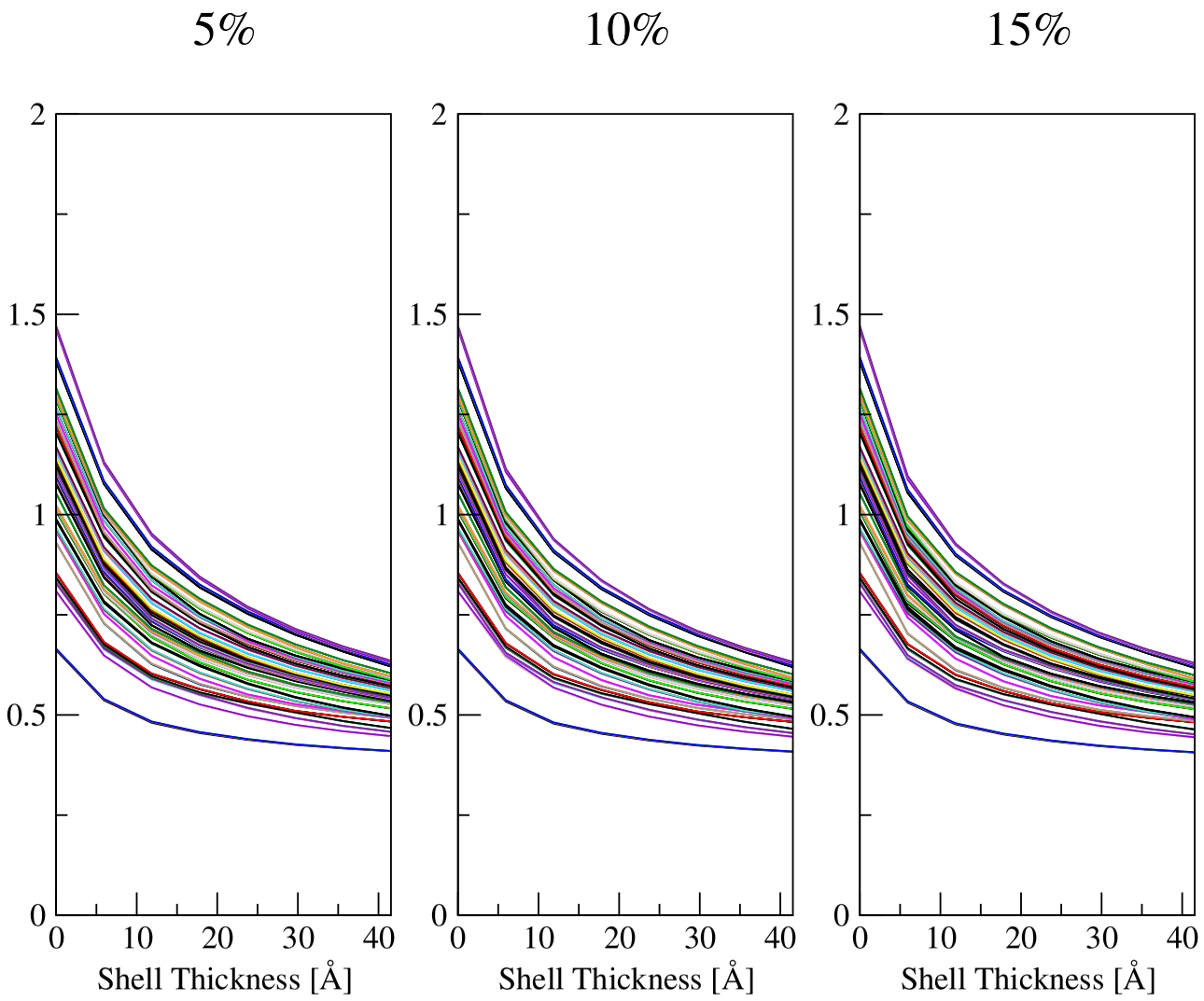

Figure 7.27.: Excitonic energy spectrum for QDs with $a = 30.60\,\text{Å}$ for increasing shell thickness. QDs are elongated by a) 5%, b) 10%, and c) 15%. Elongation of a single axis leads to reduction in the energy spectrum on the order of tens of millielectronvolts.

polarised momentum matrix elements is introduced as a result. The degree of anisotropy is similar as for the single-particle case.

7.3 RADIATIVE CARRIER LIFETIMES

The lifetime for radiative transitions have been calculated for QDs detailed above using the methodology outlined in chapter 6.5.2. The total momentum matrix elements $\boldsymbol{p}^2_{i\to f}$ required for the calculation of the rate of carrier transfer may be constructed from either the elements associate with the single-particle states from the $\mathbf{k}\cdot\mathbf{p}$ calculation or from those associate with the excitonic states originating from the CI calculation.

The lifetimes for radiative recombination between the states e_0 and h_0 in the single-particle picture are shown for several QD radii with increasing shell thickness in figure 7.29 for elongation by up to 15%. The most immediate point of note is that the radiative lifetimes for all dots shown is between 57 ns and 1080 ns. This value is extremely large even when compared to QDs of other material systems; for example, the lifetimes for radiative transitions in CdX QDs is on the order of 10 ns [185, 186]. The calculated carrier lifetimes for the PbSe core-only and PbSe/PbS core/shell quantum dots are on the order of 0.1 µs—a range which is consistent with the literature [187]. The carrier lifetime, ultimately being determined by the size-dependent energy gap and by the momentum matrix elements between the HOMO and the LUMO states, is size-dependent, varying from 62 ns for the PbSe QD of radius 18.36 Å to 248 ns for the core-only QD of radius 42.84 Å.

The lifetimes further increase in an almost linear fashion as the thickness of the PbS shell is increased for the QDs presented. As the QD radius approaches the limit of confinement the rate of change of the carrier lifetimes begins to level off (this is true for large core-only and core/shell QDs). The effect is better exemplified for the radiative carrier lifetimes of excitonic states, shown in fig-

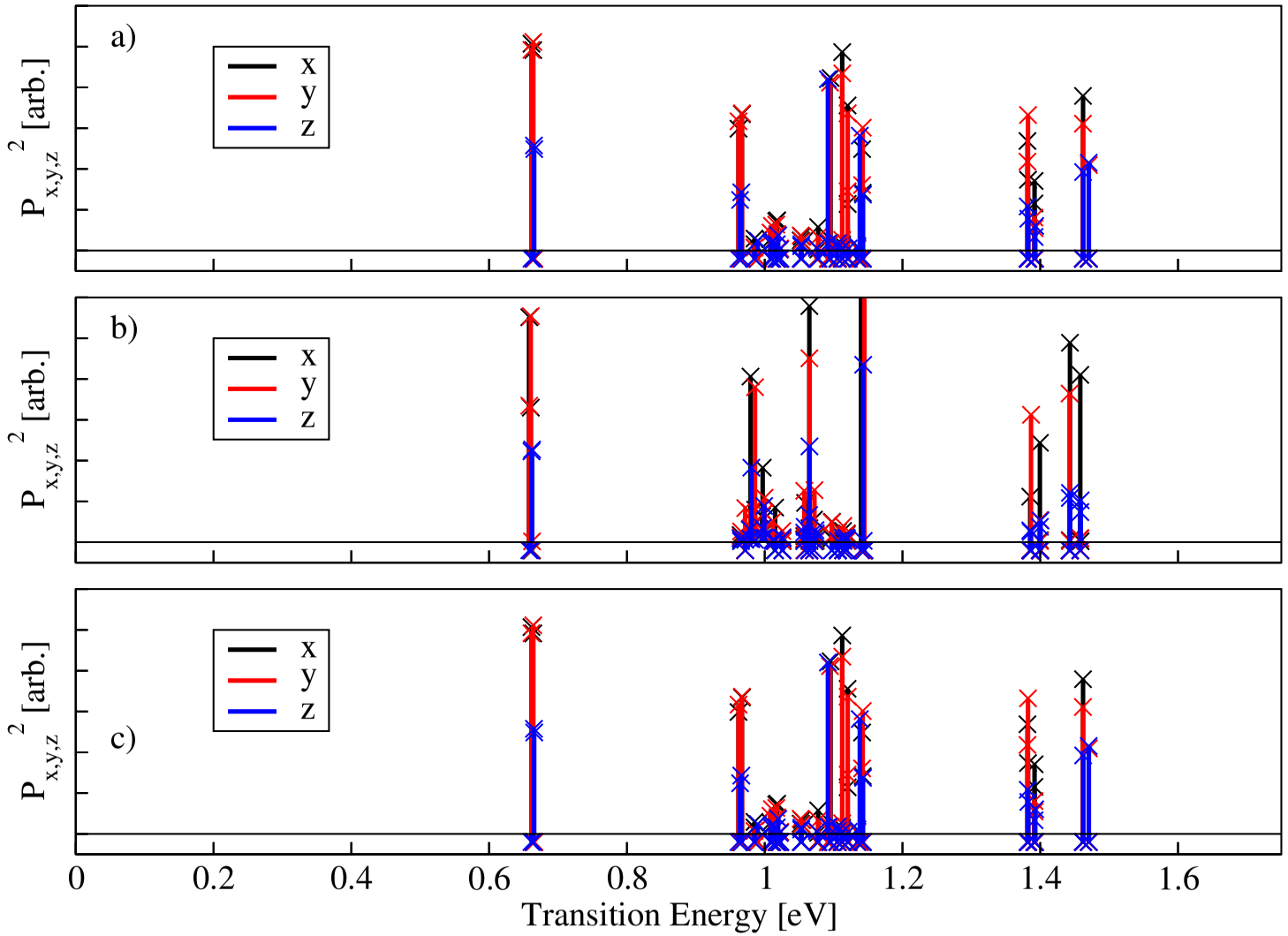

Figure 7.28.: Momentum matrix elements of core-only, $a = 30.60$ Å QDs with elongation a) 5%, b) 10%, and c) 15%. Increasing ellipticity of the dot increases the transverse-transverse anisotropy for all exciton states.

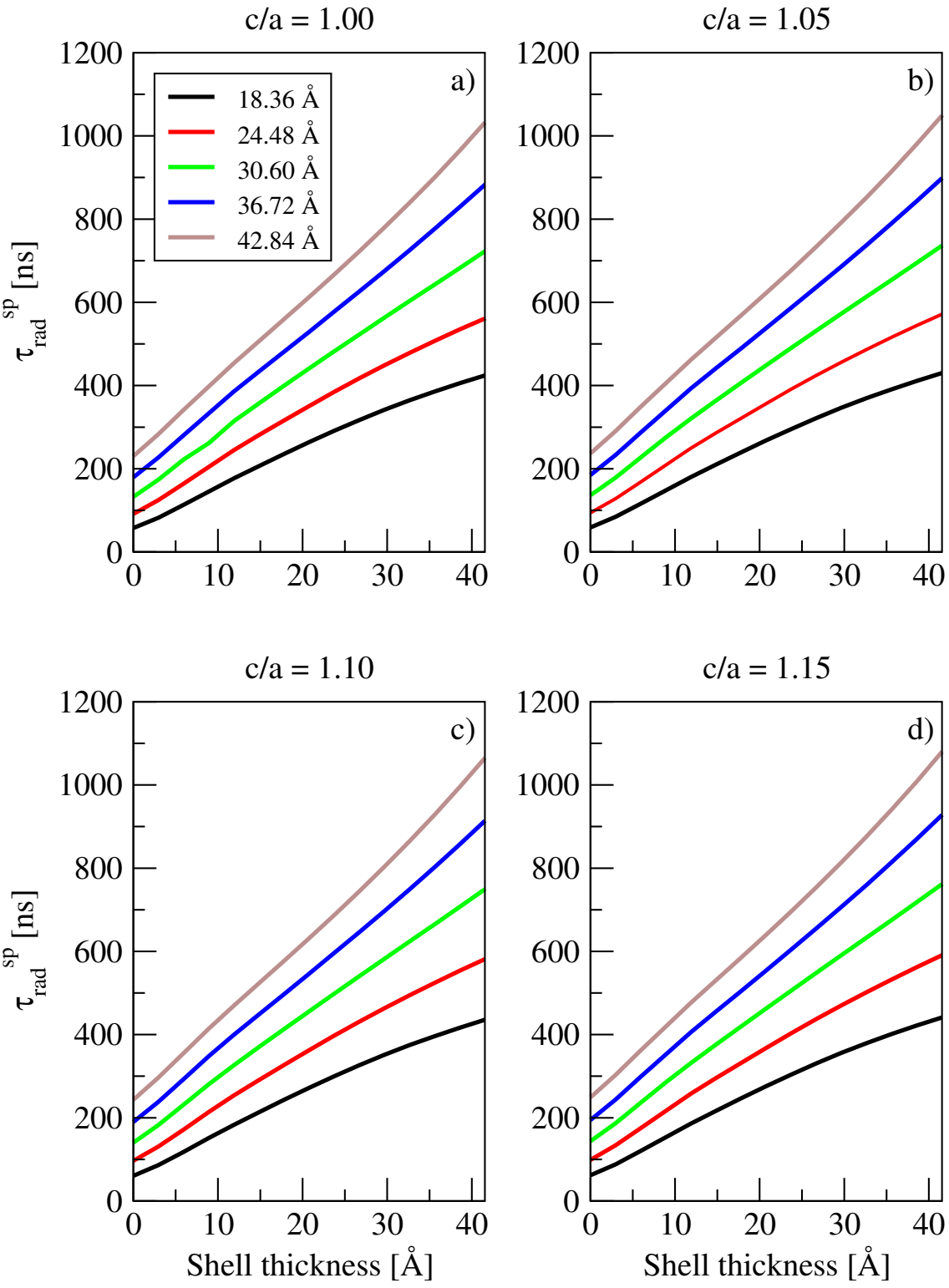

Figure 7.29.: Lifetimes for radiative recombination between bandedge states for several core sizes as a function of shell thickness. The QDs are elongated by a) 0%, b) 5%, c) 10%, and d), 15%.

ure 7.30 below. This levelling off is due to the fact that the energy states vary more rapidly between small QD of different size. Elongation of the QD, shown in figure 7.29 for QDs elongated be 5%, 10%, and 15%, causes a modest lengthening of the radiative lifetimes, largely due to the increased volume of the dot. For each subsequent elongation, the carrier lifetimes for the core-only dots are increased on the order of 5 ns, while the lifetimes for core/shell systems with the larger shells are extended by 5 ns-15 ns.

The radiative lifetimes associated with the lowest energy excitonic states are shown in figure 7.30. The lifetime of excitonic states is, for the core-only PbSe QDs, comparable to those of the single-particle states. Contrary to expectation, the differences between the radiative lifetimes of the single-particle and excitonic states are greater for larger quantum dots than for smaller dots. This is due to the dielectric screening found in the nanocrystals. The current work uses a modified Penn model to account for dielectric screening, which becomes more significant for larger QDs, being proportional to the square of the size-dependent bandgap (see equations 6.110-6.112 in chapter 6.5.2). The carrier lifetime is thus not only directly dependent on the size of the HOMO-LUMO gap, and indeed the excitonic binding energy, but also on the dielectric screening factor, F. The increasing difference between the carrier lifetime from single-particle and excitonic considerations is therefore increased for larger QDs.

The addition of the shell further serves to increase the radiative lifetimes of the exciton states. Due to carrier confinement effects, the momentum matrix elements associated with the exciton states are diminished more rapidly than for increased core radius only. Again, the dielectric screening term further augments the radiative carrier lifetime for the reasons discussed above. The volume increase caused by elongation of the dots results in increased radiative lifetimes, however, interestingly, the strength of the momentum matrix elements appear to overshadow the quantum size effect for the core-only QDs studied. As a result, the radiative lifetimes for the core-only QDs are approximately consistent. For

larger QDs, the quantum size effect dominates, resulting in longer lifetimes for radiative recombination.

7.4 MULTIPLE EXCITON GENERATION

The form of the matrix elements for multiple exciton generation is given in equation 6.126 on page 108. The matrix elements, built from the single-particle energy states obtained via the $\mathbf{k} \cdot \mathbf{p}$ calculation, are comprised of two band-edge electron states and one band-edge hole state, as well a further high-energy electron state. The calculation of this high-energy electron state and the subsequent construction and evaluation of the matrix elements associated with the direct carrier multiplication process involving this state is a challenging task. The first barrier to overcome is the construction of Coulomb integrals for single-particle states far above the bandgap. For even small QDs, easily up to 60 states in the conduction band are required to access the thermodynamic threshold of $2E_g$ for MEG. Further, as the size of the QD is increased, the HOMO-LUMO gap closes, while higher energy states are also reduced. It is well-known that the density of states becomes less sparse further into the conduction band. This effect can be seen at the extrema of the energy level diagrams on pages 113, 120, and 128. As a result, the number of energy states which must be calculated for larger dots becomes greater as more and more states in the conduction band must be accounted for. High-energy electron states are therefore more accessible for smaller quantum dots, despite the larger bandgap. Even for the smallest dots considered in the current work, the Coulomb integrals constructed from permutations of four single-particle energy states number in the millions. For this reason, it is intractable to include such non-conserving terms in the CI calculation, and the method outlined in chapter 6.6 is used instead.

Preliminary investigation into multiple exciton generation in spherical PbSe QDs of radius 18.36 Å has been undertaken for photoexcitation close to the ther-

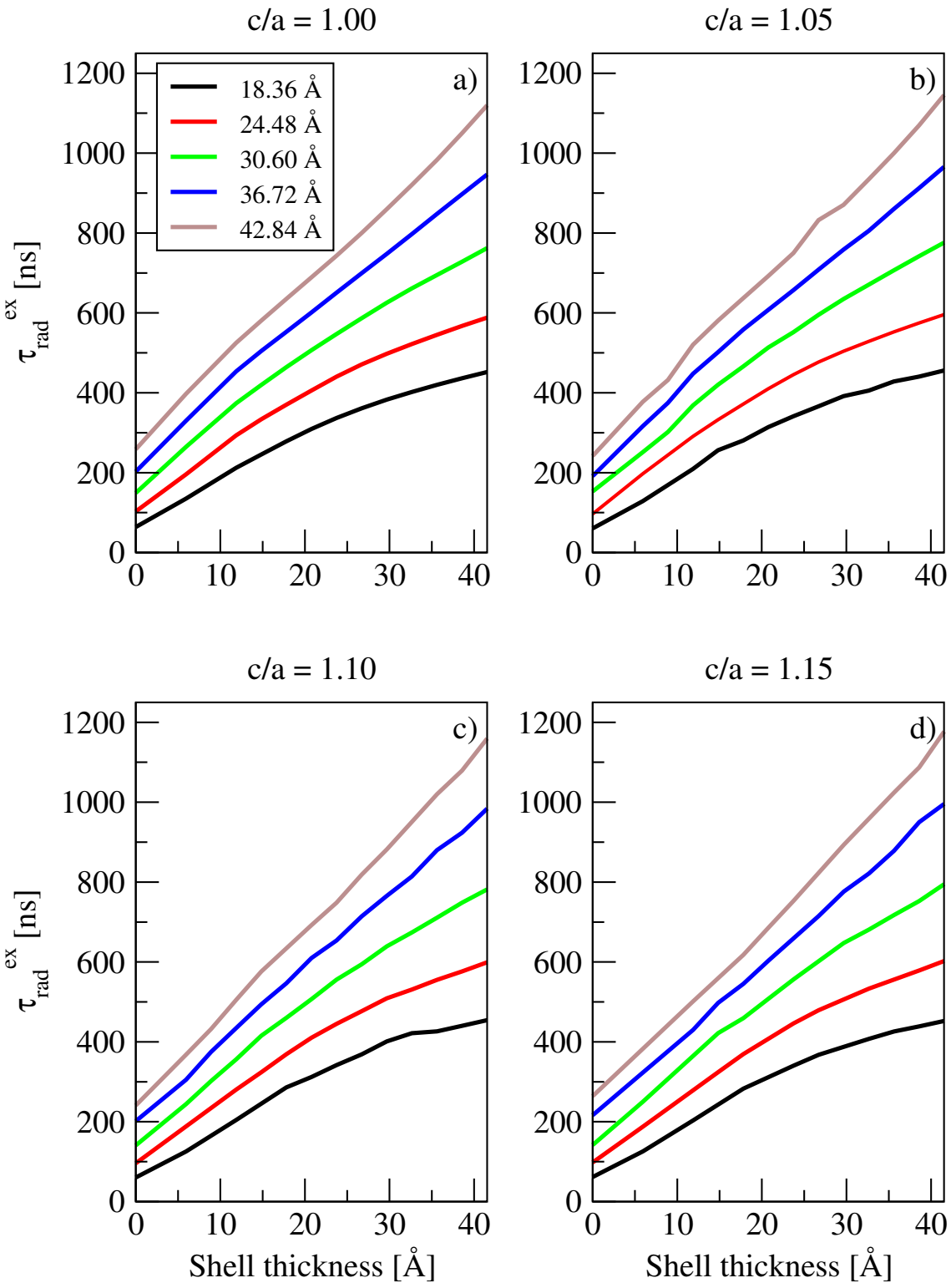

Figure 7.30.: Radiative carrier lifetimes for the lowest exciton state. Excitonic binding reduces the core-only lifetimes on the order of 1 ns. Strong size-dependence of excitonic states increases the carrier lifetime for thick shells.

modynamic limit of $2E_g$. In this particular instance, it is found that the matrix elements required for the calculation of the rate of carrier multiplication (see equation 6.124) are 32-fold degenerate for all energies considered. The bandgap energy is found to be 1.28 eV, with the 1st resonant state being e_{10} at an energy of 2.21 eV. It should be noted that, due to the reference state being chosen such that it lies in the centre of the bandgap, the energy of the hot electron state need not in fact be twice the bandgap energy, but instead must lie at $e_0 + E_g$, corresponding to photoabsorption at $2E_g$ (if the reference were coincident with the CBM, then the hot electron state would be shifted by h_0 to $2E_g$).

Lifetimes for multiple exciton generation have been calculated for the for the dot mentioned above beginning at the state e_{10} at 2.21 eV, as well as for the states immediately above (e_{11}, e_{12}, e_{13}, e_{14}), each of which may contribute to the carrier multiplication process. Using a Lorentzian distribution of width *Gamma* = 10 meV, the radiative lifetime from contributions from all of these states is found to be 71 ns. This is much longer than the picosecond timescales often observed in nanocrystal quantum dots. This is not too surprising, since the threshold for carrier multiplication in PbX NQDs is thought to be near to the $3E_g$ energy regime rather than at $2E_g$ [86]. Comparison of the 71 ns lifetime for carrier multiplication in the 18.36 Å PbSe QD to the 61.67 ns lifetime for radiative recombination from the previous section corroborates this observation. The lifetime for carrier multiplication is about 10 ns *longer* than the radiative recombination lifetime; hence carrier recombination is not observed for photoabsorption at $2E_g$ for PbX nanocrystals. Scattering events in this energy regime which result in carrier multiplication should be considered strongly off-resonant.

7.4.1 *Order of Magnitude Analysis of CM Matrix Elements*

While the initial results for the rates of multiple exciton generation are promising, it is useful to consider the behaviour of the scattering rates as dictated by

equation 6.124. For strongly resonant energy states, the energy conservation term approaches zero, and equation 6.124 may be written

$$W_n \approx \frac{\Gamma}{\hbar} \frac{|M_n|^2}{(\Gamma/2)^2}, \tag{7.3}$$

where the summations have been dropped for clarity. Assuming the broadening parameter Γ to be on the order of meV, and writing $\hbar$ in the units electronvolt-seconds,

$$W_n \sim \frac{4 \times 10^{-3}}{6.58 \times 10^{-16}} \frac{|M|^2}{10^{-6}} \frac{\text{eV}}{\text{eV s}} \frac{\text{eV}^2}{\text{eV}^2} = 6.08 \times 10^{18} \times |M|^2 \, \text{s}^{-1}. \tag{7.4}$$

Assuming the matrix elements M are found to be of the order 10^{-3}eV, as was the case for the 18.36 Å PbSe QD, then one would expect to find carrier multiplication rates comparable to 6.08×10^{12} s^{-1}, or lifetimes for carrier multiplication on the order of picoseconds for strongly resonant transitions, in line with the observations of Klimov et al. [86, 123]. The number of matrix elements of this magnitude is expected to increase drastically as high energy states are considered [180].

An additional point of note concerned with the calculation of the rates and lifetimes for carrier multiplication is the weighting of the broadening parameter Γ. For strongly resonant scattering interactions, as described by equation 7.3, improper choice of Γ may result in large discrepancy between the scattering times calculated. The variation of W_n as a function of Γ is shown in figure 7.31.

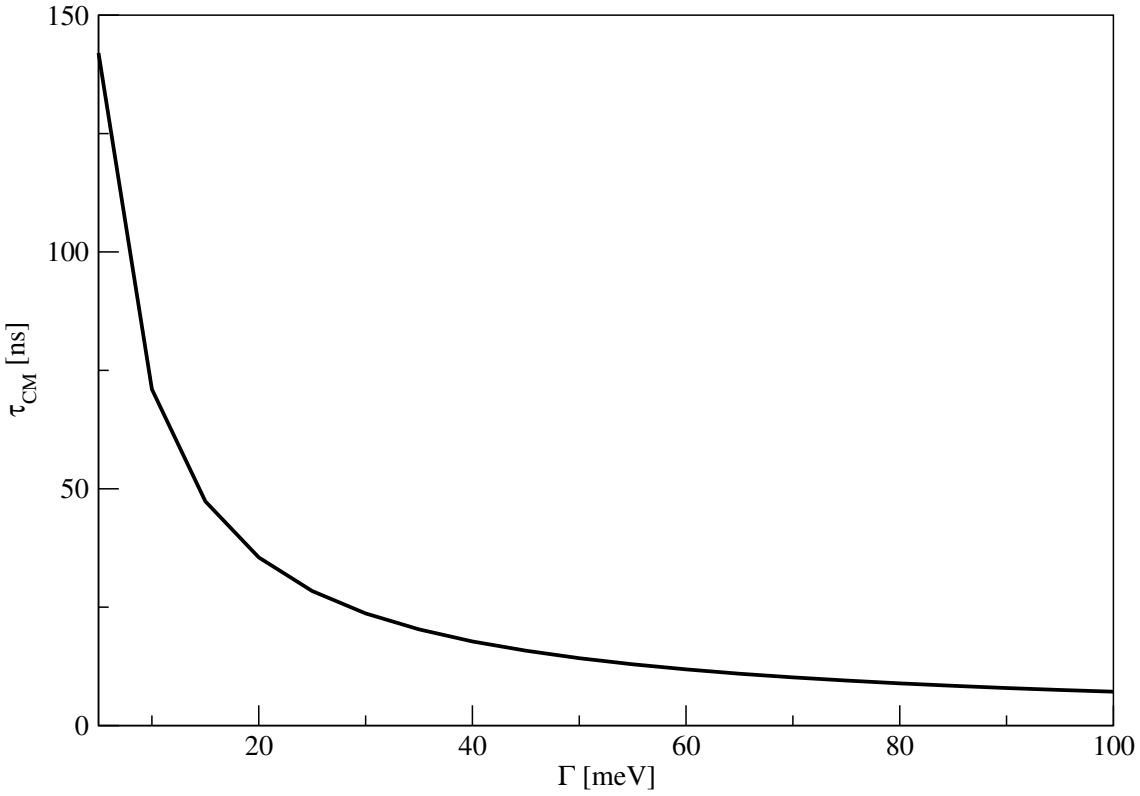

Figure 7.31.: The width of the Lorentzian distribution introduced in equation 6.124 plays a large role in the determination of the scattering rate. Improper choice of Γ results in inaccurate results.

8

CONCLUSIONS

Calculations on the electronic structure of core-only PbSe nanocrystal quantum dots and core/shell PbSe/PbS quantum dot heterostructures have been presented for spheroidal QD of varying ellipticity. Single-particle states were calculated via a four-band $\mathbf{k} \cdot \mathbf{p}$ envelope function Hamiltonian expanded at the L-point of the Brillouin zone using a basis of eight orthonormal planewaves. In keeping with reports in the literature, the size-dependent effective bandgap (HOMO-LUMO gap) was found to vary like R^{-3} for increasing core radius, and for increasing shell thickness, with only slight modification to the energy states as a consequence of the addition of the PbS shell due to the low confinement energy observed in PbSe/PbS quantum dot heterostructures. The energy spectrum of the QDs were found to vary inversely with the semi-minor axis length c^{-1} as the ellipticity of the dot was increased. Momentum matrix elements between the single-particle states were calculated via the Hellmann-Feynman theorem. It was found that the addition of the PbS shell provided sufficient confinement to subtly reduce the magnitude of the momentum matrix elements, while elongation along the x ($\langle \bar{1}\bar{1}2 \rangle$) axis resulted in a symmetry break between matrix elements polarised along the x and y axes, resulting in anisotropy in the magnitude of these elements. The degree of anisotropy was found to be on the order 1%.

Excitonic energy states have been generated from the single-particle states using the CI method. The excitonic binding energy was found to be highly size-dependent, varying between 158 meV and 28 meV for the QDs studied. The x

and y polarised momentum matrix elements associated with the excitonic states were found to occur at different exciton energies within the complex to the z polarised states.

Carrier lifetimes for radiative recombination at the bandedge have been calculated. The carrier lifetimes are found to be on the order 0.1 µs for all QDs studied here, a value range which is consistent with the literature. The carrier lifetimes were found to be size-dependent, and to vary almost linearly with the quantum dot radius. The modification to the energy spectrum and momentum matrix elements imposed by elongation of the dot was found to result in extension of the radiative carrier lifetimes by 4.56 ns for the smallest dots studied up to 47.69 ns for the largest. Excitonic corrections result in enhanced radiative lifetimes on the order of 7% of the smallest dots studied and 14% for the largest.

Finally, the lifetime for multiple exciton generation has been calculated for a small quantum dot (R = 18.36 Å) for the lowest energy electron states at the thermodynamic limit for which carrier multiplication may be possible (i.e. photoexcitation at $h\nu = 2E_g$). The carrier lifetime was found to be longer than the radiative lifetime in same QD (71 ns versus 61.67 ns), which may explain the lack of carrier multiplication observed in experiment at this energy. An order of magnitude analysis shows that, for strongly resonant high-energy states, the carrier lifetime is expected to be on the order of picoseconds to tens of picoseconds.

The long lifetimes observed for radiative recombination coupled with the short predicted lifetimes for carrier multiplication indicate that nanocrystal quantum dots composed of PbX materials are an excellent candidate for the exploitation of multiple exciton generation in the next generation of solar cell devices.

8.1 FUTURE DIRECTIONS

It should be noted that there exist several further avenues of research which may be conducted in addition to the current work. Firstly, higher energy states should

be included in calculations concerning multiple exciton generation. Since in the ideal case, the internal quantum efficiency due to carrier multiplication follows a step-like profile as the energy of the absorbed photon in increased in increments of the bandgap (i.e.$h\nu = E_g, 2E_g, 3E_g \ldots$), it would be interesting to find the transition rates/carrier lifetimes associated with high-energy electron states at or around these energies. There are two extensions to the current method of calculation which must be made in order to probe such high-energy states. Firstly, modification to the code which generates the Coulomb integrals must be undertaken in order to screen for only the necessary matrix elements, thereby making the calculation far more manageable. Secondly, carrier multiplication at $3E_g$ may include the generation of triexciton states (three bound, bandedge excitons generated from one absorption event), necessitating the generation of exciton-triexciton Coulomb integrals.

Further considerations which are missing from the current work which may be included to improve accuracy are strain and self-polarisation effects. In the former, strain is introduced at the core/shell interface of the QD heterostructure due to the lattice mismatch between the materials comprising the core and shell regions. This effect is expected to provide only very small contributions to the energy spectrum of the PbSe/PbS QDs due to the close lattice match between the two materials (6.12 Å and 5.94 Å respectively). The latter effect arises from the dielectric mismatch at the core/colloid, core/shell and shell/colloid boundaries. Both electrons and holes induce mirror charges at the dielectric boundary, resulting in an additional four interaction terms: the interaction between the negative mirror charge and the electron, between the induced negative charge and the hole, between the induced positive charge and the electron, and between the induced positive charge and the hole [177, 188]. In the exciton picture, only the self-interaction (self-polarisation) energy need be considered explicitly. Inclusion of the self-polarisation potential for spherical quantum dots has been previously implemented, however, the derivation and implementation of this potential for

any symmetry apart from spherical is far from trivial. The impact of the self-polarisation is expected to be larger than the effects of strain. Given the large dielectric constants of the lead-chalcogenides, priority should be afforded to the inclusion of the effects of self-polarisation for spheroidal quantum dots.

Appendices

A

COMMUTATION RELATIONS FOR FERMIONS

General commutation and anti-commutation brackets, respectively, are of the form

$$[a, b] = ab - ba \tag{A.1}$$

and

$$\{a, b\} = ab + ba, \tag{A.2}$$

where a, b, c, and d are fermions [46]. From these definitions it is possible to build commutation and anti-commutation relations for multiple particles. For three particles, the commutators may be expanded like

$$\begin{aligned} [a, bc] &= abc - bca = abc - bac + bac - bca \\ &= [a, b]\, c + b\, [a, c] \equiv \{a, b\}\, c - b\, \{a, c\} \end{aligned} \tag{A.3}$$

and

$$\begin{aligned} [ab, c] &= abc - cab = abc - acb + acb - cab \\ &= a\, [bc] + [a, c]\, b \equiv a\, \{c, b\} - \{a, b\}\, c, \end{aligned} \tag{A.4}$$

while the anti-commutators expand like

$$\begin{aligned} \{a, bc\} &= abc + bca = abc - bac + bac + bca \\ &= [a, b]\, c + b\, \{a, c\} \equiv \{a, b\}\, c - b\, [a, c] \end{aligned} \tag{A.5}$$

and

$$\begin{aligned} \{ab, c\} &= abc + cab = abc - acb + acb + cab \\ &= a\,[b, c] + \{a, c\}\,b \equiv a\,\{b, c\} - [a, c]\,b \end{aligned} \tag{A.6}$$

Further, using the definitions derived above, the commutation and anti-commutation relations for four particles may be expanded as follows:

$$\begin{aligned} [ab, cd] &= abcd - cdab = abcd - acdb + acdb - cdab = a\,[b, cd]\,[a, cd]\,b \\ &= a\,[b, c]\,d + ac\,[b, d] + [a, c]\,db + c\,[a, d]\,b \\ &\equiv a\,[b, c]\,d + ac\,[b, d] + \{a, c\}\,db - c\,\{a, d\}\,b \\ &\equiv a\,\{b, c\}\,d - ac\,\{b, d\} + [a, c]\,db + c\,[a, d]\,b \\ &\equiv a\,\{b, c\}\,d - ac\,\{b, d\} + \{a, c\}\,db - c\,\{a, d\}\,b, \end{aligned} \tag{A.7}$$

and

$$\begin{aligned} \{ab, cd\} &= abcd + cdab = abcd - acdb + acdb + cdab = a\,[b, cd] + \{a, cd\}\,b \\ &= a\,[b, c]\,d + ac\,[b, d] + [a, c]\,db + c\,\{a, d\}\,b \\ &\equiv a\,[b, c]\,d + ac\,[b, d] + \{a, c\}\,db - c\,[a, d]\,b \\ &\equiv a\,\{b, c\}\,d - ac\,\{b, d\} + [a, c]\,db + c\,\{a, d\}\,b \\ &\equiv a\,\{b, c\}\,d - ac\,\{b, d\} + \{a, c\}\,db - c\,[a, d]\,b. \end{aligned} \tag{A.8}$$

These important results, particularly equation A.7, are used in the derivation of the CI Hamiltonian in section 6.4 (beginning on page 85).

B

CI MATRIX ELEMENTS FOR DIRECT CARRIER MULTIPLICATION (MEG)

I order to construct the interband CI matrix elements corresponding to the direct carrier multiplication process, a reference states must first be defined. The reference state is chosen to be the true vacuum state in the Fock space, where the valence band is populated entirely by electrons, while the conduction band is entirely depopulated. The reference state is written

$$|0\rangle = \prod_{\beta \in \mathrm{VB}} c_\beta^\dagger \, |\mathrm{vac}\rangle \,, \tag{B.1}$$

where $c_\beta^\dagger$ attempts to create an electron in the valence band and $|\mathrm{vac}\rangle$ is the vacuum state state in the Fock space. Let the creation and annihilation operators for electrons be written

$$c_\alpha^\dagger \qquad \text{and} \qquad c_\alpha \qquad \text{for} \qquad \alpha \in \mathrm{CB} \tag{B.2}$$

and

$$c_\beta^\dagger \qquad \text{and} \qquad c_\beta \qquad \text{for} \qquad \beta \in \mathrm{VB}. \tag{B.3}$$

In the ground state (reference state), $|\mathrm{vac}\rangle$, the CB is empty while the VB is full. Therefore,

$$c_\alpha \, |\mathrm{vac}\rangle = 0, \tag{B.4}$$

since one cannot annihilate an electron in the empty conduction band, while,

$$c_\beta^\dagger \left|\text{vac}\right\rangle = 0 \tag{B.5}$$

since one cannot create and electron in the full valence band.

In order to construct the Hamiltonian which mixes all states comprised of two particles, all permutations of electrons in the CB and holes in the VB must be considered. To this end, the following properties of the anticommutation relations for fermions will be used [46]:

$$\left\{c_\alpha, c_{\alpha'}^\dagger\right\} = c_\alpha c_{\alpha'}^\dagger + c_{\alpha'}^\dagger c_\alpha = \delta_{\alpha\alpha'}, \tag{B.6}$$

$$\left\{c_\beta, c_{\beta'}^\dagger\right\} = c_\beta c_{\beta'}^\dagger + c_{\beta'}^\dagger c_\beta = \delta_{\beta\beta'}, \tag{B.7}$$

and

$$\left\{c_\alpha, c_\beta^\dagger\right\} = 0. \tag{B.8}$$

The derivation herein follows in the approach of reference [180].

B.1 SINGLE-PARTICLE CONTRIBUTIONS

Contributions to excitonic states arising from the single-particle states are represented by

$$\left|\alpha\beta\right\rangle = c_\alpha^\dagger c_\beta \left|\text{vac}\right\rangle, \tag{B.9}$$

i.e. from a single non-interacting electron in the conduction band and single non-interacting hole in the valence band. The Coulomb interaction between the single-particle states is

$$\mathcal{H}^{(1)} = \sum_{\gamma\gamma'} \int d^3\vec{r}\, \psi_\gamma^*\left(\vec{r}\right) V\left(\vec{r}\right) \psi_{\gamma'}\left(\vec{r}\right) c_\gamma^\dagger c_{\gamma'} = \sum_{\gamma\gamma'} V_{\gamma\gamma'} c_\gamma^\dagger c_{\gamma'}, \tag{B.10}$$

where $\gamma \in$ CB and $\gamma' \in$ VB are represent (presently unspecified) indices α and β. Contributions are then given by

$$\left\langle \alpha_1\alpha_2\beta_1\beta_2 \,\middle|\, \mathcal{H}^{(1)} \,\middle|\, \alpha\beta \right\rangle = \sum_{\gamma\gamma'} V_{\gamma\gamma'} \left\langle \mathrm{vac} \,\middle|\, c^\dagger_{\beta_2} c^\dagger_{\beta_1} c_{\alpha_2} c_{\alpha_1} c^\dagger_\gamma c_{\gamma'} c_\alpha c_\beta \,\middle|\, \mathrm{vac} \right\rangle . \tag{B.11}$$

Collecting CB and VB operators, equation B.11 rearranges to

$$\left\langle \alpha_1\alpha_2\beta_1\beta_2 \,\middle|\, \mathcal{H}^{(1)} \,\middle|\, \alpha\beta \right\rangle = -\sum_{\gamma\gamma'} V_{\gamma\gamma'} \left\langle \mathrm{vac} \,\middle|\, c_{\alpha_2} c_{\alpha 1} c^\dagger_\gamma c^\dagger_\alpha c^\dagger_{\beta_1} c^\dagger_{\beta_2} c_{\gamma'} c_\beta \,\middle|\, \mathrm{vac} \right\rangle . \tag{B.12}$$

From the anticommutation rules for fermions:

$$\begin{aligned}
& c_{\alpha_2} c_{\alpha 1} c^\dagger_\gamma c^\dagger_\alpha \\
\rightarrow & c_{\alpha_2} \left(\delta_{\alpha_1\gamma} - c^\dagger_\gamma c_{\alpha 1} \right) c^\dagger_\alpha \\
\rightarrow & \delta_{\alpha_1\gamma} c_{\alpha_2} c^\dagger_\alpha - c_{\alpha_2} c^\dagger_\gamma c_{\alpha_1} c^\dagger_\alpha \\
\rightarrow & \delta_{\alpha_1\gamma} \left(\delta_{\alpha_2\alpha} - c^\dagger_\alpha c_{\alpha_2} \right) - \left(\delta_{\alpha_2\gamma} - c^\dagger_\gamma c_{\alpha_2} \right) \left(\delta_{\alpha_1\alpha} - c^\dagger_\alpha c_{\alpha_1} \right) \\
\rightarrow & \delta_{\alpha_1\gamma}\delta_{\alpha_2\alpha} - \delta_{\alpha_1\gamma} c^\dagger_\alpha c_{\alpha_2} - \delta_{\alpha_2\gamma}\delta_{\alpha_1\alpha} + \delta_{\alpha_2\gamma} c^\dagger_\alpha c_{\alpha_1} + \delta_{\alpha_1\alpha} c^\dagger_\gamma c_{\alpha_2} - c^\dagger_\gamma c_{\alpha_2} c^\dagger_\alpha c_{\alpha_1}
\end{aligned} \tag{B.13}$$

Since one cannot annihilate an electron in the already empty conduction band (as per equation B.2), all terms in the above expression which include the annihilation operators c_{α_1} or c_{α_2} reduce to zero. Thus, the only surviving terms are those consisting only of δ-functions. Equation B.12 may then be rewritten:

$$\begin{aligned}
\left\langle \alpha_1\alpha_2\beta_1\beta_2 \,\middle|\, \mathcal{H}^{(1)} \,\middle|\, \alpha\beta \right\rangle = -\sum_{\gamma\gamma'} V_{\gamma\gamma'} & \left\langle \mathrm{vac} \,\middle|\, c^\dagger_{\beta_1} c^\dagger_{\beta_2} c_{\gamma'} c_\beta \,\middle|\, \mathrm{vac} \right\rangle \\
& \times \left(\delta_{\alpha_1\gamma}\delta_{\alpha_2\alpha} - \delta_{\alpha_2\gamma}\delta_{\alpha_1\alpha} \right)
\end{aligned} \tag{B.14}$$

In a similar manner:

$$\begin{aligned}
&c^{\dagger}_{\beta_2} c^{\dagger}_{\beta_1} c_{\gamma'} c_{\beta} \\
\rightarrow &c^{\dagger}_{\beta_2} \left(\delta_{\beta_1 \gamma'} - c_{\gamma'} c^{\dagger}_{\beta_1} \right) c_{\beta} \\
\rightarrow &\delta_{\beta_1 \gamma'} c^{\dagger}_{\beta_2} c_{\beta} - c^{\dagger}_{\beta_2} c_{\gamma'} c^{\dagger}_{\beta_1} c_{\beta} \\
\rightarrow &\delta_{\beta_1 \gamma'} \left(\delta_{\beta_2 \beta} - c_{\beta} c^{\dagger}_{\beta_2} \right) - \left(\delta_{\beta_2 \gamma'} - c_{\gamma'} c^{\dagger}_{\beta_2} \right) \left(\delta_{\beta_1 \beta} - c_{\beta} c^{\dagger}_{\beta_1} \right) \\
\rightarrow &\delta_{\beta_1 \gamma'} \delta_{\beta_2 \beta} - \delta_{\beta_1 \gamma'} c_{\beta} c^{\dagger}_{\beta_2} - \delta_{\beta_2 \gamma'} \delta_{\beta_1 \beta} + \delta_{\beta_2 \gamma'} c_{\beta} c^{\dagger}_{\beta_1} + \delta_{\beta_1 \beta} c_{\gamma'} c^{\dagger}_{\beta_2} - c_{\gamma'} c^{\dagger}_{\beta_2} c_{\beta} c^{\dagger}_{\beta_1}
\end{aligned} \tag{B.15}$$

Since one cannot create an electron in the full groundstate valence band, all terms including the creation operators $c^{\dagger}_{\beta_1}$ and $c^{\dagger}_{\beta_2}$ are zero (see equation B.3). Equation B.14 then becomes:

$$\begin{aligned}
\left\langle \alpha_1 \alpha_2 \beta_1 \beta_2 \,\middle|\, \mathcal{H}^{(1)} \,\middle|\, \alpha \beta \right\rangle = - \sum_{\gamma \gamma'} V_{\gamma \gamma'} \left(\delta_{\alpha_1 \gamma} \delta_{\alpha_2 \alpha} - \delta_{\alpha_2 \gamma} \delta_{\alpha_1 \alpha} \right) \\
\times \left(\delta_{\beta_1 \gamma'} \delta_{\beta_2 \beta} - \delta_{\beta_2 \gamma'} \delta_{\beta_1 \beta} \right).
\end{aligned} \tag{B.16}$$

where it has been assumed that $\langle \text{vac} | \text{vac} \rangle = 1$. Summing over $\gamma = \alpha_1, \alpha_2$ and $\gamma' = \beta_1, \beta_2$, the single-particle contributions are then

$$\begin{aligned}
\left\langle \alpha_1 \alpha_2 \beta 1 \beta 2 \,\middle|\, \mathcal{H}^{(1)} \,\middle|\, \alpha \beta \right\rangle = &- V_{\alpha_1 \beta_1} \delta_{\alpha_2 \alpha} \delta_{\beta_2 \beta} + V_{\alpha_1 \beta_2} \delta_{\alpha_2 \alpha} \delta_{\beta_1 \beta} \\
&+ V_{\alpha_2 \beta_1} \delta_{\alpha_1 \alpha} \delta_{\beta_2 \beta} - V_{\alpha_2 \beta_2} \delta_{\alpha_1 \alpha} \delta_{\beta_1 \beta}.
\end{aligned} \tag{B.17}$$

These terms describe the single-particle contributions between exciton and biexciton states with the implication that the particle energies of initial state $|i\rangle$ remain unchanged in the carrier multiplication process. Single-particle matrix elements do not strongly contribute to the carrier multiplication process and should therefore be neglected.

B.2 TWO-PARTICLE CONTRIBUTIONS

Two-particle contributions to the many-particle states are given by the Coulomb integrals taken between the contributing single-particle states. In terms of the electron creation/annihilation operators, two-particle contributions are generated by

$$\left|\alpha\alpha'\beta\beta'\right\rangle = \alpha^{\dagger}\alpha'^{\dagger}\beta\beta'\left|\text{vac}\right\rangle \tag{B.18}$$

The Coulomb integrals between these states are of the form

$$\begin{aligned}\mathcal{H}^{(2)} &= \frac{1}{2}\sum_{\gamma_1\gamma_2\gamma_3\gamma_4}\int d^3\vec{r}\int d^3\vec{r}'\psi^*_{\gamma_1}(\vec{r})\,\psi^*_{\gamma_2}(\vec{r}')\,V(\vec{r},\vec{r}')\,\psi_{\gamma_3}(\vec{r})\,\psi_{\gamma_4}(\vec{r})\,c^{\dagger}_{\gamma_1}c^{\dagger}_{\gamma_2}c_{\gamma_3}c_{\gamma_4}\\ &= \frac{1}{2}\sum_{\gamma_1\gamma_2\gamma_3\gamma_4}V_{\gamma_1\gamma_2\gamma_3\gamma_4}c^{\dagger}_{\gamma_1}c^{\dagger}_{\gamma_2}c_{\gamma_3}c_{\gamma_4},\end{aligned} \tag{B.19}$$

Where γ_1, γ_2, γ_3, and γ_4 may be in either the valence or conduction band. Two-particle contributions are then given by

$$\left\langle\alpha_1\alpha_2\beta_1\beta_2\,\middle|\,\mathcal{H}^{(2)}\,\middle|\,\alpha\beta\right\rangle = \frac{1}{2}\sum_{\gamma_1\gamma_2\gamma_3\gamma_4}V_{\gamma_1\gamma_2\gamma_3\gamma_4}\left\langle\text{vac}\,\middle|\,c^{\dagger}_{\beta_2}c^{\dagger}_{\beta_1}c_{\alpha_2}c_{\alpha_1}c^{\dagger}_{\gamma_1}c^{\dagger}_{\gamma_2}c_{\gamma_3}c_{\gamma_4}c^{\dagger}_{\alpha}c_{\beta}\,\middle|\,\text{vac}\right\rangle \tag{B.20}$$

There are four permutations of the "γ"s which contribute to the carrier multiplication process, while all other possible Coulomb integrals may be neglected. Each of the four permutations, outlined in table B.1, must be accounted for separately.

	γ_1	γ_2	γ_3	γ_4
Case 1	VB	CB	VB	VB
Case 2	CB	VB	VB	VB
Case 3	CB	CB	VB	CB
Case 4	CB	CB	CB	VB

Table B.1.: Contributing permutations of $\{\gamma\}$. Cases 1 and 2 correspond to the process involving an initially hot hole, while cases 3 and 4 represent the direct carrier multiplication process where the hot carrier is an electron.

Case 1

In the first case, the matrix elements are given by

$$\left\langle \alpha_1\alpha_2\beta_1\beta_2 \,\middle|\, \mathcal{H}^{(2)} \,\middle|\, \alpha\beta \right\rangle = \frac{1}{2} \sum_{\gamma_1\gamma_2\gamma_3\gamma_4} V_{\gamma_1\gamma_2\gamma_3\gamma_4} \left\langle \mathrm{vac} \,\middle|\, c^\dagger_{\beta_2} c^\dagger_{\beta_1} c_{\alpha_2} c_{\alpha_1} c^\dagger_{\gamma_1} c^\dagger_{\gamma_2} c_{\gamma_3} c_{\gamma_4} c^\dagger_{\alpha} c_{\beta} \,\middle|\, \mathrm{vac} \right\rangle \tag{B.21}$$

with $\gamma_1, \gamma_3, \gamma_4 \in$ VB and $\gamma_2 \in$ CB. Collecting conduction band and valence band operators, this rearranges to

$$\left\langle \alpha_1\alpha_2\beta_1\beta_2 \,\middle|\, \mathcal{H}^{(2)} \,\middle|\, \alpha\beta \right\rangle = \frac{1}{2} \sum_{\gamma_1\gamma_2\gamma_3\gamma_4} V_{\gamma_1\gamma_2\gamma_3\gamma_4} \left\langle \mathrm{vac} \,\middle|\, c_{\alpha_2} c_{\alpha_1} c^\dagger_{\gamma_2} c^\dagger_{\alpha} c^\dagger_{\beta_2} c^\dagger_{\beta_1} c^\dagger_{\gamma_1} c_{\gamma_3} c_{\gamma_4} c_{\beta} \,\middle|\, \mathrm{vac} \right\rangle , \tag{B.22}$$

and the conduction band operators (the "α"s) may be expanded in an identical manner to equation B.13, resulting in

$$\begin{aligned} \left\langle \alpha_1\alpha_2\beta_1\beta_2 \,\middle|\, \mathcal{H}^{(2)} \,\middle|\, \alpha\beta \right\rangle = \frac{1}{2} \sum_{\gamma_1\gamma_2\gamma_3\gamma_4} V_{\gamma_1\gamma_2\gamma_3\gamma_4} \left\langle \mathrm{vac} \,\middle|\, c^\dagger_{\beta_2} c^\dagger_{\beta_1} c^\dagger_{\gamma_1} c_{\gamma_3} c_{\gamma_4} c_{\beta} \,\middle|\, \mathrm{vac} \right\rangle \\ \times \left(\delta_{\alpha_1\gamma_2}\delta_{\alpha_2\alpha} - \delta_{\alpha_1\gamma_2}\delta_{\alpha_2\alpha} \right) . \end{aligned} \tag{B.23}$$

Using the anticommutation rules for fermions, the six remaining valance band operators (three creation, three annihilation) may be expanded thus:

$$
\begin{aligned}
& c^\dagger_{\beta_2} c^\dagger_{\beta_1} c^\dagger_{\gamma_1} c_{\gamma_3} c_{\gamma_4} c_\beta \\
\rightarrow & c^\dagger_{\beta_2} c^\dagger_{\beta_1} \left(\delta_{\gamma_1\gamma_3} - c_{\gamma_3} c^\dagger_{\gamma_1} \right) c_{\gamma_4} c_\beta \\
\rightarrow & \delta_{\gamma_1\gamma_3} c^\dagger_{\beta_2} c^\dagger_{\beta_1} c_{\gamma_4} c_\beta - c^\dagger_{\beta_2} c^\dagger_{\beta_1} c_{\gamma_3} c^\dagger_{\gamma_1} c_{\gamma_4} c_\beta \\
\rightarrow & \delta_{\gamma_1\gamma_3} c^\dagger_{\beta_2} \left(\delta_{\beta_1\gamma_4} - c_{\gamma_4} c^\dagger_{\beta_1} \right) c_\beta - c^\dagger_{\beta_2} \left(\delta_{\beta_1\gamma_3} - c_{\gamma_3} c^\dagger_{\beta_1} \right) \left(\delta_{\gamma_1\gamma_4} - c_{\gamma_4} c^\dagger_{\gamma_1} \right) c_\beta \\
\rightarrow & \delta_{\gamma_1\gamma_3}\delta_{\beta_1\gamma_4} c^\dagger_{\beta_2} c_\beta - \delta_{\gamma_1\gamma_3} c^\dagger_{\beta_2} c_{\gamma_4} c^\dagger_{\beta_1} c_\beta - \delta_{\beta_1\gamma_3}\delta_{\gamma_1\gamma_4} c^\dagger_{\beta_2} c_\beta \\
& \quad + \delta_{\beta_1\gamma_3} c^\dagger_{\beta_2} c_{\gamma_4} c^\dagger_{\gamma_1} c_\beta + \delta_{\gamma_1\gamma_4} c^\dagger_{\beta_2} c_{\gamma_3} c^\dagger_{\beta_1} c_\beta - c^\dagger_{\beta_2} c_{\gamma_3} c^\dagger_{\beta_1} c_{\gamma_4} c^\dagger_{\gamma_1} c_\beta \\
\rightarrow & \delta_{\gamma_1\gamma_3}\delta_{\beta_1\gamma_4} \left(\delta_{\beta_2\beta} - c_\beta c^\dagger_{\beta_2} \right) - \delta_{\gamma_1\gamma_3} \left(\delta_{\beta_2\gamma_4} - c_{\gamma_4} c^\dagger_{\beta_2} \right) \left(\delta_{\beta_1\beta} - c_\beta c^\dagger_{\beta_1} \right) \\
& \quad - \delta_{\beta_1\gamma_3}\delta_{\gamma_1\gamma_4} \left(\delta_{\beta_2\beta} - c_\beta c^\dagger_{\beta_2} \right) + \delta_{\beta_1\gamma_3} \left(\delta_{\beta_2\gamma_4} - c_{\gamma_4} c^\dagger_{\beta_2} \right) \left(\delta_{\gamma_1\beta} - c_\beta c^\dagger_{\gamma_1} \right) \\
& \quad + \delta_{\gamma_1\gamma_4} \left(\delta_{\beta_2\gamma_3} - c_{\gamma_3} c^\dagger_{\beta_2} \right) \left(\delta_{\beta_1\beta} - c_\beta c^\dagger_{\beta_1} \right) \\
& \quad - \left(\delta_{\beta_2\gamma_3} - c_{\gamma_3} c^\dagger_{\beta_2} \right) \left(\delta_{\beta_1\gamma_4} - c_{\gamma_4} c^\dagger_{\beta_1} \right) \left(\delta_{\gamma_1\beta} - c_\beta c^\dagger_{\gamma_1} \right)
\end{aligned}
\tag{B.24}
$$

Since one cannot create an electron in the full ground state valence band, all terms involving creation operators are identically zero; the only remaining terms are those consisting solely of δ-functions. Equation B.21 may then be rewritten in terms of the δ-functions as

$$
\begin{aligned}
\left\langle \alpha_1\alpha_2\beta_1\beta_2 \middle| \mathcal{H}^{(2)} \middle| \alpha\beta \right\rangle = \frac{1}{2} \sum_{\gamma_1\gamma_2\gamma_3\gamma_4} & V_{\gamma_1\gamma_2\gamma_3\gamma_4} \left(\delta_{\alpha_1\gamma_2}\delta_{\alpha_2\alpha} - \delta_{\alpha_2\gamma_2}\delta_{\alpha_1\alpha} \right) \\
& \times \left(\delta_{\beta_1\gamma_3}\delta_{\beta_2\gamma_4}\delta_{\gamma_1\beta} - \delta_{\beta_2\gamma_3}\delta_{\beta_1\gamma_4}\delta_{\gamma_1\beta} \right. \\
& \quad + \delta_{\gamma_1\gamma_3}\delta_{\beta_1\gamma_4}\delta_{\beta_2\beta} - \delta_{\gamma_1\gamma_3}\delta_{\beta_2\gamma_4}\delta_{\beta_1\beta} \\
& \quad \left. + \delta_{\gamma_1\gamma_4}\delta_{\beta_2\gamma_3}\delta_{\beta_1\beta} - \delta_{\gamma_1\gamma_4}\delta_{\beta_1\gamma_3}\delta_{\beta_2\beta} \right),
\end{aligned}
\tag{B.25}
$$

where $\langle \text{vac}|\text{vac}\rangle$ is assumed to be equal to unity. The δ-functions of β have been reordered for convenience. When summed over the "γ"s, equation B.25 becomes

$$\begin{aligned}\left\langle \alpha_1\alpha_2\beta_1\beta_2 \left| \mathcal{H}^{(2)} \right| \alpha\beta \right\rangle = \frac{1}{2}\left[V_{\beta\alpha_1\beta_1\beta_2}\delta_{\alpha_2\alpha} - V_{\beta\alpha_2\beta_1\beta_2}\delta_{\alpha_1\alpha} - V_{\beta\alpha_1\beta_2\beta_1}\delta_{\alpha_2\alpha} + V_{\beta\alpha_2\beta_2\beta_1}\delta_{\alpha_1\alpha}\right] \\ +\frac{1}{2}\sum_{\gamma}\left[V_{\gamma\alpha_1\gamma\beta_1}\delta_{\alpha_2\alpha}\delta_{\beta_2\beta} - V_{\gamma\alpha_1\gamma\beta_2}\delta_{\alpha_2\alpha}\delta_{\beta_1\beta} - V_{\gamma\alpha_2\gamma\beta_1}\delta_{\alpha_1\alpha}\delta_{\beta_2\beta} + V_{\gamma\alpha_2\gamma\beta_2}\delta_{\alpha_1\alpha}\delta_{\beta_1\beta}\right] \\ -\frac{1}{2}\sum_{\gamma}\left[V_{\gamma\alpha_1\beta_1\gamma}\delta_{\alpha_2\alpha}\delta_{\beta_2\beta} - V_{\gamma\alpha_1\beta_2\gamma}\delta_{\alpha_2\alpha}\delta_{\beta_1\beta} - V_{\gamma\alpha_2\beta_1\gamma}\delta_{\alpha_1\alpha}\delta_{\beta_2\beta} + V_{\gamma\alpha_2\beta_2\gamma}\delta_{\alpha_1\alpha}\delta_{\beta_1\beta}\right]\end{aligned} \tag{B.26}$$

with $\gamma \in$ VB. Equation B.29 gives the two-particle contributions to the excitonic energy structure in the electron representation. Specifically, the first line describes exciton-biexciton coupling states where one of the initial carriers remains in the same state before and after the scattering process (spectator state), while the second and third lines describe direct and exchange contributions to the electron-electron interaction [180].

The result stated in section 6.6 (page 108) then emerges by assigning the values

$$\begin{aligned}\alpha &\to e_{0i} \\ \alpha_1 &\to e_{0i} \\ \alpha_2 &\to e_{mj} \\ \beta &\to h_{ng} \\ \beta_1 &\to h_{0k} \\ \beta_2 &\to h_{0l},\end{aligned} \tag{B.27}$$

where, noting that the above definitions are given in terms of the quasiparticle creation and annihilation operators, e_{0i}, h_{0k}, and h_{0l} are in the ground state, e_{mj} is an electron in state m which is near to the groundstate, and h_{ng} is the initially hot

hole in state n with degeneracy g. In making these substitutions, the δ-functions of equation B.29 become

$$\begin{aligned}
\delta_{\alpha_1\alpha} &\to \delta_{e_{0i}e_{0i}} = 1, \\
\delta_{\alpha_2\alpha} &\to \delta_{e_{mj}e_{0i}} = 0, \\
\delta_{\beta_1\beta} &\to \delta_{h_{0k}h_{ng}} = 0, \\
\delta_{\beta_2\beta} &\to \delta_{h_{0l}h_{ng}} = 0,
\end{aligned} \tag{B.28}$$

and equation B.29 becomes

$$\begin{aligned}
&\left\langle e_{0i}e_{mj}h_{0k}h_{0l} \,\middle|\, \mathcal{H}^{(2)} \,\middle|\, e_{0i}h_{ng} \right\rangle \\
&\quad = \frac{1}{2}\Big[V_{h_{ng}e_{0i}h_{0k}h_{0l}}\delta_{e_{mj}e_{0i}} - V_{h_{ng}e_{mj}h_{0k}h_{0l}}\delta_{e_{0i}e_{0i}} \\
&\qquad - V_{h_{ng}e_{0i}h_{0l}h_{0k}}\delta_{e_{mj}e_{0i}} + V_{h_{ng}e_{mj}h_{0l}h_{0k}}\delta_{e_{0i}e_{0i}}\Big] \\
&\quad + \frac{1}{2}\sum_{\gamma}\Big[V_{\gamma e_{0i}\gamma h_{0k}}\delta_{e_{mj}e_{0i}}\delta_{h_{0l}h_{ng}} - V_{\gamma e_{0i}\gamma h_{0l}}\delta_{e_{mj}e_{0i}}\delta_{h_{0k}h_{ng}} \\
&\qquad - V_{\gamma e_{mj}\gamma h_{0k}}\delta_{e_{0i}e_{0i}}\delta_{h_{0l}h_{ng}} + V_{\gamma e_{mj}\gamma h_{0l}}\delta_{e_{0i}e_{0i}}\delta_{h_{0k}h_{ng}}\Big] \\
&\quad - \frac{1}{2}\sum_{\gamma}\Big[V_{\gamma e_{0i}h_{0k}\gamma}\delta_{e_{mj}e_{0i}}\delta_{h_{0l}h_{ng}} - V_{\gamma e_{0i}h_{0l}\gamma}\delta_{e_{mj}e_{0i}}\delta_{h_{0k}h_{ng}} \\
&\qquad - V_{\gamma e_{mj}h_{0k}\gamma}\delta_{e_{0i}e_{0i}}\delta_{h_{0l}h_{ng}} + V_{\gamma e_{mj}h_{0l}\gamma}\delta_{e_{0i}e_{0i}}\delta_{h_{0k}h_{ng}}\Big]
\end{aligned} \tag{B.29}$$

With these definitions only two terms survive, and the contribution to direct carrier multiplication is

$$\begin{aligned}
\left\langle e_{0i}e_{mj}h_{0k}h_{0l} \,\middle|\, \mathcal{H}^{(2)} \,\middle|\, e_{0i}h_{ng} \right\rangle &= -\frac{1}{2}\left(V_{h_{ng}e_{mj}h_{0k}h_{0l}}\delta_{e_{0i}e_{0i}} - V_{h_{ng}e_{mj}h_{0l}h_{0k}}\delta_{e_{0i}e_{0i}}\right) \\
&= -\frac{1}{2}\left(\left\langle h_{ng}e_{mj} \,\middle|\, V \,\middle|\, h_{0k}h_{0l} \right\rangle - \left\langle h_{ng}e_{mj} \,\middle|\, V \,\middle|\, h_{0l}h_{0k} \right\rangle\right).
\end{aligned} \tag{B.30}$$

Note that if instead the substitutions corresponding to the process where the initial hot carrier is an electron (given below) is used, then all terms in equation B.29 become null.

Case 2

The matrix elements in the second case may be expanded in much the same way as the first. The matrix elements are given by

$$\left\langle \alpha_1\alpha_2\beta_1\beta_2 \left| \mathcal{H}^{(2)} \right| \alpha\beta \right\rangle = \frac{1}{2} \sum_{\gamma_1\gamma_2\gamma_3\gamma_4} V_{\gamma_1\gamma_2\gamma_3\gamma_4} \left\langle \text{vac} \left| c^\dagger_{\beta_2} c^\dagger_{\beta_1} c_{\alpha_2} c_{\alpha_1} c^\dagger_{\gamma_1} c^\dagger_{\gamma_2} c_{\gamma_3} c_{\gamma_4} c^\dagger_\alpha c_\beta \right| \text{vac} \right\rangle \tag{B.31}$$

with $\gamma_2, \gamma_3, \gamma_4 \in$ VB and $\gamma_1 \in$ CB. In collecting the conduction band and valence band operators, this rearranges to

$$\left\langle \alpha_1\alpha_2\beta_1\beta_2 \left| \mathcal{H}^{(2)} \right| \alpha\beta \right\rangle = -\frac{1}{2} \sum_{\gamma_1\gamma_2\gamma_3\gamma_4} V_{\gamma_1\gamma_2\gamma_3\gamma_4} \left\langle \text{vac} \left| c_{\alpha_2} c_{\alpha_1} c^\dagger_{\gamma_1} c^\dagger_\alpha c^\dagger_{\beta_2} c^\dagger_{\beta_1} c^\dagger_{\gamma_2} c_{\gamma_3} c_{\gamma_4} c_\beta \right| \text{vac} \right\rangle . \tag{B.32}$$

The differences between equation B.32 and equation B.22 should be noted. First, γ_1 and γ_2 are interchanged, since in the 2nd case it is γ_1 which operates on the conduction band, not γ_2. Second, due to the anti-symmetry of fermionic wavefunctions, when changing the order of operations a minus sign must be introduced. In the first case, an even number of operators were exchanged, however, when moving from equation B.31 to equation B.32 an odd number of exchanges was carried out—hence the prefactor of -1.

From this point, the second case may be expanded in the same manner as the first. In terms of the δ-functions, equation B.32 becomes

$$\begin{aligned} \left\langle \alpha_1\alpha_2\beta_1\beta_2 \left| \mathcal{H}^{(2)} \right| \alpha\beta \right\rangle = -\frac{1}{2} \sum_{\gamma_1\gamma_2\gamma_3\gamma_4} & V_{\gamma_1\gamma_2\gamma_3\gamma_4} \left(\delta_{\alpha_1\gamma_2}\delta_{\alpha_2\alpha} - \delta_{\alpha_2\gamma_2}\delta_{\alpha_1\alpha}\right) \\ & \times \left(\delta_{\beta_1\gamma_3}\delta_{\beta_2\gamma_4}\delta_{\gamma_2\beta} - \delta_{\beta_2\gamma_3}\delta_{\beta_1\gamma_4}\delta_{\gamma_2\beta} \right. \\ & + \delta_{\gamma_2\gamma_3}\delta_{\beta_1\gamma_4}\delta_{\beta_2\beta} - \delta_{\gamma_2\gamma_3}\delta_{\beta_2\gamma_4}\delta_{\beta_1\beta} \\ & \left. + \delta_{\gamma_2\gamma_4}\delta_{\beta_2\gamma_3}\delta_{\beta_1\beta} - \delta_{\gamma_2\gamma_4}\delta_{\beta_1\gamma_3}\delta_{\beta_2\beta} \right) , \end{aligned} \tag{B.33}$$

resulting in

$$\begin{aligned}\left\langle \alpha_1\alpha_2\beta_1\beta_2 \,\middle|\, \mathcal{H}^{(2)} \,\middle|\, \alpha\beta \right\rangle = &-\frac{1}{2}\left[V_{\alpha_1\beta\beta_1\beta_2}\delta_{\alpha_2\alpha} - V_{\alpha_2\beta\beta_1\beta_2}\delta_{\alpha_1\alpha} - V_{\alpha_1\beta\beta_2\beta_1}\delta_{\alpha_2\alpha} + V_{\alpha_2\beta\beta_2\beta_1}\delta_{\alpha_1\alpha}\right] \\ &-\frac{1}{2}\sum_{\gamma}\left[V_{\alpha_1\gamma\gamma\beta_1}\delta_{\alpha_2\alpha}\delta_{\beta_2\beta} - V_{\alpha_1\gamma\gamma\beta_2}\delta_{\alpha_2\alpha}\delta_{\beta_1\beta} - V_{\alpha_2\gamma\gamma\beta_1}\delta_{\alpha_1\alpha}\delta_{\beta_2\beta} + V_{\alpha_2\gamma\gamma\beta_2}\delta_{\alpha_1\alpha}\delta_{\beta_1\beta}\right] \\ &+\frac{1}{2}\sum_{\gamma}\left[V_{\alpha_1\gamma\beta_1\gamma}\delta_{\alpha_2\alpha}\delta_{\beta_2\beta} - V_{\alpha_1\gamma\beta_2\gamma}\delta_{\alpha_2\alpha}\delta_{\beta_1\beta} - V_{\alpha_2\gamma\beta_1\gamma}\delta_{\alpha_1\alpha}\delta_{\beta_2\beta} + V_{\alpha_2\gamma\beta_2\gamma}\delta_{\alpha_1\alpha}\delta_{\beta_1\beta}\right]\end{aligned} \tag{B.34}$$

with $\gamma \in \mathrm{VB}$. As it was for case 1, all terms in equation B.34 reduce to zero when the initial hot carrier is an electron. When the hot carrier is a hole, the surviving terms, using the substitutions above (B.27), are

$$\begin{aligned}\left\langle e_{0i}e_{mj}h_{0k}h_{0l} \,\middle|\, \mathcal{H}^{(2)} \,\middle|\, e_{0i}h_{ng} \right\rangle &= -\frac{1}{2}\left(-V_{e_{mj}h_{ng}h_{0k}h_{0l}}\delta_{e_{0i}e_{0i}} + V_{e_{mj}h_{ng}h_{0l}h_{0k}}\delta_{e_{0i}e_{0i}}\right) \\ &= \frac{1}{2}\left(\left\langle e_{mj}h_{ng} \,\middle|\, V \,\middle|\, h_{0k}h_{0l} \right\rangle - \left\langle e_{mj}h_{ng} \,\middle|\, V \,\middle|\, h_{0l}h_{0k} \right\rangle\right).\end{aligned} \tag{B.35}$$

Summing this result with that of case 1 (equations B.30 and B.35), the total contribution to the direct carrier multiplication process where the initial hot carrier is a hole is found to be:

$$\begin{aligned}\left\langle e_{mi}e_{0j}h_{ng}h_{0l} \,\middle|\, \mathcal{H}^{(2)} \,\middle|\, e_{0l}h_{ng} \right\rangle = &\frac{1}{2}\left(\left\langle e_{mj}h_{ng} \,\middle|\, V \,\middle|\, h_{0k}h_{0l} \right\rangle - \left\langle e_{mj}h_{ng} \,\middle|\, V \,\middle|\, h_{0l}h_{0k} \right\rangle\right) \\ &-\frac{1}{2}\left(\left\langle h_{ng}e_{mj} \,\middle|\, V \,\middle|\, h_{0k}h_{0l} \right\rangle - \left\langle h_{ng}e_{mj} \,\middle|\, V \,\middle|\, h_{0l}h_{0k} \right\rangle\right).\end{aligned} \tag{B.36}$$

Case 3

Cases three and four, corresponding to processes where the initial hot carrier is an electron, are somewhat similar cases one and two. The matrix element for case 3 may be written as

$$\left\langle \alpha_1\alpha_2\beta_1\beta_2 \,\middle|\, \mathcal{H}^{(2)} \,\middle|\, \alpha\beta \right\rangle = \frac{1}{2}\sum_{\gamma_1\gamma_2\gamma_3\gamma_4} V_{\gamma_1\gamma_2\gamma_3\gamma_4}\left\langle \mathrm{vac} \,\middle|\, c^\dagger_{\beta_2}c^\dagger_{\beta_1}c_{\alpha_2}c_{\alpha_1}c^\dagger_{\gamma_1}c^\dagger_{\gamma_2}c_{\gamma_3}c_{\gamma_4}c^\dagger_{\alpha}c_{\beta} \,\middle|\, \mathrm{vac} \right\rangle, \tag{B.37}$$

with $\gamma_1, \gamma_2, \gamma_4 \in$ CB and $\gamma_3 \in$ VB. Collecting CB and VB operators results in

$$\left\langle \alpha_1\alpha_2\beta_1\beta_2 \middle| \mathcal{H}^{(2)} \middle| \alpha\beta \right\rangle = \frac{1}{2} \sum_{\gamma_1\gamma_2\gamma_3\gamma_4} V_{\gamma_1\gamma_2\gamma_3\gamma_4} \left\langle \text{vac} \middle| c^\dagger_{\beta_2} c^\dagger_{\beta_1} c_{\gamma_3} c_\beta c_{\alpha_2} c_{\alpha_1} c^\dagger_{\gamma_1} c^\dagger_{\gamma_2} c_{\gamma_4} c^\dagger_\alpha \middle| \text{vac} \right\rangle . \tag{B.38}$$

The valence band operators (the "β"s) can be expanded in much the same way as the conduction band operators ("α"s) were for the first two cases. The process and result are the same as equation B.15, with the γ' replaced with γ_3, i.e.

$$\begin{aligned} \to \delta_{\beta_1\gamma_3}\delta_{\beta_2\beta} - \delta_{\beta_1\gamma_3} c_\beta c^\dagger_{\beta_2} - \delta_{\beta_2\gamma_3}\delta_{\beta_1\beta} \\ + \delta_{\beta_2\gamma_3} c_\beta c^\dagger_{\beta_1} + \delta_{\beta_1\beta} c_{\gamma_3} c^\dagger_{\beta_2} - c_{\gamma_3} c^\dagger_{\beta_2} c_\beta c^\dagger_{\beta_1}, \end{aligned} \tag{B.39}$$

with all operators not consisting solely of δ-functions being null (since one cannot create an electron in the full valence band in the ground state). Equation B.38 may then be written as

$$\begin{aligned} \left\langle \alpha_1\alpha_2\beta_1\beta_2 \middle| \mathcal{H}^{(2)} \middle| \alpha\beta \right\rangle = \frac{1}{2} \sum_{\gamma_1\gamma_2\gamma_3\gamma_4} V_{\gamma_1\gamma_2\gamma_3\gamma_4} \left\langle \text{vac} \middle| c_{\alpha_2} c_{\alpha_1} c^\dagger_{\gamma_1} c^\dagger_{\gamma_2} c_{\gamma_4} c^\dagger_\alpha \middle| \text{vac} \right\rangle \\ \times \left(\delta_{\beta_1\gamma_3}\delta_{\beta_2\beta} - \delta_{\beta_2\gamma_3}\delta_{\beta_1\beta}\right). \end{aligned} \tag{B.40}$$

After slight rearrangement to collect creation and annihilation operators the conduction band operators may then be dealt with in a similar manner as above:

$$
\begin{aligned}
& c_{\alpha_2} c_{\alpha_1} c_{\gamma_4} c^\dagger_{\gamma_1} c^\dagger_{\gamma_2} c^\dagger_{\alpha} \\
\rightarrow & c_{\alpha_2} c_{\alpha_1} \left(\delta_{\gamma_4\gamma_1} - c^\dagger_{\gamma_1} c_{\gamma_4} \right) c^\dagger_{\gamma_2} c^\dagger_{\alpha} \\
\rightarrow & \delta_{\gamma_4\gamma_1} c_{\alpha_2} c_{\alpha_1} c^\dagger_{\gamma_2} c^\dagger_{\alpha} - c_{\alpha_2} c_{\alpha_1} c^\dagger_{\gamma_1} c_{\gamma_4} c^\dagger_{\gamma_2} c^\dagger_{\alpha} \\
\rightarrow & \delta_{\gamma_4\gamma_1} c_{\alpha_2} \left(\delta_{\alpha_1\gamma_2} - c^\dagger_{\gamma_2} c_{\alpha_1} \right) c^\dagger_{\alpha} - c_{\alpha_2} \left(\delta_{\alpha_1\gamma_1} - c^\dagger_{\gamma_1} c_{\alpha_1} \right) \left(\delta_{\gamma_4\gamma_2} - c^\dagger_{\gamma_2} c_{\gamma_4} \right) c^\dagger_{\alpha} \\
\rightarrow & \delta_{\gamma_4\gamma_1} \delta_{\alpha_1\gamma_2} c_{\alpha_2} c^\dagger_{\alpha} - \delta_{\gamma_4\gamma_1} c_{\alpha_2} c^\dagger_{\gamma_2} c_{\alpha_1} c^\dagger_{\alpha} - \delta_{\alpha_1\gamma_1} \delta_{\gamma_4\gamma_2} c_{\alpha_2} c^\dagger_{\alpha} \\
& \quad + \delta_{\alpha_1\gamma_1} c_{\alpha_2} c^\dagger_{\gamma_2} c_{\gamma_4} c^\dagger_{\alpha} + \delta_{\gamma_4\gamma_2} c_{\alpha_2} c^\dagger_{\gamma_1} c_{\alpha_1} c^\dagger_{\alpha} - c_{\alpha_2} c^\dagger_{\gamma_1} c_{\alpha_1} c^\dagger_{\gamma_2} c_{\gamma_4} c^\dagger_{\alpha} \\
\rightarrow & \delta_{\gamma_4\gamma_1} \delta_{\alpha_1\gamma_2} \left(\delta_{\alpha_2\alpha} - c^\dagger_{\alpha} c_{\alpha_2} \right) - \delta_{\gamma_4\gamma_1} \left(\delta_{\alpha_2\gamma_2} - c^\dagger_{\gamma_2} c_{\alpha_2} \right) \left(\delta_{\alpha_1\alpha} - c^\dagger_{\alpha} c_{\alpha_1} \right) \\
& \quad - \delta_{\alpha_1\gamma_1} \delta_{\gamma_4\gamma_2} \left(\delta_{\alpha_1\gamma_1} \delta_{\gamma_4\gamma_2} \delta_{\alpha_2\alpha} - c^\dagger_{\alpha} c_{\alpha_2} \right) + \delta_{\alpha_1\gamma_1} \left(\delta_{\alpha_2\gamma_2} - c^\dagger_{\gamma_2} c_{\alpha_2} \right) \left(\delta_{\gamma_4\alpha} - c^\dagger_{\alpha} c_{\gamma_4} \right) \\
& \quad + \delta_{\gamma_4\gamma_2} \left(\delta_{\alpha_2\gamma_1} - c^\dagger_{\gamma_1} c_{\alpha_2} \right) \left(\delta_{\alpha_1\alpha} - c^\dagger_{\alpha} c_{\alpha_1} \right) \\
& \quad - \left(\delta_{\alpha_2\gamma_1} - c^\dagger_{\gamma_1} c_{\alpha_2} \right) \left(\delta_{\alpha_1\gamma_2} - c^\dagger_{\gamma_2} c_{\alpha_1} \right) \left(\delta_{\gamma_4\alpha} - c^\dagger_{\alpha} c_{\gamma_4} \right),
\end{aligned}
\tag{B.41}
$$

with all terms which contain annihilation operators disappearing, since one cannot annihilate an electron from an empty conduction band. Equation B.37 can now be rewritten as

$$
\begin{aligned}
\left\langle \alpha_1\alpha_2\beta_1\beta_2 \,\middle|\, \mathcal{H}^{(2)} \,\middle|\, \alpha\beta \right\rangle = \frac{1}{2} \sum_{\gamma_1\gamma_2\gamma_3\gamma_4} & V_{\gamma_1\gamma_2\gamma_3\gamma_4} \left(\delta_{\beta_1\gamma_3} \delta_{\beta_2\beta} - \delta_{\beta_2\gamma_3} \delta_{\beta_1\beta} \right) \\
& \times \left(\delta_{\alpha_1\gamma_1} \delta_{\alpha_2\gamma_2} \delta_{\gamma_4\alpha} - \delta_{\alpha_2\gamma_1} \delta_{\alpha_1\gamma_2} \delta_{\gamma_4\alpha} \right. \\
& \quad + \delta_{\gamma_4\gamma_1} \delta_{\alpha_1\gamma_2} \delta_{\alpha_2\alpha} - \delta_{\gamma_4\gamma_1} \delta_{\alpha_2\gamma_2} \delta_{\alpha_1\alpha} \\
& \quad \left. + \delta_{\gamma_4\gamma_2} \delta_{\alpha_2\gamma_1} \delta_{\alpha_1\alpha} - \delta_{\gamma_4\gamma_2} \delta_{\alpha_1\gamma_1} \delta_{\alpha_2\alpha} \right),
\end{aligned}
\tag{B.42}
$$

where the order of δ-functions has been changed for convenience. Again, the assumption $\langle \text{vac}|\text{vac}\rangle \rightarrow 1$ has been made. Carrying out the summation over $\{\gamma\}$ yields

$$\begin{aligned}\left\langle \alpha_1\alpha_2\beta_1\beta_2 \,\middle|\, \mathcal{H}^{(2)} \,\middle|\, \alpha\beta \right\rangle = \frac{1}{2}\left[V_{\alpha_1\alpha_2\beta_1\alpha}\delta_{\beta_2\beta} - V_{\alpha_1\alpha_2\beta_2\alpha}\delta_{\beta_1\beta} - V_{\alpha_2\alpha_1\beta_1\alpha}\delta_{\beta_2\beta} + V_{\alpha_2\alpha_1\beta_2\alpha}\delta_{\beta_1\beta}\right] \\ +\frac{1}{2}\sum_{\gamma}\left[V_{\gamma\alpha_1\beta_1\gamma}\delta_{\alpha_2\alpha}\delta_{\beta_2\beta} - V_{\gamma\alpha_1\beta_2\gamma}\delta_{\alpha_2\alpha}\delta_{\beta_1\beta} - V_{\gamma\alpha_2\beta_1\gamma}\delta_{\alpha_1\alpha}\delta_{\beta_2\beta} + V_{\gamma\alpha_2\beta_2\gamma}\delta_{\alpha_1\alpha}\delta_{\beta_1\beta}\right] \\ -\frac{1}{2}\sum_{\gamma}\left[V_{\alpha_1\gamma\beta_1\gamma}\delta_{\alpha_2\alpha}\delta_{\beta_2\beta} - V_{\alpha_1\gamma\beta_2\gamma}\delta_{\alpha_2\alpha}\delta_{\beta_1\beta} - V_{\alpha_2\gamma\beta_1\gamma}\delta_{\alpha_1\alpha}\delta_{\beta_2\beta} + V_{\alpha_2\gamma\beta_2\gamma}\delta_{\alpha_1\alpha}\delta_{\beta_1\beta}\right]\end{aligned} \tag{B.43}$$

with $\gamma \in \text{CB}$. For the case that the initially hot carrier is an electron, the appropriate substitutions for the "α"s and the "β"s are

$$\begin{aligned}\alpha &\rightarrow e_{ng} \\ \alpha_1 &\rightarrow e_{0i} \\ \alpha_2 &\rightarrow e_{0j} \\ \beta &\rightarrow h_{0l} \\ \beta_1 &\rightarrow h_{mk} \\ \beta_2 &\rightarrow h_{0l}.\end{aligned} \tag{B.44}$$

In making these substitutions equation B.51 reduces to

$$\begin{aligned}\left\langle e_{0i}e_{0j}h_{mk}h_{0l} \,\middle|\, \mathcal{H}^{(2)} \,\middle|\, e_{ng}h_{0l} \right\rangle &= \frac{1}{2}\left[V_{e_{0i}e_{0j}h_{mk}e_{ng}}\delta_{h_{0l}h_{0l}} - V_{e_{0j}e_{0i}h_{mk}e_{ng}}\delta_{h_{0l}h_{0l}}\right] \\ &= \frac{1}{2}\left(\left\langle e_{0i}e_{0j} \,\middle|\, V \,\middle|\, h_{mk}e_{ng}\right\rangle - \left\langle e_{0j}e_{0i} \,\middle|\, V \,\middle|\, h_{mk}e_{ng}\right\rangle\right),\end{aligned} \tag{B.45}$$

since all terms in equation B.51 involving $\delta_{e_{0i}e_{ng}}$ or $\delta_{e_{0j}e_{ng}}$ are zero. If instead the substitutions for the initially hot hole are made (equation B.27), all terms in equation B.51 become zero.

Case 4

Case 4 may be dealt with in the same way as case 3. The matrix elements may be written

$$\left\langle \alpha_1\alpha_2\beta_1\beta_2 \left| \mathcal{H}^{(2)} \right| \alpha\beta \right\rangle = \frac{1}{2} \sum_{\gamma_1\gamma_2\gamma_3\gamma_4} V_{\gamma_1\gamma_2\gamma_3\gamma_4} \left\langle \text{vac} \left| c^\dagger_{\beta_2} c^\dagger_{\beta_1} c_{\alpha_2} c_{\alpha_1} c^\dagger_{\gamma_1} c^\dagger_{\gamma_2} c_{\gamma_3} c_{\gamma_4} c^\dagger_{\alpha} c_{\beta} \right| \text{vac} \right\rangle , \tag{B.46}$$

with $\gamma_1, \gamma_2, \gamma_3 \in$ CB and $\gamma_4 \in$ VB. Collecting CB and VB operators results in

$$\left\langle \alpha_1\alpha_2\beta_1\beta_2 \left| \mathcal{H}^{(2)} \right| \alpha\beta \right\rangle = -\frac{1}{2} \sum_{\gamma_1\gamma_2\gamma_3\gamma_4} V_{\gamma_1\gamma_2\gamma_3\gamma_4} \left\langle \text{vac} \left| c^\dagger_{\beta_2} c^\dagger_{\beta_1} c_{\gamma_4} c_{\beta} c_{\alpha_2} c_{\alpha_1} c^\dagger_{\gamma_1} c^\dagger_{\gamma_2} c_{\gamma_3} c^\dagger_{\alpha} \right| \text{vac} \right\rangle . \tag{B.47}$$

Note the "-" sign originating from fermionic anti-symmetry (as in was the case in case 2). With the interchange of c_{γ_3} and c_{γ_4}, the valence band operators (the "β"s) may be expanded as

$$c^\dagger_{\beta_2} c^\dagger_{\beta_1} c_{\gamma_4} c_{\beta} \rightarrow \delta_{\beta_1\gamma_4}\delta_{\beta_2\beta} - \delta_{\beta_2\gamma_4}\delta_{\beta_1\beta}, \tag{B.48}$$

resulting in

$$\begin{aligned} \left\langle \alpha_1\alpha_2\beta_1\beta_2 \left| \mathcal{H}^{(2)} \right| \alpha\beta \right\rangle = -\frac{1}{2} \sum_{\gamma_1\gamma_2\gamma_3\gamma_4} V_{\gamma_1\gamma_2\gamma_3\gamma_4} \left\langle \text{vac} \left| c_{\alpha_2} c_{\alpha_1} c^\dagger_{\gamma_1} c^\dagger_{\gamma_2} c_{\gamma_3} c^\dagger_{\alpha} \right| \text{vac} \right\rangle \\ \times \left(\delta_{\beta_1\gamma_4}\delta_{\beta_2\beta} - \delta_{\beta_2\gamma_4}\delta_{\beta_1\beta} \right). \end{aligned} \tag{B.49}$$

The conduction band operators (the "α"s) may then be expanded in the same way as in case 3 (except with γ_4 replaced with γ_3). Equation B.46 then becomes

$$\begin{aligned}\left\langle \alpha_1\alpha_2\beta_1\beta_2 \,\middle|\, \mathcal{H}^{(2)} \,\middle|\, \alpha\beta \right\rangle = -\frac{1}{2} \sum_{\gamma_1\gamma_2\gamma_3\gamma_4} V_{\gamma_1\gamma_2\gamma_3\gamma_4} \left(\delta_{\beta_1\gamma_4}\delta_{\beta_2\beta} - \delta_{\beta_2\gamma_4}\delta_{\beta_1\beta}\right) \\ \times \left(\delta_{\alpha_1\gamma_1}\delta_{\alpha_2\gamma_2}\delta_{\gamma_3\alpha} - \delta_{\alpha_2\gamma_1}\delta_{\alpha_1\gamma_2}\delta_{\gamma_3\alpha} \right. \\ + \delta_{\gamma_3\gamma_1}\delta_{\alpha_1\gamma_2}\delta_{\alpha_2\alpha} - \delta_{\gamma_3\gamma_1}\delta_{\alpha_2\gamma_2}\delta_{\alpha_1\alpha} \\ \left. + \delta_{\gamma_3\gamma_2}\delta_{\alpha_2\gamma_1}\delta_{\alpha_1\alpha} - \delta_{\gamma_3\gamma_2}\delta_{\alpha_1\gamma_1}\delta_{\alpha_2\alpha} \right),\end{aligned} \tag{B.50}$$

After carrying out the summation, equation B.50 becomes

$$\begin{aligned}\left\langle \alpha_1\alpha_2\beta_1\beta_2 \,\middle|\, \mathcal{H}^{(2)} \,\middle|\, \alpha\beta \right\rangle = &-\frac{1}{2}\left[V_{\alpha_1\alpha_2\alpha\beta_1}\delta_{\beta_2\beta} - V_{\alpha_1\alpha_2\alpha\beta_2}\delta_{\beta_1\beta} - V_{\alpha_2\alpha_1\alpha\beta_1}\delta_{\beta_2\beta} + V_{\alpha_2\alpha_1\alpha\beta_2}\delta_{\beta_1\beta}\right] \\ &-\frac{1}{2}\sum_{\gamma}\left[V_{\gamma\alpha_1\gamma\beta_1}\delta_{\alpha_2\alpha}\delta_{\beta_2\beta} - V_{\gamma\alpha_1\gamma\beta_2}\delta_{\alpha_2\alpha}\delta_{\beta_1\beta} - V_{\gamma\alpha_2\gamma\beta_1}\delta_{\alpha_1\alpha}\delta_{\beta_2\beta} + V_{\gamma\alpha_2\gamma\beta_2}\delta_{\alpha_1\alpha}\delta_{\beta_1\beta}\right] \\ &+\frac{1}{2}\sum_{\gamma}\left[V_{\alpha_1\gamma\gamma\beta_1}\delta_{\alpha_2\alpha}\delta_{\beta_2\beta} - V_{\alpha_1\gamma\gamma\beta_2}\delta_{\alpha_2\alpha}\delta_{\beta_1\beta} - V_{\alpha_2\gamma\gamma\beta_1}\delta_{\alpha_1\alpha}\delta_{\beta_2\beta} + V_{\alpha_2\gamma\gamma\beta_2}\delta_{\alpha_1\alpha}\delta_{\beta_1\beta}\right].\end{aligned} \tag{B.51}$$

When the initial hot carrier is an electron, the two remaining terms are

$$\begin{aligned}\left\langle e_{0i}e_{0j}h_{mk}h_{0l} \,\middle|\, \mathcal{H}^{(2)} \,\middle|\, e_{ng}h_{0l} \right\rangle &= -\frac{1}{2}\left[V_{e_{0i}e_{0j}e_{ng}h_{mk}}\delta_{h_{0l}h_{0l}} + V_{e_{0j}e_{0i}e_{ng}h_{mk}}\delta_{h_{0l}h_{0l}}\right] \\ &= -\frac{1}{2}\left(\left\langle e_{0i}e_{0j} \,\middle|\, V \,\middle|\, e_{ng}h_{mk}\right\rangle - \left\langle e_{0j}e_{0i} \,\middle|\, V \,\middle|\, e_{ng}h_{mk}\right\rangle\right).\end{aligned} \tag{B.52}$$

Again, there is zero contribution from equation B.51 when the initial hot carrier is a hole. Summation of equations B.45 and B.52 results in the total matrix element for direct carrier multiplication where the initial hot carrier is an electron:

$$\begin{aligned}\left\langle e_{0i}e_{0j}h_{mk}h_{0l} \,\middle|\, \mathcal{H}^{(2)} \,\middle|\, e_{ng}h_{0l} \right\rangle = &\frac{1}{2}\left(\left\langle e_{0i}e_{0j} \,\middle|\, V \,\middle|\, h_{mk}e_{ng}\right\rangle - \left\langle e_{0j}e_{0i} \,\middle|\, V \,\middle|\, h_{mk}e_{ng}\right\rangle\right) \\ &-\frac{1}{2}\left(\left\langle e_{0i}e_{0j} \,\middle|\, V \,\middle|\, e_{ng}h_{mk}\right\rangle - \left\langle e_{0j}e_{0i} \,\middle|\, V \,\middle|\, e_{ng}h_{mk}\right\rangle\right).\end{aligned} \tag{B.53}$$

REFERENCES

[1] International Energy Agency. *World Energy Outlook 2014, Executive Summary*. URL: http://www.iea.org/textbase/npsum/weo2014sun.pdf.

[2] Shahriar Shafiee and Erkan Topal. 'When will fossil fuel reserves be diminished?' In: *Energy Policy* 37.1 (2009), pp. 181–189. ISSN: 0301-4215. DOI: http://dx.doi.org/10.1016/j.enpol.2008.08.016. URL: http://www.sciencedirect.com/science/article/pii/S0301421508004126.

[3] NASA. *Global Climate change–Cital Signs of the Planet*. URL: http://climate.nasa.gov/vital-signs/global-temperature/.

[4] Center for Climate and Energy Solutions. *Outcomes of the U.N. Climate Chance Conference in Paris*. URL: http://www.c2es.org/docUploads/cop-21-paris-summary-12-2015-final.pdf.

[5] William Shockley and Hans J. Queisser. 'Detailed Balance Limit of Efficiency of p-n Junction Solar Cells'. In: *Journal of Applied Physics* 32.3 (1961), pp. 510–519. DOI: http://dx.doi.org/10.1063/1.1736034. URL: http://scitation.aip.org/content/aip/journal/jap/32/3/10.1063/1.1736034.

[6] *Solar Energy Research*. University of Wisconsin Press, Madison, 1955. Chap. Maximum Efficiency of Solar Energy Conversion by Quantum Processes.

[7] Alexander P. Kirk. *Chapter 3 - Device Operation*. Oxford: Academic Press, 2015, pp. 25–56. ISBN: 978-0-12-802329-7. DOI: http://dx.doi.org/10.1016/B978-0-12-802329-7.00003-1. URL: http://www.sciencedirect.com/science/article/pii/B9780128023297000031.

[8] Antonio Luque and Antonio Martí. 'Increasing the Efficiency of Ideal Solar Cells by Photon Induced Transitions at Intermediate Levels'. In: *Phys. Rev. Lett.* 78 (26 June 1997), pp. 5014–5017. DOI: 10.1103/PhysRevLett.78.5014. URL: http://link.aps.org/doi/10.1103/PhysRevLett.78.5014.

[9] Antonio Luque and Antonio Martí. 'The Intermediate band Solar Cell: Progress Toward the Realization of an Attractive Concept'. In: *Advanced Matrials* 22 (2010), pp. 160–174.

[10] Antonio Luque, Antonio Martí and Arthur J. Nozik. 'Solar Cells Based on Quantum Dots: Multiple Exciton Generation and Intermediate Bands'. In: *MRS Bulletin* 32 (03 2007), pp. 236–241. ISSN: 1938-1425. DOI: 10.1557/mrs2007.28. URL: http://journals.cambridge.org/article_S0883769400006928.

[11] P. T. Landsberg, H. Nussbaumer and G. Willeke. 'Band-band impact ionization and solar cell efficiency'. In: *Journal of Applied Physics* 74.2 (1993), pp. 1451–1452. DOI: http://dx.doi.org/10.1063/1.354886. URL: http://scitation.aip.org/content/aip/journal/jap/74/2/10.1063/1.354886.

[12] Sabine Kolodinski et al. 'Quantum efficiencies exceeding unity due to impact ionization in silicon solar cells'. In: *Applied Physics Letters* 63.17 (1993), pp. 2405–2407. DOI: http://dx.doi.org/10.1063/1.110489. URL: http://scitation.aip.org/content/aip/journal/apl/63/17/10.1063/1.110489.

[13] Arthur J. Nozik. 'SPECTROSCOPY AND HOT ELECTRON RELAXATION DYNAMICS IN SEMICONDUCTOR QUANTUM WELLS AND QUANTUM DOTS'. In: *Annual Review of Physical Chemistry* 52.1 (2001). PMID: 11326064, pp. 193–231. DOI: 10.1146/annurev.physchem.52.1.193. eprint: http://dx.doi.org/10.1146/annurev.physchem.52.1.193. URL: http://dx.doi.org/10.1146/annurev.physchem.52.1.193.

[14] Benisty, H. and Sotomayor-Torrès, C. M. and Weisbuch, C. 'Intrinsic mechanism for the poor luminescence properties of quantum-box systems'. In: *Phys. Rev. B* 44 (19 Nov. 1991), pp. 10945–10948. DOI: 10.1103/PhysRevB.44.10945. URL: http://link.aps.org/doi/10.1103/PhysRevB.44.10945.

[15] Stanko Tomić, Andrew Sunderland and Ian Bush. 'Parallel multi-band k.p code for electronic structure of zinc blend semiconductor quantum dots'. In: *Journal of Materials Chemistry* 16 (2006), pp. 1963–1972.

[16] A.E. Becquerel. 'Mémoire sur les effets électriques produits sous l'influence des reyons solaires'. In: *Compt. rend.* 9 (1839), pp. 561–567.

[17] Richard Williams. 'Becquerel Photovoltaic Effect in Binary Compounds'. In: *The Journal of Chemical Physics* 32.5 (1960), pp. 1505–1514. DOI: http://dx.doi.org/10.1063/1.1730950. URL: http://scitation.aip.org/content/aip/journal/jcp/32/5/10.1063/1.1730950.

[18] W. Smith. 'The action of light on selenium'. In: *Telegraph Engineers, Journal of the Society of* 2.4 (1873), pp. 31–33. DOI: 10.1049/jste-1.1873.0023.

[19] F. Braun. *Semiconductor Devices: Pioneering Papers*. Ed. by S.M. Sze. 1991. Chap. On the current conduction in metal sulphides.

[20] F. Braun. 'Uber die Stromleitung durch Schwefelmetalic'. In: *Annalen der Physik and Chemie* 153.4 (1876), pp. 556–563.

[21] Peter Y. Yu and Manuel Cardona. *Fundamentals of Semiconductors, Physics and Materials Properties*. Springer, 1996. ISBN: 3-540-58307-6.

[22] E. Wigner and F. Seitz. 'On the Constitution of Metallic Sodium'. In: *Phys. Rev.* 43 (10 May 1933), pp. 804–810. DOI: 10.1103/PhysRev.43.804. URL: http://link.aps.org/doi/10.1103/PhysRev.43.804.

[23] Jan Czochralski. 'Ein neues Verfahren zur Messung der Kristallisationsgeschwindigkeit der Metalle'. In: *Zeitchrift f u Physikalische Chemie* (1918).

[24] Robert S. Feigelson. '1 - Crystal Growth through the Ages: A Historical Perspective'. In: *Handbook of Crystal Growth (Second Edition)*. Ed. by Tatau Nishinaga. Second Edition. Boston: Elsevier, 2015, pp. 1–83. ISBN: 978-0-444-56369-9. DOI: http://dx.doi.org/10.1016/B978-0-444-56369-9.00001-0. URL: http://www.sciencedirect.com/science/article/pii/B9780444563699000010.

[25] J.J. Derby, L.J. Atherton and P.M. Gresho. 'An integrated process model for the growth of oxide crystals by the Czochralski method'. In: *Journal of Crystal Growth* 97.3 (1989), pp. 792–826. ISSN: 0022-0248. DOI: http://dx.doi.org/10.1016/0022-0248(89)90583-6. URL: http://www.sciencedirect.com/science/article/pii/0022024889905836.

[26] J. H. Scaff and R. S. Ohl. 'Development of Silicon Crystal Rectifiers for Microwave Radar Receivers'. In: *Bell System Technical Journal* 26.1 (1947), pp. 1–30. ISSN: 1538-7305. DOI: 10.1002/j.1538-7305.1947.tb01310.x. URL: http://dx.doi.org/10.1002/j.1538-7305.1947.tb01310.x.

[27] R.S. Ohl. *Light-sensitive electric device*. US Patent 2,402,662. June 1946. URL: http://www.google.co.uk/patents/US2402662.

[28] Charles E. Fritts. 'On a New Form of Selenium Photocell'. In: *Americal Journal of Science* 26 (1883), pp. 465–472.

[29] W. Shockley. 'The Theory of p-n Junctions in Semiconductors and p-n Junction Transistors'. In: *Bell System Technical Journal* 28.3 (1949), pp. 435–489. ISSN: 1538-7305. DOI: 10.1002/j.1538-7305.1949.tb03645.x. URL: http://dx.doi.org/10.1002/j.1538-7305.1949.tb03645.x.

[30] C. t. Sah, R. N. Noyce and W. Shockley. 'Carrier Generation and Recombination in P-N Junctions and P-N Junction Characteristics'. In: *Proceedings of the IRE* 45.9 (1957), pp. 1228–1243. ISSN: 0096-8390. DOI: 10.1109/JRPROC.1957.278528.

[31] W. Shockley and W. T. Read. 'Statistics of the Recombinations of Holes and Electrons'. In: *Phys. Rev.* 87 (5 1952), pp. 835–842. DOI: 10.1103/PhysRev.87.835. URL: http://link.aps.org/doi/10.1103/PhysRev.87.835.

[32] R. N. Hall. 'Electron-Hole Recombination in Germanium'. In: *Phys. Rev.* 87 (2 1952), pp. 387–387. DOI: 10.1103/PhysRev.87.387. URL: http://link.aps.org/doi/10.1103/PhysRev.87.387.

[33] M.A. Green et al. 'Solar cell efficiency tables (version 46)'. In: *Progress in Photovoltaics Research and Applications* (June 2015), pp. 805–812.

[34] K. Masuko et al. 'Achievement of more than 25% conversion efficiency with crystalline silicon heterojunction solar cell.' In: *IEEE Journal of Photovoltaics 2014* 4.6 (2014).

[35] T. Tibbits et al. 'New efficiency frontiers with wafer-bonded multi-junction solar cells'. In: *Proceedings of the 29th European Photovoltaic Solar energy Conference* (2014), pp. 1975–1978.

[36] Fraunhofer Institute for solar energy systems. Press Release. 2014. URL: https://www.ise.fraunhofer.de/en/press-and-media/press-releases/press-releases-2014/new-world-record-for-solar-cell-efficiency-at-46-percent.

[37] J. Zhao et al. '20 000 PERL silicon cells for the '1996 World Solar Challenge' solar car race'. In: *Prog. Photovolt: Res. Appl.* 5 (1997), pp. 269–276. DOI: 10.1002/(SICI)1099-159X(199707/08)5:4<269::AID-PIP174>3.0.CO;2-1.

[38] Donlad A. Neamen. *Semiconductor Physics and Devices, Basic Principles*. 3rd ed. McGraw-Hill, 2003.

[39] Niel W. Ashcroft and N. David. Mermin. *Solid State Physics*. Saunders College, 1976.

[40] Jacques I Pankove. *Optical processes in semiconductors*. Courier Corporation, 2012.

[41] S.M. Sze. *Physics of Semiconductor Devices*. 3rd ed. Wiley, 1981.

[42] A.J. Nozik. 'Chapter 15 - Quantum Structured Solar Cells'. In: *Nanostructured Materials for Solar Energy Conversion*. Ed. by Tetsuo Soga. Amsterdam: Elsevier, 2006, pp. 485–516. ISBN: 978-0-444-52844-5. DOI: http://dx.doi.org/10.1016/B978-044452844-5/50016-0. URL: http://www.sciencedirect.com/science/article/pii/B9780444528445500160.

[43] Jasprit Singh. *Electronic and Optoelectronic Properties of Semiconductors*. Cambridge University Press. Chap. 5.5.

[44] Jasprit Singh. *Physics of semiconductors and Their Heterostructures*. McGraw-Hill Electrical and Computer engineering Series. McGraw-Hill.

[45] P. A. M. Dirac. 'The Quantum Theory of the Emission and Absorption of Radiation'. In: *Proceedings of the Royal Society of London A: Mathematical, Physical and Engineering Sciences* 114.767 (1927), pp. 243–265. ISSN: 0950-1207. DOI: 10.1098/rspa.1927.0039. eprint: http://rspa.royalsocietypublishing.org/content/114/767/243.full.pdf. URL: http://rspa.royalsocietypublishing.org/content/114/767/243.

[46] Leonard I. Schiff. *Quantum Mechanics*. 3rd ed. McGraw Hill Education.

[47] Enrico Fermi. *Nuclear Physics*. page 142. University of Chicargo Press. Chap. 8.

[48] M.C. Hanna and A.J. Nozik. 'Solar conversion efficiency of photovoltaic and photoelectrolysis cells with carrier multiplication absorbers'. In: *Journal of Applied Physics* 100.7, 074510 (2006), pages. DOI: http://dx.doi.org/10.1063/1.2356795. URL: http://scitation.aip.org/content/aip/journal/jap/100/7/10.1063/1.2356795.

[49] Antonio Luque and Steven Hegedus, eds. *Handbook of Photovoltaic Science and Engineering*. Wiley, 2003. ISBN: 0-471-49196-9.

[50] Masumi Takeshima. 'Auger recombination in InAs, GaSb, InP, and GaAs'. In: *Journal of Applied Physics* 43.10 (1972), pp. 4114–4119. DOI: http://dx.doi.org/10.1063/1.1660882. URL: http://scitation.aip.org/content/aip/journal/jap/43/10/10.1063/1.1660882.

[51] U. Strauss, W.W. Rühle and K. Köhler. 'Auger recombination in intrinsic GaAs'. In: *Applied Physics Letters* 62.1 (1993), pp. 55–57. DOI: http://dx.doi.org/10.1063/1.108817. URL: http://scitation.aip.org/content/aip/journal/apl/62/1/10.1063/1.108817.

[52] B. R. Bennett, R. A. Soref and J. A. Del Alamo. 'Carrier-induced change in refractive index of InP, GaAs and InGaAsP'. In: *IEEE Journal of Quantum Electronics* 26.1 (Jan. 1990), pp. 113–122. ISSN: 0018-9197. DOI: 10.1109/3.44924.

[53] A. A. Guzelian et al. 'Colloidal chemical synthesis and characterization of InAs nanocrystal quantum dots'. In: *Applied Physics Letters* 69.10 (1996), pp. 1432–1434. DOI: http://dx.doi.org/10.1063/1.117605. URL: http://scitation.aip.org/content/aip/journal/apl/69/10/10.1063/1.117605.

[54] Shigeo Yamaguchi et al. 'Thermoelectric properties and figure of merit of a Te-doped InSb bulk single crystal'. In: *Applied Physics Letters* 87.20, 201902 (2005). DOI: http://dx.doi.org/10.1063/1.2130390. URL: http://scitation.aip.org/content/aip/journal/apl/87/20/10.1063/1.2130390.

[55] A R Beattie, R A Abram and P Scharoch. 'Realistic evaluation of impact ionisation and Auger recombination rates for the ccch transition in InSb and InGaAsP'. In: *Semiconductor Science and Technology* 5.7 (1990), p. 738. URL: http://stacks.iop.org/0268-1242/5/i=7/a=018.

[56] Xavier P. Maldague. *Theory and Practivce of Infrared Technology for Nondestructive Testing*. Wiley, 2001. ISBN: 978-0-471-18190-3.

[57] S Marchetti, M Martinelli and R Simili. 'The InSb Auger recombination coefficient derived from the IR-FIR dynamical plasma reflectivity'. In: *Journal of Physics: Condensed Matter* 13.33 (2001), p. 7363. URL: http://stacks.iop.org/0953-8984/13/i=33/a=316.

[58] Stephen T. Thorn and Andrew Rex. *Modern Physics for Scientists and Engineers*. 2nd ed. 2005. ISBN: 0534417817.

[59] Mahesh R. Junnarkar and R. R. Alfano. 'Photogenerated high-density electron-hole plasma energy relaxation and experimental evidence for rapid expansion of the electron-hole plasma in CdSe'. In: *Phys. Rev. B* 34 (10 Nov. 1986), pp. 7045–7062. DOI: 10.1103/PhysRevB.34.7045. URL: http://link.aps.org/doi/10.1103/PhysRevB.34.7045.

[60] L. A. Padilha et al. 'Recombination processes in CdTe quantum-dot-doped glasses'. In: *Applied Physics Letters* 85.15 (2004), pp. 3256–3258. DOI: http://dx.doi.org/10.1063/1.1801683. URL: http://scitation.aip.org/content/aip/journal/apl/85/15/10.1063/1.1801683.

[61] E. D. Palik, D. L. Mitchell and J. N. Zemel. 'Magneto-Optical Studies of the Band Structure of PbS'. In: *Phys. Rev.* 135 (3A Aug. 1964), A763–A778. DOI: 10.1103/PhysRev.135.A763. URL: http://link.aps.org/doi/10.1103/PhysRev.135.A763.

[62] J. Vaitkus et al. 'Picosecond photoconductivity of CdSe and CdTe thin films'. In: *Journal of Crystal Growth* 101.1 (1990), pp. 826–827. ISSN: 0022-0248. DOI: http://dx.doi.org/10.1016/0022-0248(90)91088-8. URL: http://www.sciencedirect.com/science/article/pii/0022024890910888.

[63] H. Preier. 'Recent advances in lead-chalcogenide diode lasers'. In: *Applied physics* 20.3 (), pp. 189–206. ISSN: 1432-0630. DOI: 10.1007/BF00886018. URL: http://dx.doi.org/10.1007/BF00886018.

[64] P. C. Findlay et al. 'Auger recombination dynamics of lead salts under picosecond free-electron-laser excitation'. In: *Phys. Rev. B* 58 (19 Nov. 1998),

pp. 12908–12915. DOI: 10.1103/PhysRevB.58.12908. URL: http://link.aps.org/doi/10.1103/PhysRevB.58.12908.

[65] 'CHAPTER 11 - Auger Recombination'. In: *Nonradiative Recombination in Semiconductors*. Ed. by V.I. PEREL V.N. ABAKUMOV and I.N. YASSIEVICH. Vol. 33. Modern Problems in Condensed Matter Sciences. Elsevier, 1991, pp. 189–226. DOI: http://dx.doi.org/10.1016/B978-0-444-88854-9.50018-7. URL: http://www.sciencedirect.com/science/article/pii/B9780444888549500187.

[66] Jenny Nelson. *The Physics of Solar Cells*. Imperial College Press, 2003.

[67] Peter Würfel. *Physics of Solar Cells: From Principles to New Concepts*. Wiley, 2005. ISBN: 9783527404285.

[68] E.D. Jackson. *Solar energy Converter*. US Patent 2,949,498 A. 1955. URL: http://www.google.co.uk/patents/US2949498.

[69] 'Leo Esaki - Biographical'. In: *nobel Lectures, Physics 1971-1980* (1992). Ed. by Stig Lundqvist.

[70] Simon P. Philipps, Frank Dimroth and Andreas W. Bett. *Solar Cells–Materials, Manufacture and Operation*. Ed. by Augustin McEvoy, Tom Markvart and Luis Castañer. 2nd ed. 2013. Chap. 6. ISBN: 978-0-12-386964-7.

[71] Alexis de Vos. 'Limit of the Efficiency of Tandem Solar Cells'. In: *J. Phys. D: Appl. Phys.* 13 (1980), pp. 839–846.

[72] C. H. Henry. 'Limiting efficiencies of ideal single and multiple energy gap terrestrial solar cells'. In: *Journal of Applied Physics* 51.8 (1980), pp. 4494–4500. DOI: http://dx.doi.org/10.1063/1.328272. URL: http://scitation.aip.org/content/aip/journal/jap/51/8/10.1063/1.328272.

[73] William H. Press. 'Theoretical Maximum for Energy from Direct and Diffuse sunlight'. In: *Nature* 264 (1976), pp. 734–735.

[74] R. R. King et al. '40% efficienct metamorphic GaInP/GaInAs/Ge multijunction solar cells'. In: *Applied Physics Letters* 90.18, 183516 (2007). DOI: http://dx.doi.org/10.1063/1.2734507. URL: http://scitation.aip.org/content/aip/journal/apl/90/18/10.1063/1.2734507.

[75] Andrew S Brown, Martin A Green and Richard P Corkish. 'Limiting efficiency for a multi-band solar cell containing three and four bands'. In: *Physica E: Low-dimensional Systems and Nanostructures* 14.1 (2002), pp. 121–125. ISSN: 1386-9477. DOI: http://dx.doi.org/10.1016/S1386-9477(02)00375-2. URL: http://www.sciencedirect.com/science/article/pii/S1386947702003752.

[76] Gavin Conibeer. 'Third Generation Photovoltaics'. In: *Materials Today* 10.11 (2007).

[77] Stanko Tomić. 'Intermediate-band solar cells: Influence of band formation on dynamical processes in InAs/GaAs quantum dot arrays'. In: *Physics Review B* 82 (2010).

[78] A. Marti, L. Cuadra and A. Luque. 'Quantum dot intermediate band solar cell'. In: *Photovoltaic Specialists Conference, 2000. Conference Record of the Twenty-Eighth IEEE*. 2000, pp. 940–943. DOI: 10.1109/PVSC.2000.916039.

[79] Rune Strandberg and Turid Worren Reenaas. 'Photofilling of intermediate bands'. In: *Journal of Applied Physics* 105.12, 124512 (2009). DOI: http://dx.doi.org/10.1063/1.3153141. URL: http://scitation.aip.org/content/aip/journal/jap/105/12/10.1063/1.3153141.

[80] A. Martí et al. 'Production of Photocurrent due to Intermediate to Conduction Band Transitions: A Demonstration of a Key Operating Principle of the Intermediate-Band Solar Cell'. In: *Phys. Rev. Lett.* 97 (24 Dec. 2006), p. 247701. DOI: 10.1103/PhysRevLett.97.247701. URL: http://link.aps.org/doi/10.1103/PhysRevLett.97.247701.

[81] S. A. Blokhin et al. 'AlGaAs/GaAs photovoltaic cells with an array of InGaAs QDs'. In: *Semiconductors* 43.4 (2009), pp. 514–518. ISSN: 1090-6479. DOI: 10.1134/S1063782609040204. URL: http://dx.doi.org/10.1134/S1063782609040204.

[82] T. Trupke, M. A. Green and P. Würfel. 'Improving solar cell efficiencies by down-conversion of high-energy photons'. In: *Journal of Applied Physics* 92.3 (2002), pp. 1668–1674. DOI: http://dx.doi.org/10.1063/1.1492021. URL: http://scitation.aip.org/content/aip/journal/jap/92/3/10.1063/1.1492021.

[83] M.C. Beard and R.J. Ellingson. 'Multiple exciton generation in semiconductor nanocrystals: Toward efficient solar energy conversion'. In: *Laser & Photonics Reviews* 2.5 (2008), pp. 377–399. ISSN: 1863-8899. DOI: 10.1002/lpor.200810013. URL: http://dx.doi.org/10.1002/lpor.200810013.

[84] David J. Binks. 'Multiple exciton generation in nanocrystal quantum dots - controversy, current status and future prospects'. In: *Phys. Chem. Chem. Phys.* 13 (28 2011), pp. 12693–12704. DOI: 10.1039/C1CP20225A. URL: http://dx.doi.org/10.1039/C1CP20225A.

[85] Randy J. Ellingson et al. 'Highly Efficient Multiple Exciton Generation in Colloidal PbSe and PbS Quantum Dots'. In: *Nano Letters* 5.5 (2005). PMID: 15884885, pp. 865–871. DOI: 10.1021/nl0502672. eprint: http://dx.doi.org/10.1021/nl0502672. URL: http://dx.doi.org/10.1021/nl0502672.

[86] Richard D. Schaller, Melissa A. Petruska and Victor I. Klimov. 'Effect of electronic structure on carrier multiplication efficiency: Comparative study of PbSe and CdSe nanocrystals'. In: *Applied Physics Letters* 87 (2005). DOI: 10.1063/1.2142092. URL: http://dx.doi.org/10.1063/1.2142092.

[87] Richard D. Schaller et al. 'Seven Excitons at a Cost of One: Redefining the Limits for Conversion Efficiency of Photons into Charge Carriers'. In: *Nano Letters* 6.3 (2006). PMID: 16522035, pp. 424–429. DOI: 10.1021/

nl052276g. eprint: http://dx.doi.org/10.1021/nl052276g. URL: http://dx.doi.org/10.1021/nl052276g.

[88] Richard D. Schaller, Jeffrey M. Pietryga and Victor I. Klimov. 'Carrier Multiplication in InAs Nanocrystal Quantum Dots with an Onset Defined by the Energy Conservation Limit'. In: *Nano Letters* 7.11 (2007). PMID: 17967043, pp. 3469–3476. DOI: 10.1021/nl072046x. eprint: http://dx.doi.org/10.1021/nl072046x. URL: http://dx.doi.org/10.1021/nl072046x.

[89] Matthew C. Beard et al. 'Comparing Multiple Exciton Generation in Qunatum Dots to Impact Ionisation in Bulk Semiconductors: Implications for Enhancement of Solar Energy Conversion'. In: *Nano Letters* 10 (2010), pp. 3019–3027. DOI: 10.1021/nl101490z.

[90] Arthur J. Nozik. 'Multiple exciton generation in semiconductor quantum dots'. In: *Chemical Physics Letters* 457.1 (2008), pp. 3–11. ISSN: 0009-2614. DOI: http://dx.doi.org/10.1016/j.cplett.2008.03.094. URL: http://www.sciencedirect.com/science/article/pii/S000926140800479X.

[91] Victor I. Klimov. 'Detailed-balance power conversion limits of nanocrystal-quantum-dot solar cells in the presence of carrier multiplication'. In: *Applied Physics Letters* 89.12 (2006). DOI: http://dx.doi.org/10.1063/1.2356314. URL: http://scitation.aip.org/content/aip/journal/apl/89/12/10.1063/1.2356314.

[92] Peter Würfel. 'Solar energy conversion with hot electrons from impact ionisation'. In: *Solar Energy Materials and Solar Cells* 46.1 (1997), pp. 43–52. ISSN: 0927-0248. DOI: http://dx.doi.org/10.1016/S0927-0248(96)00092-X. URL: http://www.sciencedirect.com/science/article/pii/S092702489600092X.

[93] A.I. Ekimov and A.A.Onushchenko. 'Quantum size effect in three-dimensional microscopic semiconductor crystals'. In: *JETP Lett.* 34.6 (1981). URL: http://www.jetpletters.ac.ru/ps/1517/article_23187.pdf.

[94] Frank W. Wise. 'Lead Salt Quantum Dots: the Limit of Strong Quantum Confinement'. In: *Accounts of Chemical Research* 33.11 (2000). PMID: 11087314, pp. 773–780. DOI: 10.1021/ar970220q. eprint: http://dx.doi.org/10.1021/ar970220q. URL: http://dx.doi.org/10.1021/ar970220q.

[95] Jin Young Kim et al. '25th Anniversary Article: Colloidal Quantum Dot Materials and Devices: A Quarter-Century of Advances'. In: *Advanced Materials* 25 (2013), pp. 4986–5010.

[96] Tom Wenckebach. *Essentials of Semiconductors*. Wiley, 1999. ISBN: 0-471-96540-5.

[97] Nenad Vukmirovć and Stanko Tomić. 'Plane wave methodology for single quantum dot electronic structure calculations'. In: *Journal of Applied Physics* 103.10, 103718 (2008). DOI: http://dx.doi.org/10.1063/1.2936318. URL: http://scitation.aip.org/content/aip/journal/jap/103/10/10.1063/1.2936318.

[98] Charles Kittel. *Introduction to Solid State Physics*. 8th ed. Wiley, 2005. ISBN: 0-471-41526-X.

[99] R. Dingle, W. Wiegmann and C. H. Henry. 'Quantum States of Confined Carriers in Very Thin $Al_xGa_{1-x}As$-GaAs-$Al_xGa_{1-x}As$ Heterostructures'. In: *Phys. Rev. Lett.* 33 (14 1974), pp. 827–830. DOI: 10.1103/PhysRevLett.33.827. URL: http://link.aps.org/doi/10.1103/PhysRevLett.33.827.

[100] Bart Van Zeghbroeck. *Principles of Semiconductor Devices*. 2011. URL: http://ecee.colorado.edu/~bart/book/.

[101] Catherine J Murphy, Nikhil R Jana et al. 'Controlling the aspect ratio of inorganic nanorods and nanowires'. In: *Advanced Materials* 14.1 (2002), p. 80.

[102] B.D. Busbee, S.O. Obare and C.J. Murphy. 'An Improved Synthesis of High-Aspect-Ratio Gold Nanorods'. In: *Advanced Materials* 15.5 (2003),

pp. 414–416. ISSN: 1521-4095. DOI: 10.1002/adma.200390095. URL: http://dx.doi.org/10.1002/adma.200390095.

[103] S.M. Sze. *Physics os Semiconductor Devices*. 3rd ed. Wiley, 2007. ISBN: 0-0471-14323-5.

[104] E. Borovitskaga and M. S. Shur. *Quantum Dots*. Ed. by E. Borovitskaga and M. S. Shur. Vol. 25. Selected Topics in Electronics and Systems. EBSCO Publishing.

[105] H. P. Rocksby. 'The Colour of Selenium Ruby Glasses'. In: *Journal of the Society of Glass Technology* 16 (1932).

[106] M. A. Reed et al. 'Observation of discrete electronic states in a zero-dimensional semiconductor nanostructure'. In: *Phys. Rev. Lett.* 60 (6 Feb. 1988), pp. 535–537. DOI: 10.1103/PhysRevLett.60.535. URL: http://link.aps.org/doi/10.1103/PhysRevLett.60.535.

[107] L. E. Brus. 'Electron-electron and electron-hole interactions in small semiconductor crystallites: The size dependence of the lowest excited electronic state'. In: *The Journal of Chemical Physics* 80.9 (1984), pp. 4403–4409. DOI: http://dx.doi.org/10.1063/1.447218. URL: http://scitation.aip.org/content/aip/journal/jcp/80/9/10.1063/1.447218.

[108] Louis Brus. 'Electronic wave functions in semiconductor clusters: experiment and theory'. In: *The Journal of Physical Chemistry* 90.12 (1986), pp. 2555–2560. DOI: 10.1021/j100403a003. eprint: http://dx.doi.org/10.1021/j100403a003. URL: http://dx.doi.org/10.1021/j100403a003.

[109] A.I. Ekimov, A.L. Efros and A.A. Onushchenko. 'Quantum Size Effect in Semiconductor Microcrystals'. In: *Solid State Communications* 56.11 (1985), pp. 921–924.

[110] C. B. Murray, D. J. Norris and M. G. Bawendi. 'Synthesis and characterization of nearly monodisperse CdE (E = sulfur, selenium, tellurium) semiconductor nanocrystallites'. In: *Journal of the American Chemical Soci-*

ety 115.19 (1993), pp. 8706–8715. DOI: 10.1021/ja00072a025. eprint: http://dx.doi.org/10.1021/ja00072a025. URL: http://dx.doi.org/10.1021/ja00072a025.

[111] D. Leonard et al. 'Direct formation of quantum-sized dots from uniform coherent islands of InGaAs on GaAs surfaces'. In: *Applied Physics Letters* 63.23 (1993), pp. 3203–3205. DOI: http://dx.doi.org/10.1063/1.110199. URL: http://scitation.aip.org/content/aip/journal/apl/63/23/10.1063/1.110199.

[112] A. E. Zhukov et al. 'Injection heterolaser based on an array of vertically aligned InGaAs quantum dots in a AlGaAs matrix'. In: *Semiconductors* 31.4 (), pp. 411–414. ISSN: 1090-6479. DOI: 10.1134/1.1187173. URL: http://dx.doi.org/10.1134/1.1187173.

[113] R. Leon et al. 'Visible luminescence from semiconductor quantum dots in large ensembles'. In: *Applied Physics Letters* 67.4 (1995), pp. 521–523. DOI: http://dx.doi.org/10.1063/1.115175. URL: http://scitation.aip.org/content/aip/journal/apl/67/4/10.1063/1.115175.

[114] A.F. Tsatsulńikov et al. 'Optical properties of InAlAs quantum dots in an AlGaAs matrix'. In: *Applied Surface Science* 123-124 (1998), pp. 381–384. ISSN: 0169-4332. DOI: http://dx.doi.org/10.1016/S0169-4332(97)00493-5. URL: http://www.sciencedirect.com/science/article/pii/S0169433297004935.

[115] C.B. Murray et al. 'Colloidal synthesis of nanocrystals and nanocrystal superlattices'. In: *IBM J. Res. & Dev.* 45.1 (2001). URL: http://citeseerx.ist.psu.edu/viewdoc/download?doi=10.1.1.83.9060&rep=rep1&type=pdf.

[116] C.B. Murray, C.R. Kagan and M.G. Bawendi. 'Synthesis and Characterisation of Monodisperse Nanocrystals and Close-Packed Nanocrystal As-

semblies'. In: *Annu. Rev. Mater. Sci.* 30 (2000), pp. 545–610. URL: http://www.annualreviews.org/doi/pdf/10.1146/annurev.matsci.30.1.545.

[117] Weigang Lu et al. 'Shape Evolution and Self Assembly of Monodisperse PbTe Nanocrystals'. In: *Journal of the American Chemical Society* 126.38 (2004). PMID: 15382907, pp. 11798–11799. DOI: 10.1021/ja0469131. eprint: http://dx.doi.org/10.1021/ja0469131. URL: http://dx.doi.org/10.1021/ja0469131.

[118] L. Pavesi et al. 'Optical gain in silicon nanocrystals'. In: *Nature* 408.6811 (Nov. 2000), pp. 440–444. ISSN: 0028-0836. DOI: 10.1038/35044012. URL: http://dx.doi.org/10.1038/35044012.

[119] Goki Eda et al. 'Blue Photoluminescence from Chemically Derived Graphene Oxide'. In: *Advanced Materials* 22.4 (2010), pp. 505–509. ISSN: 1521-4095. DOI: 10.1002/adma.200901996. URL: http://dx.doi.org/10.1002/adma.200901996.

[120] D. S. Boudreaux, F. Williams and A. J. Nozik. 'Hot carrier injection at semiconductor-electrolyte junctions'. In: *Journal of Applied Physics* 51.4 (1980), pp. 2158–2163. DOI: http://dx.doi.org/10.1063/1.327889. URL: http://scitation.aip.org/content/aip/journal/jap/51/4/10.1063/1.327889.

[121] U. Bockelmann and G. Bastard. 'Phonon scattering and energy relaxation in two-, one-, and zero-dimensional electron gases'. In: *Phys. Rev. B* 42 (14 Nov. 1990), pp. 8947–8951. DOI: 10.1103/PhysRevB.42.8947. URL: http://link.aps.org/doi/10.1103/PhysRevB.42.8947.

[122] H. Benisty. 'Reduced electron-phonon relaxation rates in quantum-box systems: Theoretical analysis'. In: *Phys. Rev. B* 51 (19 May 1995), pp. 13281–13293. DOI: 10.1103/PhysRevB.51.13281. URL: http://link.aps.org/doi/10.1103/PhysRevB.51.13281.

[123] R. D. Schaller and V. I. Klimov. 'High Efficiency Carrier Multiplication in PbSe Nanocrystals: Implications for Solar Energy Conversion'. In: *Phys. Rev. Lett.* 92 (18 2004), p. 186601. DOI: 10.1103/PhysRevLett.92.186601. URL: http://link.aps.org/doi/10.1103/PhysRevLett.92.186601.

[124] U. Bockelmann and T. Egeler. 'Electron relaxation in quantum dots by means of Auger processes'. In: *Phys. Rev. B* 46 (23 Dec. 1992), pp. 15574–15577. DOI: 10.1103/PhysRevB.46.15574. URL: http://link.aps.org/doi/10.1103/PhysRevB.46.15574.

[125] Al. L. Efros and M. Rosen. 'Random Telegraph Signal in the Photoluminescence Intensity of a Single Quantum Dot'. In: *Phys. Rev. Lett.* 78 (6 Feb. 1997), pp. 1110–1113. DOI: 10.1103/PhysRevLett.78.1110. URL: http://link.aps.org/doi/10.1103/PhysRevLett.78.1110.

[126] M. Nirmal et al. 'Fluorescence intermittency in single cadmium selenide nanocrystals'. In: *Nature* 383.6603 (1996), pp. 802–804. DOI: 10.1038/383802a0. URL: http://dx.doi.org/10.1038/383802a0.

[127] Philippe Guyot-Sionnest et al. 'Intraband relaxation in CdSe quantum dots'. In: *Phys. Rev. B* 60 (4 1999), R2181–R2184. DOI: 10.1103/PhysRevB.60.R2181. URL: http://link.aps.org/doi/10.1103/PhysRevB.60.R2181.

[128] Victor I. Klimov and Duncan W. McBranch. 'Femtosecond 1*P*-to- 1*S* Electron Relaxation in Strongly Confined Semiconductor Nanocrystals'. In: *Phys. Rev. Lett.* 80 (18 May 1998), pp. 4028–4031. DOI: 10.1103/PhysRevLett.80.4028. URL: http://link.aps.org/doi/10.1103/PhysRevLett.80.4028.

[129] M. E. Prise et al. 'Picosecond measurement of Auger recombination rates in InGaAs'. In: *Applied Physics Letters* 45.6 (1984), pp. 652–654. DOI: http://dx.doi.org/10.1063/1.95344. URL: http://scitation.aip.org/content/aip/journal/apl/45/6/10.1063/1.95344.

[130] Al. L. Efros, V.A. Kharchenko and M. Rosen. 'Breaking the phonon bottleneck in nanometer quantum dots: Role of Auger-like processes'. In: *Solid State Communications* 93.4 (1995), pp. 281–284. ISSN: 0038-1098. DOI: http://dx.doi.org/10.1016/0038-1098(94)00760-8. URL: http://www.sciencedirect.com/science/article/pii/0038109894007608.

[131] Igor Vurgaftman and Jasprit Singh. 'Steady-state performance of microcavity surface-emitting lasers with quantum confinement of electrons and photons'. In: *Applied Physics Letters* 64.12 (1994), pp. 1472–1474. DOI: http://dx.doi.org/10.1063/1.111889. URL: http://scitation.aip.org/content/aip/journal/apl/64/12/10.1063/1.111889.

[132] Peter C. Sercel. 'Multiphonon-assisted tunneling through deep levels: A rapid energy-relaxation mechanism in nonideal quantum-dot heterostructures'. In: *Phys. Rev. B* 51 (20 1995), pp. 14532–14541. DOI: 10.1103/PhysRevB.51.14532. URL: http://link.aps.org/doi/10.1103/PhysRevB.51.14532.

[133] T. Inoshita and H. Sakaki. 'Electron relaxation in a quantum dot: Significance of multiphonon processes'. In: *Phys. Rev. B* 46 (11 Sept. 1992), pp. 7260–7263. DOI: 10.1103/PhysRevB.46.7260. URL: http://link.aps.org/doi/10.1103/PhysRevB.46.7260.

[134] Takeshi Inoshita and Hiroyuki Sakaki. 'Density of states and phonon-induced relaxation of electrons in semiconductor quantum dots'. In: *Phys. Rev. B* 56 (8 1997), R4355–R4358. DOI: 10.1103/PhysRevB.56.R4355. URL: http://link.aps.org/doi/10.1103/PhysRevB.56.R4355.

[135] F. Williams and A. J. Nozik. 'Solid-state perspectives of the photoelectrochemistry of semiconductor-electrolyte junctions'. In: *Nature* 312.5989 (Nov. 1984), pp. 21–27. DOI: 10.1038/312021a0. URL: http://dx.doi.org/10.1038/312021a0.

[136] Wan Ki Bae et al. 'Controlled Alloying of the Core-Shell Interface in CdSe/CdS Quantum Dots for Suppression of Auger Recombination'. In: *ACS Nano* 7.4 (2013). PMID: 23521208, pp. 3411–3419. DOI: 10.1021/nn4002825. eprint: http://dx.doi.org/10.1021/nn4002825. URL: http://dx.doi.org/10.1021/nn4002825.

[137] Margaret A. Hines and Philippe Guyot-Sionnest. 'Synthesis and Characterization of Strongly Luminescing ZnS-Capped CdSe Nanocrystals'. In: *The Journal of Physical Chemistry* 100.2 (1996), pp. 468–471. DOI: 10.1021/jp9530562. eprint: http://dx.doi.org/10.1021/jp9530562. URL: http://dx.doi.org/10.1021/jp9530562.

[138] Charles T. Smith et al. 'Energy Sturcture of CdSe/CdTe type II colloidal quantum dots—Do phonon bottlenecks remain for thick shells?' In: *Solar Energy Materials & Solar Cells* (2016). DOI: 10.1016/j.solmat.2015.12.015.

[139] L. P. Balet et al. 'Inverted Core/Shell Nanocrystals Continuously Tunable between Type-I and Type-II Localization Regimes'. In: *Nano Letters* 4.8 (2004), pp. 1485–1488. DOI: 10.1021/nl049146c. eprint: http://dx.doi.org/10.1021/nl049146c. URL: http://dx.doi.org/10.1021/nl049146c.

[140] James E. Murphy et al. 'PbTe Colloidal Nanocrystals: Synthesis, Characterization, and Multiple Exciton Generation'. In: *Journal of the American Chemical Society* 128.10 (2006). PMID: 16522105, pp. 3241–3247. DOI: 10.1021/ja0574973. eprint: http://dx.doi.org/10.1021/ja0574973. URL: http://dx.doi.org/10.1021/ja0574973.

[141] Yoichi Kobayashi, Takeshi Udagawa and Naoto Tamai. 'Carrier Multiplication in CdTe Quantum Dots by Single-photon Timing Spectroscopy'. In: *Chemistry Letters* 38.8 (2009), pp. 830–831. DOI: 10.1246/cl.2009.830.

[142] David Gachet et al. 'An Upper Bound to Carrier Multiplication Efficiency in Type II Colloidal Quantum Dots'. In: *Nano Letters* 10.1 (2010). PMID:

19911830, pp. 164–170. DOI: 10.1021/nl903172f. eprint: http://dx.doi.org/10.1021/nl903172f. URL: http://dx.doi.org/10.1021/nl903172f.

[143] J. J. H. Pijpers et al. 'Carrier Multiplication and Its Reduction by Photodoping in Colloidal InAs Quantum Dots'. In: *The Journal of Physical Chemistry C* 112.12 (2008), pp. 4783–4784. DOI: 10.1021/jp800834h. eprint: http://dx.doi.org/10.1021/jp800834h. URL: http://dx.doi.org/10.1021/jp800834h.

[144] Matthew C. Beard et al. 'Multiple Exciton Generation in Colloidal Silicon Nanocrystals'. In: *Nano Letters* 7.8 (2007). PMID: 17645368, pp. 2506–2512. DOI: 10.1021/nl071486l. eprint: http://dx.doi.org/10.1021/nl071486l. URL: http://dx.doi.org/10.1021/nl071486l.

[145] Shujing Wang et al. 'Multiple Exciton Generation in Single-Walled Carbon Nanotubes'. In: *Nano Letters* 10.7 (2010). PMID: 20507082, pp. 2381–2386. DOI: 10.1021/nl100343j. eprint: http://dx.doi.org/10.1021/nl100343j. URL: http://dx.doi.org/10.1021/nl100343j.

[146] Gautham Nair and Moungi G. Bawendi. 'Carrier multiplication yields of CdSe and CdTe nanocrystals by transient photoluminescence spectroscopy'. In: *Phys. Rev. B* 76 (8 Aug. 2007), p. 081304. DOI: 10.1103/PhysRevB.76.081304. URL: http://link.aps.org/doi/10.1103/PhysRevB.76.081304.

[147] Gautham Nair et al. 'Carrier multiplication yields in PbS and PbSe nanocrystals measured by transient photoluminescence'. In: *Phys. Rev. B* 78 (12 Sept. 2008), p. 125325. DOI: 10.1103/PhysRevB.78.125325. URL: http://link.aps.org/doi/10.1103/PhysRevB.78.125325.

[148] Meirav Ben-Lulu et al. 'On the Absence of Detectable Carrier Multiplication in a Transient Absorption Study of InAs/CdSe/ZnSe Core/Shell1/Shell2 Quantum Dots'. In: *Nano Letters* 8.4 (2008). PMID: 18341299, pp. 1207–

1211. DOI: 10.1021/nl080199u. eprint: http://dx.doi.org/10.1021/nl080199u. URL: http://dx.doi.org/10.1021/nl080199u.

[149] Gautham Nair et al. 'Carrier multiplication yields in PbS and PbSe nanocrystals measured by transient photoluminescence'. In: *Phys. Rev. B* 78 (12 2008), p. 125325. DOI: 10.1103/PhysRevB.78.125325. URL: http://link.aps.org/doi/10.1103/PhysRevB.78.125325.

[150] Matthew C. Beard et al. 'Variations in the Quantum Efficiency of Multiple Exciton Generation for a Series of Chemically Treated PbSe Nanocrystal Films'. In: *Nano Letters* 9.2 (2009). PMID: 19170560, pp. 836–845. DOI: 10.1021/nl803600v. eprint: http://dx.doi.org/10.1021/nl803600v. URL: http://dx.doi.org/10.1021/nl803600v.

[151] Milan Sykora et al. 'Effect of Air Exposure on Surface Properties, Electronic Structure, and Carrier Relaxation in PbSe Nanocrystals'. In: *ACS Nano* 4.4 (2010). PMID: 20369900, pp. 2021–2034. DOI: 10.1021/nn100131w. eprint: http://dx.doi.org/10.1021/nn100131w. URL: http://dx.doi.org/10.1021/nn100131w.

[152] John A. McGuire et al. 'New Aspects of Carrier Multiplication in Semiconductor Nanocrystals'. In: *Accounts of Chemical Research* 41.12 (2008). PMID: 19006342, pp. 1810–1819. DOI: 10.1021/ar800112v. eprint: http://dx.doi.org/10.1021/ar800112v. URL: http://dx.doi.org/10.1021/ar800112v.

[153] Aaron G. Midgett et al. 'Flowing versus Static Conditions for Measuring Multiple Exciton Generation in PbSe Quantum Dots'. In: *The Journal of Physical Chemistry C* 114.41 (2010), pp. 17486–17500. DOI: 10.1021/jp1057786. eprint: http://dx.doi.org/10.1021/jp1057786. URL: http://dx.doi.org/10.1021/jp1057786.

[154] Samantha J. O. Hardman et al. 'Electronic and surface properties of PbS nanoparticles exhibiting efficient multiple exciton generation'. In: *Phys.*

Chem. Chem. Phys. 13 (45 2011), pp. 20275–20283. DOI: 10.1039/C1CP22330E. URL: http://dx.doi.org/10.1039/C1CP22330E.

[155] Su-Huai Wei and Alex Zunger. 'Electronic and structural anomalies in lead chalcogenides'. In: *Phys. Rev. B* 55 (20 May 1997), pp. 13605–13610. DOI: 10.1103/PhysRevB.55.13605. URL: http://link.aps.org/doi/10.1103/PhysRevB.55.13605.

[156] G. Bauer. 'Narrow Gap Semiconductors Physics and Applications: Proceedings of the International Summer School Held in Nimes, France, September 3 – 15, 1979'. In: ed. by Wlodek Zawadzki. Berlin, Heidelberg: Springer Berlin Heidelberg, 1980. Chap. Magnetooptical properties of IV–VI compounds, pp. 427–446. ISBN: 978-3-540-38382-6. DOI: 10.1007/3-540-10261-2_56. URL: http://dx.doi.org/10.1007/3-540-10261-2_56.

[157] Inuk Kang and Frank W. Wise. 'Electronic structure and optical properties of PbS and PbSe quantum dots'. In: *J. Opt. Soc. Am. B* 14.7 (July 1997), pp. 1632–1646. DOI: 10.1364/JOSAB.14.001632. URL: http://josab.osa.org/abstract.cfm?URI=josab-14-7-1632.

[158] Valery I. Rupasov and Victor I. Klimov. 'Carrier multiplication in semiconductor nanocrystals via intraband optical transitions involving virtual biexciton states'. In: *Phys. Rev. B* 76 (12 Sept. 2007), p. 125321. DOI: 10.1103/PhysRevB.76.125321. URL: http://link.aps.org/doi/10.1103/PhysRevB.76.125321.

[159] Evan O. Kane. 'The semi-empirical approach to band structure'. In: *Journal of Physics and Chemistry of Solids* 8 (1959), pp. 38–44. ISSN: 0022-3697. DOI: http://dx.doi.org/10.1016/0022-3697(59)90269-0. URL: http://www.sciencedirect.com/science/article/pii/0022369759902690.

[160] Evan O. Kane. 'Band structure of indium antimonide'. In: *Journal of Physics and Chemistry of Solids* 1.4 (1957), pp. 249–261. ISSN: 0022-3697. DOI: http:

//dx.doi.org/10.1016/0022-3697(57)90013-6. URL: http://www.sciencedirect.com/science/article/pii/0022369757900136.

[161] E.O. Kane. 'Energy band structure in p-type germanium and silicon'. In: *Journal of Physics and Chemistry of Solids* 1.1 (1956), pp. 82–99. ISSN: 0022-3697. DOI: http://dx.doi.org/10.1016/0022-3697(56)90014-2. URL: http://www.sciencedirect.com/science/article/pii/0022369756900142.

[162] Lok C. Lew Yan Voon and Mortzen Willatzen. *The $\boldsymbol{k}\cdot\boldsymbol{p}$ Method–Electronic Properties of Semiconductors*. Springer, 2009. ISBN: 978-3-540-92871-3. DOI: 10.1007/978-3-540-92872-0.

[163] E.O. Kane. 'Chapter 3 The $\vec{k}\cdot\vec{p}$ Method'. In: *Semiconductors and Semimetals*. Ed. by R.K. Willardson and Albert C. Beer. Semiconductors and Semimetals. Elsevier, 1966, pp. 75–100. DOI: http://dx.doi.org/10.1016/S0080-8784(08)62376-5. URL: http://www.sciencedirect.com/science/article/pii/S0080878408623765.

[164] Ahun Lien Chuang. *Physics of Optoelectronic Devices*. Wiley, 1995. ISBN: 0-471-10939-8.

[165] Roman Vaxenburg and Efrat Lifshitz. 'Alloy and heterostructure architectures as promising tools for controlling electronic properties of semiconductor quantum dots'. In: *Phys. Rev. B* 85 (7 Feb. 2012), p. 075304. DOI: 10.1103/PhysRevB.85.075304. URL: http://link.aps.org/doi/10.1103/PhysRevB.85.075304.

[166] D. L. Mitchell and R. F. Wallis. 'Theoretical Energy-Band Parameters for the Lead Salts'. In: *Phys. Rev.* 151 (2 Nov. 1966), pp. 581–595. DOI: 10.1103/PhysRev.151.581. URL: http://link.aps.org/doi/10.1103/PhysRev.151.581.

[167] J.O. Dimmock. *The Physics of Semimetals and Narrow-Gap Semiconductors*. Ed. by D. L. Carter and R.T. Bates. Pergamon, Oxford, 1971.

[168] G. A. Baraff and D. Gershoni. 'Eigenfunction-expansion method for solving the quantum-wire problem: Formulation'. In: *Phys. Rev. B* 43 (5 Feb. 1991), pp. 4011–4022. DOI: 10.1103/PhysRevB.43.4011. URL: http://link.aps.org/doi/10.1103/PhysRevB.43.4011.

[169] D. Gershoni, C. H. Henry and G. A. Baraff. 'Calculating the optical properties of multidimensional heterostructures: Application to the modeling of quaternary quantum well lasers'. In: *IEEE Journal of Quantum Electronics* 29.9 (1993), pp. 2433–2450. ISSN: 0018-9197. DOI: 10.1109/3.247701.

[170] Marek Korkusinski, Oleksandr Voznyy and Pawel Hawrylak. 'Fine Structure and Size Dependence of Exciton and Biexciton Optical Spectra in CdSe Nanocrystals'. In: *Phys. Rev. B.* 82 (2010).

[171] Marek Korkusinski, Oleksandr Voznyy and Pawel Hawrylak. 'Theory of highly excited semiconductor nanostructures including Auger coupling: Exciton-biexciton mixing in CdSe nanocrystals'. In: *Phys. Rev. B* 84 (15 Oct. 2011). DOI: 10.1103/PhysRevB.84.155327. URL: http://link.aps.org/doi/10.1103/PhysRevB.84.155327.

[172] Urs Aeberhard et al. 'Fluorescence of colloidal PbSe/PbS QDs in NIR luminescent solar concentrators'. In: *Phys. Chem. Chem. Phys.* 14 (47 2012), pp. 16223–16228. DOI: 10.1039/C2CP42213A. URL: http://dx.doi.org/10.1039/C2CP42213A.

[173] Michael A. Parker. *Physics of Optoelectronics*. Taylor and Francis, 2005.

[174] Al. L. Efros. 'Luminescence polarization of CdSe microcrystals'. In: *Phys. Rev. B* 46 (12 1992), pp. 7448–7458. DOI: 10.1103/PhysRevB.46.7448. URL: http://link.aps.org/doi/10.1103/PhysRevB.46.7448.

[175] Marco Califano, Alberto Franceschetti and Alex Zunger. 'Temperature Dependence of Excitonic Radiative Decay in CdSe Quantum Dots: The Role of Surface Hole Traps'. In: *Nano Letters* 5.12 (2005). PMID: 16351178,

pp. 2360–2364. DOI: 10.1021/nl051027p. eprint: http://dx.doi.org/10.1021/nl051027p. URL: http://dx.doi.org/10.1021/nl051027p.

[176] A. Franceschetti et al. 'Many-Body Pseudopotential Theory of Excitons in InP and CdSe Quantum Dots'. In: *Physical Review B* 60.3 (1999).

[177] P G Bolcatto and C R Proetto. 'Partially confined excitons in semiconductor nanocrystals with a finite size dielectric interface'. In: *Journal of Physics: Condensed Matter* 13.2 (2001), p. 319. URL: http://stacks.iop.org/0953-8984/13/i=2/a=309.

[178] Lin-Wang Wang et al. 'Pseudopotential Theory of Auger Processes in CdSe Quantum Dots'. In: *Phys. Rev. Lett.* 91 (5 July 2003), p. 056404. DOI: 10.1103/PhysRevLett.91.056404. URL: http://link.aps.org/doi/10.1103/PhysRevLett.91.056404.

[179] Marco Califano, Alex Zunger and Alberto Franceschetti. 'Direct carrier multiplication due to inverse Auger scattering in CdSe quantum dots'. In: *Applied Physics Letters* 84.13 (2004), pp. 2409–2411. DOI: http://dx.doi.org/10.1063/1.1690104. URL: http://scitation.aip.org/content/aip/journal/apl/84/13/10.1063/1.1690104.

[180] Maryam Azizi and Paweł Machnikowski. 'Interband Coulomb coupling in narrow-gap semiconductor nanocrystals: $\mathbf{k}\cdot\mathbf{p}$ theory'. In: *Physical Review B* 91 (19 2015). DOI: 10.1103/PhysRevB.91.195314. URL: http://link.aps.org/doi/10.1103/PhysRevB.91.195314.

[181] Celso de Mello Donegá and Rolf Koole. 'Size Dependence of the Spontaneous Emission Rate and Absorption Cross Section of CdSe and CdTe Quantum Dots'. In: *The Journal of Physical Chemistry C* 113.16 (2009), pp. 6511–6520. DOI: 10.1021/jp811329r. URL: http://dx.doi.org/10.1021/jp811329r.

[182] E. Sadeghi and A. Avazpour. 'Binding energy of an off-center donor impurity in ellipsoidal quantum dot with parabolic confinement potential'.

In: *Physica B: Condensed Matter* 406.2 (2011), pp. 241–244. ISSN: 0921-4526. DOI: http://dx.doi.org/10.1016/j.physb.2010.10.051. URL: http://www.sciencedirect.com/science/article/pii/S0921452610010070.

[183] G Cantele, D Ninno and G Iadonisi. 'Confined states in ellipsoidal quantum dots'. In: *Journal of Physics: Condensed Matter* 12.42 (2000), p. 9019. URL: http://stacks.iop.org/0953-8984/12/i=42/a=308.

[184] E. Sadeghi. 'Optical nutation in multilayered ellipsoidal quantum dots'. In: *Physica E: Low-dimensional Systems and Nanostructures* 73 (2015), pp. 1–6. ISSN: 1386-9477. DOI: http://dx.doi.org/10.1016/j.physe.2015.05.015. URL: http://www.sciencedirect.com/science/article/pii/S1386947715300497.

[185] Marco Califano, Alberto Franceschetti and Alex Zunger. 'Lifetime and polarization of the radiative decay of excitons, biexcitons, and trions in CdSe nanocrystal quantum dots'. In: *Phys. Rev. B* 75 (11 Mar. 2007), p. 115401. DOI: 10.1103/PhysRevB.75.115401. URL: http://link.aps.org/doi/10.1103/PhysRevB.75.115401.

[186] Marina A. Leontiadou et al. 'Influence of elevated radiative lifetime on efficiency of CdSe/CdTe Type {II} colloidal quantum dot based solar cells'. In: *Solar Energy Materials and Solar Cells* (2016), pages. ISSN: 0927-0248. DOI: http://dx.doi.org/10.1016/j.solmat.2016.01.018. URL: http://www.sciencedirect.com/science/article/pii/S0927024816000295.

[187] J. M. An, A. Franceschetti and A. Zunger. 'The Excitonic Exchange Splitting and Radiative Lifetime in PbSe Quantum Dots'. In: *Nano Letters* 7.7 (2007), pp. 2129–2135. DOI: 10.1021/nl071219f. URL: http://dx.doi.org/10.1021/nl071219f.

[188] Jacek M Miloszewski, Thomas Walsh and Stanko Tomić. 'Influence of dielectric environment on exciton and bi-exciton properties in colloidal,

type II quantum dots'. In: *Journal of Physics: Conference Series* 609.1 (2015), p. 012003. URL: http://stacks.iop.org/1742-6596/609/i=1/a=012003.